CRANFIELD UNIVERSITY

JEREMY DOUCET

FATIGUE LIFE ENHANCEMENT OF AIRCRAFT STRUCTURES THROUGH BONDED CRACK RETARDERS (BCR)

PhD
Academic Year: 2015 - 2016

Supervisor: Dr. X. Zhang and Prof. P.E. Irving
September 2015

CRANFIELD UNIVERSITY

School of Aerospace, Transport and Manufacturing

PhD

Academic Year 2015 - 2016

JEREMY DOUCET

FATIGUE LIFE ENHANCEMENT OF AIRCRAFT STRUCTURES THROUGH BONDED CRACK RETARDERS (BCR)

Supervisor: Dr. X. Zhang and Prof. P.E. Irving
September 2015

ABSTRACT

The trend in aircraft design is to produce greener airplanes through lighter structures and/or structures with extended life and reduced maintenance. Bonded crack retarders (BCR) are one of the solutions towards that objective. BCR are reinforcing straps bonded to the structure in order to improve the fatigue and damage tolerance properties of the assembly. The aim of this study was to demonstrate that the BCR hybrid technology – beneficial for upper wing cover – could also be applied to lower wing covers. The project also focused on evaluating BCR most important parameters.

The fatigue life improvement obtained from BCR was evaluated through a series of coupons and skin-stringer assemblies tested under constant and variable amplitude loading. While the coupon tests demonstrated a life improvement of only 17% under constant amplitude loading, the variable amplitude load tests performed on the skin-stringer assembly demonstrated increased fatigue lives with a factor of 5 and reduced crack growth rates with a factor of 5 to 6.

A finite element calculation tool was developed in order to conduct a parametric analysis of BCR geometry through the evaluation of the substrate stress intensity factor in the case of fatigue loading. The main difficulty was to include the interacting mechanism of the substrate lead crack and the disbond of the adhesive layer. The novelty of the approach was to incorporate the fatigue delamination calculation in order to evaluate the fatigue disbond propagation with crack growth. This was embedded in a 3D finite element design tool ReSLIC (Reinforced Structures Life Improvement Calculation). A necessary step to the development of ReSLIC was the analysis of fatigue properties of the adhesive system in order to provide input data for fatigue delamination calculations. To that end, a series of fatigue tests were performed in pure Mode I, pure Mode II and mixed mode with ratios of 25%, 50% and 75% of mode II.

The design tool predictions were validated against coupon test results and demonstrated life calculation errors of 16% for constant amplitude loading. No

disbond was predicted for the M(T) coupons, as observed during testing. The calculation tool was then used to carry out a parametric analysis on the coupons geometry. It was found that stress intensity factors of the reinforced M(T) coupons stay unchanged with disbonding and present a greater reduction with a wide strap than a narrow one. Changing the thickness of the substrate with the same ratio of reinforcement showed not influence on the stress intensity factors.

Hence, the difference in life improvement and crack growth rate reduction observed between M(T) coupons and panels was explained by FE analysis that demonstrated that secondary bending was one of the major mechanisms influencing the amount of retardation and that it must be avoided in order to get the most benefit out of the BCR technology. This was demonstrated by the difference in crack retardation observed between the panel tests and the coupon tests.

Keywords: Life enhancement, bonded crack retarder, bonded strap, integral metallic structure, FEA, fatigue delamination, mixed mode delamination.

ACKNOWLEDGEMENTS

I would like to thank my supervisors Prof. Phil Irving and Dr. Xiang Zhang for their constant support throughout this research project and for the guidance that they have been providing me with.

I would also like to acknowledge the support of Airbus and Alcoa and the financial support of the Technology Strategy Board.

On the technical side of things, testing would not have been possible without the help of Jim Hurley at the Composite Centre, Ben Hopper and Dr. Isidro Durazo. I cannot put a figure on the number of bolts that we tightened and untightened on the panel tests. I also have to thank all the students from the Australian Air Force who contributed to this research through their individual projects.

Special thanks go to my colleagues from the Damage Tolerance Group, Niall, Danny, Octave, Muktar, Thomas, Osman and Yao with whom I shared very good moments in and out of the office.

I am also grateful to my family for everything they have done to make things easier for me throughout these years.

Finally, I would like to thank my partner Céline who has constantly been supporting me and who has always been there to help me overcome difficult moments and stay on track. Thank you for your patience.

TABLE OF CONTENTS

LIST OF ABBREVIATIONS and SYMBOLS

BCR	Bonded Crack Retarders
VCCT	Virtual Crack Closure Technique
MVCCT	Modified Virtual Crack Closure Technique
SIF	Stress Intensity Factor
CGR	Crack Growth Rate
FML	Fibre Metal Laminate
DCB	Double Cantilevered Beam
ELS	End-Loaded Split
MMB	Mixed Mode Bending
CZM	Cohesive Zone Model
SERR	Strain Energy Release Rate
ARALL	Aramid Aluminium Laminate
GLARE	Glass LAminate Reinforced Epoxy
μ	Reinforcement stiffness ratio - $\mu = \frac{\sum(E_{Strap}A_{Strap})}{(E_{Al}A_{Al})+\sum(E_{Strap}A_{Strap})}$ **(0-1)**
E_{Strap}	Strap modulus of elasticity
A_{Strap}	Strap cross sectional area (all reinforcement)
E_{Al}	Substrate modulus of elasticity
A_{Al}	Substrate cross sectional area
HDT	High Damage Tolerance

Chapitre 1 : Introduction:

1.1 Background

The current goal in the design of airplane structures is towards structures that have reduced weight, reduced cost, reduced maintenance and are easily certifiable [1]. This corresponds to a demand from customers for lighter structures in order to achieve environmental objectives.

This creates a growing competition between metals and composite design. Hence aluminium companies together with aircraft manufacturer work on new solutions based on metallic designs that present enhanced performance in comparison to the previous designs. Among these solutions are the use of materials with enhanced properties and reduced density (aluminium lithium alloys like 2199-T8E79 alloys [2], AlMgSc alloys, and fibre metal laminates) and the use of new technologies such as friction stir welding or metal bonding (Figure 1-1). The combination of these technologies will lead to integral structures that have reduced cost and reduced weight. The drawback of such a technology is the lack of damage tolerance.

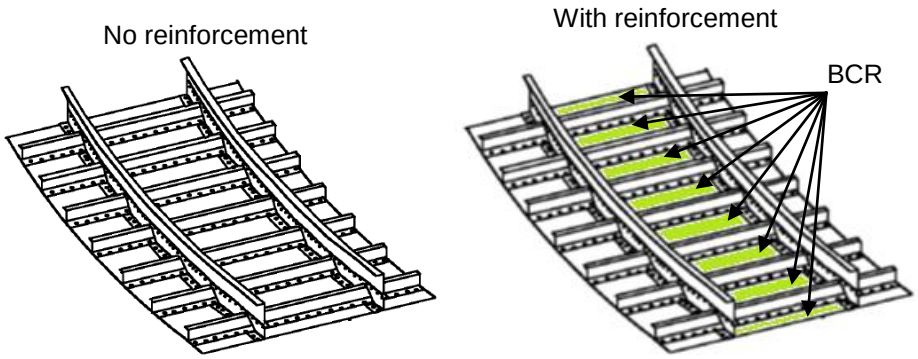

Figure 1-1 : Built up design without reinforcement (left) and with reinforcement bonded to the skin structure (right) – green straps [3]

Aircraft regulations state [4] that an aircraft structure must be able to sustain certain loads even in the situation of a failed part or the presence of a crack. This is a damage tolerance requirement. In addition, the fatigue analysis of the structure must be done so that the detection of the crack is made before it has reached a catastrophic length. If a design complies with these two requirements it is then qualified as damage tolerant.

The current issue with integral structure damage tolerance comes from the fact that if a crack starts to develop in the structure, either from a rivet hole or a material defect, the crack will propagate -- due to the fatigue loading to which the structure is subjected -- and no feature will provide crack retardation before it reaches a critical length. The structure is also not damage tolerant as it possesses a single load path in comparison to multiple load path designs found in riveted structures. In addition, the developments made on aluminium alloy have improved fatigue strength but not the crack growth resistance.

One solution to that lack of damage tolerance is the use of selective reinforcement (Figure 1-1 and Figure 1-2) which consists of adhesively bonded doublers that will improve the damage tolerance of the integral structure in order to achieve the regulation requirements. In the present case, the terminology Bonded Crack Retarders (BCR) will be used for these items.

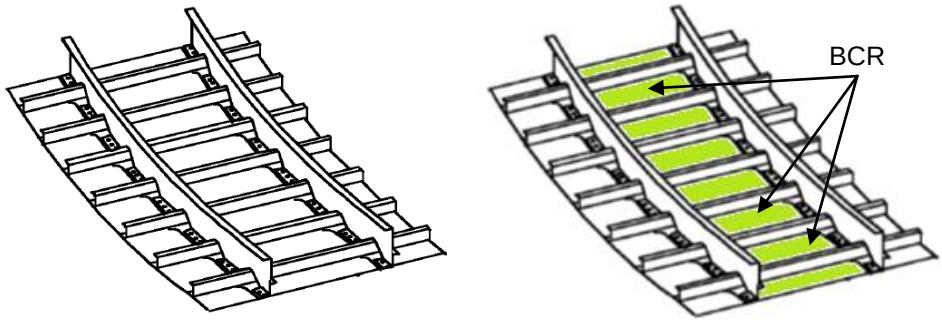

Figure 1-2 : Integrally machined design without reinforcement (left) and with reinforcement (right) [3]

Not only can the BCR technology be used to provide damage tolerant performance to integral structure, it can also be employed with bolted assemblies in order to provide crack retardation. This will increase the interval between inspections. Its use in such assemblies will also make it possible to optimise the weight of the components due to the additional load path brought by the reinforcements.

Modelling and testing work performed in past investigations [5]–[19] have proved that BCR can be beneficial to the life improvement of aircraft structures. This was demonstrated in particular for upper wing applications in [5] during the ‘BCR’ project. All specimens referring to that study will be referred to as ‘BCR’

specimen. These are specific of an upper wing case with substrates of 10 mm in thickness reinforced with different strap geometries and materials.

Despite that work, no 3D design tool has been produced in order to define the use of BCR in primary aircraft structures and little is known on the parameters that are most likely to change the behaviour of BCR structures such as the influence of geometry, disbonding, etc. Hence the aim of the AIRstream project, a successor to the BCR project was to study and clarify all the points cited above. The AIRstream project [20] on the other hand was focused on lower wing applications, which implies thinner structure – specimen used will be 5 mm thick instead of 10 mm in the past project – and the loading envelope will also be representative of the main tensile stresses observed in a lower wing case. All specimens referring to that project will be designated ‘AIRstream’ coupons and panels.

1.2 Aim and Objectives

The aims of the current study are to demonstrate that bonded crack retarders can be applied to an aircraft lower wing cover and to perform a study of the design variables for BCR. The objectives are:

- To evaluate the most important parameters regarding the interaction between the substrate and the reinforcement with a particular focus on the interaction between the substrate crack and the disbonding observed at the interface reinforcement /substrate.
- To establish the fatigue disbonding growth law of the interface between reinforcement and substrate.
- To develop a finite element based design tool for the calculation of the stress intensity factor of reinforced structure, then used to evaluate the fatigue life of the assembly.
- To measure the fatigue life improvement due to the use of BCR both through experimental evidence and finite element analysis.

1.3 Thesis structure

The thesis has two major subjects, the **testing** of coupons and reinforced structures and the **modelling** of BCR. The first part of the thesis – Chapter 2 – gives the theoretical framework used in the calculation developed later in the thesis. Chapter 3 presents a survey of the development of BCR with a review of the technology and how it has been modelled through finite element analysis. A particular focus will be the modelling of the disbonding that is thoroughly studied in that thesis.

The second part of the thesis reviews all the coupons and panels test that have been performed with first the M(T) coupons, secondly the experimental work carried out on the reinforced panels and finally the collection of fatigue data of the adhesive system.

Chapter 7 describes the methodology adopted for the modelling of bonded crack retarders. Chapter 8 presents the development and algorithm used to build the finite element design tool –based on the previously described methodology - that is used to calculate the stress intensity factor of BCR structures and Chapter 9 demonstrates the validity of the tool.

Chapter 10 makes use of the design tool in order to conduct a parametric study of the effects of the BCR geometry and disbonding on the retardation level.

The final three chapters first cover different discussion points following the test and modelling results and give the conclusions of the work carried out in this thesis as well as recommendations for future work.

Chapitre 2 : Theoretical framework for fracture and fatigue of aircraft

The aim of this chapter is to give a background on fracture mechanics and the use of fracture mechanics to predict the fatigue life of structures.

The first section of the chapter is dedicated to the definition of the stress intensity factor (SIF). The next section will summarize the different techniques used to calculate the SIF using the finite element method. The third section will review the fatigue crack growth laws. The final section will discuss the calculation of the fatigue crack growth life of a cracked specimen.

Fracture mechanics is a mature field and there are books written by Anderson [21], Schive [22], Broek [23], [24] which describe in detail the subject. What follows is a summary of the points of most relevance to bonded crack retarders for aerospace.

2.1 Fracture mechanics

The traditional design of structures is based on the strength of materials and states that the strength should be greater than the applied stress. Brittle fracture is avoided by applying safety factors combined with the rule of having a minimum tensile elongation of the material. The fracture mechanics approach is based on the combination of the flaw size and the fracture toughness as the main material properties as opposed to the yield or tensile strength of the material. Two approaches are employed in fracture mechanics in order to evaluate the crack tip stress field; the stress intensity factor approach and the energy approach.

2.1.1 Fracture modes

Displacement of crack faces can be reduced to a combination of the following modes. Mode I corresponds to an opening mode and the displacement is applied normal to the plane of the crack. Mode II is a shear mode where one face is sliding in opposite direction to the other. Mode III is an out-of-plane shear where the two cracked surface foresee shear displacement normal to the

crack plane. The crack phenomenon can be any of these configurations or a combination of these mechanisms.

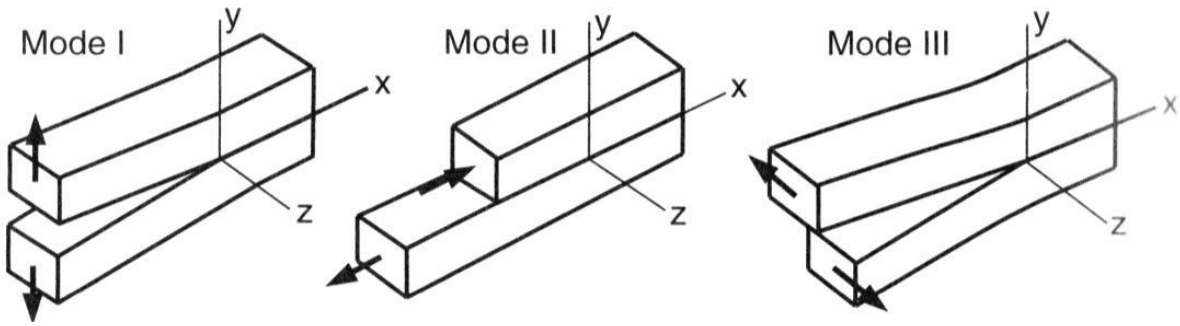

Figure 2-1 : Mode of loading of a crack

2.1.2 Stress Intensity Factor (SIF) and energy approach

Irwin [25] developed an approach of fracture mechanics to apply to metals based on the early work from Westergaard [26]: the Stress Intensity Factor (SIF). This is based on an expression of the stresses in a body that is submitted to external loads assuming that the material is linear elastic. If one assumed a crack as represented in Figure 2-2 with the local coordinate system, it is possible to define the stress in the plate.

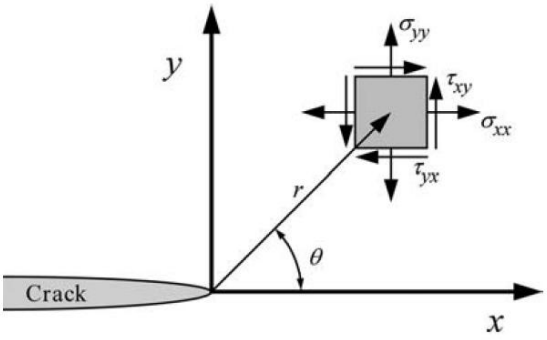

$$\sigma_{ij} = \left(\frac{k}{\sqrt{r}}\right) f_{ij}(\theta) + \sum_{m=0}^{\infty} A_m r^{\frac{m}{2}} g_{ij}^{(m)}(\theta) \qquad \textbf{(2-1)}$$

Figure 2-2 : Coordinate system at the crack tip and definition of stress field [21]

σ_{ij}, is the stress tensor, and *r* and θ the polar coordinates of the point where the stress is studied. *k* is a constant and f_{ij} is a dimensionless function that depends on θ. The second part of the expression depends on the geometry of the case studied. It is noticed though that a dominant term in the expression is $1/\sqrt{r}$. Hence the stress near the crack tip varies with $1/\sqrt{r}$ and as $r \rightarrow 0$, the first term in the expression goes to an infinite value while the second term tends to zero.

It shows that at the crack tip ($r \rightarrow 0$) there is a stress singularity that depends on $1/\sqrt{r}$, k and f_{ij}. This is applicable for each mode of loading described in the previous paragraph. Introducing the factor $K = k\sqrt{2\pi}$ **(2-2)**, it is possible to give the following expressions for each mode of loading in the case of an isotropic linear elastic material.

$$\lim_{r\to 0} \sigma_{ij}^{(I)} = \frac{K_I}{\sqrt{2\pi r}} f_{ij}^{(I)}(\theta) \qquad \lim_{r\to 0} \sigma_{ij}^{(II)} = \frac{K_{II}}{\sqrt{2\pi r}} f_{ij}^{(II)}(\theta) \qquad \lim_{r\to 0} \sigma_{ij}^{(III)} = \frac{K_{III}}{\sqrt{2\pi r}} f_{ij}^{(III)}(\theta)$$

(2-3) **(2-4)** **(2-5)**

In the case of a structure that is under a mixture of mode, the contribution of each mode is added together:

$$\sigma_{ij}^{(total)} = \sigma_{ij}^{(I)} + \sigma_{ij}^{(II)} + \sigma_{ij}^{(III)} \quad \textbf{(2-6)}$$

In the case of mode I, the stress field components are:

$$\sigma_{xx} = \frac{K_I}{\sqrt{2\pi r}} cos\left(\frac{\theta}{2}\right)\left[1 - sin\left(\frac{\theta}{2}\right) sin\left(\frac{3\theta}{2}\right)\right] \qquad \tau_{xy} = \frac{K_I}{\sqrt{2\pi r}} cos\left(\frac{\theta}{2}\right) sin\left(\frac{\theta}{2}\right) cos\left(\frac{3\theta}{2}\right)$$

(2-7) **(2-8)**

$$\sigma_{yy} = \frac{K_I}{\sqrt{2\pi r}} cos\left(\frac{\theta}{2}\right)\left[1 + sin\left(\frac{\theta}{2}\right) sin\left(\frac{3\theta}{2}\right)\right]$$

$\tau_{xz} = 0$

(2-9)

$$\sigma_{zz} = \begin{cases} 0 & (Plane\ Stress) \\ \nu(\sigma_{xx} + \sigma_{yy}) & (Plane\ Strain) \end{cases}$$

$\tau_{yz} = 0$

(2-10)

Where K_I is the mode I stress intensity factor.

In the case where $\theta = 0$, the equations above simplify to:

$$\sigma_{xx} = \sigma_{yy} = \frac{K_I}{\sqrt{2\pi r}} \quad \textbf{(2-11)}$$

The shear stress becomes zero and that implies that the crack plane is the plane of principal stress for that configuration. In that particular case the

equation is only valid near the crack tip. In fact, as $r \rightarrow 0$, the stresses go to infinity as shown in Figure 2-3.

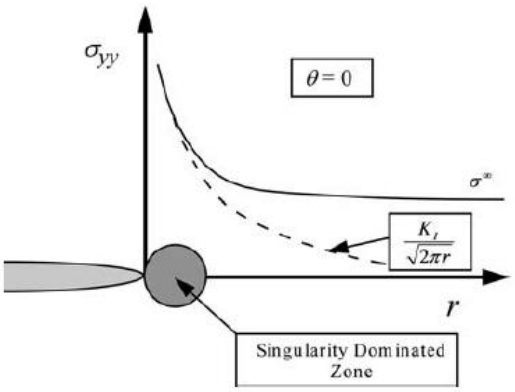

Figure 2-3 : Mode I singularity

Hence there is a stress singularity near the crack tip. Nevertheless as *r* becomes bigger the expression tends to become null but this is not the case as away from the crack the stress σ_{∞} will be governed by the applied loads and the boundary conditions. This shows that the previous equation is only valid near the crack tip in a singularity dominated area.

Hence in order to describe the stress singularity near the crack tip, one needs a more general expression of the stress intensity factor at the crack tip. In the particular application of a Mode I loading, the *K* solution can always be seen as a through crack configuration using a correction factor.

$$K_I = \beta\sigma\sqrt{\pi a} \quad \textbf{(2-12)}$$

Where β is a dimensionless correction factor that depends on the geometry of the specimen and the applied boundary conditions. σ is the remote applied stress and *a* is the half crack length.

Expressions for simple geometries can be found in the literature [21], [27], [28] in order to find a solution for a given specimen. In the case of the middle crack tension specimens used in this thesis, the solution is given by $\beta = \frac{1}{\sqrt{cos\left(\frac{\pi a}{2b}\right)}}$ **(2-13)** with *a* the half crack length and *2b* the width of the specimen.

Irwin reformulated Griffith's formulation of the state of equilibrium of a cracked surface with the introduction of the strain energy release rate constant *G* giving it a more convenient form for solving engineering problems.

$$G = -\frac{d\pi}{dA} \quad \textbf{(2-14)}$$

G represents the energy available for the crack extension, π is the potential energy due to the internal strain energy and *dA* is the increase in crack area. The crack extension occurs when *G* has reached the critical value G_c which is the fracture toughness of the material. By definition of the potential energy π, it is demonstrated that a general expression of *G* is:

$$G = \frac{P^2}{2b}\frac{dC}{dA} \quad \textbf{(2-15)}$$

with $C = \frac{\Delta}{P}$ **(2-16)** the compliance of the plate (inverse of the plate stiffness) and *P* the applied load.

2.1.3 Relation between K and G.

In the case of linear elastic materials, a relationship exists between K and G. In the assumption of a through crack in an infinite plate subjected to uniform tensile stress, the relationship is:

$$G = \frac{K_I^2}{E'} \quad \textbf{(2-17)} \qquad \text{with} \quad \begin{cases} E' = E \text{ for plane stress} \\ E' = \frac{E}{1-\nu^2} \text{ for plane strain} \end{cases}$$

2.2 Calculation of K by FEM

As developed earlier in this chapter, it was demonstrated that the stress intensity factor can be calculated using the expression $K_I = \beta\sigma\sqrt{\pi a}$ **(2-18)**. Solutions can be found in the literature for the most common geometries [27], [29] and Anderson [21] gives some of the solution for the most common geometries studied in fracture mechanics. Nevertheless when structures

become more complex, no compendium exist for the β values and it needs to be calculated.

This can be done through experimental methods (photo elasticity, compliance measurement, data extrapolation), analytical methods (Westergaard stress function, superposition Green's functions, weight functions or dislocation method) and also through numerical method (Finite element analysis, boundary element method) [28], [30].

The most common analysis is through finite element computations. Two aspects need to be considered when trying to determine the stress intensity factor through finite element modelling:

- Modelling of the crack tip singularity

- Calculation of *K* from the finite element model output.

The modelling of the crack tip can be performed using different techniques. It can be done using refined mesh at the crack tip in order to be able to accurately calculate the stress and strain fields at the crack tip. Special crack tip elements can also be used. They use special displacement shape functions that take into account the singularity of the crack tip and can use coarse meshes. Byskov technique is one of them [31]. Another solution is the use of crack tip singularity elements that have modified positions of the mid-node positions of quadratic element such as the one developed by Barsoum [32] and Henshell and Shaw [33]. Additional transformation to this formulation is to merge nodes together in order to obtain the $1/\sqrt{r}$ singularity at the crack tip. Nevertheless, with the advance in computation capacity, the most common method used nowadays is a refinement of the mesh at the crack tip.

Several techniques exist in order to get the beta function i.e. the stress intensity factor K of the studied geometry through finite element analysis. They are divided into two categories, the direct or substitution approaches and the indirect or energy approaches.

2.2.1 Direct approaches

These methods require a fine mesh in the vicinity of the crack but this can be avoided if special purpose elements are used.

The first method is the **displacement extrapolation** [34]–[36]method. The displacement obtained from the finite element analysis is used together with analytical solution in order to extrapolate the solution of the stress intensity factor near the crack tip. The **stress extrapolation** [37]–[39] method is based on the same principal but uses the stress equations in order to approximate the stress intensity factor.

2.2.2 Indirect approaches

These methods are not dependent on the mesh size as they are based on a change in energy due to the crack extension.

The first method is the **finite crack extension method** [40]. This method calculates the strain energy difference between two scenarios of crack length that correspond to one increment of crack length. It requires two finite element calculations and is less mesh dependent than the two previous direct methods. The second method is the **virtual crack extension method** [40], [41]. This method requires only one calculation to evaluate the energy release rate and one additional calculation of the stiffness matrix of the elements at the crack tip. The third method is the **virtual crack closure technique** [42]. This method is based on the crack closure method. It assumes that the energy necessary to extend the crack is identical to the energy to close the crack for one crack extension. Extensive details of the formulation have been outlined by Krueger in [42]. This method is widely used in finite element modelling of fracture mechanics. The final method is the calculation of the **J-integral**. This method requires only one FE model and is path independent. It is directly related to the stress intensity factor *K*.

2.3 Fatigue crack growth models

The phenomenon of fatigue cracking in metallic components can be divided into 3 steps which are the initiation, the propagation and the final failure. For example, crack initiation can be due to defects contained in the material, environmental degradation or in service damage. When a material is submitted to fatigue loading, cracks will propagate through plastic deformation. Despite the fact that the nominal stresses applied are below the fatigue limit of the material, the presence of notches or defects will result in stress concentration locally that produce stresses that are greater than those required to initiate cracks.

2.3.1 Governing parameters

The fatigue crack growth life calculation is based on the similitude principle. It states that the conditions at the crack tip are uniquely defined by the values of K_{max} and K_{min} (Figure 2-4). Hence if two structures of the same material containing a crack have an identical stress intensity factor range ΔK, they should have the same crack growth rate da/dN. In the case of constant amplitude cyclic loading, the relationship between the crack growth rate and the stress intensity factor takes the form:

$$\frac{da}{dN} = f(\Delta K, R) \quad \textbf{(2-19)}$$

where $\Delta K = K_{max} - K_{min}$ **(2-20)** and $R = K_{min}/K_{max}$ **(2-21)**

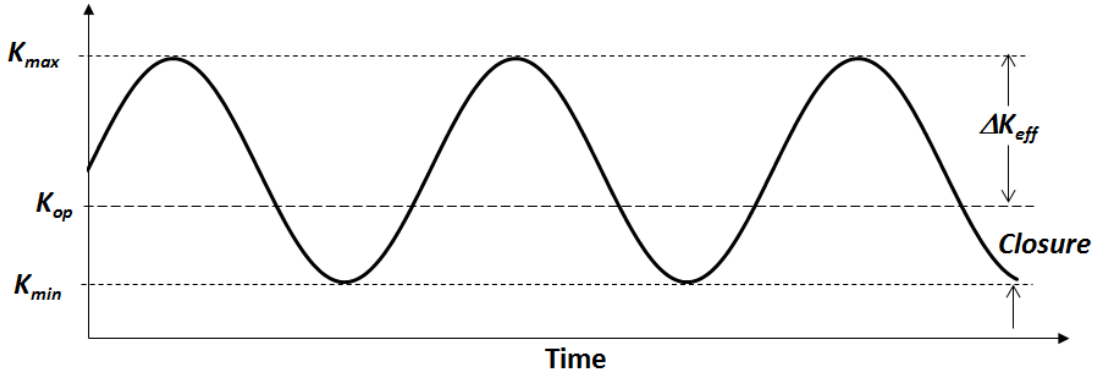

Figure 2-4 : Definition of governing parameters

This is assuming that the plastic zone is small enough to be contained within an elastic singularity zone.

Empirical equations *f* have been developed in order to represent the material crack growth rates. The integration of these equations leads to the evaluation of the fatigue life of the structure.

In case of variable amplitude cyclic loading, the values of K_{max} and K_{min} will also depend on the loading history. Hence the crack growth rates need to be defined using an additional parameter that takes into account any load history effect. The crack growth rate takes the form:

$\frac{da}{dN} = f(\Delta K, R, H)$ **(2-22)** with *H*, parameter that takes into account any history dependence.

Figure 2-5 shows a typical plot of *Log da/dN vs. Log ΔK* with a sigmoid shape. In that curve, the crack growth life is divided into three regions.

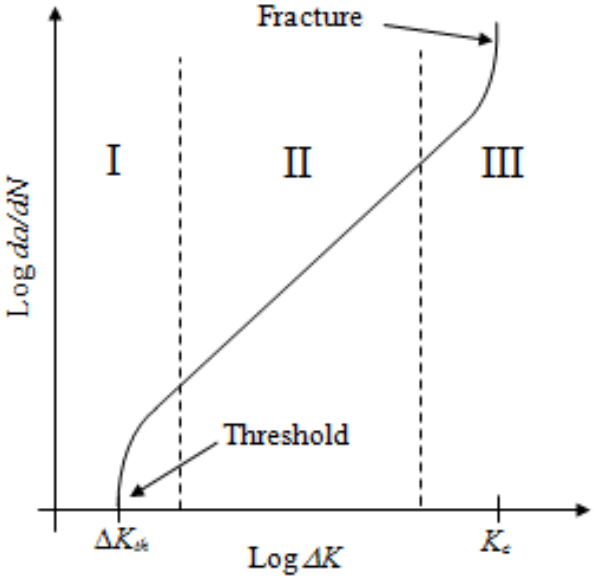

Figure 2-5 : Typical fatigue crack growth curve for metals [21]

Region I: Lower threshold region. The values are lower than 10^{-8} m/cycle which indicates slow crack growth rates. If ΔK is less than ΔK_{th}, no crack growth will be observed.

Region II: Slow and stable crack growth rate. It is the stable region of crack growth rates with a growth rate between 10^{-8} and 10^{-6} m/cycle.

Region III: Critical region where the crack growth rate is fast with values greater than 10^{-6} m/cycle.

The influence of the R-ratio depends on the region studied. While it will be insignificant in region II, it will have a greater influence in region I and III. In region I, a larger R-ratio means that the mean stress is increased, hence ΔK is increased which results in a larger crack growth rate. There is also an increase in crack growth rate with the R-ratio in region III.

2.3.2 Crack closure

The crack closure approach is based on the observation made by Elber [43]. He observed that for fatigue specimens, under high loads the compliance formulation agreed with standard formulation of fracture mechanics but under low loads, this compliance was not respected and corresponded to an un-cracked specimen. It was suggested that this was due to the contact between the surfaces at low loads greater than zero. Hence it was said that the stress intensity factor range was reduced which causes the crack growth rate to be reduced as well (Figure 2-4). It shows that for K below K_{op} (where the crack is still open) the crack becomes closed. Hence it does not contribute to the crack growth rate. An effective stress intensity factor was defined, using that observation with: $\Delta K_{eff} = K_{max} - K_{op}$ **(2-23)**.

Residuals stress fields are also responsible for crack closure. Residual stresses may apply a closure force to the crack faces. It is referred to as plasticity induced closure. It will shift the mean stress of the fatigue cycles but not change the stress amplitude.

2.3.3 Empirical fatigue crack growth laws

Paris and Erdogan [44] were the first to develop a power law associated to the region II of the crack growth rate based on experimental evidence. Commonly called the Paris Law, it is widely used in order to describe the crack growth rates of materials.

$$\frac{da}{dN} = C(\Delta K)^m \text{ (Paris equation) } \textbf{(2-24)}$$

Constant *C* and *m* are determined experimentally through curve fitting. The drawbacks of this equation are that it is not able to describe the exact behaviour in region I and III that are seen in Figure 2-5 as it restricted to the linear behaviour in region II and it does not take into account the influence of different R-ratios. ΔK becomes ΔK_{eff} in the case of crack closure.

Modifications were brought to the Paris equation in order to incorporate the effect of the R-ratio as well as a description of regions I and III. One of them is the Walker's law [45]. This law introduces the R-ratio effect.

$$\frac{da}{dN} = C\left\{\frac{\Delta K^m}{(1-R)^c}\right\} \text{ (Walker's equation) } \textbf{(2-25)}$$

Despite the improvement brought by the presence of the R-ratio in the equation, this formulation is still missing the accurate description of the region I and III

Forman [46], [47] developed another law that focuses on region II and III as well as taking into account the effect of the R-ratio.

$$\frac{da}{dN} = \frac{C\Delta K^m}{(1-R)K_c-\Delta K} \text{ (Forman's equation) } \textbf{(2-26)}$$

This formulation shows that as K_{max} reaches K_c, the crack growth rate reaches an infinite value. This equation assumes that the region III is defined by a superposition of fracture and fatigue rather than a plastic zone effect. The parameters *C* and *m* are found from curve fitting.

Forman's equation was later modified in order to also incorporate the effects of region I, the threshold region by incorporating the threshold term ΔK_{th}.

$$\frac{da}{dN} = \frac{C(\Delta K-\Delta K_{th})^m}{(1-R)(K_C-\Delta K)} \text{ (Modified Forman's equation) } \textbf{(2-27)}$$

This equation provides better results for low values of ΔK. Hence this equation covers all three region of the crack growth rate.

One of the most recent formulations is the NASGRO equation developed at NASA by Forman and Mettu [47], [48]. This equation takes into account the material behaviour in all three regions of the crack growth rate as well as the influence of the R-ratio.

$$\frac{da}{dN} = C\left[\left(\frac{1-f}{1-R}\right)\Delta K\right]^n \frac{\left(1-\frac{\Delta K_{th}}{\Delta K}\right)^p}{\left(1-\frac{K_{max}}{K_{crit}}\right)^q} \text{ (NASGRO equation) } \textbf{(2-28)}$$

With *C* and *n*, the material parameters defining the region II

p and *q* are also material parameters that respectively define the region I (near threshold) and region III (critical SIF).

f is a function that defines the crack opening (Figure 2-4).as:

$$f = \frac{K_{op}}{K_{max}} \begin{cases} max(R, A_0 + A_1 R + A_2 R^2 + A_3 R^3) & R \geq 0 \\ A_0 + A_1 R & -2 \leq R < 0 \\ A_0 - 2A_1 & R < -2 \end{cases} \textbf{(2-29)}$$

A_0, A_1, A_2 and A_3 definition can be found in [48]. K_{op} is the opening stress intensity factor (Figure 2-4). These parameters will take into account the plane stress/strain conditions and are defined by the loading conditions. The parameter K_{crit} takes into account any thickness effect.

Another method used to describe the fatigue crack growth rate of a material is point by point. In that case the rates are not defined by an equation but rather through a point by point definition that represent the best fitted line of the experimental data. The effect of the R-ratio is described through the use of that is not given, it can be interpolated using the Harter T-method [49]. The Harter T-method makes use of the Walker's equation previously described in order to interpolate the crack growth rate da/dN for a specific R-ratio [50] .

2.4 Calculation of the fatigue crack growth life

The calculation of the fatigue crack growth life of a structure can be carried out through the integration of the material law. In addition to the material law, the stress intensity factor and the R-ratio are necessary.

For any step *i* of the integration the crack length is a_i and the stress intensity factor is $\Delta K_i = \beta_i \Delta\sigma\sqrt{\pi a_i}$ **(2-30)** with β_i the stress intensity factor coefficient than can be obtained either through an analytical solution or through finite element modeling.

For each value of ΔK_i is associated a crack growth rate $^{da}/_{dN}\Big)_i$ for a certain R-ratio, $R = \frac{\sigma_{min}}{\sigma_{max}}$ **(2-31)** according to the material law (Figure 2-6).

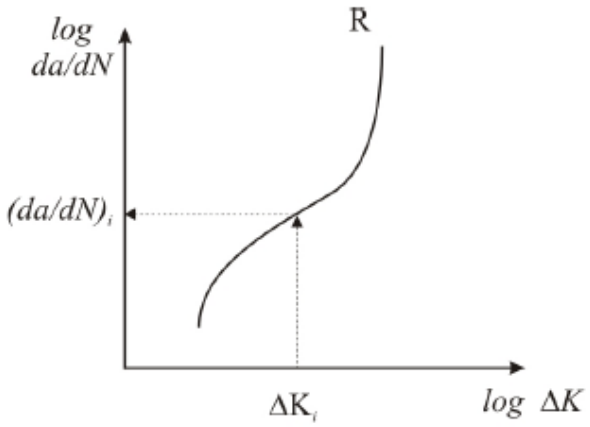

Figure 2-6 : Material law for the determination of the crack growth rate [51]

The integration step is defined as a certain number of cycles ΔN. Considering a small cycle increment, the stress intensity factor is assumed to stay constant during that increment which leads to:

$$\frac{\Delta a_i}{\Delta N} = \frac{da}{dN}\Big)_i \textbf{ (2-32)} \text{ hence } \Delta a_i = \frac{da}{dN}\Big)_i \Delta N \textbf{ (2-33)}$$

This leads to an increment in crack length and the total number of cycles with:

$$a_{i+1} = a_i + \Delta a_i \textbf{ (2-34)} \text{and } N_{i+1} = N_i + \Delta N \textbf{ (2-35)}$$

The integration is finished when the structure has reached a failure condition that can be either fracture or net section yield. The integration then gives the life of the structure as *a* vs. *N* as well as *da/dN* vs *a*.

Numerical solution such as AFGROW exists in order to conduct this calculation with the possibility to define retardation effects.

Chapitre 3 : Literature search

3.1 Bonded crack retarders

The literature survey of bonded crack retarders is in three parts. The first part reviews the work that has been performed on BCR since its first study in 1990 [14]. It describes briefly how bonded crack retarders work and outlines all the parameters that have been discovered as major contributor to the behaviour of BCR. The second part of the survey focuses on the modelling of reinforced structure through a review of the different techniques that have been used in the past. The final part of the survey focuses on the particular aspect of modelling the disbonding in BCR with a thorough audit of the state of the art techniques to model fatigue in adhesively bonded joints.

3.1.1 Bonded Crack Retarders: History, development and important parameters

- **The BCR history and development**

The first use of bonded strap to improve fatigue and damage tolerance of aircraft structures appeared through the development of composite patch repair [52]. Patch repair consists of the addition of material to a structure in a location of an existing crack in order to reduce the fatigue propagation of that crack. It was first developed in 1972 by the Defence Science and Technology Organisation (DSTO) to repair damaged aircraft. It differs from the BCR technology in a sense that the BCR are applied to a non-damaged part of the aircraft as a means to improve the damage tolerance when a crack develops whereas patch repair is applied when damage is detected in the structure. BCR are reinforcing straps bonded to the structure in order to **provide** an alternative loading path and slow down the propagation of an eventual crack. An example is shown in Figure 3-1.

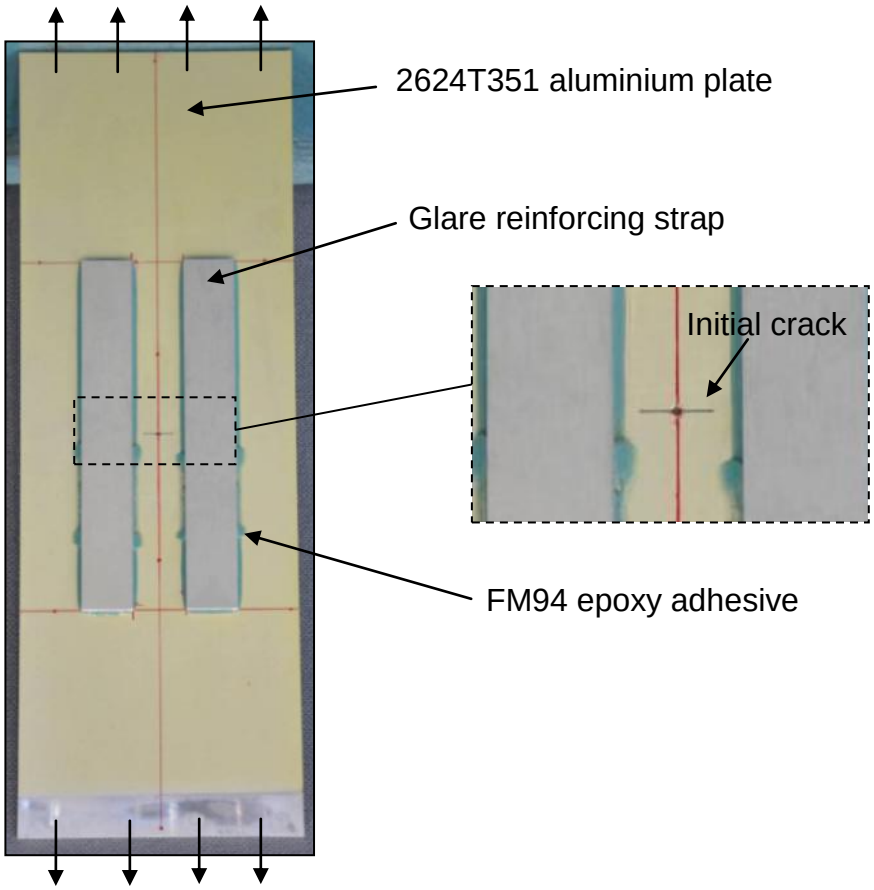

Figure 3-1 : Middle crack tension coupon with Glare BCR straps

BCR can be found in two major applications. The first one is the aeronautical industry [5], [7]–[9], [11]–[14], [53]–[57]. They are used to improve the damage tolerance of aluminium structures. Within this sector, there are different applications such as reinforcement of integrally machined panels [5], [12], [55], the reinforcement of bolted structures [14], [55] or also the reinforcement of friction stir welds [58], [59]. Early research carried out by Delft University [14] showed a possible increase in life of 80% for aluminium panels reinforced with ARALL straps. Recent research done at Cranfield University claimed a maximum improvement of 280% of the baseline fatigue life (test performed 3.8 times the life of the baseline) for the particular case of reinforced coupons tested at low stresses with the use of an aluminium strap [5]. Alcoa [12] reported an improvement of up to 4 times the life of the baseline for an application to reinforced panels with a possible weight reduction of 25%. Yu E Ma et al. [58], [59] proved that the BCR technology could also be used for improving the damage tolerance of welds with an increase in fatigue life of up to 200%.

The most recent “flying” application of this technology in aircraft structure is found on the A400M (Figure 3-2). In that case, it is used to reinforce the inner flange of the mainframe that carries heavy load due to wing bending and torque [56].

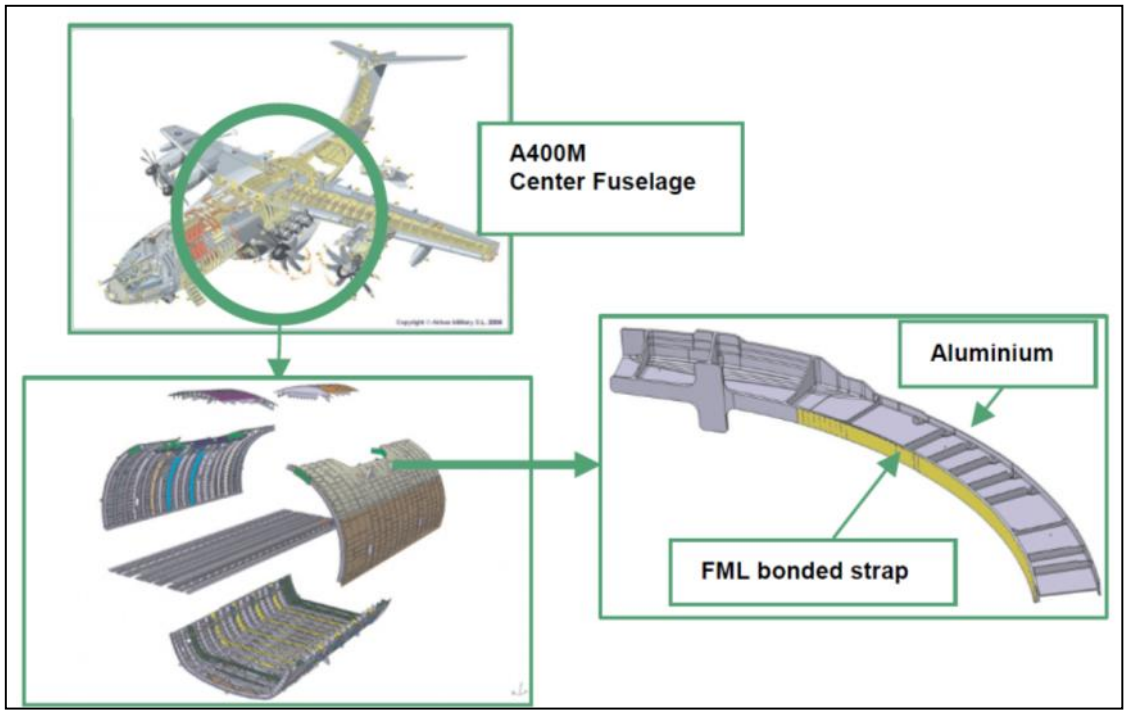

Figure 3-2: A 400M fuselage with central section and reinforced mainframe using the BCR technology through fibre metal laminates (FML) reinforcements [56]**.**

As seen in Figure 3-2, the reinforcement that is adhesively bonded to the inner flange is acting as a doubler on that frame. It will reduce the tensile stresses of the flange and inhibit cracks initiation or slow the propagation of eventual cracks.

The second application is found in the civil engineering industry where bonded straps are used to improve the damage tolerance of steel structures [10], [57], [60], [61]. Colombi studied the case of pre-stressed composite bonded to notched steel plates and conducted a parametric study of that configuration. It demonstrated that it was a promising technique to reinforce cracked part or prevent fatigue cracking due to crack closure effects and crack bridging that reduces the stresses range at the crack tip.

Other technologies for crack retardation is the use of crenulations [11], [14], [62]–[65] that demonstrated an increase in fatigue life as well but shows limitations in terms of damage tolerance as no secondary load path is present in the structure.

- **BCR: how do they work?**

The past studies carried out on BCR [5]–[14], [17], [19], [50], [53], [54], [56], [62], [66]–[68] gave a better understanding of the technology by demonstrating the phenomenon observed in BCR structures as well as studying the influence of different parameters such as the strap dimension, position and material, the effect of disbonding and thermal residual stresses as well as the effect of loading levels.

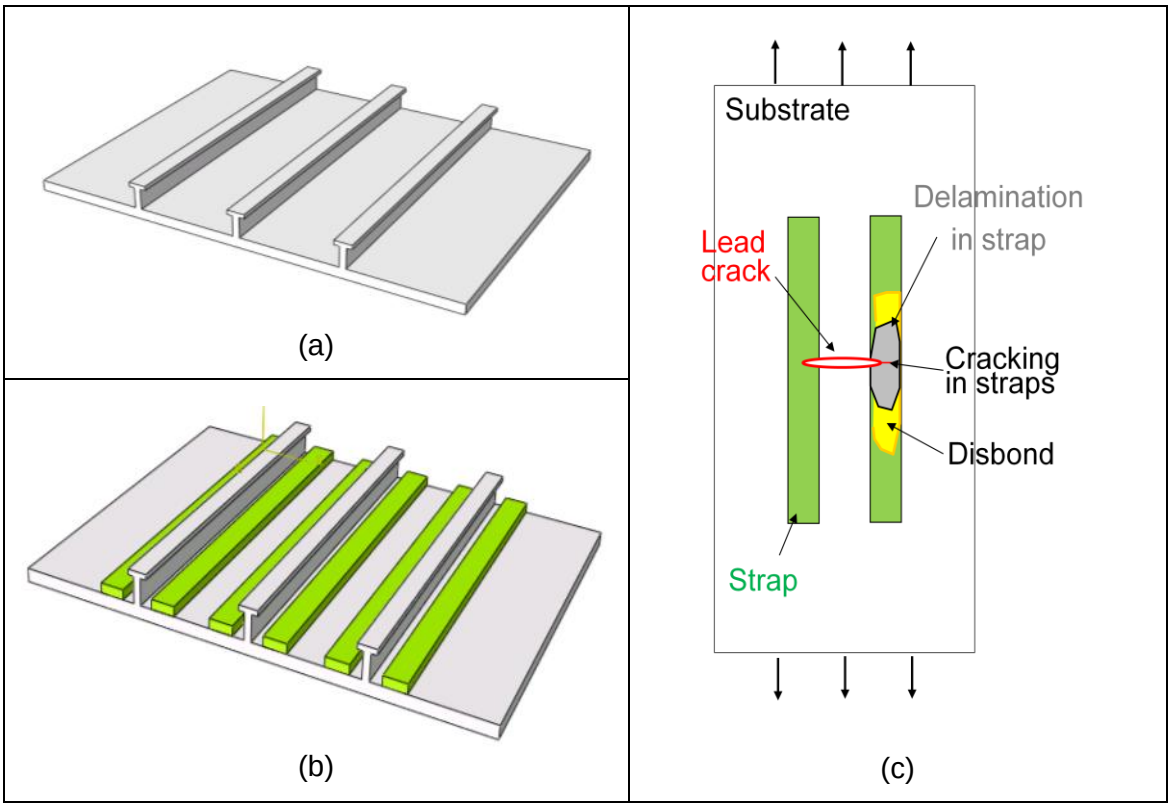

Figure 3-3 : Integrally machined structure without (a) and with BCR (b) and (c) representation of the mechanisms found in BCR [5]

Figure 3-3 (c) illustrates all the mechanisms of crack retardation that can be found in an M(T) coupon reinforced by two straps when submitted to fatigue loading. It shows that as the substrate crack propagates, its propagation rate is reduced due to the presence of the strap. As the crack goes underneath the

strap, the crack opening is reduced as the strap acts to bridge the two sides of the crack. Crack initiation can be observed in the strap as has been observed for aluminium straps in previous research [5], [53]–[55]. Disbonding of the strap from the substrate can also occur in the adhesive system along the crack path or at the end of the strap [5]. Delamination may also develop within the strap.

Due to the difference in coefficient of thermal expansion between the substrate and the strap, thermal residual stresses arise in the substrate due to the curing process of the adhesive used to bond the strap to the substrate. Because the reinforcement is applied on only one side of the specimen, secondary bending is observed. Finally moisture and thermal cycles also play major roles in the behaviour of bonded crack retarders.

Parametric studies looking at the most influential parameters governing the behaviour of BCRs are reported in the next section.

3.1.2 Parametric studies

- **Strap material and geometry**

The material used for the reinforcement are varied, with aluminium [5]–[7], [13], [14], [53]–[56], [58], [59], titanium [5]–[7], [13]–[15], [53]–[56], ARALL [14], GLARE [5]–[9], [13], CFRP [5], [10], [61], GFRP [5] as well as straps made of Boron/Epoxy [18].

The use of fibre metal laminates (FML) as a BCR material was first investigated by Schijve in 1990 [14] with the use of ARALL in comparison to other materials such as Titanium and aluminium. Heinimann et al. [12] later studied the use of another fibre metal laminate GLARE as a possible reinforcement for integrally machined panels. They also compared GLARE to straps made of aluminium. In both cases, it was proved that the fibre metal laminate was the most appropriate material to be used as BCRs. Heinimann in particular made the statement that the strap should use a material that is fatigue insensitive and possess a high static strength [12].

ARALL: Aramid Aluminium Laminate was developed by Delft University [14] with an objective to reduce the structural weight of aircraft. It consists of adhesively bonded aluminium layers and pre-impregnated aramid layer that provide fatigue and fracture resistance. This material presents good fatigue strength with very slow crack growth propagation properties. It is possible to obtain weight savings up to 20% by using Arall.

GLARE: Glass LAminate Reinforced Epoxy is a fibre metal laminate that consists of thin aluminium layers bonded together with glass fibre reinforced epoxy layers [70]. It was developed after ARALL in order to overcome the failure of aramid fibres under fatigue loading for fuselage section. GLARE possesses a reduced density in comparison to monolithic aluminium, good fire resistance properties as well as excellent fatigue and damage properties together with a satisfactory behaviour after impact. It is used for some parts of the fuselage on the A 380 aircraft [69].

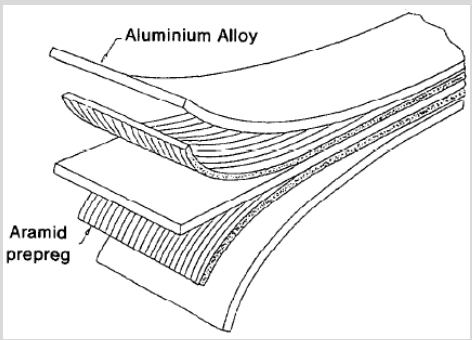

(a) ARALL: aluminium and aramid layers [72]

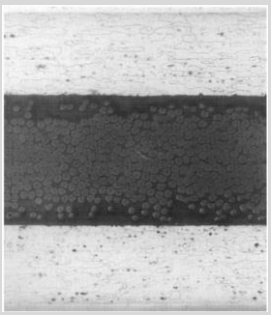

(b) ARALL cross section [17]

(c) Glare layup

Figure 3-4 : Fibre metal laminates ARALL and GLARE

GLARE can be found in different forms depending on the number of layers, orientation of the prepreg fibres as well as the aluminium gradient used. Table 3-1 illustrates these different grades.

Table 3-1 : Glare characteristics [70]

Glare grade	sub	Metal sheet thickness [mm] & alloy	Prepreg orientation* in each fibre layer**	Main beneficial characteristics
Glare1	-	0.3-0.4 7475-T761	0/0	fatigue, strength, yield stress
Glare 2	Glare 2A	0.2–0.5 2024-T3	0/0	fatigue, strength
	Glare 2B	0.2-0.5 2024-T3	90/90	fatigue, strength
Glare 3	-	0.2-0.5 2024-T3	0/90	fatigue, impact
Glare 4	Glare 4A	0.2-0.5 2024-T3	0/90/0	fatigue, strength in 0° direction
	Glare 4B	0.2-0.5 2024-T3	90/0/90	fatigue, strength in 90° direction
Glare 5	-	0.2-0.5 2024-T3	0/90/90/0	impact
Glare 6	Glare 6A	0.2-0.5 2024-T3	+45/-45	shear, off-axis properties
	Glare 6B	0.2-0.5 2024-T3	-45/+45	shear, off-axis properties

* All aluminium rolling directions in standard laminates are in the same orientation; the rolling direction is defined as 0°, the transverse rolling direction is defined as 90°.

** The number of orientations in this column is equal to the number of prepregs (each nominally 0.127 mm thick) in each fibre layer.

GLARE was also used by Irving et al. [5] in comparison to GFRP, titanium and aluminium with different loading configuration. It proved that for a case of high stress at variable amplitude; GLARE outstand the other material as indicated in Figure 3-5.

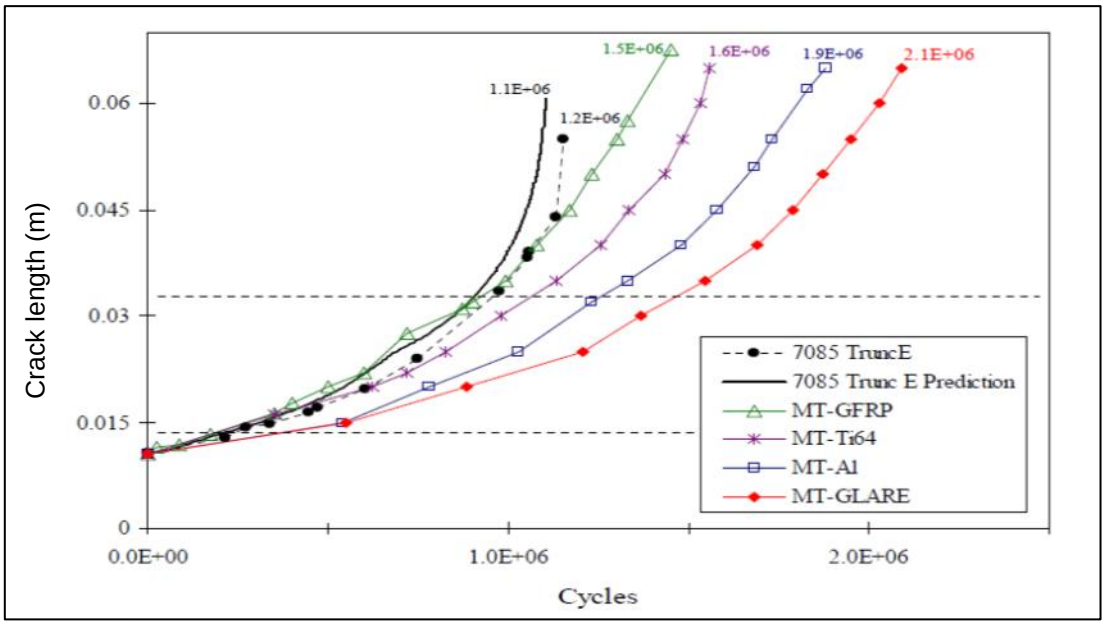

Figure 3-5 : Strap comparison under spectrum loading with maximum stress = 49 MPa [5]

During the tests conducted by Irving et al. and Schijve [5], [14], one particular aspect of the use of fibre metal laminates was the initiation of a crack in the first aluminium layer of the FML bonded to the substrate which would cause disbonding in the strap.

The aluminium straps also demonstrated very good fatigue results in [5], [10], [14]. This was mainly due to the absence of thermal residual stresses after curing of the strap. The major drawback was the crack nucleation observed into the straps which caused fatigue crack to initiate and propagate in the strap and later, failure of the reinforced panel.

Titanium was investigated as a possible material for BCR [5], [13]–[15], [53]–[56] and demonstrated good performance in retarding the crack propagation but a major issue was the difference in coefficient of thermal expansion between titanium strap and aluminium substrate which caused tensile residual stresses in the substrate and reduced the BCR effect. Titanium also demonstrates a higher density in comparison to GLARE or aluminium which means that it cannot achieve as much weight reduction as for the other materials.

CFRP was used in various tests for coupon reinforcement [5], [10], [19], [57] as well as panel reinforcement [16]. It was demonstrated [9] that when cured at room temperature CFRP could bring a reduction of crack growth rate of up to 3.5 times the crack growth rate of a non-reinforced specimen. Nevertheless, when cured at higher temperature – which will guarantee the best performance of the adhesive – the retardation was much reduced [6], [7], [9]. This was proved in [5] where the calculated residual stress intensity factor was the highest for CFRP in comparison to other material.

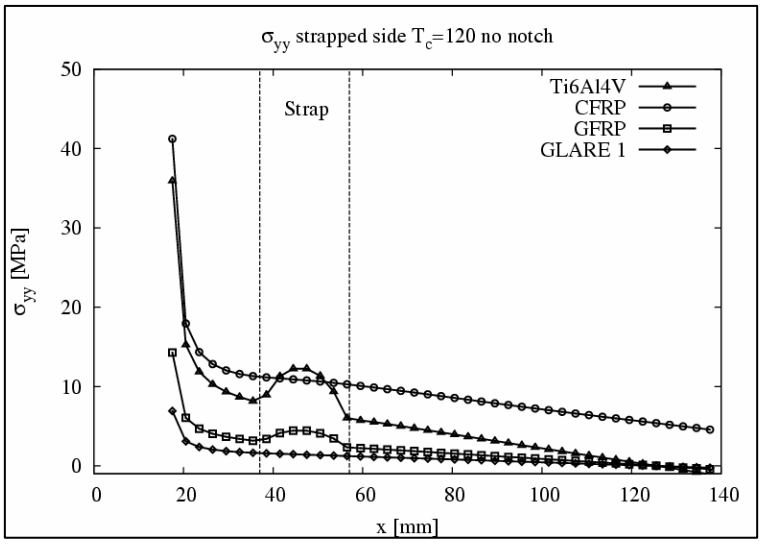

Figure 3-6 : Calculated thermal residual stresses on strap side of substrate for notched SENT specimen with different strap materials [7]

Despite reduced life improvement in comparison to other materials, CFRP proved beneficial in reinforcing integral panels, as samples with CFRP had twice the life of baseline unreinforced samples as proved in [16] even though there are detrimental thermal residual stresses. Colombi [10] demonstrated that the use of pre-stressed CFRP on steel members was a good means of retarding the crack. It was also confirmed in [66] that CFRP patches was a good method for crack arrest but with higher benefit when used as a double sided patch than a single sided one.

GFRP also proved effective as a crack retarder. Under room temperature cure [13] and high temperature cure [7] it is less beneficial than titanium and aluminium (Figure 3-6) but it remains better than CFRP. Due to its reduced density and the reduced thermal residual stress (Figure 3-6), GFRP may appear as a better choice in comparison to aluminium and titanium. This choice of strap material was confirmed by Hosseini-Toudeshky [18] with a crack growth life increase up to 236% from the baseline case.

- The influence of strap geometry was first investigated by Schijve [14] with the introduction of the stiffness ratio μ as a parameter to characterise BCR systems. E_{Strap} and A_{Strap} are respectively the Young's modulus and the total cross section of the strap while E_{AL} and A_{AL} are the Young's modulus and the total cross section of the substrate to which it is applied.

$$\mu = \frac{\sum(E_{Strap}A_{Strap})}{(E_{Al}A_{Al})+\sum(E_{Strap}A_{Strap})} \quad \textbf{(3-1)}$$

Schijve showed that a stiffer strap (increase in μ value) was more beneficial as well as a wider strap. Hence according to Schijve, the strap should possess a stiffness ratio as high as physically possible.

This was later confirmed by Molinari [55] where highest ratio of w/t – w being the width and t the thickness of the strap – resulted in better performance. In particular, comparison between titanium and aluminium using the same stiffness ratio resulted in better results for the titanium strap [7].

Studies over the width of the strap considered by Sun [15] and Irving et al. [5] showed that wide straps were more beneficial than narrow strap for a case of constant stiffness ratio of 0.2. The thickness of the strap has been studied by Zhang et al. [7] with the test of 2 Glare configurations, a thin one (1.8 mm) and a thick one (5.4 mm) where the thick Glare proved better as it had a higher stiffness ratio. On the contrary, for an aluminium strap case studied in [54] by Meneghin, it was demonstrated that thick and narrow straps behaved better than thin and wide straps as the crack nucleation took longer in the thick strap than the narrow one. As a conclusion, a higher stiffness ratio provides a better retardation with a preference towards wider straps made of Glare as was proved during a series of large panel tests performed by Irving et al. [5]. One of the other advantages in using wider straps is the fact that the contact area will be bigger, hence this reduces the shear stresses in the adhesive layers which in turn reduces the amount of disbond [14]. Concerning the effect of position of the strap, when BCR are used to reinforce monolithic aluminium plate, it has been demonstrated that the retardation effect is seen before the crack has entered the strapped area and that the effect remains as the crack propagates underneath the strap and after the strap [5].

- **Adhesive choice**

The parametric studies carried out on the strap material also demonstrated the importance of the interface between the reinforcement and the substrate and

how that can influence the benefit of BCR. One particularly interesting result was obtained by Meneghin [54] where the use of unidirectional glass fibres placed at the interface between the aluminium reinforcement and the skin could prevent the aluminium strap crack nucleation.

Colombi [10] conducted testing and a numerical analysis of steel plates reinforced by composite patch and demonstrated that a thin adhesive layer produced a larger disbonding due to an increase of shear stresses in the adhesive as opposed to thick adhesives that have reduced shear stresses.

- **Substrate**

Hosseini-Toudeshky [18] showed that the thickness of the substrate can play a major role in the retardation effect. Two substrate thicknesses were studied, one at 2.29 mm and one at 6.35 mm with patch repairs of the same dimensions (Length = 40 mm; width = 35 mm) and varying thickness of patch with 0.72 mm, 1.44 mm and 2.88 mm. For all straps configurations, thicker substrates demonstrated reduced retardation in comparison to the thinner one. The highest improvement was reached with a 2.29 mm thick substrate and a 2.88 mm thick patch with 240% of life improvement.

- **Loading effects**

Airplane structures are subjected to complex loading depending on the studied area. For the wing application, two major configurations are observed. The upper part of the wing is submitted to predominantly compressive loads (mean value of -45 MPa) with excursions of tensile loads (mean value of 20 MPa). In contrast the lower part of the wing is subjected to predominantly tensile load (mean value of 60 MPa) with excursion of compressive loads (mean value of -10 MPa).

During the work conducted by Irving et al. [5], coupon tests were performed under different stress levels at constant and variable amplitude and it was demonstrated that this could have an influence on the retardation effect as illustrated in Figure 3-7. Under constant amplitude loading, it showed that tests performed at higher load level (60 MPa) gave better retardation effect than

lower load levels for the Glare strap while the effect was opposite for the aluminium straps due to the failure of the aluminium strap under high load cases.

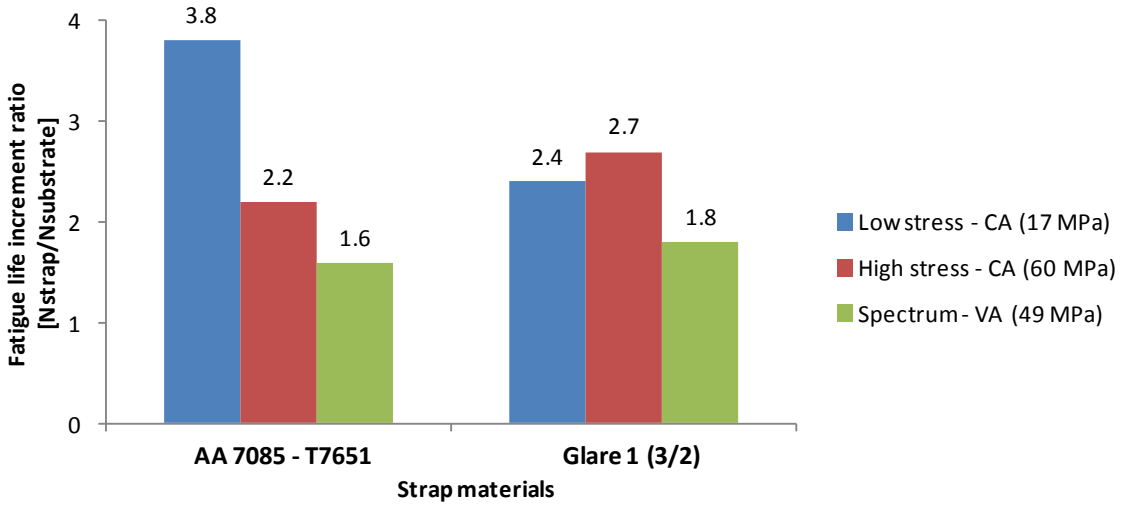

Figure 3-7 : Fatigue life improvement for different strap configurations under constant amplitude load – high and low as well as variable amplitude loading [5]

3.2 Modelling of bonded reinforced structures

Two methods can be employed for the calculation of the stress intensity factor of a crack in a reinforced structure, either through an analytical solution or finite element modelling. The current section will briefly review these two methods.

3.2.1 Stress intensity factor analytical solutions

Rooke and Cartwright [71] published a series of analytical and numerical solutions of stress intensity factors for stiffened sheets. These solutions can be used as a first estimate but are restricted to specific geometrical cases.

Ratwani [72] developed an analytical solution for a reinforced plate. This model represented two plates of the same dimensions bonded together with one of the plate with a centre through crack. The secondary bending effect due to the presence of the crack in one of the plates, away from the mid plane of the specimen was also considered in the solution. No thermal residual stresses were considered. Calculated stress intensity factor agreed well with

experimental results when considering the secondary bending and the disbonding corrections.

Rose's model [73]–[75] that was developed for the case of patch repair is based on the formulation of the stress distribution of a plate reinforced by an elliptical patch. The formulation assumes that the presence of the patch has two effects on the substrate, first the redistribution of stresses and then the crack opening restriction. While it is restricted to double sided reinforcement Rose also gives a solution for the case of partial reinforcement. The formulation is the same as the case of an elliptical patch but consider the effect of the reinforcement on the opening of the crack through the use of distributed springs between the crack faces. This formulation is used to evaluate the importance of design parameters. It does not assume disbonding effect and is limited to simple patch geometries.

Wang et al [76]–[78] developed an analytical method that combines the effects of membrane loads and bending loads for one-sided repairs. They formulated a crack bridging method that consists of using tension and bending springs to represent the effect of the patch on the cracked surfaces. This methodology was later used on a parametric analysis [77].

Yu et al. [79] studied the effect of double sided and single sided repairs made of Carbon Fibre Reinforced Composites on steel plates. The analytical model was based on the fracture mechanics theory and gives a solution to the stress in the repaired plate by formulation of the equilibrium of forces between each layer. This formulation agreed well with experimental results and was used in order to conduct a parametric study.

Kim and Lee [80]presented an analytical solution for the stress intensity factor of a patch repair with a disbonded area. They developed a crack-bridging model with a distribution of springs between the cracked faces using a weight function method. Their formulation was compared to Rose's model and good correlation was obtained between the two. It proved that a weight function can be used in order to formulate the effect of disbonding in an analytical solution.

Clark and Romilly [81] corrected the earlier analysis of Wang and Rose [76]. They developed close form equations in order to establish the stress intensity factor for a reinforced plate with an arbitrary crack length. These equations were found by developing a new method of interpolation between short cracks and long cracks. The method was tested against a line-spring model and a 3D finite element model and showed accurate results.

All methods outlined here agreed well with test results but they are all restricted to specific geometrical cases together with particular assumptions. This can be overcome with the use of finite element methods that once developed and verified can be adapted to a different geometry and cases. This is outlined in the next section.

3.2.2 Finite element solutions of stress intensity factor

The finite element modelling of reinforced structures (bonded crack retarders or adhesively bonded stiffener) or more generally bonded structures (single lap joints) are required to take into account a number of mechanisms such as the presence of a crack in the reinforcement or the adherent, secondary bending, the presence or not of thermal residual stresses and the cases of disbonding. The next section will review the modelling techniques that have been developed in order to consider these mechanisms.

A large number of numerical models have been developed for single sided and double sided patch repair [72], [75], [80]–[99]. Other models involve skin/stiffener assemblies [100]–[102] as well as the development of bonded crack retarders [103], [104].

- **2D models vs. 3D models**

With advances in computation capacities, modellers can use 3D finite element modelling rather than 2D. Nevertheless a number of 2D models have proved to be very effective in the modelling of patch repairs.

Ratwani [72] was one of the first to develop a 2D finite element model for a patch repair application. In that particular case, patch, adhesive and substrate

had the same dimensions and only the patch and the substrate were modelled with 2D elements.

Another way of looking at patch repair models is through the representation of the assembly (patch, adhesive and substrate) as a single layer of 2D elements but with a stiffness of elements representative of the assembly as developed by Jones and Callinan [94] and Chandra [87].

Other more conventional methods are a mixture of the classical 2D elements for the representation of the patch and the substrate and the adhesive layer is represented as spring elements, another 2D layer or a 3D layer. Arrendt and Sun [85], Klug et al. [98] Sun et al. [105] and Boscolo [103], [104] used 2D plates and spring elements. Naboulsi and Mall [106], Ouinas [107], [108] and Giannis [101] used 2D elements for all three layers. Arrendt and Sun [85] looked at the possibility of using 3D elements for the adhesive layer but faced numerical errors due to the large aspect ratios of the elements for the representation of the adhesive layer.

Callinan et al. [86], Sablekin et al. [109], [110], Lee et al. [99], [111], Hoseini-Toudesky et al. [90]–[92] and Gu et al. [89] all used 3D elements in order to model all three layers of the assembly. Their models differed based on the number of elements used through the thickness of each part. In order to take into account the large aspect ratio of the adhesive thickness, Callinan et al. [86] used a reduced integration formulation of the brick elements.

- **Adhesive modelling**

The modelling of the adhesive layer mainly depends on the type of analysis performed (2D or 3D). In Ratwani's 2D model [72], rectangular, prismatic-shaped elements were used to connect the two layers of elements representing the patch and the substrate. The thickness of these elements was representative of the thickness of the adhesive.

Arendt and Sun [85] used 2 shear spring elements in order to represent the adhesive layer with the addition of constraint equation between each layer in order to guarantee the continuity of displacement which will incorporate the

effect of secondary bending. Sun et al. [105] improved this approach with 3 spring elements modelling the adhesive with 2 elements for shear component and 1 element as a peel component. In that model as well as in Klug et al. [98] and Naboulsi et al [106] models, a constraint equation was used in order to impose the continuity of displacement through the thickness in order to consider the secondary bending effect. In Boscolo's model [103], the adhesive was modelled with two rigid elements that model the thickness of the adhesive and 3 springs to link this rigid element (Figure 3-8).

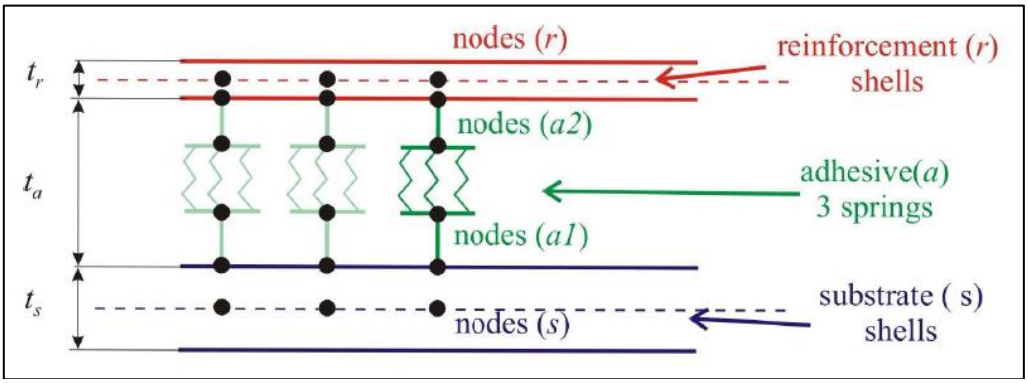

Figure 3-8 : Boscolo's 3 layers + spring model [50]

In 3D models, the adhesive layer is usually connected to the rest of the model using tie constraint between each layer. In some cases [109], [110] a contact property is added to this constraint in order to allow for disbonding of the adhesive layer.

- **Type of analysis**

One of the major features observed with single sided patch repair / reinforcement is the secondary bending effect. As stated by Boscolo [50], this involves a geometrically non-linear effect. While most modellers used a linear analysis, some considered the non-linear effect by conducting a geometrically non-linear analysis such as Sun et al. [105], Klug et al. [98], Lee et Al. [99], [111] , Gu [89] and Giannis [101]. For the cases where no geometrically non-linear effects were considered, the formulation of the stress intensity factor or the use of equations of continuity through the thickness has been used to consider this effect.

- **Disbond considerations**

The presence of disbonding with crack advance is an important factor in the design of reinforced structures. Authors have chosen various approaches towards this phenomenon. The first one is to consider disbonding based on what was observed on test samples and reproduce the shape of disbonding in the FE analysis [72], [85], [98], [105], [106]. Sablekin et al. [109], [110] used a surface to surface contact with a small sliding option in order to simulate the disbonding effect. Other more advanced approaches to delamination are the one adopted by Boscolo [103] where the disbonding is approximated by a quasi-static critical condition in order to grow the disbonding as the crack is propagating in the substrate. Giannis [101] and Maligno [112] used approaches in which the fatigue behaviour of the adhesive was taken into account. All other authors don't consider the case of disbonding [81]–[83], [86], [88]–[92], [97], [99], [107], [108], [111], [113]–[115].

- **Thermal residual stresses (TRS)**

The bonding process - when performed at high temperature – results at ambient temperature in thermal residual stresses that must be considered in the calculations of the stress intensity factor. In fact, these TRS can vary through the thickness of the specimen, hence they must be considered in the calculations of the stress intensity factor for both 2D and 3D models. The two methods that are considered to calculate the residual stress intensity factor are the weight function method and the calculation through finite element analysis.

Klug et al [98] considered a thermal step in their FE analysis with a temperature defined as the one observed during curing of the specimen. They studied a particular case where the R- ratio was zero hence simplified the approach to $\Delta K_{eff} = K_{m,max} + K_T$ **(3-2)** where $K_{m,max}$ is the stress intensity factor induced by the maximum mechanical load and K_T is the component due to thermal residual stresses. In that approach, no component at minimum load is considered which limits its use. Moreover the results of the thermal analysis were not compared to measurements.

Sablekin et al. [109], [110] used a similar method with a temperature decrease in the analysis but instead of using the exact difference, simulations were run in order to get the temperature drop that would give the exact fatigue life through simulation of the specimen upon comparison with test results. Despite good agreement with the test results this method can be criticized for the fact that it uses the results of the test in order to tune the model and then uses these same tests in order to validate the model.

Boscolo [103], [104] on the other hand modelled the thermal residual stresses through the exact temperature drop observed during the preparation of the specimens. The approach undertaken was similar to Klug et al. [98] but the R-ratio used was not zero and the formulation used calculates the effective stress intensity factor as $\Delta K_{eff} = K_{max}^{tot} - K_{min}^{tot}$ **(3-3)** and $R_{eff} = \frac{K_{min}^{tot}}{K_{max}^{tot}}$ **(3-4)** where K_{max}^{tot} and K_{min}^{tot}, are the contribution of the thermal stress and mechanical load to the stress intensity factor. This formulation takes into account the geometric non-linearity of the single sided reinforcement as well as the coupling between thermal and mechanical loading. Good agreement was obtained through this formulation when compared to residual stress measurements.

Hosseini et al. [92] developed a finite element methodology in order to study the thermal residual stresses due to the curing process in a patch repair assembly as well as the influence of those TRS on the fatigue life of the specimen. The method consisted in two steps. First a linear analysis is performed in order to calculate the thermal residuals stresses. A second linear analysis is performed in order to calculate the stress distribution due to the mechanical loading. The results of these two steps are then accumulated in order to get the stress distribution due to both TRS and applied loads. During the thermal analysis, particular conditions are imposed in order to avoid interpenetration of nodes through a constraint condition. Using that method, they were able to demonstrate that for FML patches, the thermal residual stresses stayed relatively small and were not sensitive to the curing temperature.

- **Crack front asymmetry**

When looking at single sided patch repair or reinforcement, one phenomenon that has been observed is the asymmetry of the substrate crack front due to the presence of the strap on only one side and the secondary bending effect (Figure 3-9).

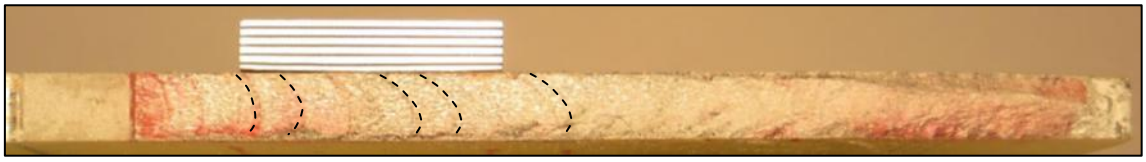

Figure 3-9 : Asymmetric crack front in bonded crack retarder [116]

The asymmetry must be considered during the calculation of the distribution of the stress intensity factor through the thickness. This can be done for both 2D and 3D models. Once it has been calculated, a choice needs to be made on a single value of stress intensity factor that must be used to integrate the fatigue crack growth law in order to predict the fatigue life of the specimen. The most popular choices are the maximum stress intensity factor through the thickness – as a conservative choice -, the mean value through the thickness or the root mean square. Nevertheless, it is also possible to predict the fatigue life of the specimen using an iterative process, with a distribution of the stress intensity factor rather than a single value as was performed in [90]–[92]. Hence it is important to differentiate the role of asymmetry for the calculation of the stress intensity factor as well as for the calculation of the fatigue life.

Most of the 2D models were not able to represent this asymmetry of the crack front and in these cases, the crack front is assumed to be constant through the thickness [72], [85], [87], [94], [95]. In particular, Arendt et al. [85] concluded that the variation of stress intensity factor was not large enough to be considered.

Nevertheless some 2D FE models did consider the effect of the bending on the curvature of crack front [98], [104], [105], [113]. In these cases, the calculation of the stress intensity factors takes into account the components due to membrane load as well as bending load hence a distribution of K through the thickness is calculated.

In Klug et al. [98], K_{max} (maximum stress intensity factor through the thickness), K_{mean} (mean value of stress intensity factor distribution through the thickness) and K_{RMS} (Root mean square of stress intensity factor distribution through the thickness) were compared for the calculation of the fatigue life. K_{max} proved over-conservative, K_{mean} proved over-predictive but K_{RMS} showed good results.

Umamaheswar et al. [113] suggested as an approximation method that the distributed SIF through the thickness could be approximated by a uniform value but no life predictions were estimated using that method.

Boscolo [104] developed a more advanced calculation of the stress intensity factor through the thickness in two steps. The first step gives a formulation of the SIF through the thickness based on a parabolic distribution. The second step consists of using a weight function associated with the first formulation in order to compute a unique value of the stress intensity factor to be used for life prediction calculations. This weight functions considers the fact that the crack front on the non-reinforced side is influenced by the rest of the crack front. This method is based on the observation made by Hosseini-Toudesky et al. [90]–[92]on 3D models that states that a unique value of the SIF can be used to give a good approximation of the fatigue life despite the fact that the SIF varies through the thickness. Both RMS and weighted formulations were used for life predictions in [103] and showed very good agreement.

With the use of 3D finite element model, the variation of the stress intensity factor through the thickness can be automatically calculated depending on the refinement of the mesh used. Sablekin et al. for example [109], [110] were able to obtain values for each side of the reinforced substrate and used an average of these two values in a 2D life calculation. Lee et al. [99], [111] and Hosseini-Toudesky et al. [90]–[92] used successive calculation in order to predict the exact shape of the crack front instead of using a straight approximation. Both obtained very good agreement with tests results but Hosseini-Toudesky [92] showed one particularly interesting conclusion that was used by Boscolo [104] which is that despite the asymmetric crack front observed during the tests, the crack can be approximated by one single value through the thickness. In their

study this value was approximately the stress intensity factor located at 0.32-0.37 of the plate thickness, from the un-patched side.

3.2.3 Summary, limitations and possible improvements

The survey conducted here showed that the calculation of the SIF in bonded crack retarders could be performed through analytical studies. Nevertheless, the issue with such methods is the geometry restriction and the numerous assumptions. Models developed by Ratwani, Rose and Wang [72]–[74], [76]–[78]correspond to a very specific case and it was demonstrated that the issue of secondary bending is not always treated. In addition, when disbonding was considered the shape of disbonding was based on experimental observations and the evolution of disbonding was not studied. Thermal residual stresses are another issue, with very few papers considering its effect in the calculations and the curvature of the crack front was scarcely raised in these models.

The finite element modelling techniques reviewed in the previous paragraphs are summarized here with a critical scrutiny:

- **Element choice:** It was demonstrate that 2D finite element modelling together with the right formulation can be used to accurately calculate the stress intensity factor and consequently approximate the fatigue life of bonded crack retarders [104]. It was shown that accurate formulation must be used in order to consider the effects of secondary bending and the possible asymmetry of the crack front. 3D modelling coupled to the appropriate constraint between each part of the assembly proved to be a better solution in representing reinforced structures [90]–[92]. Nevertheless the effect of the element aspect ratio must be carefully monitored when using 3D elements.
- **Adhesive model:** The adhesive modelling mainly depends on the type of analysis performed (2D/3D) as well as whether or not disbonding is considered in the model. Further details of the adhesive model can be found in the next section which outlines how to model the fatigue disbonding in the adhesive system.

- **Analysis:** As demonstrated, not all analysis considered geometric non-linear effects while secondary bending is considered as a non-linear effect. Hence in the case of 3D modelling of a one-sided reinforcement, it is recommended that geometrically non-linear analysis be conducted.
- **Disbonding:** Must be considered when modelling reinforced structures but it was shown that very few papers consider the exact fatigue disbonding effect and used imposed shape of disbonding [72], [84], [85], [98], [105], [106]. Some papers did not even consider disbonding. One fatigue model in particular used a static approach for the disbonding effect [104]. Hence a major improvement in modelling of bonded crack retarders would be the computation of the fatigue disbond advance with the substrate crack advance in order to study the interaction effect between one-another.
- **Thermal residual stresses:** As stated earlier two methods can be used in order to consider the TRS caused by the curing of the adhesive. It appears that the most common method used in finite element modelling would be the implementation of a thermal step that corresponds to the temperature drop associated with the curing of the adhesive.
- **Crack front asymmetry:** It was demonstrated in [5] that when using BCR, asymmetry of the substrate crack front is observed. Hence this phenomenon must be modelled. It was reported that this can be done through either 2D or 3D modelling. It showed that if 2D model is used, a series of formulations needs to be used in order to mimic this behaviour [104] while with 3D models a more direct approach can be undertaken[90]–[92]. Nevertheless the fatigue life calculation requires a single choice of stress intensity factor range hence critical analysis must be performed when it comes to the selection of this single value.

The present review has demonstrated that the analytical solution are restricted to simple geometries and assumptions hence building a design tool using an analytical approach would not be as straightforward as is currently possible with finite element analysis.

3.3 Finite element modelling of fatigue delamination in adhesive bonds

Delamination in adhesive bonds can occur due to two mechanisms. The first case is under static load where the load is high enough to initiate disbonding and as the load increases, the disbonding progresses. The second case is disbonding under fatigue load. In that case, disbonding initiates under lower load in comparison to the static case and propagates during the cyclic loading. Disbond initiation may be due to defect in the adhesive system, run-outs stress concentration or impact damages.

Modelling of the fatigue disbond mechanism is an important aspect of BCR as it will modify the efficiency of the reinforcement. The present survey will focus on the finite element modelling of fatigue delamination only. This section gives a review of the fracture mechanics approach to model delamination of adhesively bonded joints and focuses in particular on the finite element modelling of the bonded joint. The fracture mechanics approach was chosen as the most appropriate method to correlate delamination data and FE analysis as opposed to the total life method [117]and the damage mechanics approach [118]–[120].

3.3.1 The fracture mechanics approach

This approach calculates only the propagation of disbond. It assumes that the geometry either presents an initial defect or that initiation occurs in an early stage of the cycling process. This approach is based on the principle that the delamination growth rate da/dN is correlated to a fracture parameter, either G (Strain energy release rate) or K (the stress intensity) (Figure 3-10).

Stress based approach	Energy based approach
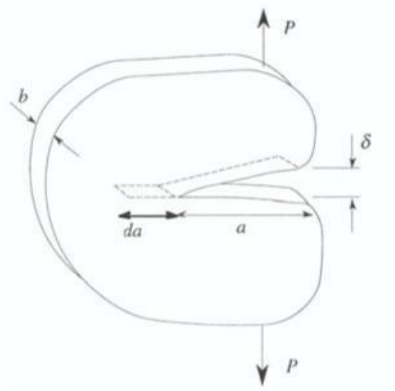	
$K = \beta\sigma\sqrt{\pi a}$ **(3-5)**	$G = \frac{P^2}{2b}\frac{\partial C}{\partial a}$ (C = compliance) **(3-6)**
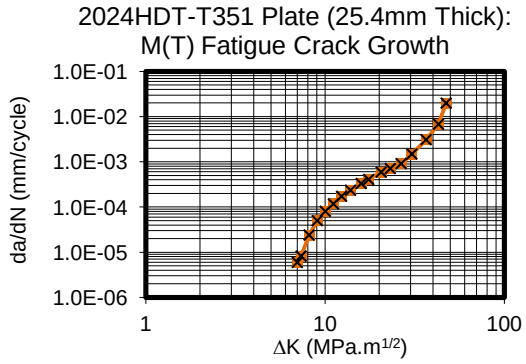 (a) Stress based approach [116]	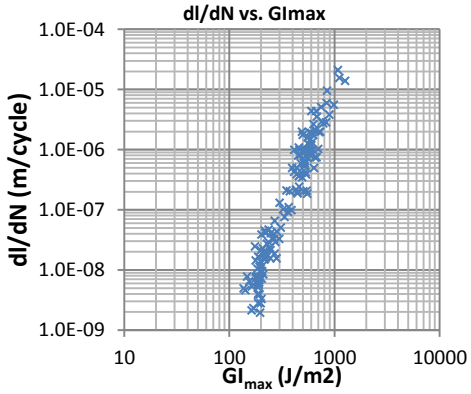 (b) Energy based approach (Chapter 6)

Figure 3-10: Stress based (a) and energy based (b) approaches

The stress intensity factor *K* can be evaluated with confidence in homogenous materials with the use of known analytical or numerical solutions. On the other hand the definition of the stress field surrounding the crack tip in bonded structures is more complex because of heterogeneous and anisotropic properties. Because energy based methods don't require the definition of the stress field, they are preferred for the definition of fracture properties of composite laminates and adhesively bonded structures.

Several expressions can be used to characterise the strain energy release rate, G_{max}, $\Delta G = G_{max} - G_{min}$ **(3-7)** or $\Delta G = \left[\sqrt{G_{max}} - \sqrt{G_{min}}\right]^2$ **(3-8)** [121]. It is not clear which is the most appropriate. G_{max} is often used as debris created during

the delamination may interfere during the closing process and cause an artificially high G_{min} value. The value of G can be calculated through analytical solution or finite element analysis. The most common numerical evaluation of G is through the Virtual Crack Closure Technique [42].

While the measured data may be given for a single mode (mode I or mode II) or a mixed mode (ratio of mode I/mode II maintained constant during the test), the calculation needs to consider the mixture of modes observed during the crack propagation in case the mode of delamination is a mixed one. That can be done by using a mixture parameter such as $G_{tot} = G_{Imax}+G_{IImax}$ **(3-9)** or $G_{eq} = G_I + \frac{G_{II}}{G_I+G_{II}} G_{II}$ **(3-10)** [122].

3.3.2 Modelling of delamination in finite element analysis through the fracture mechanics based approach

Details of this approach are given here and other finite element methods are also outline with the cohesive zone model approach and the X-FEM approach.

- **Fracture mechanics based models**

The fracture mechanics models are based on the relation between the stress intensity factor (SIF – K) or strain energy release rate (SERR - G) and the fatigue crack growth rate ($\frac{da}{dN} = f(G)$). Several methods exist for the determination of the SERR as outlined in section 2.2. There are a number of examples that used this finite element approach and they differ based on the material employed and more particularly on the formulation employed to describe the fatigue delamination growth rate.

Krueger [123] developed several benchmark examples on the double cantilever beam geometry made of graphite epoxy laminates in order to predict the fatigue delamination. The approach used a simple Paris law of delamination growth based on test data. Good results were obtained through that method and it was pointed out that if applied to more complex geometries that involve a mixture of modes of delamination the solution depends on the parameters employed in the formulation.

Brussat et al. [124], [125] performed an analysis of disbonding in an FM73 adhesive system. They investigated both mode I and mixed mode and in particular produced data for the cases of hot water immersed conditions. They used these data together with the calculation of the strain energy release rate through finite element modelling in order to predict the crack growth rate of single lap joints and showed good correlation between test results and predictions.

Pascoe [126] studied the delamination of bonded repairs and tried to predict the advance of delamination. The methodology employed a series of simple geometry tests in order to determine the parameters for Paris like type equations that describe the delamination growth rate and use these equations in order to predict the delamination propagation.

Giannis et al. [101] produced a series of mode I and mixed mode fatigue delamination test in order to obtain fatigue fracture data. These data were then used in order to predict the fatigue life of skin stringer specimen made of Glare using a method developed by Martin [127]. Despite over-predicted results, they were able to demonstrate the importance of using mixed mode data in the predictive model.

Quaresimin et al. [128] used a two part method in order to predict the fatigue life of a single lap joint. The fatigue initiation was based on a SIF to number of cycles approach where the SIF at the initiation of delamination was compared to SIF vs. number of cycles data. The propagation calculation was using a fracture mechanics approach. One interesting point is that they studied different approach of strain energy release rate, using in particular an equivalent value of the strain energy release rate $G_{eq.}$ to incorporate the mixed mode as for example ΔG_{tot} does not incorporate the mixed mode aspect of disbonding. Their results showed that the $\Delta G_{tot,}$ approach gave more conservative results than the $G_{eq.}$ method but each result stayed within the scatter of such predictions.

$$G(a)_{eq} = G_I(a) + \frac{G_{II}(a)}{G_I(a)+G_{II}(a)}.G_{II}(a)$$ (Quaresimin equivalent G value) **(3-11)**

Hoyt et al. [129] studied the fatigue life of skin-stiffener T-joints and bonded repair lap-joints. The method that they used was based on the calculation of the cycle increment for a certain crack increment using the fatigue crack growth rate data. Mixed mode was not considered in their approach and they used ΔG_{tot} in order to quantify the variation in SERR during the cyclic loading. They also assumed no R-ratio effect during their calculation. No comparisons of their prediction to fatigue test on the studied structures were given.

Other methodologies make use of the fracture mechanics approach and are similar to the one quoted above except that the crack advance is based on a quasi-static criterion rather than a fatigue criterion. The delamination progresses if the fracture criterion is met by deletion of the connecting elements/node. Despite this restriction Xie and Biggers [130] and Boscolo [103], [104] proved good correlation with test results using this fracture principle.

$\left(\frac{G_I}{G_{IC}}\right)^{\alpha} + \left(\frac{G_{II}}{G_{IIC}}\right)^{\beta} + \left(\frac{G_{III}}{G_{IIIC}}\right)^{\gamma} \geq 1$ (Xie and Biggers quasi static formulation) **(3-12)**

- **Cohesive zone models**

The cohesive zone formulation was first introduced by Dugdale [131] and Barenblatt [132] and was further developed for static decohesion problems [133]. The cohesive zone modelling uses the finite element method to model the interface disbonding by using special purpose cohesive elements. The advantages of this method in comparison to the fracture mechanics approach are that no remeshing of the disbond front is necessary and it can model the damage initiation. The elements are defined through a traction-displacement relationship (Figure 3-11) that is non-linear [50].

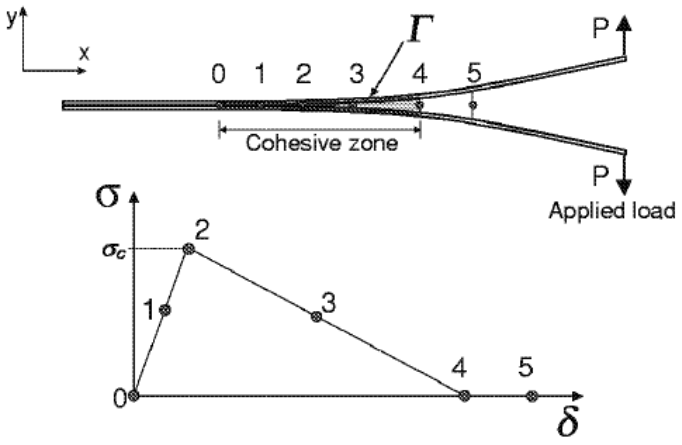

Figure 3-11 : Cohesive zone modelling: Stress vs. displacement non-linear relationship

The behaviour of the cohesive elements is usually defined as:

$$\sigma_i = K_i \delta_i \;\; if \;\; 0 \leq \kappa_i \leq \delta_i^0$$

$$\sigma_i = (1 - D_i) K_i \delta_i \;\; if \;\; \delta_i^0 \leq \kappa_i \leq \delta_i^f \qquad \textbf{(3-13)}$$

$$\sigma_i = 0 \;\; if \;\; \delta_i^f \leq \kappa_i$$

where $\kappa(t)_i = max_{0 \leq \tau \leq t} \delta_i(\tau)$, $\delta_i(\tau)$ is the relative displacement of the faces of the cohesive element at time t, D_i is the damage parameter, *i* is the direction, δ_i^0 is the displacement at the onset of softening of the element (#2 in Figure 3-11), δ_i^f is the displacement at failure (#4 in Figure 3-11), K_i is the stiffness and σ_i is the traction stress.

The damage growth is simulated by reducing the stiffness of the element using the damage parameter *D*. This is used to simulate fatigue delamination by introducing the damage parameter *D* in the formulation of the cohesive element behaviour.

Cohesive elements have been used in several fatigue problems. Foulk et al [134] introduced the loading/ unloading behaviour in their formulation which was later re-used by De Andrés et al [138] together with an additional damage parameter *D* that is defined for a limited number of cycles and avoids a cycle by cycle computation. Camanho et al [133] used a formulation that integrates the

mixed mode behaviour using a criterion developed by Benzeggagh and Kenane [135].

The Robinson et al [136] formulation of the cohesive elements was built in order to reproduce both static and fatigue delamination growth. A pseudo-time approach representative of the number of cycles was used. Their formulation is dependent on a parameter that has not been properly linked to a fracture parameter hence concerns have been raised on the validation of such formulation. In particular, the parameters used in Robinson's formulation are only valid for one ratio of mixed loading and the formulation needs to be changed depending on that ratio.

Harper and Hallet [137] used the model of fatigue delamination growth rate developed by Blanco [138] in order to calculate the fatigue component of their damage by linking the fatigue damage zone size to the fatigue damage growth rate as done by Turon et al. [139]. No initiation life is calculated in their model.

May, M. and Hallett, S. R [140], [141] used a fatigue life approach – S-N curves – for the initiation of delamination and used a fracture mechanics approach for the fatigue propagation calculations. In both cases they used a cohesive element approach in the FE model. The stiffness of the element was changed based on the amount of damage calculated. They demonstrated good results for simple geometries but it was also shown that when using more complex structure, they could not achieve the same accuracies in the predictions. As stated their model is highly dependent on the user inputs which may limit its use. Another drawback of their method is that the damage parameter D does not have a physical meaning which is what Pascoe outlined in [126], [142] where he mentioned the lack of coherence between the methods used to predict fatigue delamination and the actual physics of the delamination process.

Landry and LaPlante [143] used a similar approach that linked the cohesive zone model to fracture mechanics through a modified Paris relation in order to predict the fatigue behaviour under variable amplitude loading.

Khoramishad et al. [144] used a strain approach in order to define the damage parameter. They also showed good agreement with their tests results.

- **X-FEM based model**

The extended finite element method (X-FEM) [145] is a finite element technique that allows modelling of an arbitrary crack. In fact, while in fracture mechanics models or cohesive zone models the crack is defined at the interface between elements, in the X-FEM case the crack can propagate through the elements. This is due to enrichments functions at the nodes that allow the crack to propagate through the adjacent elements. It was first introduced by Belyteschko and Black [146]. Further studies have been carried out on that method and are summarized in [147].

The studies using the X-FEM methodology have been restricted to quasi-static problems. For example, Campilho et al. [148] used it to study the fracture in adhesive joints. The method was also used by Curiel Sosa and Karpurah [149] in order to study the fatigue delamination in fibre metal laminates. As suggested by Pascoe [126], it should be possible to combine this technique with a damage approach in order to predict fatigue disbonding, the same way it has been performed in the CZM approach. Bacarreza and Aliabadi [150] used the X-FEM technique in order to simulate fatigue delamination in composite. They adopted a fracture mechanics approach in order to calculate the crack advance, using the VCCT to calculate the strain energy release rate. They used the X-FEM approach in order to avoid remeshing of the delamination front.

3.3.3 Summary

Three major finite element modelling techniques use the fracture mechanics approach in order to model fatigue delamination. The fracture mechanics based models demonstrate a direct link between the crack front condition (SERR) and the fatigue crack growth rate allowing for accurate predictions. This method treats cases of mixed mode ratio at the crack front. Nevertheless it does not take into account the initiation problem. The cohesive modelling approach has demonstrated very accurate modelling results for quasi-static cases. It also

showed good results for fatigue life calculation when using a damage mechanics approach but it is restricted by a damage parameter that does not have a physical meaning and some analysis have shown high dependency on the crack growth rate data [140], [141]. X-FEM demonstrates promising results for the modelling of fatigue crack propagation using a fracture mechanics approach especially for the modelling of the crack front but further investigation is necessary in order to link the X-FEM results to fatigue crack growth rate data.

Most of the models presented here have been validated with comparison of predictions to experimental results on simple geometries. Nevertheless in more complex situation as the one encountered in an aircraft structure there will be mixed mode loading situation which needs to be addressed in the model. Hence models that work well on a single mode of delamination may not be accurate when used on more complex geometries.

Chapitre 4 : Experimental investigation of crack growth in reinforced middle crack tension specimens

4.1 Introduction:

The current chapter describes the tests performed on reinforced middle crack tension specimens M(T) using a 2624-T351 aluminium substrate and a Glare 2A-6/5 (0.4) strap, with a stiffness ratio μ = 0.2. This is part of a large test program conducted during the course of the project which additional results will be described for means of comparison in the discussion chapter. The aim of this chapter is first to study the benefit of bonded crack retarders at a coupons level and second to provide a set of data in order to validate the finite element models.

4.2 Sample materials, design and manufacture

4.2.1 Materials

The samples were made of 2624-T351 aluminium. Glare 2A-6/5 (0.4) was used for the reinforcement of the M(T) coupons. FM94 epoxy adhesive was used to bond the reinforcement to the aluminium substrate.

2624-T351 adherent plate

The aluminium alloy 2624-T351 used for the substrate was provided by Alcoa. The substrates were surface treated with phosphoric acid anodising and a BR 127 primer was applied prior to delivery in order to guarantee better bonding performances. The chemical properties of the aluminium alloy 2624-T351 are given in Table 4-1.

Table 4-2 outlines the mechanical properties of the 2624-T351 aluminium alloy and also give the mechanical properties for 2024-T3 and 7085-T7651 for means of comparison.

Table 4-1: 2624-T351 specified chemical composition [151]

Component	Al	Cr	Cu	Fe	Mg	Mn
Weight (%)	90.7 - 94.7	0.05	3.8 - 4.3	0.08	1.2 - 1.6	0.45 - 0.7
Component	Si	Ti	Zn	Other, total		
Weight (%)	0.08	0.10	Max 0.25	Max 0.15		

Table 4-2: Mechanical properties for 2624-T351, 2024-T3 and 7085-T7651

Property	**2624 – T351** [152]	**2024 – T3** [153]	**7085 - T7651** [154]
Et (MPa)	71,000	73,000	71,000
ν	0.33	0.33	0.33
ρ (g/cm^3)	2.77	2.77	2.77
α (°C^{-1})	23.2	23.6	23.6

The 2624-T351 material demonstrates high damage tolerance, fatigue durability and resistance to stress corrosion cracking.

No further surface preparation of the substrate was required prior to the bonding process except cleaning of it with acetone.

Glare 2A-6/5-(0.4) straps

Glare 2A-6/5-(0.4) is a fibre metal laminate that consist of 6 aluminium layers (2024 – T3) together with 5 unidirectional GFRP layers made of S2-prepreg glass fibres pre-impregnated with FM94 epoxy adhesive (Figure 4-1). Each layer of aluminium is surface treated with the same surface treatment as the substrate. The material was provided by Alcoa in its final form and then cut to the required dimension of the straps following Alcoa's recommendations [155].

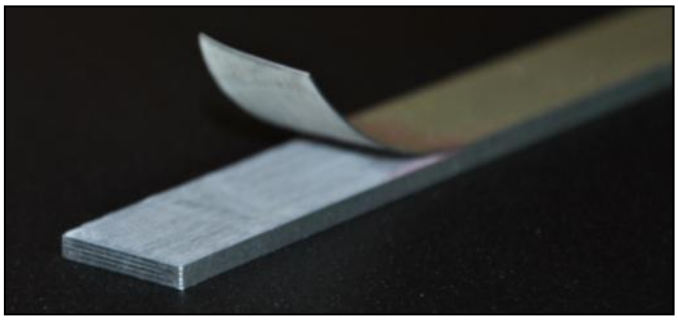

Figure 4-1: Glare2A – 6/5 (0.4)

As mentioned before, Glare 2A-6/5-(0.4) was chosen as the most appropriate material for the reinforcing strap because of its matching coefficient of thermal expansion to the one of aluminium that reduces the thermal residual stresses

and proves to be the best material to use according to earlier design studies [5] due to high fracture resistance. The thermo-mechanical properties of the Glare constituents are given in Table 4-3. It shows the orthotropic properties of the Glare employed for these tests.

Table 4-3: Thermo-mechanical properties of Glare constituent as given in [156], [157]

Property	UD S2 prepreg/FM94 FVF = 60%	2024-T3
E_1 (MPa)	50,300	72,000
E_2 (MPa)	5,500	72,000
$\mu_{12} = \mu_{23}$	0.310	0.300
μ_{21}	0.034	0.300
G_{12} (MPa)	1,995	28,000
G_{23} (MPa)	2,099	28,000
α_1 (°C^{-1})	2.88×10^{-6}	2.32×10^{-5}
α_2 (°C^{-1})	4.03×10^{-5}	2.32×10^{-5}
ρ (kg/m^3)	1,975	2770
t (mm)	0.13	0.40

FM94 adhesive

The adhesive employed to bond the specimen together was FM94. This is a widely used adhesive in aerospace industry which performance have been tested [5] and showed high level of mode I and mode II toughness with respectively 3000 J/m^2 and 9000 J/m^2 [5], [158]. The static and fatigue delamination growth behaviour of this adhesive are further developed in the Chapter 6 in order to accurately model the fatigue disbonding observed in BCR.

4.2.2 Design

The tests substrates specimen geometry was based on the ASTM E647 recommendations [159] and is illustrated in Figure 4-2.

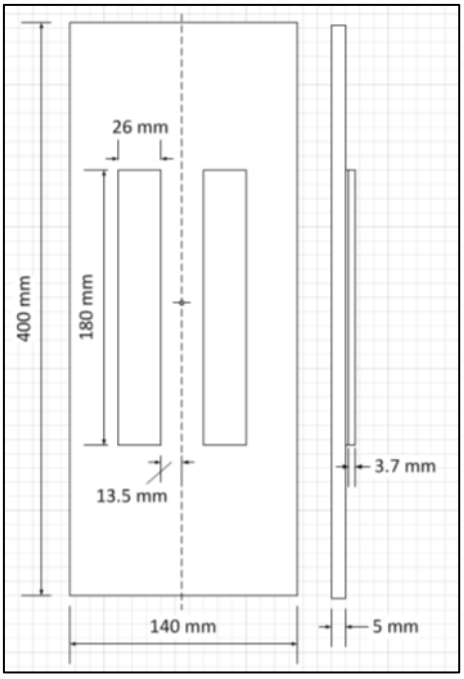

Figure 4-2 : Reinforced M(T) specimen

The substrate used for the coupon tests was 400 x 140 mm and 5 mm thick with the grain direction orthogonal to the crack propagation direction. They were reinforced with Glare 2A 6/5 (0.7) straps, 26 mm wide and 180 mm long. The width and thickness of the strap is of particular importance as it defines the stiffness ratio μ of the specimen $\mu = \frac{\sum E_{Strap}.A_{Strap}}{\sum E_{Strap}.A_{Strap} + E_{Substrate}.A_{Substrate}}$ **(4-1)**

With E_{strap}, the Young's modulus of the reinforcing strap
A_{strap}, the cross sectional area of the reinforcing strap
$E_{substrate}$, the Young's modulus of the substrate
$A_{substrate}$, the cross sectional area of the substrate

As Glare is made of alternating layer of aluminium and glass fibre reinforced epoxy adhesive, an equivalent Young's modulus is used here for the calculations with E_{Glare} = 66.5 GPa. This value is based on classical laminate theory.

Hence $\mu = \frac{2 \times 26 \times 3.7 \times 66.5}{2 \times 26 \times 3.7 \times 66.5 + 140 \times 5 \times 71} = 0.2$

Therefore the stiffness ratio used in these tests was 0.2.

4.2.3 Manufacturing procedure

The specimens were delivered in their final dimensions of 400 x 140 x 5 mm. Electro Discharge Machining (EDM) was used prior to bonding in order to introduce a 16 mm long notch in the substrates.

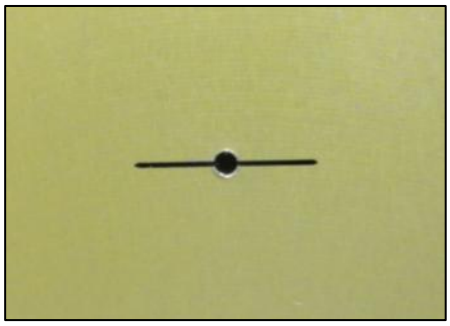

Figure 4-3 : EDM notch

The Glare straps were cut using a high speed milling machine to their final dimension of 180 x 26 x 3.7 mm.

The bonding assembly was performed at Cranfield University Composite Centre. The steps of the bonding assembly were done in the following order according to Alcoa's recommendation [160]:

1. Get adhesive out of the freezer. This gives a better handling as it gets to room temperature
2. Cleaning of the specimen using acetone in order to remove any contaminant from the bonding surface.
3. Marking of straps location on the substrate using permanent pen.
4. Cutting of adhesive strips to dimension by placing the strap on the adhesive (it is recommended to cut it slightly larger in order to guarantee a good bonding at the edges). Hand pressure is then applied on the adhesive in order to remove any air at the interface adhesive/strap.
5. Adhesion of adhesive + strap to the substrate. Once the strap is in the exact position, pressure can be applied to the strap in order to guarantee that it will stay in its position during handling of the specimens prior to curing.

Figure 4-4 : Reinforced M(T) ready prior to vacuum bagging [161]

6 – Vacuum bagging of the specimens

7 – Curing of the specimens according to Cytec recommendation [162]

- Heat at 3 C/min up to 121 C
- Apply a 40 psi pressure
- Cure at 121 C ± 3 C for 60 minutes

Figure 4-5 : Specimens in vacuum bags prior to curing

Due to the thermal lag caused by the number of specimen to bond, the curing temperature was increased to 90 minutes in order to guarantee a good bonding quality.

8 – Once cured the specimen were left to cool down and removed from the vacuum bags.

A slight curvature could be observed on the specimen after curing. This was due to the difference in coefficients of thermal expansion between the aluminium and the Glare. Figure 4-6 illustrates this slight curvature.

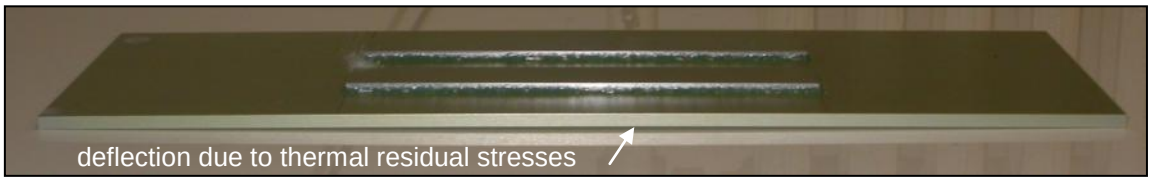

Figure 4-6: Specimen after curing -Thermal residual stresses effect with out-of-plane bending

These were confirmed by measurements performed by Syed [163] where a deflection of approximately 0.9 mm was observed on the unreinforced side of an M(T) specimen after bonding.

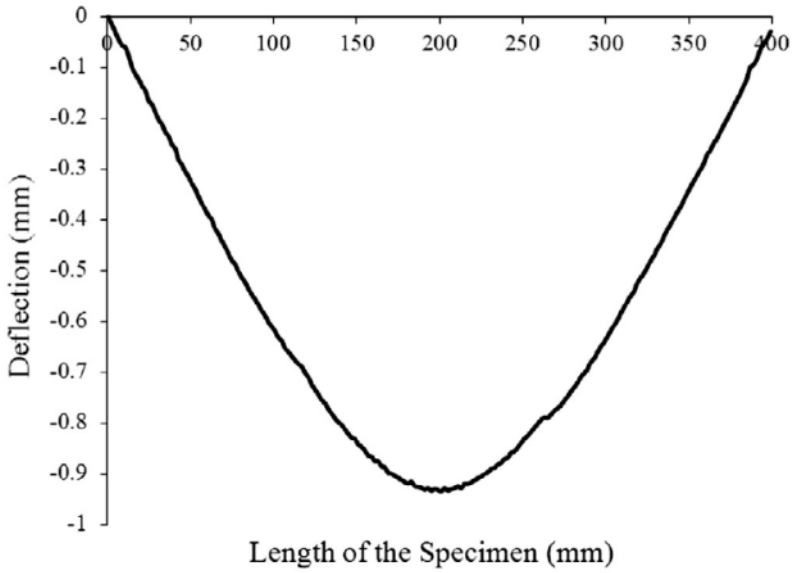

Figure 4-7 : Out-of-plane deflection measurement of reinforced M(T) specimen after curing – from unreinforced side [163]

4.3 Testing methodology

Prior to testing, a 1 mm scale was scribed on the non-reinforced side of the specimen in order to monitor the crack advance Figure 4-8. The tests were performed under constant amplitude loading on a 250 kN servo–hydraulic machine fitted with a digital control. An optical microscope was used to monitor the position of the crack tip on each side of the crack (Figure 4-9). The crack was monitored on the non-reinforced side of the specimen only as it was impossible to monitor it on the reinforced side due to the presence of the strap. The crack was monitored every 2,500 cycles up to a certain point where crack growth became too fast and the frequency of measurement had to be reduced.

The tests were performed in two stages. The first stage consisted of initiating a pre-crack of 2 mm on each side of the artificial EDM notch, as recommended in the ASTM E647. This is a necessary step in order to sharpen the crack tip and it ensures that the effect of the machined notched is removed and that the effect of changing the crack front shape is eliminated in terms of crack growth rate data.

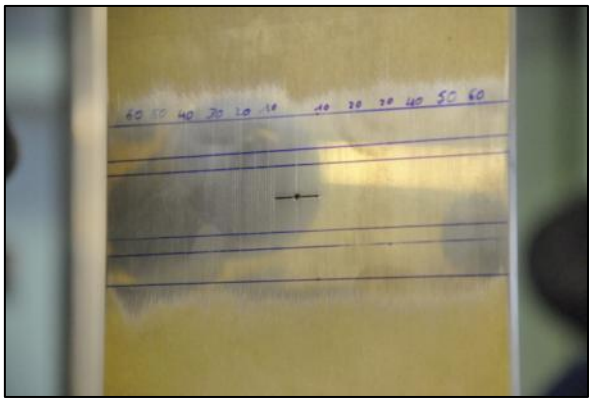

Figure 4-8 : Scribe on specimen for crack monitoring

Figure 4-9 : Test set-up

A nominal stress of 74 MPa and a nominal stress ratio of R = 0.1 were employed for that pre-crack. The pre-crack was stopped as soon as each side of the artificial damage had grown of 2 mm hence ending-up with an initial crack length of 20 mm. A second stage consisted of a constant amplitude cyclic load at a maximum nominal stress of 60 MPa and a nominal stress ratio R = 0.1. The test parameters are summarized in Table 4-4. The chosen nominal stress of 60 MPa takes into account the full cross section of the substrate and the reinforcement.

Table 4-4 : Fatigue test parameters

Phase	Max – Min applied load (N)	Max – Min applied stress (MPa)
Fatigue pre-crack	66.2 – 6.6	74.0 – 7.4
Fatigue crack propagation	53.4 – 5.3	60.0 – 6.0

The test was stopped when one of the crack tip reached final fracture and the specimens were then statically ruptured.

After testing inspection were performed on the broken specimen using optical observation, optical microscope and an Olympus Omniscan MX coupled to a Phased Array (PA) probe in order to perform C-scan inspection (Figure 4-10). Those inspections were aiming at the determination of the amount of

disbonding that had occurred during testing, at the interface between the strap and the substrate, in the adhesive system. A C-scan gives a detailed image of the state of the interface similar to an X-ray scan, where the colours define the amplitude of the signal which is attenuated in case of disbonding.

Figure 4-10 : Olympus Omniscan and PA probe

In order to study the results of the test, the ASTM E647 [159] recommends two data reduction techniques for the computation of the crack growth rates with the secant method or point to point technique and the incremental polynomial method. An alternative post processing method was used. It consists on using a linear curve between seven data points and then uses the slope of that linear curve in order to get the fatigue crack growth rate. The average crack length over these seven data points is then used to calculate ΔK.

4.4 Testing results

The results of these tests are compared to test results performed on the baseline specimen of AA 2024-T351 (non-reinforced) [116] at the same nominal stress of 60 MPa and the stress ratio R = 0.1. The reinforced specimens are designated as MTR1 and MTR2 and the non-reinforced baseline are designated as MT1 and MT2.

4.4.1 Fatigue lives

The two specimens MTR1 and MTR2 required respectively 13,583 cycles and 12,911 cycles in order to reach the 20 mm initial crack. MTR1 reached 151,460 cycles and MTR2 reached 152,990 cycles. This number of cycles does not take into account the number of cycles required for the pre-crack. Hence the average life of the reinforced specimens is 152,225 cycles. On the other hand, the plain specimens reported in [116] showed an average fatigue life of 129,930 cycles. It

demonstrates that the use of bonded crack retarders gives a life improvement factor, *LIF* of 17%.

$$LIF = \frac{N_{Strapped} - N_{Unstrapped}}{N_{Unstrapped}} \quad \textbf{(4-2)}$$

The crack lengths monitored during the tests are illustrated in Figure 4-11. The figure shows the results for the reinforced specimens MTR1 and MTR2 as well as the non –reinforced specimens MT1 and MT2. Figure 4-11 shows that up to a half crack length of approximately 26 mm non-reinforced specimens and reinforced one have a similar profile. Nevertheless the reinforced case appears to have a slightly longer crack length (difference is less than 2 mm) from 12 mm to 26 mm half crack length in comparison to the non-reinforced case. Once the half crack has reached 26 mm, the curves for the reinforced specimens start to separate from the reinforced one with a gradient that is reduced for the reinforced specimens, hence showing the effect of the presence of the strap. As the crack emerges from the strap (a > 39 mm) the difference in half crack length is of 8 to 15 mm between the two configurations. Overall, the presence of the strap gives an increase in fatigue life as well as an increased residual strength of the specimen with the half crack propagating over an additional 6-8 mm before failure.

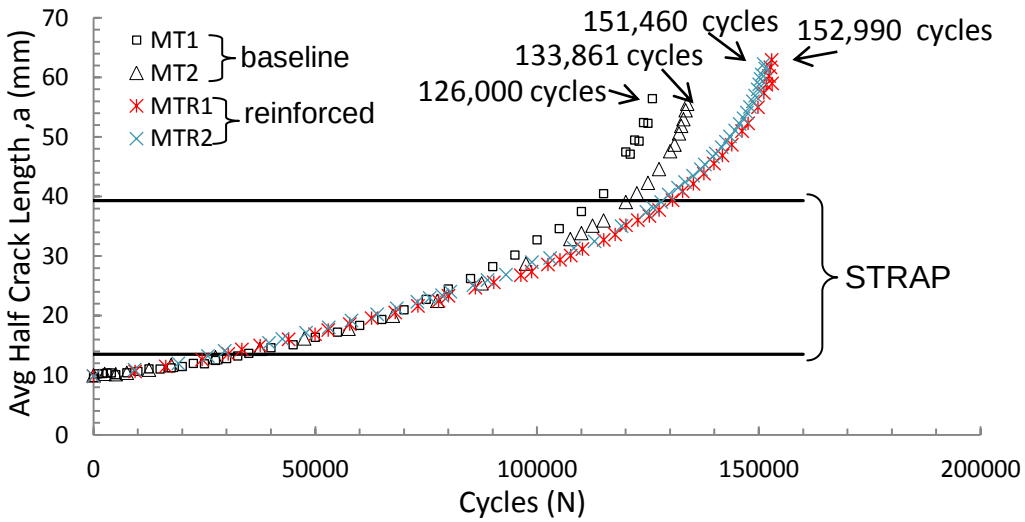

Figure 4-11 : Half crack length vs. cycles – Reinforced and unreinforced specimens

4.4.2 Fatigue crack growth rates vs. half crack length

Figure 4-12 shows that the presence of the strap starts to affect the fatigue crack growth rate after 20 mm. In fact, the curves between reinforced and unreinforced specimens start to separate after this crack length. Before that, no major difference is observed.

Past the half crack length of 20 mm, the crack growth rate is lower for the reinforced specimen as opposed to the baseline. The difference is of the order of 1.0×10^{-7} m/cycle within scatter for the test performed here. This difference stays approximately the same up to 42.5 mm where the difference between, baseline and reinforced is clearly marked with a lower crack growth rate of the order to 1.0×10^{-5} m/cycles.

Moreover the gradient of crack growth rate increases at 45 mm half crack length for the reinforced specimen while it was increasing at 39 mm for the baseline.

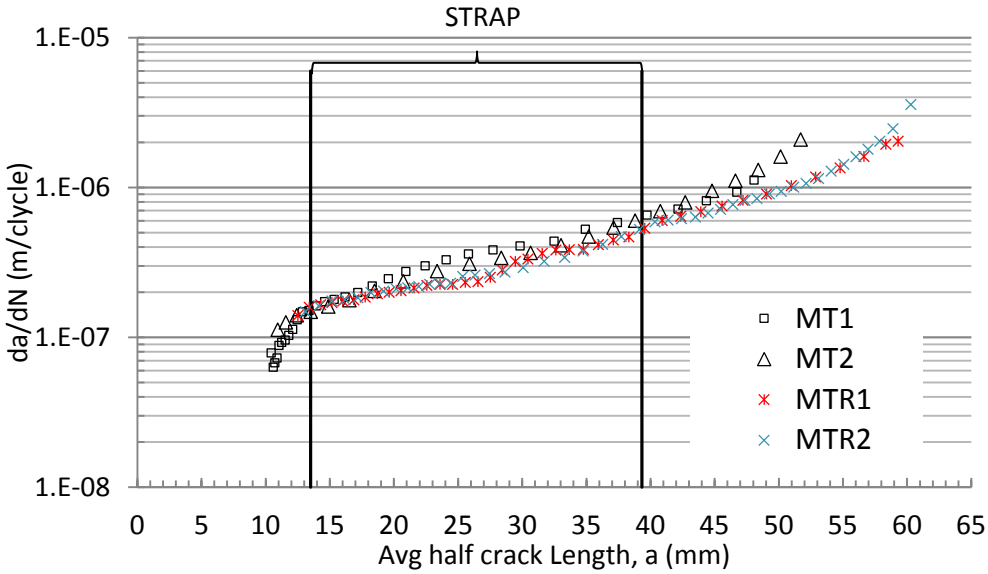

Figure 4-12 : Crack growth rate vs. half crack length for reinforced and unreinforced specimens

4.4.3 C-scan

As mentioned in the methodology section, C-scanning was used in order to establish whether or not disbonding was present at the interface between the strap and the substrate. Figure 4-13 shows an ultrasound C-scan of the strap bond (left hand side) before testing with good bonding between the strap and the substrate.

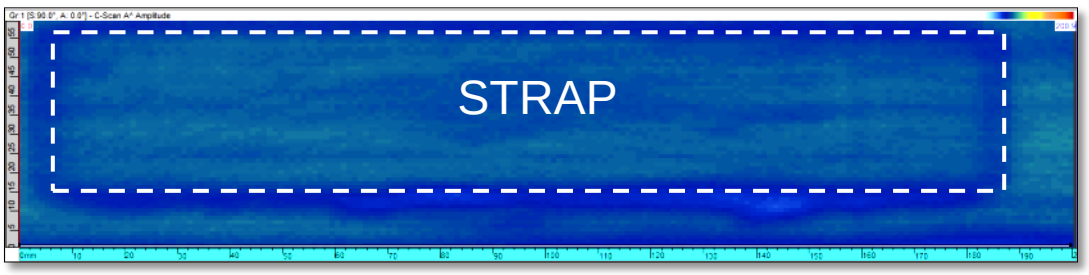

Figure 4-13 : Ultrasound C-SCAN of AIRstream reinforced M(T) specimen prior to testing (a =10 mm) showing no unbounded area prior to testing

C-scan was then performed for the second reinforced specimen MTR2 before it was pulled apart (no data for MTR1). The scan was performed after 124,651 cycles of fatigue crack growth with a total substrate crack length of 74 mm. The C-scan is illustrated in Figure 4-14.

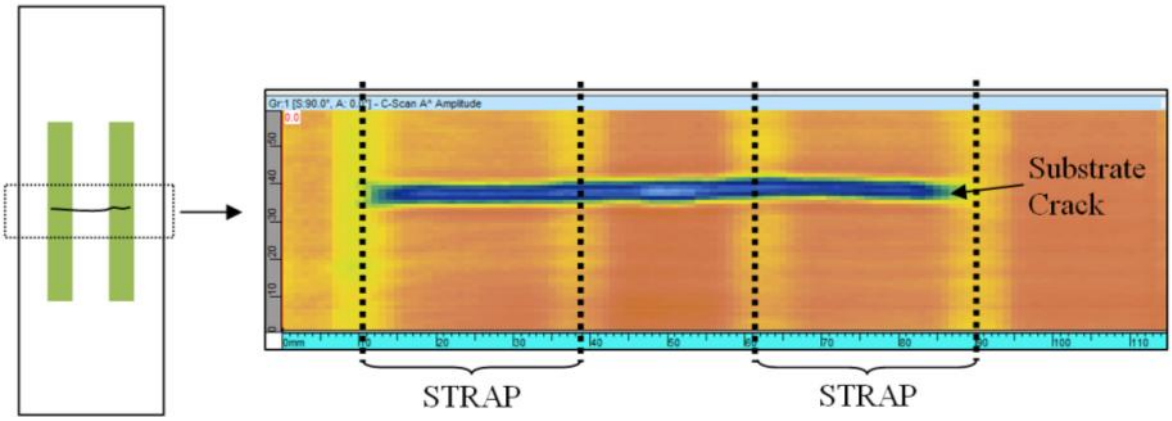

Figure 4-14 : C-scan of central area of MTR2 specimen in cracked region after 124,651 cycles – The scan was performed over the full width of the specimen, over the crack in the direction of the crack.

No obvious disbonding was observed at that stage of the test as no attenuation of the signal is seen in the area around the crack path. This may also be attributed to the sensitivity of the probe that is not high enough to detect the disbonding as the interface is very small in that un-failed situation. Hence it was not possible through C-scanning to establish whether or not disbonding was present at that stage of the test.

4.4.4 Fracture surface

After the crack had reached one edge of the specimen, the specimen was pulled apart using static loads. The specimen interface between the strap and the substrate were then visually inspected in order to identify signs of fatigue delamination that could have occurred during the fatigue failure phase of the specimen (Figure 4-15; Figure 4-16; Figure 4-17; Figure 4-18).

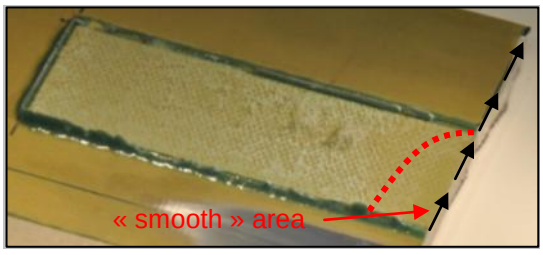

Figure 4-15 : Specimen MTR2 – Reinforced side / Part 1 zoom on disbonded area

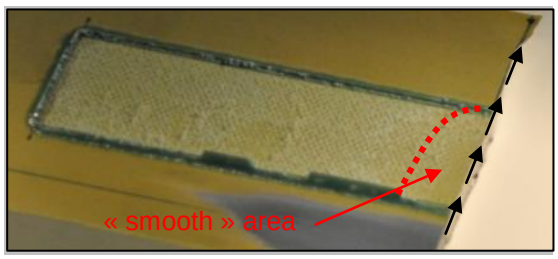

Figure 4-16 : Specimen MTR2 – Reinforced side / Part 2 zoom on disbonded area

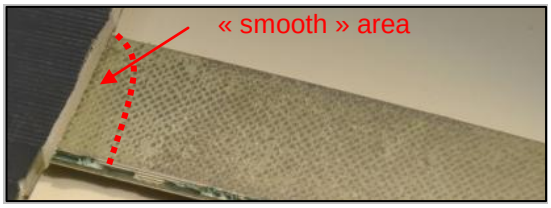

Figure 4-17 : Specimen MTR2 – Back side / Part 1 zoom on disbonded area

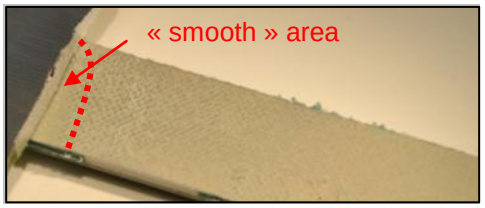

Figure 4-18 : Specimen MTR2 – Back side / Part 2 zoom on disbonded area

The figures show that adhesive was remaining on both part of the assembly (substrate and strap) which defines a cohesive failure. It also shows the presence of porosity in the adhesive layer estimated to more than 50% of the overall surface. No evidence of fatigue disbonding was observed on the fracture surface despite the presence of a smoother area of 5-6 mm from the substrate crack.

4.5 Conclusions

These test results showed the effect of the addition of bonded crack retarders to a substrate in the case of constant amplitude fatigue loading at an R ratio of 0.1 and a maximum stress of 60 MPa. It demonstrated that the fatigue life can be increased with an improvement factor of 17%, which is noticeable but not significant in comparison to previous results using that technology [5]. No disbonding was observed through C-scan and fracture surface observations did not demonstrate evidence of fatigue disbonding. These test results will be used to validate the finite element results by comparison of fatigue life, fatigue crack growth rate and delamination.

Chapitre 5 : Panel testing

5.1 Background and introduction

In addition to the program of coupon tests performed on 2624 – T351 that was reported in the previous chapter a series of 5 skin-stringer panels was tested. The aim of these tests was to:

- Evaluate the retardation effect of BCR on bolted skin stringer sub-assembly made of 2624-T351 aluminium alloy.
- Evaluate the improvement brought by the use of an aluminium-lithium 2199 –T8E80 material for the skin in addition to BCR.
- Determine the benefit of using a reinforced integrally machined skin-stringer panel over bolted panels.
- Carry out experimental test under spectrum loading condition on skin stringer assemblies and evaluate the variations with single coupons.

Two bolted 2624 –T351 skin panels – this alloy is frequently referred to as 2024 HDT for its High Damage Tolerance properties – with one baseline and one reinforced panel, two 2199 –T8E80 (2199 al-lith) bolted skin panels with again, one baseline and one reinforced panel and one Integrally Stiffened Panel (ISP) made of 2099 – T81 (2099 ISP) – reinforced – were tested.

The tests were conducted under variable amplitude loading using the lower cover test spectrum of an A320 aircraft. Its maximum stress was 101 MPa (originally 140.3 MPa) with a minimal stress of -19 MPa (originally -32.39 MPa) that was obtained from gating and clipping of the original spectrum to accommodate the machine load capacity limitation of 800 kN. While the original spectrum was made of 138,230 cycles, the manipulated spectrum resulted in 58,010 cycles with no major influence on panel fatigue responses as described in Appendix A.

5.2 Panel design

The bolted assembly of 5 stringer panel can be seen in Figure 5-2 and Figure 5-3. All panels were of dimensions 1200 x 780 mm with 5 stringers and a rib.

The skin was 3.85 mm in thickness for the 2024 panels and 3.5 mm in thickness for the 2199 Al-lith panels. All bolted panels were designed by Airbus UK and the 2099 ISP panel was designed by Alcoa. Detailed drawings can be found in the Appendix B. Figure 5-1 shows the front and back views of the panel with indications of the dimensions.

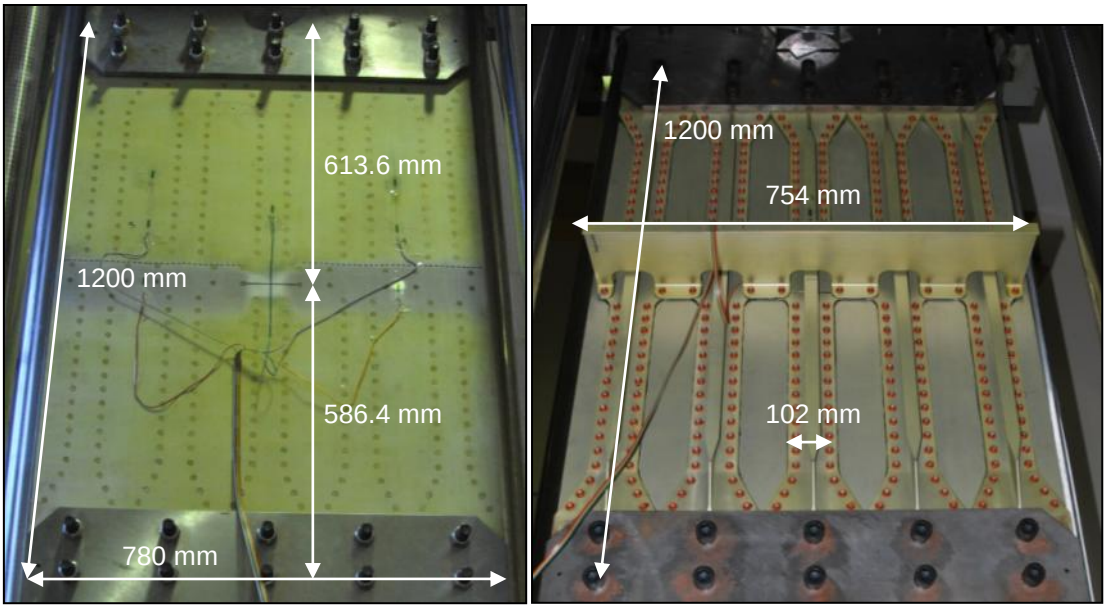

Figure 5-1 : Front and back views of bolted panel (baseline)

- Bolted panels

The baseline panels (no reinforcement) were assembled by Airbus prior to testing with one panel made of a 2624-T351 skin, 2026-T3511 stringer and a 7010 rib. The second baseline was made of a 2199-T8E80 skin, 2099-T81 stringers and a 7010 rib. The two reinforced panel were made of the same materials as the baseline one but with the inclusion of the bonded GLARE straps. The bonding was performed at Cranfield University by adhesively bonding the 5 Glare 2A-6/5 (0.4) straps to the skin using FM94 adhesive before final assembly by Airbus. The straps were 136 mm wide by 1200 mm long and 3.7 mm in thickness. They were located under each stringer. Following the bonding process, the bonding quality was inspected by Airbus using an ultrasound scan. The inspection revealed no disbonding with an attenuation of approximately 10 dB for the 2024 HDT assembly and 9 dB for the 2199 al-lith panel.

Once the inspection was completed, the panels were assembled by Airbus.

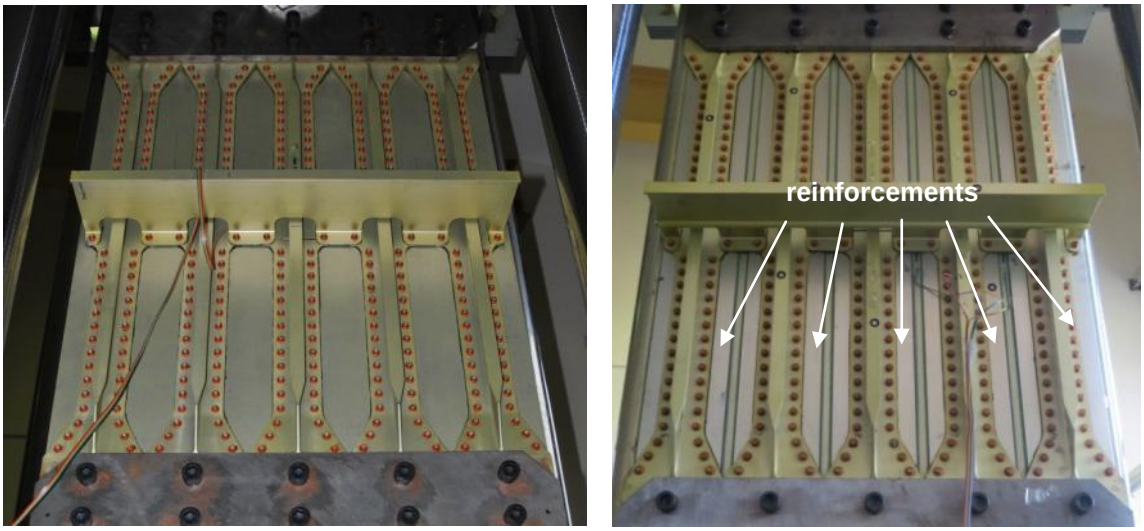

(a) Baseline panel (2024 HDT) (b) Reinforced panel (2024 HDT)

Figure 5-2 : Bolted panels with (a) baseline and (b) reinforced

Note: During the manufacturing process of the aluminium lithium bolted panel, it was noticed that the thickness of the skin tapered from 3.5 to 3.85 mm while the thickness of the 2024 HDT panel was 3.85 mm.

- Integrally stiffened panel

Only one reinforced ISP panel was tested (Figure 5-3). The panel was made of extruded 2099 – T81 aluminium with the two outer stringers friction stir welded to the 3 central stringers. The panel was 780 x 1200 mm with 4 reinforcing straps of dimensions 70 x 640 mm made of Glare 2A 6/5 (0.4). The straps were adhesively bonded to the panel in Cranfield using Cytec FM94 with the same procedure as used in the bolted panel bonding process. The bonding quality was inspected by Airbus using an ultrasound scan. The scan showed an attenuation of 4dB which indicates an acceptable bonding quality. Airbus performed the final assembly by adding the rib.

(a) Panel before bonding

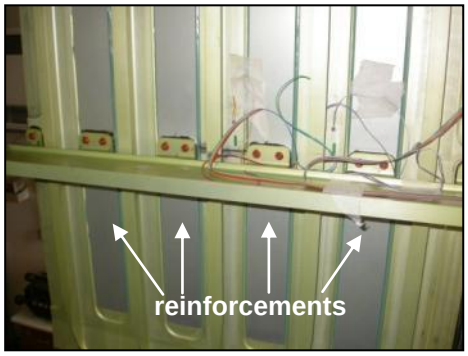

(b) Panel ready for testing

Figure 5-3 : ISP reinforced panel

An artificial crack starter of 129 mm with a width of 3 mm was introduced into the skin of all the panels at the centre line, half way along the width, the centre stringer being severed completely. This was similarly applied to the ISP panel. Detailed drawings of that pre-cut can be found in Appendix B.

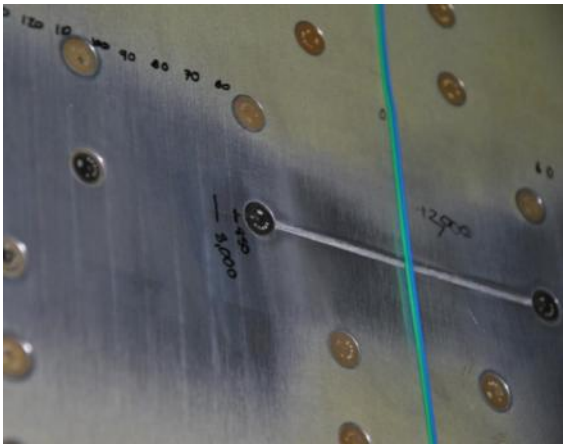

(a) Front view of pre-cut skin

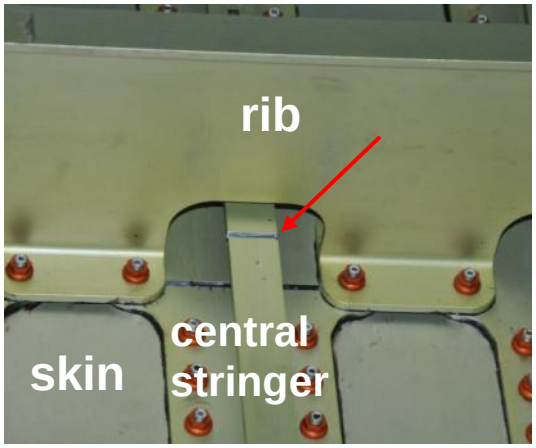

(b) Back view of pre-cut skin and central stringer

Figure 5-4 : Artificial damage used as crack nucleation for bolted panel

Table 5-1 : Panel test matrix

Test	Description	Skin material	Stringer material	BCR
P_COU_01	2024 HDT baseline	2624 – T351	2026 – T3511	NO
P_COU_02	2024 HDT reinforced panel	2624 – T351	2026 – T3511	YES
P_ALC_01	2199 al-lith. baseline	2199 – T8E80	2099 – T81	NO
P_ALC_02	2199 al-lith. reinforced	2199 – T8E80	2099 – T81	YES
P_COU_03	2099 ISP reinforced	2099 - T81	N/A (integral structure)	YES

The panels were tested in a 1 MN servo-hydraulic machine equipped with an Instron 8600 series digital control system associated to a computer control that used RANDOM software to apply a variable amplitude sequence to the specimens.

5.3 Strain gauge monitoring of skin-stringer panels

5.3.1 Introduction

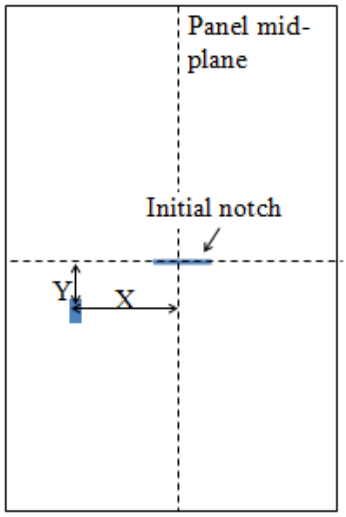

Figure 5-5 : Strain gauge position

In order to verify the stresses applied to the panels, a set of strain gauges was installed on each panel. The data obtained from the strain gauges were collected using a National Instruments data acquisition system. The gauge positions were designed to check for panel out of plane and in plane bending, and to provide a reference calibration of strain Vs applied load at a defined location on the sample horizontal centreline at a position remote from the influence of the crack starter notch and stress concentrations associated with stringer locations

and individual bolt holes. The reference location was on the sample horizontal centreline, 234 mm from the vertical centreline as shown in Figure 5-5. Table 5-2 shows the actual location of the strain gauges on the 4 bolted panels. The calibration gauge allowed the determination of the panel load which would provide the same remote skin stress in each panel despite differences in thickness dimensions, construction and the presence of bonded retarders. The values of stress in Table 5-2 were used to set the maximum loads achieved in the load spectrum.

Table 5-2: Calibration results at maximum load and actual strain gauge positions

Panel	X position (mm)	Y position (mm)	Max load (kN)	Strain	Modulus (MPa)	Stress (MPa)
2024HDT baseline	229	0	585	1.47×10^{-3}	71,000	104
2024HDT reinforced	234	0	790	1.38×10^{-3}		98
2199 Al-lith baseline	234	19	582	1.30×10^{-3}	75,200	98
2199 Al-lith reinforced	235	0	790	1.27×10^{-3}		96

Table 5-2 shows the difference in position for the strain gauges which means that the stress values for the 2624 baseline and the 2199 baseline should be modified. This was performed by the measurement of strain in both positions and establishing a correction factor. Hence a strain gauge positioned at X = 229 mm and Y = 0 mm was added to the 2199 reinforced panel as well as a strain gauge at the position X = 234 mm and Y = 19 mm. The ratio between strains in this position and the position X = 234 mm and Y = 0 mm was then used to calculate the strain in the 2624 baseline as well as the 2199 baseline. The revised values of stress and strain are summarized in Table 5-3; the sign * indicates the values that have been evaluated using the recalibration of the 2199 Al- Li reinforced panel. These stress and load values are the ones which were applied as the maximum stresses in the spectrum during variable amplitude load testing of the panels. In the case of the 2099 ISP panel, the strain gauge was accurately positioned at X=234 and Y = 0, and the loads required to produce a stress of 101 MPa were calculated from the strain

readings obtained, noting that the elastic modulus of this panel skin was 78 GPa.

Table 5-3 : Modified stress and load spectra maxima for all bolted panels as evaluated from re-calibration

Panel	X position (mm)	Y position (mm)	Max load (kN)	Strain	Modulus (MPa)	Stress (MPa)
2024 HDT baseline	234	0	585	1.47×10^{-3}*	71,000	104*
2024 HDT reinforced	234	0	790	1.38×10^{-3}		97.7
2199 Al-lith baseline	234	0	582	1.35×10^{-3}*	75,200	102*
2199 Al-lith reinforced	235	0	790	1.27×10^{-3}		95.8

5.3.2 Example of calibration stress calculations

Detailed calibrations are given as examples for the 2024 HDT baseline and reinforced panels. All other strain gauge measures are presented in Appendix C.

- Panel 1: 2624 - T351 – bolted – no reinforcement (P_COU_01)

The maximum stress selected for the test according to the spectrum manipulation was 101 MPa. Calculation showed that the cross section of this panel was 5786 mm^2. Hence the maximum load to reach 101 MPa was calculated as 584 kN. The panel was loaded using a ramp loading up to that maximum load and back to zero while recording the strain gauge measurements.

Figure 5-6 and Figure 5-7 illustrate the location of the strain gauges. During the calibration, it was noticed that the strain gauge #2 did not work. The calibration measures are given in Figure 5-8 to Figure 5-10. The results are given in Table 5 –4. It shows the maximum values obtained for each strain gauge.

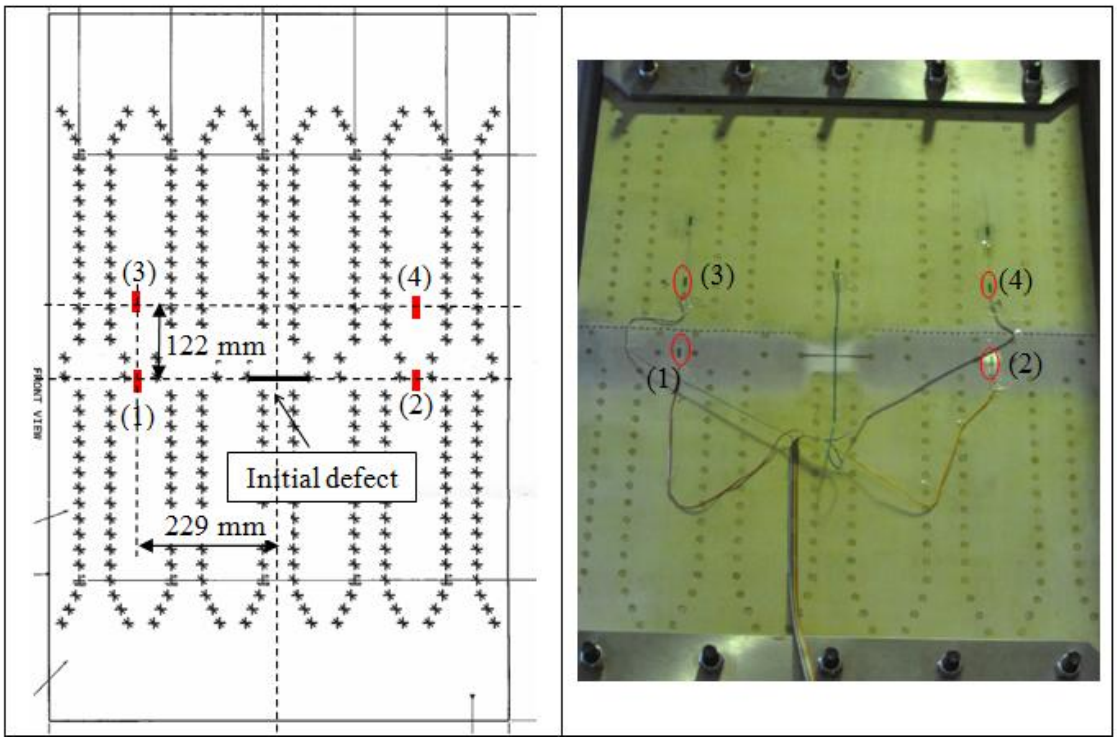

Figure 5-6: Panel 1 strain gauge location – Front view (strain gauge 1, 2, 3, 4)

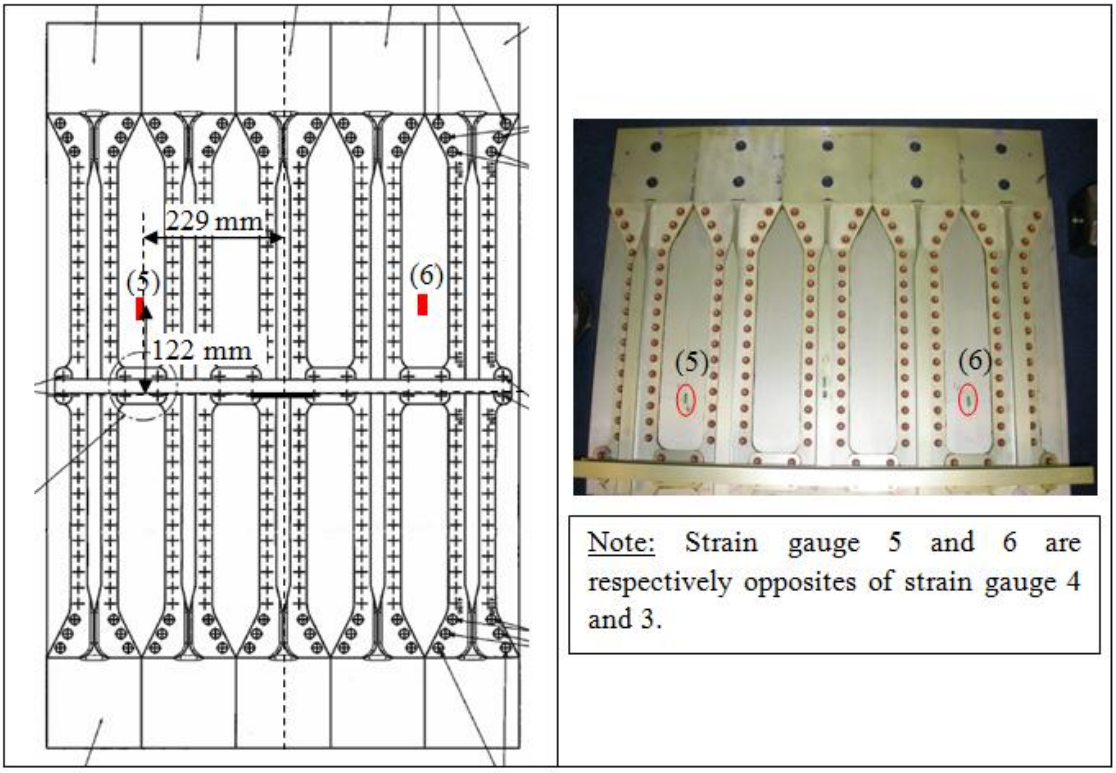

Figure 5-7: Panel 1 strain gauge location – Back view (strain gauge 5, 6)

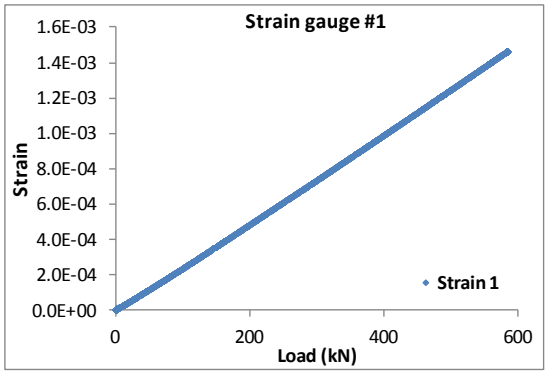

Figure 5-8 : Strain gauge results from calibration at maximum load for strain gauge 1 – Panel 1.

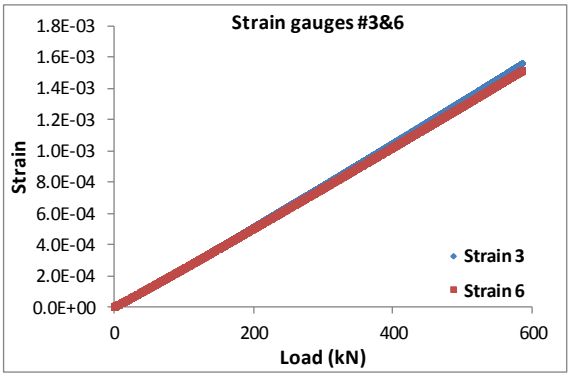

Figure 5-9 : Strain gauge results from calibration at maximum load for strain gauge 3 and 6; opposite strain gauges on skin side and stringer side – panel 1.

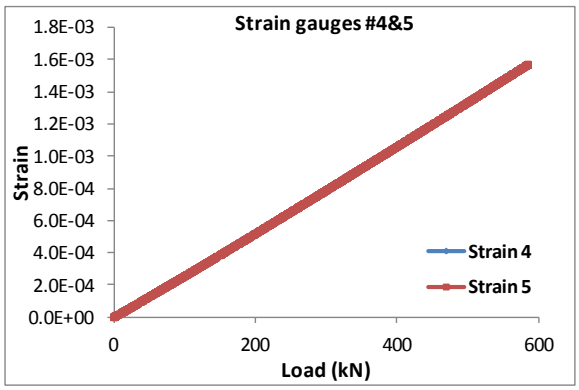

Figure 5-10 : Strain gauge results from calibration at maximum load for strain gauges 3 and 6; opposite strain gauge on skin side and stringer side – panel 1.

Table 5-4 : Strain gauge measurements for 2024 HDT baseline panel

Strain gauge	Location	Max strain	Modulus (MPa)	Max stress (MPa)
#1	Skin-side / crack direction	$1.47x10^{-3}$	71,000	**104**
#3	Skin-side / 122 mm up the crack	$1.56x10^{-3}$		111
#4	Skin-side / 122 mm up the crack	$1.57x10^{-3}$		111
#5	Stringer-side / 122 mm up the crack	$1.58x10^{-3}$		112
#6	Stringer-side / 122 mm up the crack	$1.52x10^{-3}$		108

One strain gauge that is of particular interest here is strain gauge #1 as it is used to check that the stress used for the test was close to the required 101 MPa. It shows a value of 104 MPa in the location of strain gauge #1, which is 3% higher than the 101 MPa expected. No load adjustment was performed.

Figure 5-8 shows a linear behaviour as measured by the strain gauge #1. This linear behaviour was also observed on the other strain gauges. This means that no geometrical non-linearity is observed on the panels. This is critical in determining the effect of the retarders as the behaviour is linear.

- Panel 2: 2624 - T351 – bolted –reinforced (P_COU_02)

Calculation showed that the cross section of this panel was 8149 mm^2. Hence the maximum load to reach 101 MPa is 823 kN. Since the test machine is restricted to 800 kN, this is not an achievable load. Hence the method used here was to perform a calibration of the panel up to a maximum load of 790 kN and check the stress in a strain gauge position comparable to strain gauge 1 of the baseline. 790 kN was selected as the maximum possible load that could be used during the fatigue test in order to avoid possible failure of the machine.

Figure 5-11 and Figure 5-12 illustrate the location of the strain gauges. The calibration measures are given in Figure 5-13 to Figure 5-16. The results obtained during the calibration at maximum load are given in Table 5-5. It shows the maximum strain and corresponding stress obtained for each strain gauge.

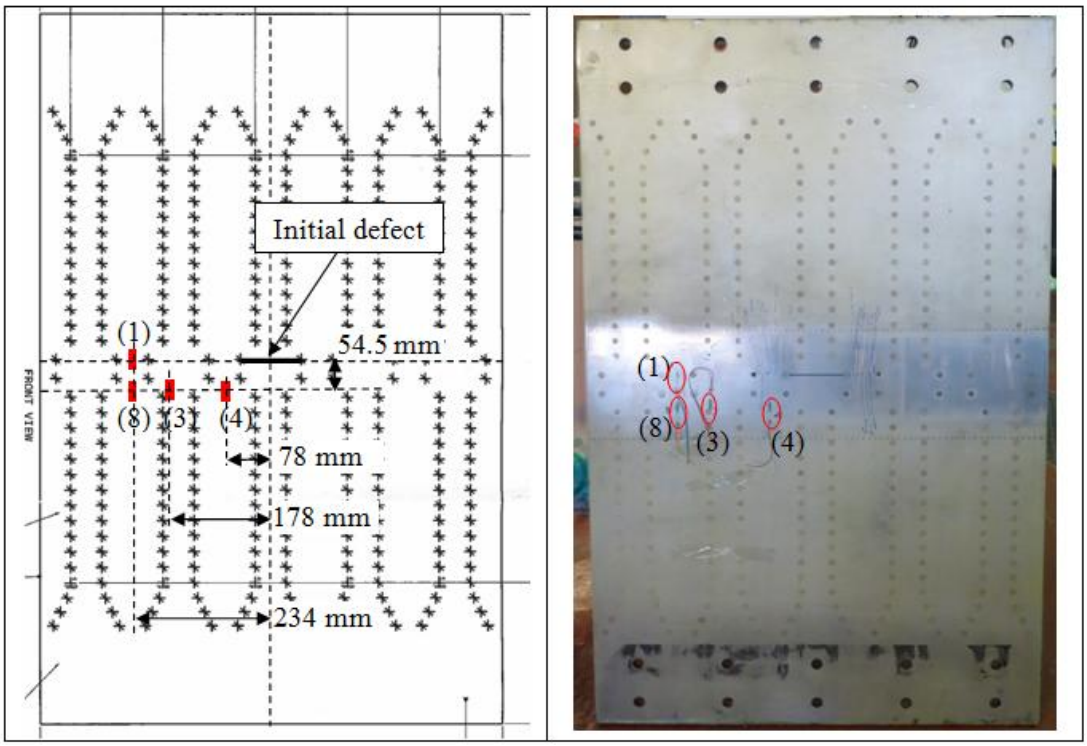

Figure 5-11 : Panel 2 strain gauge location – Front view (strain gauge 1, 3, 4, 8)

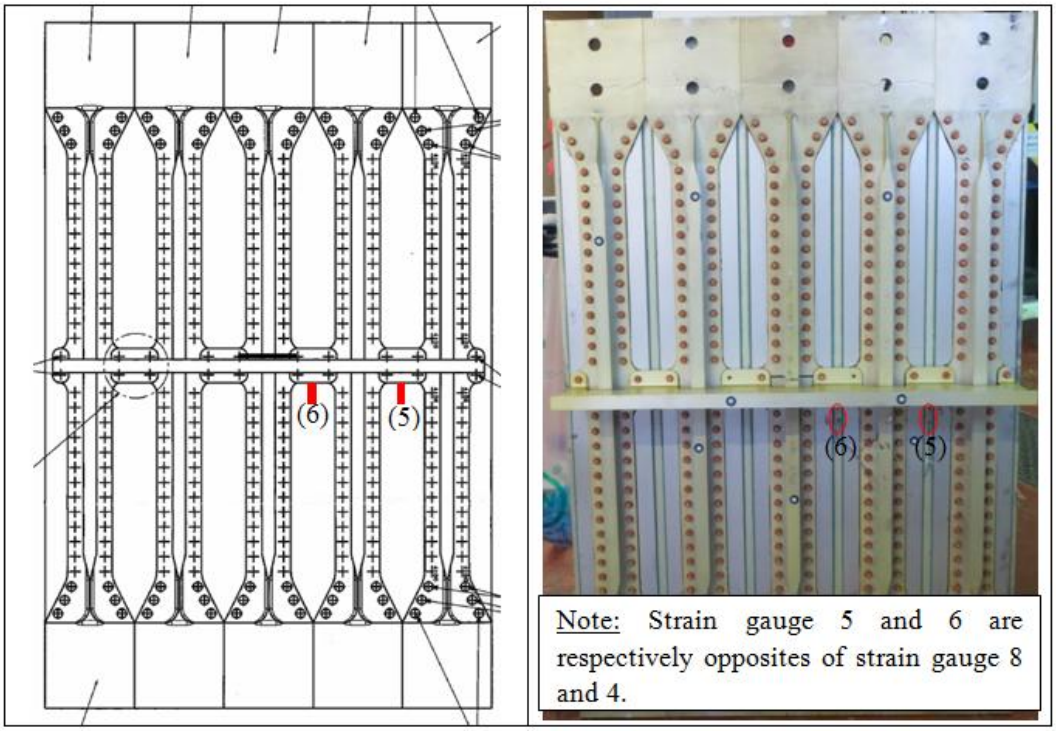

Figure 5-12 : Panel strain gauge location – Back view (strain gauge 5, 6)2

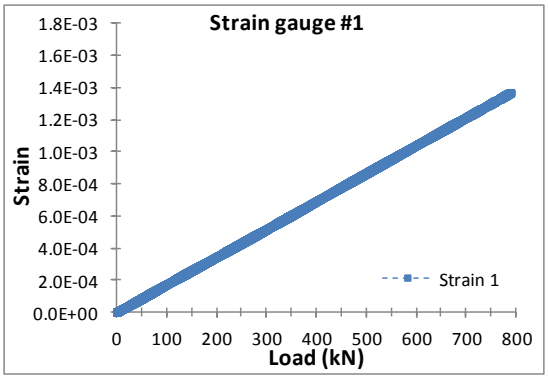

Figure 5-13 : Strain gauge results from calibration at maximum load for strain gauge 1 – Panel 2

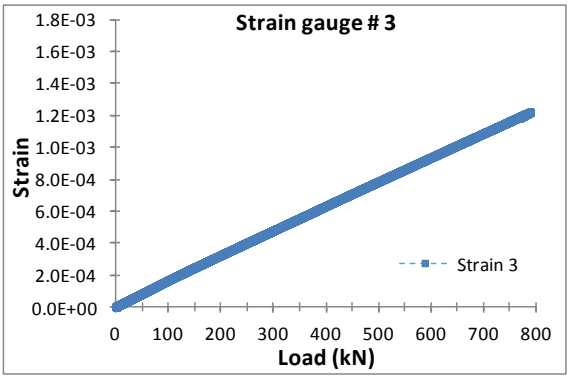

Figure 5-14 : Strain gauge results from calibration at maximum load for strain gauge 3 – Panel 2

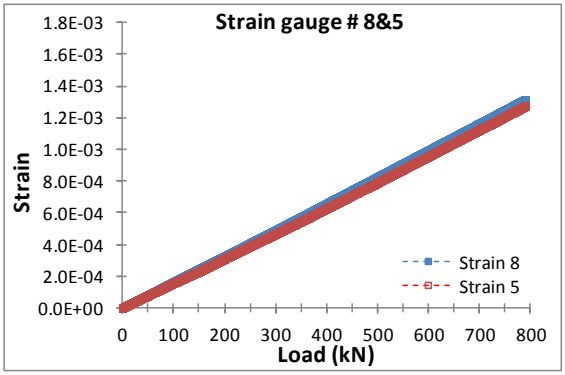

Figure 5-15 : Strain gauge results from calibration at maximum load for strain gauge 8 and 5; opposite strain gauges on skin side and stringer side – panel 2

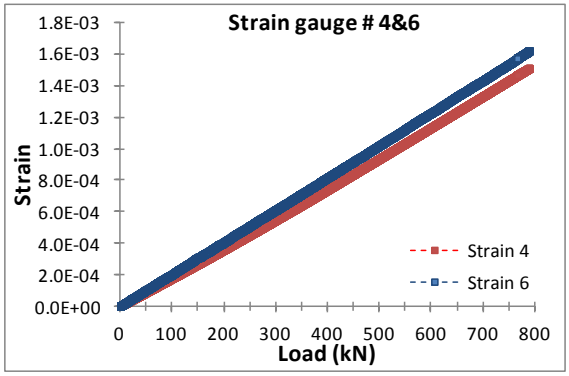

Figure 5-16 : Strain gauge results from calibration at maximum load for strain gauge 4 and 6; opposite strain gauges on skin side and stringer side – panel 2

Table 5-5 : Strain gauge measurements for panel 2 - 2024 HDT reinforced panel

Strain gauge	Location	Max strain	Modulus (MPa)	Max stress (MPa)
#1	Skin-side / crack direction	$1.38x10^{-3}$	71,000	**97.7**
#3	Skin-side / 54.5 mm from crack / 178 mm from panel centre	$1.22x10^{-3}$		86.9
#4	Skin-side / 54.5 mm from crack / 78 mm from panel centre	$1.51x10^{-3}$		107
#8	Skin-side / 54.5 mm from crack / 234 mm from panel centre	$1.32x10^{-3}$		93.5
#5	Stringer-side / 54.5 mm from crack / 78 mm from panel centre	$1.28x10^{-3}$		90.6
#6	Stringer-side / 54.5 mm from crack / 234 mm from panel centre	$1.62x10^{-3}$		115

Strain gauge #1 is used as a mean of comparison to the baseline panel as it is in a similar position to a strain gauge location of the baseline panel (strain gauge #1).

The calibration showed a maximum stress of 97.7 MPa which is lower than the 101 MPa required. Hence, it was decided to clip the spectrum again to a maximum stress of 97.7 MPa. All the cycles with maxima less than 97.7 MPa will be unchanged and only the cycles with stress maxima between 97.7 and 101 MPa will be reduced. Strain gauge #4 and #6 show higher stresses with respectively 107 MPa and 115 MPa which can be explained by the proximity of the initial crack which will locally increase the stresses in the panel. Strain gauges #8 and #5 showed smaller strains than #1. All strain gauge measures were linear.

The different levels of strain for the remaining strain gauges are due to their location. In fact as strain gauge #4 is the closest to the crack tip; it presents the highest strain level. Nevertheless the results obtained for strain gauge #3 are slightly anomalous as one would expect the strain to be higher than strain

gauge 8 in that location. This might be explained by the presence of the reinforcing stringer on the other side of the skin.

The same method of calibration was applied to the remaining panels. The calibration results were shown in Table 5-2 and are reported in Appendix C.

5.4 Panels bending measures

Panel bending is calculated from opposite strain gauges on the skin side and on the stringer side placed on the panels.

- **2024 HDT baseline panel :** Figure 5-17 shows the percentage of bending calculated according to the measurements performed on strain gauges 3&6 and 4&5 for the 2024 HDT baseline panel.

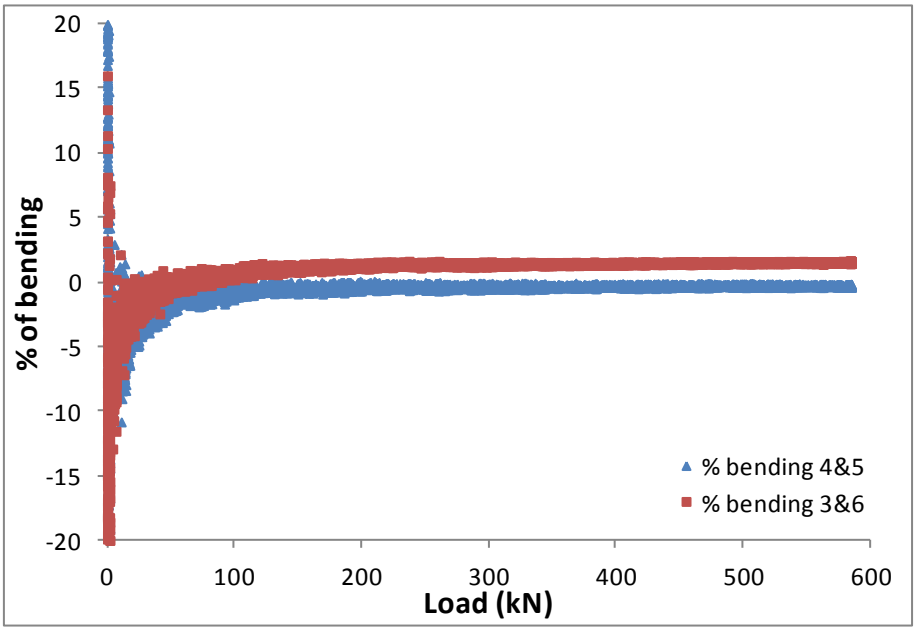

Figure 5-17 : Bending percentage results for 2024 HDT baseline panel

Figure 5-17 shows less than 5% bending in the panel. The higher values observed at the beginning of the test correspond to measurement errors and are not taken into account here.

- **2024 HDT reinforced panel :** Figure 5-18 shows the percentage of bending calculated according to the measurements performed on strain gauges 8&5 and 4&6 for the 2024 HDT reinforced panel.

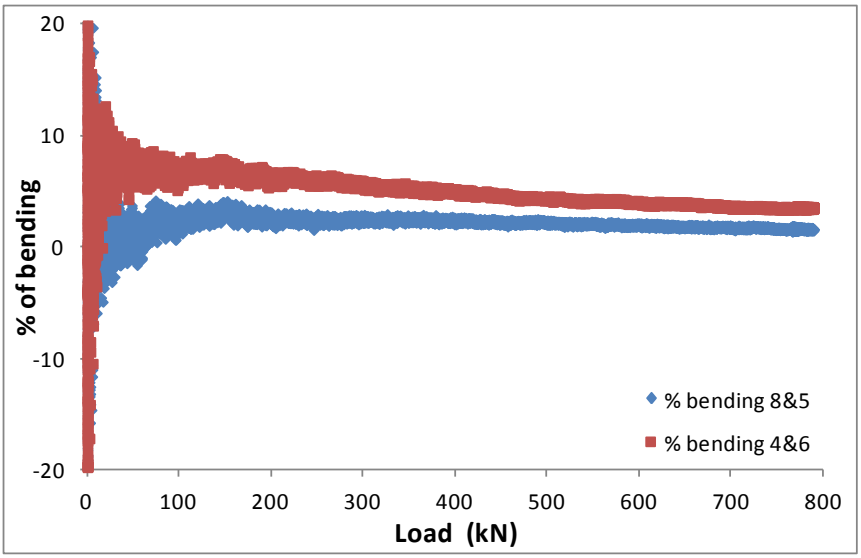

Figure 5-18 : Bending percentage results for 2024 HDT reinforced panel

The level of bending for the 2024 HDT reinforced panel is less than 10% in both cases with 4 & 6 greater at the beginning of the calibration than 8 & 5. This can be due to the fact that the central stringer, near this location is totally broken, allowing more movement in that particular location.

- **2199 al-lith baseline panel :** Figure 5-19 shows the percentage of bending calculated according to the measurements performed on strain gauges 3&5 and 1&6 for the 2199 al-lith baseline panel.

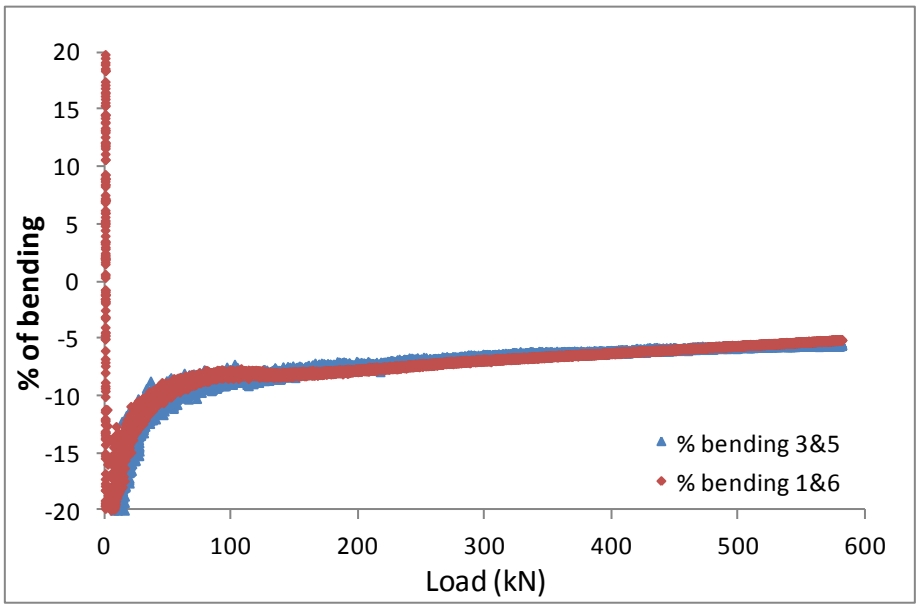

Figure 5-19 : Bending percentage results for 2199 al-lith baseline panel

Overall, the level of bending for the 2199 al-lith panel is less than 10%. It is interesting to note though that the bending direction is different as the sign is negative. This may be due to changes in the geometry of the panel such as the skin thickness that was lower than the 2024 HDT panel skin thicknesses.

- **<u>2199 al-lith reinforced panel :</u>** Figure 5-20 shows the percentage of bending calculated according to the measurements performed on strain gauges 3&5 and 1&6 for the 2199 al-lith reinforced panel.

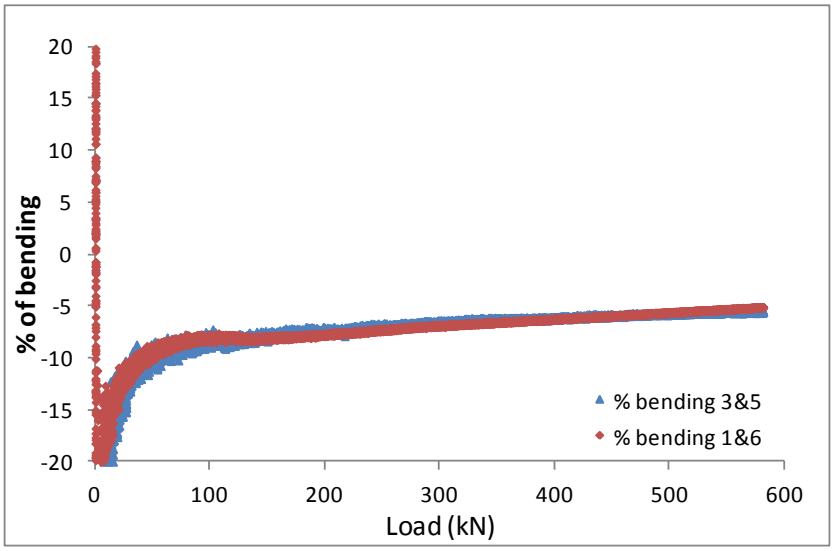

Figure 5-20 : Bending percentage results for 2199 al-lith reinforced panel

Overall, the level of bending for the 2199 al-lith reinforced panel is less than 10%. As for the baseline panel, the bending direction is different as the sign is negative.

- **<u>2099 ISP reinforced panel :</u>** Figure 5-21 shows the percentage of bending calculated according to the measurements performed on strain gauges 2&4 for the 2099 ISP reinforced panel.

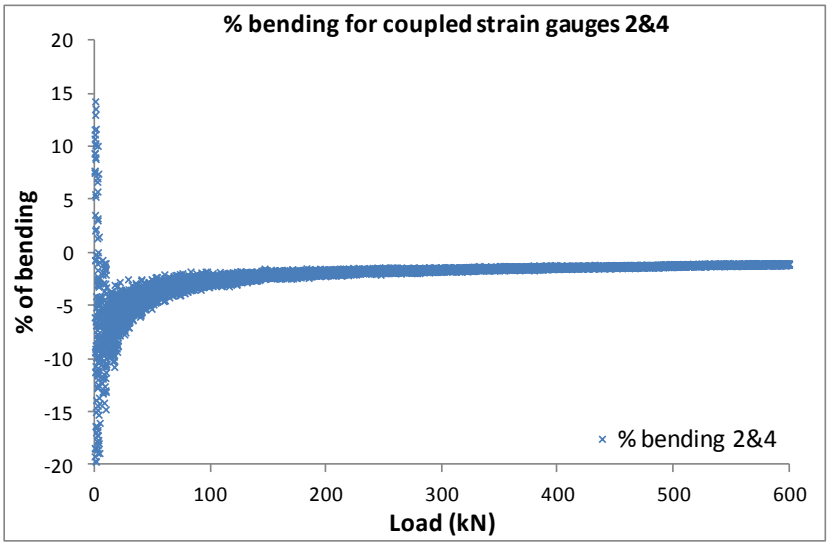

Figure 5-21 : Bending percentage results for 2099 ISP reinforced panel

The level of bending for the 2099 ISP reinforced panel is less than 5% and in the same direction as the Al-lith panels. Bending appears to be lower for this panel in comparison to the other panels. This may be explained by the fact that this panel is fully machined, hence is stiffer than the other panels.

Table 5-6 : Summary of bending percentage at maximum loads for panels (peak of loads for panels) and coupons

Panel	Skin	BCR	Bending stress (MPa)	Bending %
2024 HDT baseline	2024HDT	No	+1.5	1.5%
2024 HDT reinforced	2024HDT	Yes	+1.45	1.5%
2199 Al-lith baseline	2199 Al-lith	No	**-5.7**	**5.6%**
2199 Al-lith reinforced	2199 Al-lith	Yes	-4.7	4.9%
2099 ISP reinforced	2099 - T81	Yes	-1	1%
M(T) Airstream design (current)		Yes	**9.2**	**15.3%**
M(T) BCR design (former)		Yes	4.7	7.8%

Under maximum loads, it shows that bending percentages are lower for the panels than for the coupons. It also demonstrate that there is variation in bending from one panel to another with positive bending that is less than 2% for the 2024 HDT panels and negative bending for the 2199 Al-lith panel that is around 5%. The ISP panel bending is at its lowest with only 1%. The difference in bending amounts from bolted to ISP panels may be explained by the difference in stiffness between the panels. In fact the stiffness for the ISP panel is higher than the one for the bolted panels if one compares the level of strain gauges at equivalent loads.

Bending amounts are further discussed in Chapter 11 by comparing panel bending and coupons bending and the effect this may have on the life improvement for the BCR technology.

5.5 Variable amplitude fatigue testing of panels

The same procedure was followed for all the panels tested. The panel was first calibrated at its maximum load in order to check the maximum stress by use of the strain gauge installed on the panel. The panel was then either subjected to constant amplitude loading to initiate the crack – and then loaded under variable amplitude - or run directly in variable amplitude.

The crack advance was measured optically by eye on the panel with the aid of scribe marks and a ruler with a precision of +/- 0.5 mm. The crack tip was marked using a permanent pen for each measurement and the crack length – right and left sides – were reported in a datasheet together with the number of cycles. In case of a crack appearing in an unexpected location the crack tip was also marked with the corresponding number of cycles elapsed.

5.5.1 2024 HDT panels

The baseline panel was tested with a maximum spectrum stress of 104 MPa**,** while the reinforced one was tested with a maximum spectrum stress of 98 MPa.

The baseline panel failed after **231,938 cycles** with a left crack length of 302 mm and a right one of 390 mm where the panel was fully broken by the end of the test. The maximum load used for this baseline panel was 584.4 kN with a respective minimum load of - 109.6 kN. After failure of one side, the panel was statically broken using displacement control. Hence the panel had performed approximately 4 sequences of the variable amplitude spectrum. The crack propagated in the skin and the failure of the stringer was observed as the crack in the skin was located in the stringer area.

The reinforced panel was first pre-cracked using a constant amplitude loading up to 134,535 cycles which resulted in crack lengths of 68.5 mm on the left hand side and 61 mm on the right hand side. The variable amplitude test was then started using the modified clipped spectrum with a maximum stress of 98 MPa. The maximum load was set to 790 kN. The respective minimum load was -153 kN. The reinforced panel performed **389,100 cycles** with a half crack length of 100 mm that had reached the rivet and the test had to be stopped because of failure occurring in other areas of the panel. Re-initiation of the crack from the bolt was performed with variable and constant amplitude loading but it proved un-successful. Instead, cracks appeared in other areas than the main crack (stringer run-out and holes of pin loading) and the test had to be stopped.

Figure 5-22 shows a plot of the average half crack length vs. cycles for the reinforced and baseline 2024HDT panels. It can be seen that the baseline panel took 5 x 10^4 cycles to achieve a skin crack length of 100 mm. It shows a regular crack growth up to 50,000 cycles where a discontinuity in the data is observed due to the crack tip entering the first bolt hole. Then the crack growth stays regular up to 200,000 cycles where it accelerates rapidly up to failure. The reinforced panel took 389,100 cycles to achieve the same crack length- a life improvement ratio of 1.7. It shows a constant gradient from approximately 66 mm up to 100 mm. However panels were tested at two different stress levels.

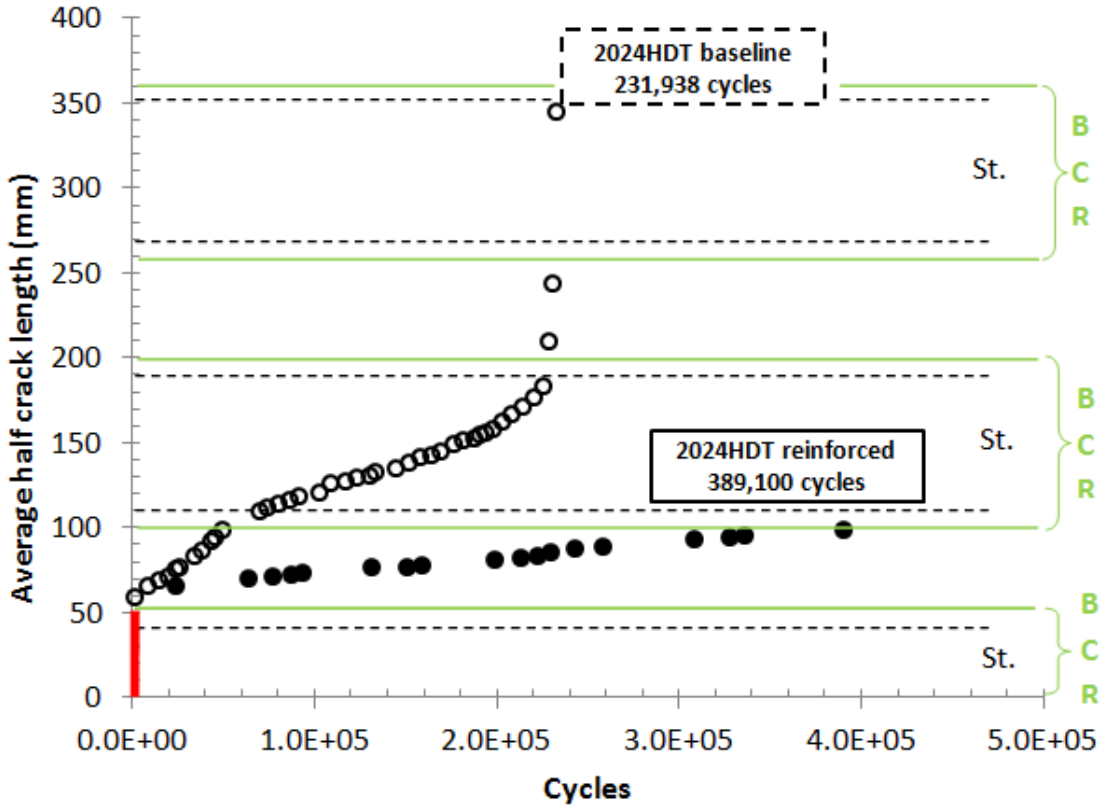

Figure 5-22 : Half crack length average vs. cycles comparison for 2024HDT baseline vs. 2024HDT reinforced

Figure 5-23 shows the crack growth rates vs. average half crack length for the reinforced and baseline 2024HDT panels. It shows for the baseline panel that from the start of the test, the fatigue crack growth rate is accelerating from $7.0x10^{-7}$ m/cycle to $8.0x10^{-7}$ m/cycle up to a crack length of approximately 80 mm. From that point, the crack growth rate decreases up to $3.0x10^{-7}$ m/cycle for a crack length of 130 mm. Past this point, the crack growth rate accelerates again up to $8.0x10^{-6}$ m/cycle before final failure. The decrease in the fatigue crack growth rate is thought to be due to the stringer which slows down the propagation of the crack. The crack growth rate for the reinforced panel is varying from 7.0×10^{-8} m/cycle to 10^{-7} m/cycle; a small variation in crack growth rate in comparison to the baseline case. Nevertheless the crack growth rate is slowing at the early stage of the test before accelerating in the non-reinforced area and slowing down again as it reached the reinforced area. The variation in crack growth rate could be interpreted as a consequence of the straps as well as the presence of the stringer for that crack length.

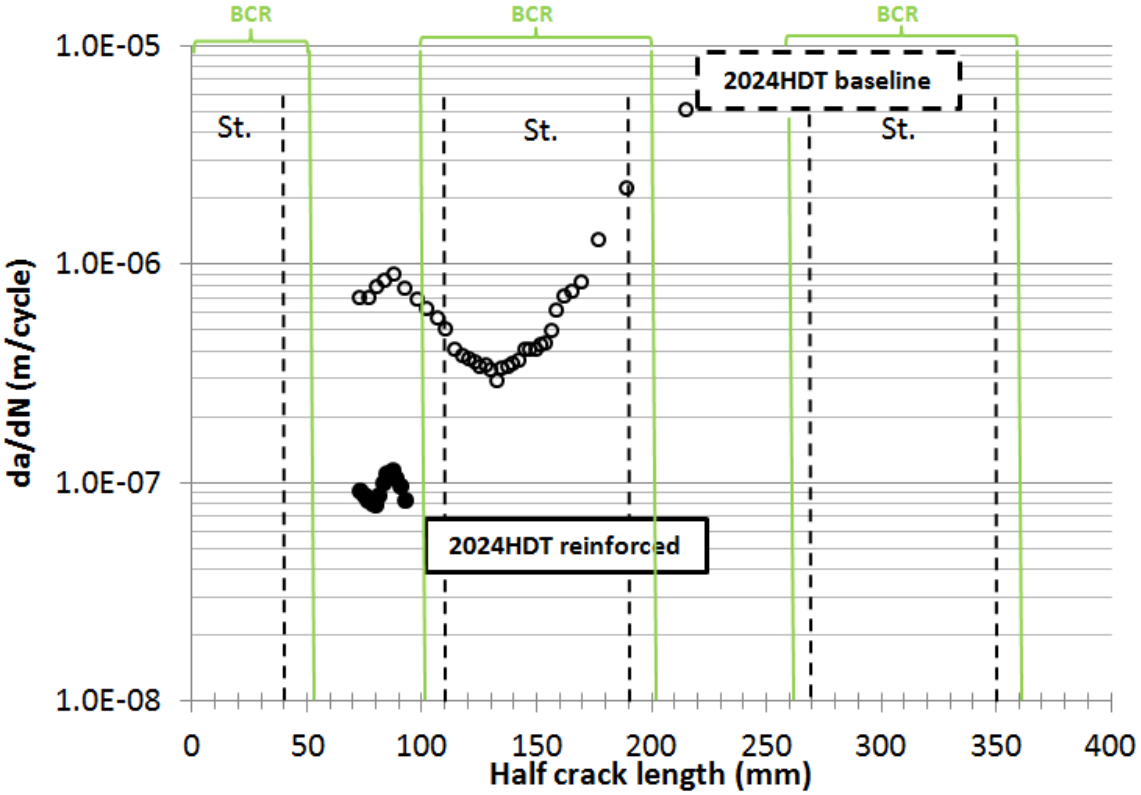

Figure 5-23 : Fatigue crack growth rates comparison for 2024HDT baseline vs. 2024HDT reinforced

The major difference between the reinforced panel da/dN and the baseline is a factor of between 3 and 10 difference in crack growth rates.

At the end of the test the reinforced panel had multiple cracks in the area of pin loading at the stringer ends as well as in the skin and the stringer run-outs. The baseline panel which had only to endure 2 x 10^5 cycles had no signs of such failure. The 389,100 cycles that the reinforced panel performed were responsible for the crack advance only as this number does not take into account the numerous cycles used to re-initiate the crack from the rivet.

The multiple cracks observed at the pin loading and the stringer run-outs can be explained as consequences of the loads being re-distributed due to the presence of the straps together with the fact that a crack did not re-initiate from the main crack.

Conclusions:

- The presence of the retarder strap has improved the fatigue life of the baseline panel by a nominal factor of 6.9. In fact at equivalent crack length of 100 mm, the baseline panel performed 49,000 cycles for 389,100 cycles for the reinforced one.
- Crack growth rates in the strapped panel were reduced by a factor of between 3 and 10. The reinforced panel test had to be abandoned after almost 4 x 10^5 cycles because of cracking in other panel locations which had exceeded their fatigue life at this juncture (Figure 5-24).
- Exploitation of the full life extension potential of bonded crack retarders requires accurate investigation of the design of the entire structure it is applied to in order to check for load redistributions.
- The life obtained is several times the anticipated life of the aircraft.

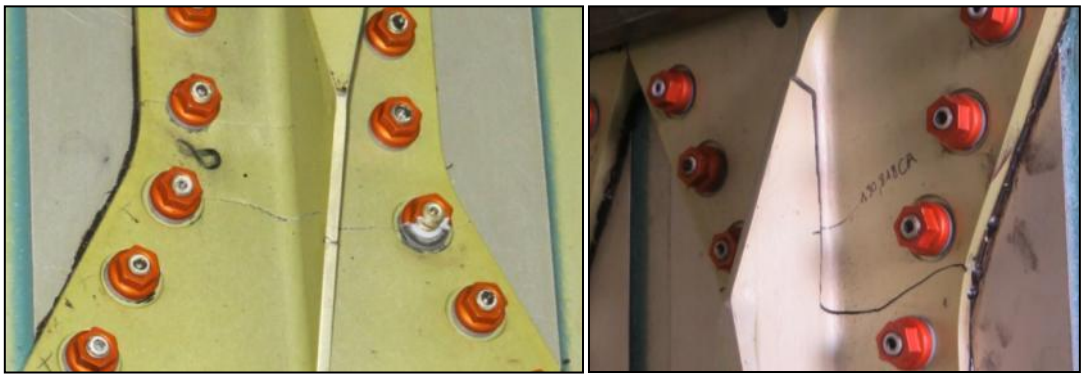

Figure 5-24 : Fatigue failure in stringer run-outs; away from crack location

5.5.2 2199 Al-lith. panels

The baseline was tested at a maximum stress of 102 MPa, while the reinforced panel was tested with a maximum stress of 96 MPa.

The baseline panel performed **206,694 cycles** with a total half crack length of 390 mm as the panel was fully broken by the end of the test. It was tested under spectrum loading with a maximum load of 582 kN and a minimum load of -112 kN. This was performed following constant amplitude loading for 3444 cycles with a maximum load of 500 kN and an R-ratio of 0.1 in order to initiate the crack which resulted in a 64 mm crack on the left and 60 mm on the right. The

crack propagated under variable amplitude for 194,800 cycles which produced a right hand crack of 182 mm and left hand one of 204 mm. At this point cracks were observed in the two stringers to the right and left from the central stringer that was cut. The right hand stringer failed first at 204,307 cycles while the left hand one- failed at 205,517 cycles. The test was then stopped and an additional 1175 cycles were necessary to fail the panel entirely on the left. The panel was then statically pulled apart to fail the remaining ligament. Overall, the panel lasted 206,694 cycles with a complete failure on the left hand side (half crack = 390 mm) and a partial failure on the right hand side (half crack = 265 mm).

The reinforced panel performed **1,131,654 cycles** with a half crack length of 190.5 mm. The crack was first initiated under constant amplitude loading at an R ratio of 0.1 with a maximum load of 700 kN and a minimum of 70 kN. When the crack had grown 6 mm from the edge of the starter notch on both sides, the loading was switched to the variable amplitude loading spectrum with a maximum stress of 96 MPa. The maximum load was 790 kN while the respective minimum load was -156 kN. The crack continued to grow until it merged with the first fastener hole located at about 100 mm half crack length. This occurred at about 57,873 cycles. The test was stopped at this point and the fastener removed at each crack tip. A small saw cut 2-3 mm long was made at the opposite side (the outer) of each hole, and the end of the saw cut was sharpened with a razor blade cut. After this, testing was resumed under constant amplitude load. The crack successfully re initiated on each side of the crack and after growth of 2-3 mm, the loading was switched back to spectrum loading. Following this re initiation from the edge of the hole, the crack grew steadily at virtually constant rate, until it attained a half-length of 190 mm, and 1,134,689 cycles, where the test was stopped, as test machine maintenance was required.

Figure 5-25 shows a plot of the average half crack length vs. cycles for the reinforced and baseline Al-lith. panels. The baseline panel shows steady crack growth up to 50,000 cycles where a discontinuity in the data is observed. This corresponds to the first bolt. Then the crack growth stays regular up to 200,000

cycles where it accelerates rapidly up to failure. The presence of the stringer slows the propagation of the crack but once this stringer fails, the crack advance accelerates up to the final failure of the panel. It can be seen that there is virtually constant growth rate throughout the entire test of the reinforced panel. It shows that up to crack lengths of 190 mm (the limit of the strapped data) there is considerable benefit in the bonded straps with increases in life of up to a factor of between 5 and 6 (the life improvement ratio is 5.5 by the end of the test). The discontinuity in the curve at the fastener hole can be seen. The stringers do not appear to be influencing the crack growth. Nevertheless the panels were tested under two different stress levels.

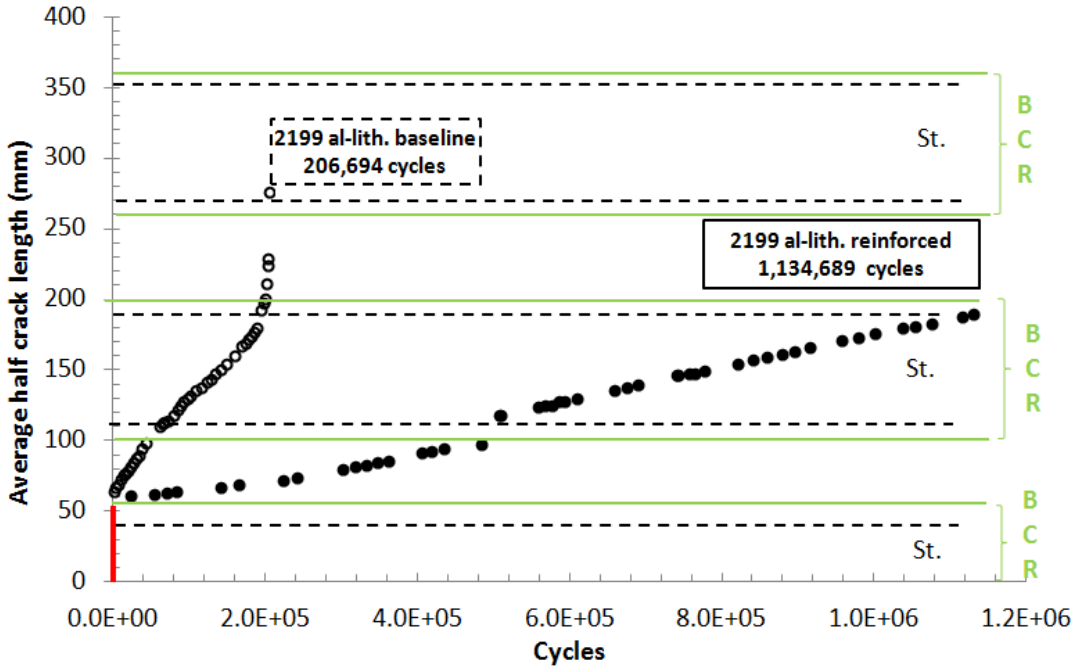

Figure 5-25 : Plot of crack half-length vs. cycles comparison for Al – lith. baseline vs. Al – lith. reinforced.

Figure 5-26 shows the crack growth rates vs. average half crack length for the reinforced and baseline Al – lith. panels. It shows that for the baseline panel, from the start of the test, the fatigue crack growth rate remains fairly constant for 20 mm with a crack growth rate between 7.0×10^{-7} m/cycle and 8.0×10^{-7} m/cycle, reducing slightly as it reaches the stringer to 5×10^{-7} m/cycle, before increasing steadily to failure at a final growth rate of 6×10^{-6} m/cycle. As for the reinforced panel, it can be seen that the crack growth rates begin at the very low value of 5×10^{-8} mm/cycle, increase to about 10^{-7} mm/cycle, and continue at

that rate almost unchanged for the rest of the test. The discontinuity at the fastener hole can be seen. As in the crack length cycles plot in Figure 5-25, there is little sign that the stringer lines are associated with local changes in crack growth rates.

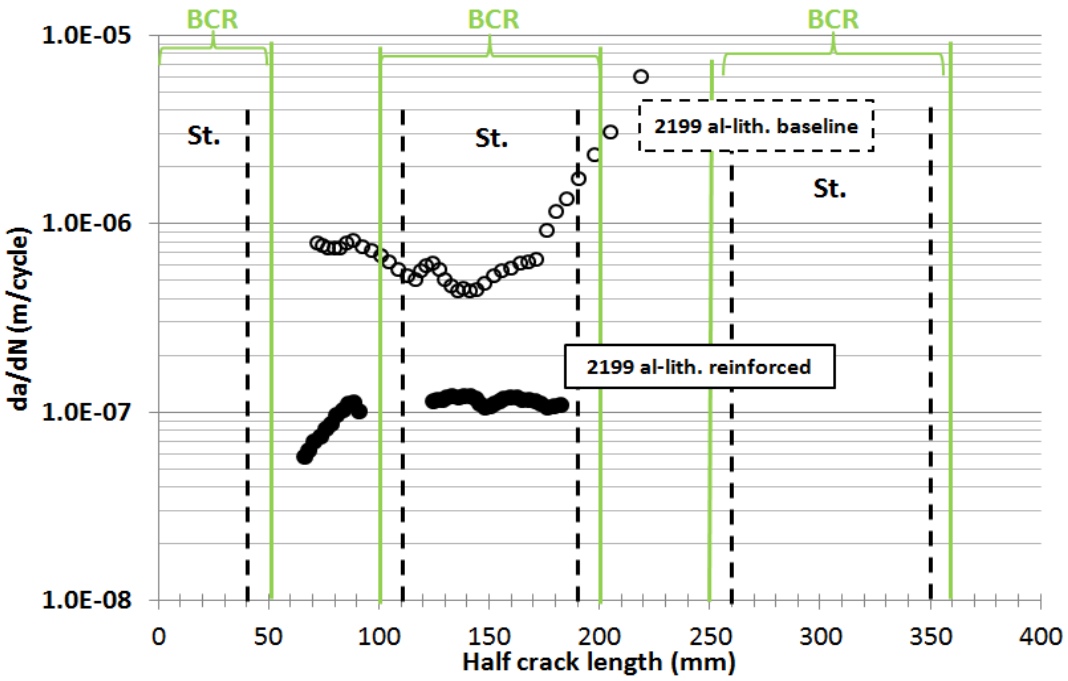

Figure 5-26 : Fatigue crack growth rates comparison for Al – lith. baseline vs. Al – lith. reinforced.

It can be seen that crack growth rates in the strapped panel are reduced by a factor of between 5 and 6. The baseline panel shows some influence of the presence of the stringer, as growth rates decline as the stringer is approached, and increase as the crack tip moves beyond it. This behaviour is not observed in the strapped panel which after early crack acceleration has an almost constant crack growth rate throughout.

Conclusions:

- The reinforced panel demonstrate an increase in life with a factor of 4.5 at equivalent crack length.
- Crack growth rates in the reinforced panel demonstrate a reduction of 5 to 6 compared to the baseline due to the presence of the straps.

- The current test demonstrates the efficiency of BCR despite the fact that the panel have been tested under two different stress levels.

5.5.3 2099 ISP reinforced panel

Calibration was used like the previous panels in order to check the stress level of the 2099 ISP panel (reported in Appendix C). It was tested under variable amplitude loading clipped at 101 MPa (gated at 25 MPa) which corresponds to a maximum load of 712,555 N and a respective minimum load of -133,604 N. It reached the first rivet on the left (91.5 mm) after 193,640 cycles and the right hand crack reached the first rivet after 203,900 cycles. Constant amplitude loading at 600 kN and an R-ratio of 0.1 (freq. = 0.75 Hz) was applied in order to re-initiate the crack from the rivet. This was successful and the crack reached 108 mm on the left hand side and 102 mm on the right hand side. The test was re-started under variable amplitude loading, growing the crack to 144 mm on the left hand side and 148 mm on the right hand side after **727,094** cycles. New cracks were detected in other panel locations than the main crack and it was decided to stop the test before complete failure of the panel (Figure 5-27, Figure 5-28 and Figure 5-29).

A crack appeared after 666,102 cycles at the end of a “pocket” machined into the rear surface of the skin (Figure 5-27) and kept growing during the rest of the test. Two additional cracks were observed at stringer run-outs (Figure 5-28) after 676,560 cycles. A fourth crack was detected on a similar location to the first one after 686,225 cycles (Figure 5-29).

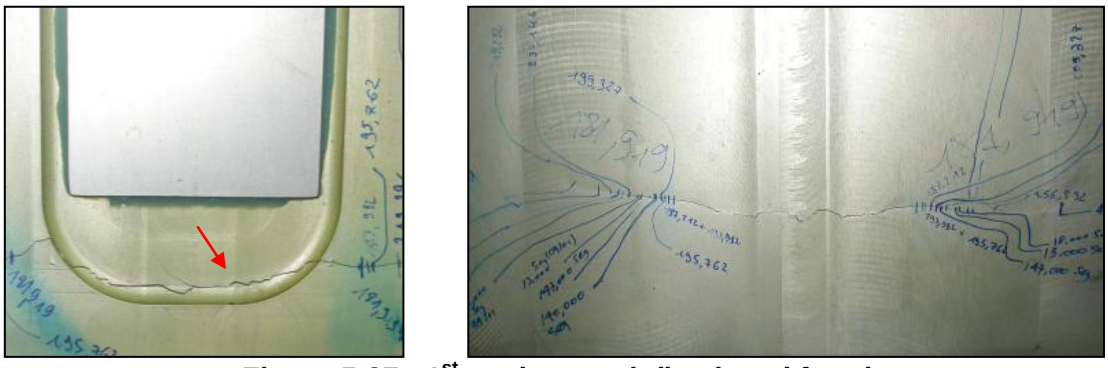

Figure 5-27 : 1st pocket crack (back and front)

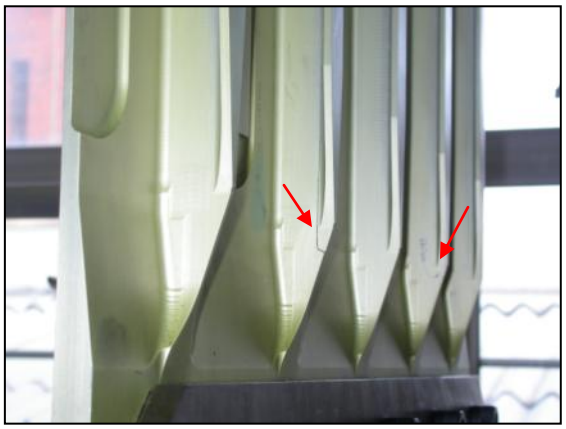

Figure 5-28 : Stinger run-out cracks

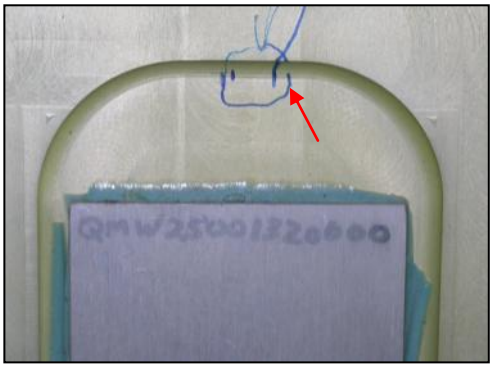

Figure 5-29 : 4th pocket crack

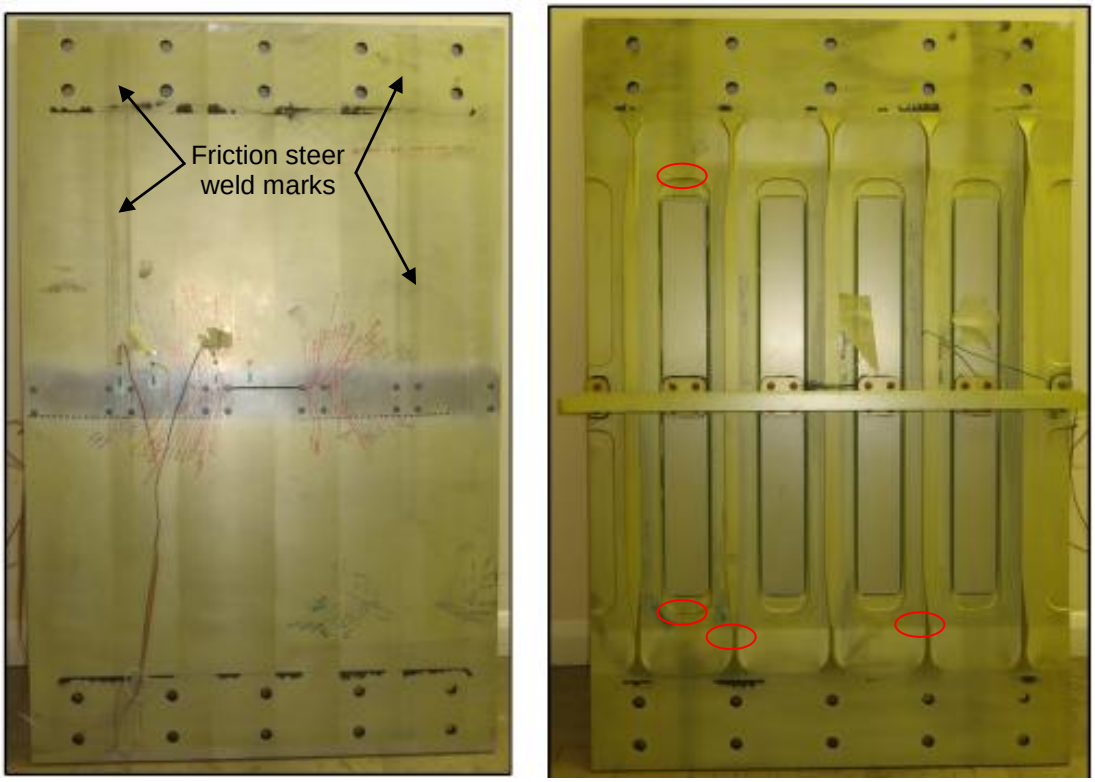

Figure 5-30 : 2099 ISP panel front (left) and back (right) views after testing and un-gripping of the panel. Red circles mark the locations of the new crack initiations

Areas of crack initiation away from the main crack can be attributed to two factors (Figure 5-30). The first concerns the crack that initiated on the pocket area after 666,102 cycles and in the second pocket area. In fact, both outer stringers had been friction steer welded to the rest of the panel (3 internal stringers) with visible marks of the steer weld on the Figure 5-30, where crack initiated. These areas are areas of residual stresses that may cause crack

initiation. There is also an additional geometric effect due to the fact that the pocket is an area of stress concentration; hence this location was likely to have crack initiation. As concern the stringer run-outs initiations, these are also areas of stress concentration in the design of the panel. In addition, initiation on the left and right stringer of the middle one can be explained by load redistribution from the middle stringer that is totally severed.

Figure 5-31 shows the crack length as a function of the cycles with the crack length calculated as the average crack length between the left hand and right hand crack.

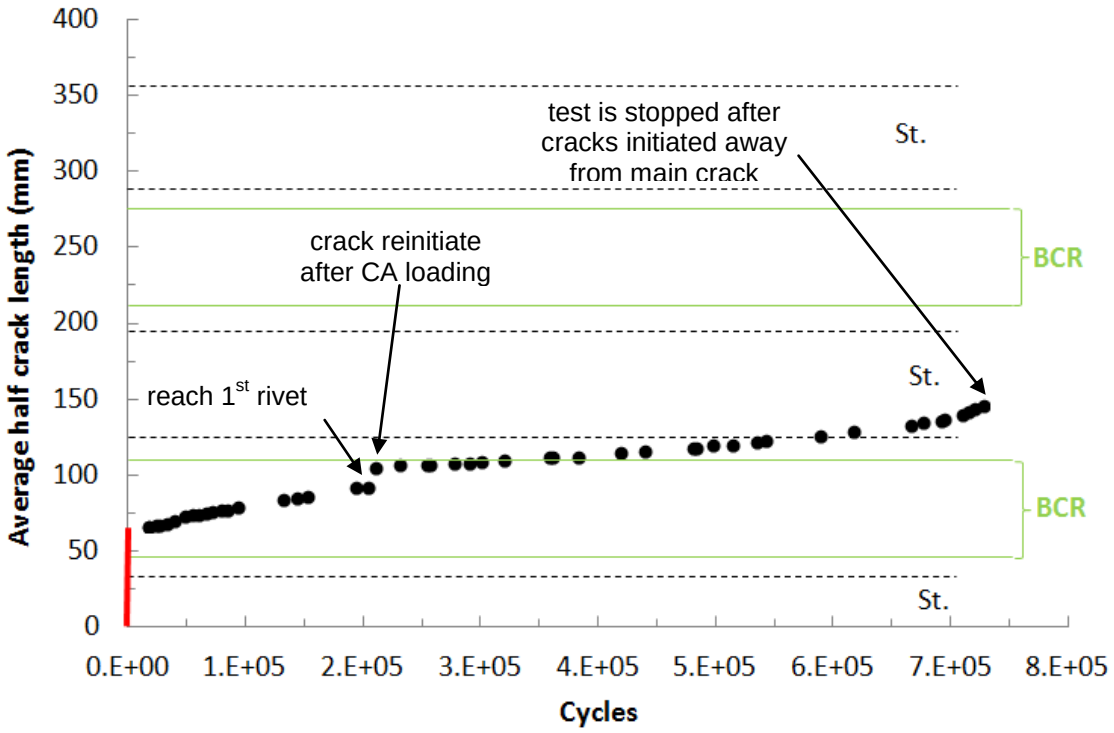

Figure 5-31 : Crack length Vs cycles for reinforced 2099 ISP panel

The crack grew steadily up to a discontinuity at about 2 x 10^5 cycles and 90-100 mm half crack length. This marks the point where the crack tip entered the first bolt hole at 90 mm and re-initiates at 100 mm on the other side of the bolt hole. The crack then shows a regular crack growth with a slight increase in growth rate as the crack progresses across the panel. At a crack length of approximately 133 mm / 666,000 cycles the crack growth rate is observed to increase significantly.

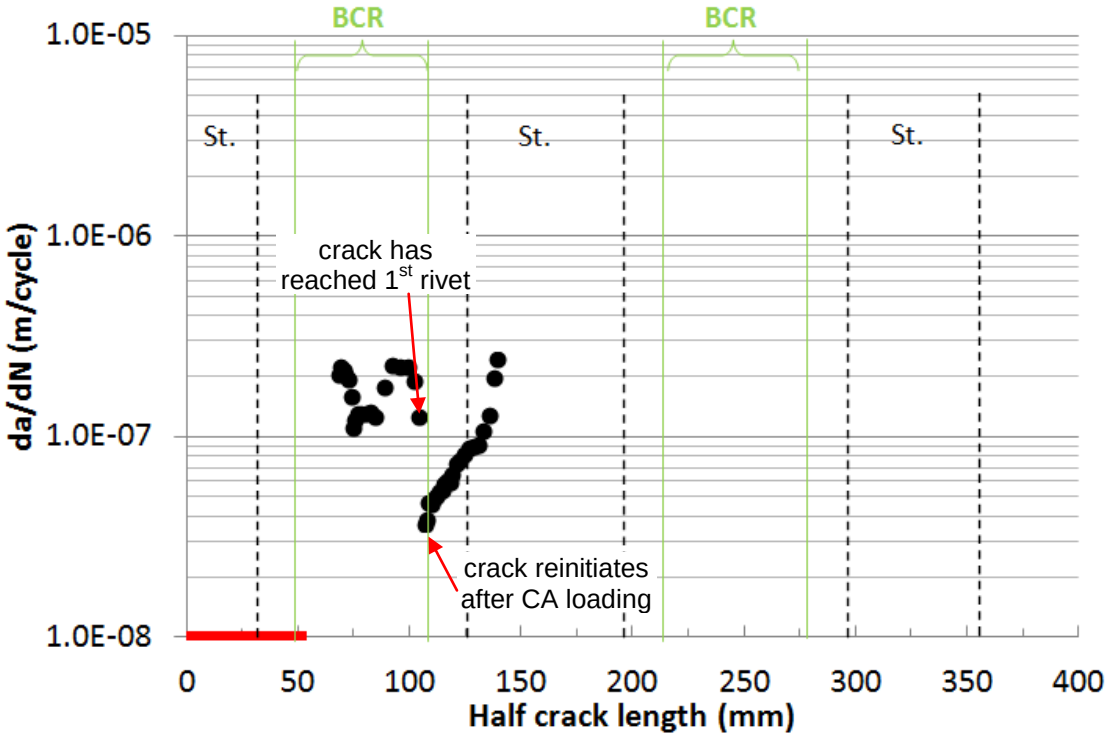

Figure 5-32 : 2099 ISP panel fatigue crack growth rates

Figure 5-32 shows the crack growth rate as a function of crack length calculated from the data of the previous figure. The crack growth rate was observed to vary between 1.0×10^{-7} m/cycle and 3.0×10^{-7} m/cycle before the crack reaches the first bolt hole. In that area, the crack is propagating under the bonded strap. Hence variation in crack growth rate in that section may be due to the fact that the crack opening is restricted by the presence of the strap. Growth rate reduction towards the bolt was also observed for the bolted panel. This may be due to compressive residual stresses observed in the surroundings of the bolts as was observed by Syed [164] for bolted assemblies.

The re-initiation of the crack from the bolt hole is marked by a much smaller growth rate with approximately 3.5×10^{-8} m/cycle which is the smallest rate observed during the test. When the crack re-initiated from the first bolt, the crack is still in a reinforced area. Hence the low crack growth rate can be attributed to first, the fact that there is re-initiation and also due to the presence of the first straps encountered by the crack (left and right of the central stringer) that act as a patch and redistribute the loads.

The rate then accelerated regularly up to $1.0x10^{-7}$ m/cycles before it accelerates very quickly, reaching the maximum observed during the test with a rate of $2.4x10^{-7}$ m/cycle at the end of the test. The acceleration may be a consequence of the absence of a strap in that area that cannot redistribute the load and the fact that the effect of the first strap is not predominant in that area. The step in growth observed at $10x10^{-7}$ m/cycles may correspond to a change in thickness when the crack is located in the thinnest part of the panel without a reinforcement (skin only thickness) and starts to enter a thicker section that correspond to the start of the stringer area .

In summary, the first part of the test where crack growth rate varies very quickly can be a mixture of the presence of the strap and residual stresses due to the bolt. The second part of the growth rate can be interpreted as first re-initiation of the crack and then changes in thicknesses in that area.

Also, as other locations of crack propagation were observed during the test, this may actually slow down the propagation of the main crack. One parameter that was not investigated here could be the presence of delamination between the straps and the panel, which may contribute to changes in crack growth rates. Further FE analysis of this current panel in complement to the one conducted by Peyron [165] may help give a better interpretation of the results observed here.

5.6 Summary and conclusions

The panel tests are summarized in Table 5-7 together with details of the tests and their fatigue performances. The max stresses given in the table are the stresses that were back calculated from the analysis of the strain gauge readings.

Table 5-7 : Summary of panel test and performances

Panel	Max load (kN)	Spectrum – Max stress (MPa)	Test max stress (MPa)	End of test status	Total nb of cycles (crack length)	% of improvement
2024 HDT baseline	585	Spectrum (1) 101 MPa	104	Fully broken	231,938 (390 mm)	N/A
2024 HDT reinforced	790	Spectrum (2) 97.7 MPa	97.7	Part-through crack	389,100 (100 mm)	68%
2199 al-lith baseline	582	Spectrum (2) 97.7 MPa	102*	Fully broken	206,694 (390 mm)	N/A
2199 al-lith reinforced	790	Spectrum (3) 96 MPa	96	Part-through crack 190 mm	1,131,654 (190.5 mm)	448%
2099 ISP	712	Spectrum (1) 101 MPa	104	Part-through crack	727,094	N/A

The % of improvement calculated for the 2024 HDT panels is 68% while the improvement for the 2199 al-lith panels is 448%. Hence there appears to be a much larger increase in fatigue life for the 2199 al-lith panels than for the 2024 HDT panels. This can be explained by the fact that the % of improvement obtained for the reinforced panel are for different final crack length of the reinforced panel as full failure of those panels proved non successful. Hence to get a better comparison between the 2024 HDT panels and the 2199 al-lith ones, they must be compared at equivalent crack length (Table 5-8).

Table 5-8 : Summary of panel improvement at equivalent crack length

Panel	Comparative crack length (mm)	Life for baseline panel	Life for reinforced panel	Life Ratio
2024 HDT	100	49,000	389,100	6.9
2199 Al-lith	180 (96.25)	189,750 (38,750)	1,054,550 (484,660)	4.6 (11.5)

It shows that for an equivalent crack length of approximately 100 mm, the life improvement ratio for the 2024 HDT panel is 6.9 (corresponding to a 694% of life improvement) and 11.5 (corresponding to an 1151% of life improvement) for the 2199 Al-lith panels. Hence it appears here that the 2199 Al-lith baseline panel has a lower life than the 2024 HDT one – at the same crack length – but the BCR technology then appears more beneficial for the 2199 Al-lith case as the reinforced panel reaches a larger life. This may be partly explained by the fact that the stress level used for the 2199 Al-lith reinforced panel was slightly lower than for the 2024 HDT one.

From the panel test, it is possible to conclude that:

- For bolted assemblies with 2624-T351 skins the addition of BCR to the design is beneficial with a life improvement of 6.9 between the baseline and the reinforced case (Table 5-7). This is directly related to a reduction of crack growth rates with a factor of 3 to 10 due to the presence of the straps.
- For bolted assemblies with 2199-T8e80 skins the addition of BCR to the design is beneficial with a life improvement of 4.5 between the baseline and the reinforced case (Table 5-8).This relates to the reduction in crack growth rate with a factor of 5 to 6 due to the presence of the straps.
- Despite the changes in applied stresses between the baseline and the reinforced panels for the two series of test, it can be said that BCR is a beneficial technology for the retardation of crack propagation in bolted assemblies for 2024-T351 and 2199-T8E80 skins that are submitted to a lower wing spectrum loading.

- As no baseline was tested for the 2099-T81 integrally machined panel, it is difficult to judge the efficiency of the technology for this case. Nevertheless, it showed the importance of load re-distribution with the appearance of new crack fronts due to the presence of the straps.
- The increase in life improvement compared to coupons may be attributed to two factors. First there is a reduced amount of secondary bending as opposed to the reinforced M(T) specimens (Chapter 10 and 11). This will be reviewed in the discussion chapter. Second, there is a different mode of loading to the coupons case where the strap are loaded through shear loading while in the case of the panels, they are directly loaded in the loading grip, hence are submitted to more load than shear loaded specimens.

Chapitre 6 : Delamination testing of FM 94 adhesive bonds

6.1 Introduction

The test results given in Chapter 0 and the literature showed that one of the phenomena observed in BCR coupons was the presence of disbonding at the interface between the strap and the substrate.

The objective of the current chapter was to establish a set of fatigue delamination growth rate data to be used as input in a finite element tool used to design bonded crack retarder structures. This would allow a fatigue approach to delamination rather than a static one as employed in previous calculation [50]

Another objective was the choice of adhesive to be used for assembling the bonded crack retarders to the structure. FM94 epoxy adhesive [162] was used in the BCR-1 project where delamination was observed within the GLARE reinforcing straps [5]. In order to overcome this phenomenon, FM94/S2-prepreg [166] was also evaluated.

This chapter describes the design, manufacture and test data of delamination research.

6.2 Sample materials, design, manufacture and test matrix

6.2.1 Materials

The specimens used to investigate the different modes of fatigue delamination were all based on the same geometry. Two plates of aluminium (2024-T351) were bonded together with FM94 epoxy adhesive – or FM94/S2-prepreg adhesive – following the general bonding recommendations from Alcoa [160].

❖ **Adhesives**

- **FM94/S2-prepreg adhesive**

FM94-S2 glass unidirectional (UD) tape is a toughened epoxy prepreg system that is used in Glare assembly (Figure 6-1). It consists of unidirectional Glass fibres within a FM94 matrix (60% fibre volume fraction). Properties are given in Table 6-1.

Table 6-1 : FM94/S2-prepreg mechanical properties (for test temperature of 23 °C)

Property	Value
Single lap shear strength, [MPa] EN2243-1 0° fibre direction	22
Floating roller peel strength, [N/25 mm] EN 2243-2 90° fibre direction	150
0° Tensile strength, [MPa] EN 2747	1700
0° Tensile modulus, [GPa] EN 2747	50
±45°C Tensile strength, [MPa] EN 6031	200

- **FM94 epoxy adhesive**

The FM94 epoxy adhesive used to bond the specimens was provided by Cytec (Figure 6-2). FM94 adhesive is a 104°C service temperature, modified epoxy adhesive film designed to bond metallic and composite structures. FM94 is manufactured as a supported adhesive with a knit carrier. In the present case, FM94K film adhesive with a nominal weight of 293 g/m² was employed. It has a nominal thickness of 0.25 mm. The mechanical, properties of FM94 are detailed in Table 6-2.

Table 6-2: FM94 mechanical properties (for test temperature of 24 °C)

Property	Value
Tensile shear [MPa] (ASTM D1002)	46.6
Floating roller peel [N/mm] (ASTM D3167)	12.9
Shear linear limit [MPa]	19.5
Shear ultimate limit [MPa]	48.2
Shear modulus [MPa]	823
Fatigue (ASTM D3166-93) Max stress = 17.94 MPa ; R = 0.1 Frequency = 30 Hz	> 10^7 cycles, no failure

Figure 6-1 : FM94-S2 prepreg surface aspect after curing - disbonding specimen

Figure 6-2 : FM94 surface aspect after curing - disbonding specimen

- **<u>Adherent : 2624 - T351</u>**

The adherent aluminium 2624-T351 was provided by Alcoa with the necessary surface treatment to have an adequate bonding. BR14737 primer was applied to the surface.

6.2.2 Design and manufacture

The acronyms used to define the mechanical tests samples are:

- DCB for Double Cantilevered Beam used for mode I disbonding

- ELS for End Loaded Split used for mode II disbonding

- MMB for Mixed Mode Bending used for the mixed mode disbonding

DCB and ELS specimen were prepared using two aluminium plates of 25 x 250 mm, 5 mm thick bonded together. Because of the dimension of the jig used for the MMB tests, the width of the adherent was reduced to 20 mm with the same length, 250 mm.

A 10 μm thick PTFE film was introduced during the preparation of the specimen in the aluminium plates of the assembly in order to initiate disbonding during the tests. The initial disbonding length was set to 50 mm as recommended in the BS ISO 15024:2001 [167]. In order to take into account an 11 mm offset due to the presence of loading tabs on the specimen, a 61 mm long piece of PTFE film was placed between the adhesive layer and the aluminium substrate during the assembly process as illustrated in Figure 6-3.

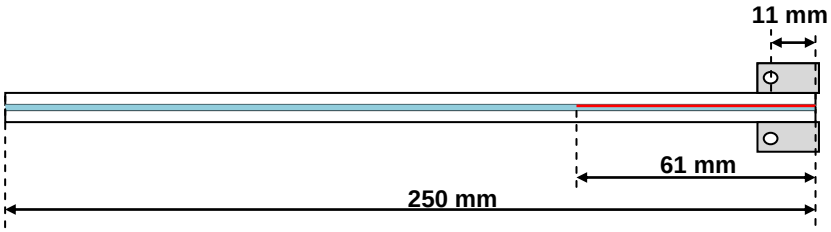

Figure 6-3 : DCB specimen

The specimens were prepared individually rather than preparing a larger plate of specimens and then cutting the coupons in accordance with BS ISO 15024:2001 [167]. In order to guarantee the positioning of the aluminium arms on the coupons, tape was used to clamp the assembly together (Figure 6-4).

The procedure for preparing the specimens before bonding was the following one:

1) Place PTFE release film on substrate arm 1, using tape to help maintain the position of the film.
2) Apply adhesive layer on the full length of substrate arm 2.
3) After removing any air entrapped remove the protective layer from the adhesive on substrate arm 2.
4) Without any pressure, apply substrate arm 1 onto substrate arm 2.
5) Check the alignment.
6) Once the alignment is correct, apply pressure in order to guarantee the adhesion of one substrate to the other

7) Clamp the two assembled substrate on a minimum of two locations (each end) in order to guarantee the positioning during curing.

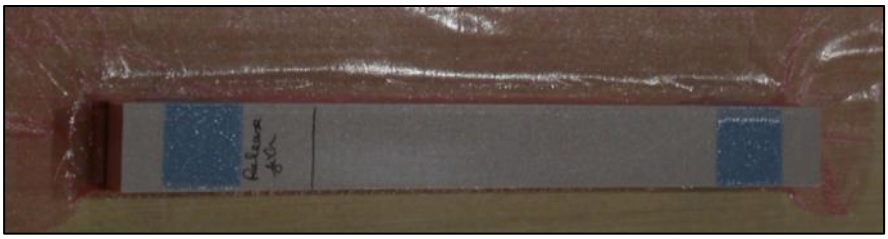

Figure 6-4 : DCB test specimen after curing

The specimens are then place under vacuum bagging for the bonding procedure [160].

- Heat at 3 C/min up to 121 C
- Apply a 40 psi pressure
- Cure at 121 C ± 3 C for 60 minutes

Prior to testing, it was necessary to bond loading tabs at the end of the specimen in order to transfer the load to the specimens. A final step in the preparation of the specimen was to apply white paint on the side of the coupons and draw a scale. This allowed for monitoring of the disbond crack during testing (Figure 6-5).

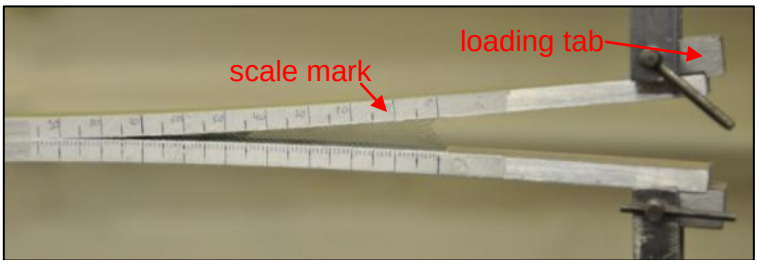

Figure 6-5 : DCB specimen with loading tabs, white paint and scale marks after testing

6.2.3 Test matrix

The tests were performed for two major objectives. The first one was looking at the type of adhesive with the investigation between the FM94/S2-prepreg and the FM94 through mode I testing. The second was to obtain fatigue delamination data in mode I, mode II and mixed mode to be used in the modelling design tool.

In the case of FM94/S2-prepreg, it was necessary to bond two layers together in order to reproduce a system similar to the one encountered in GLARE. One particular specimen configuration made use of the GLARE 2A-6/5 (0.4) as the arms of the DCB specimens as illustrated in Figure 6-6. These specimens were used in order to evaluate the fracture toughness and the mode I fatigue crack growth rate of a delamination within the GLARE itself. The specimens consisted of two straps of Glare bonded together with FM94. Prior to bonding, the external aluminium layer of one of the arms was unbonded in order to introduce an initial crack. A razor blade was used in order to “open” the sample from the outer layer of aluminium (Figure 6-7). A PTFE film was then placed in that interface in order to act as an initial delamination before bonding of the opposite arm.

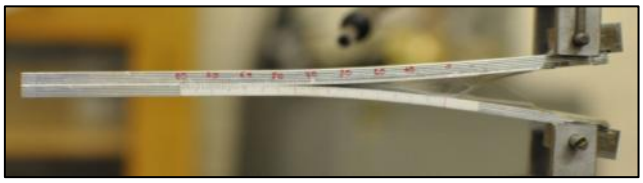

Figure 6-6 : DCB specimen made from GLARE

Figure 6-7 : Razor blade introduced in Glare

Table 6-3 shows all the mode I quasi static test specimens with details of the adhesive system and configuration as well as the substrate used for the arms of the DCB specimens.

Table 6-3 : Mode I quasi-static test matrix for DCB samples.

Batch	Designation	Adhesive	Substrate	Interface
#1 Alcoa specimens	DCB#1-1-S	FM94-S2	2024 HDT 5 mm BR 14737	prepreg/prepreg
	DCB#2-1-S			
	DCB#3-1-S			
	DCB#4-1-S			
	DCB#5-1-S			substrate/prepreg
	DCB#6-1-S			
	DCB#7-1-S			
	DCB#8-1-S			
#2 Cranfield specimens	DCB#1-2-S			prepreg/prepreg
	DCB#2-2-S			
	DCB#3-2-S			substrate/prepreg
	DCB#4-2-S			
#3 Glare specimens	DCB#1-3-S		Glare 2A-6/5 (0.4)	substrate/prepreg
	DCB#2-3-S			
#4 Cranfield specimens	DCB#1-4-S	FM94	2024 HDT 5 mm BR 14737	N/A
	DCB#2-4-S			
	DCB#3-4-S			
	DCB#4-4-S			
	DCB#5-4-S			
	DCB#6-4-S			
	DCB#7-4-S			
	DCB#8-4-S			
	DCB#9-4-S			
	DCB#10-4-S			
	DCB#11-4-S			

Batch #1 was prepared directly by the sponsor Alcoa while the batch #2, #3 and #4 were prepared at Cranfield, with batch #3 using the Glare arms as described previously.

Table 6-4 gives details of the tests that were performed in order to get the fatigue crack growth rates of FM94 adhesive systems in mode I, mode II and mixed mode.

Table 6-4 : Fatigue delamination test matrix

Mode	Batch	Designation	Adhesive	Substrate
Mode I	#4 Cranfield	DCB#3 DCB#4	FM94	2024 HDT 5 mm
Mode II	#4 Cranfield specimens	ELS#1 ELS#2 ELS#3	FM94	2024 HDT 5 mm BR 14737
Mixed Mode	#4 Cranfield specimens	MMB#1 - pure mode II MMB#2 - ratio = 0.75 MMB#3 - ratio = 0.75 MMB#4 - ratio = 0.5 MMB#5 - ratio = 0.25	FM94	2024 HDT 5 mm BR 14737

6.3 Testing methodology

6.3.1 Mode I static delamination

All quasi-static tests were performed on a Zwick Z010 screw driven testing machine fitted with a 2kN load cell. The test specimens were fitted in the test machine using a pins and clevises assembly together with the loading tabs that have been described in the previous paragraph (Figure 6-8). The tests were performed according to the standard BS 7991:2001 [168].

The test was started with a 1 mm/min displacement of the cross head. Load, displacement and crack length were recorded. A hand magnifier was used in order to get a better view of the delamination tip. The crack was grown for approximately 50 mm before the test was stopped and the load set back to zero. This allowed for enough data points to determine the fracture toughness. In order to investigate the fracture surface, the specimens were eventually completely failed.

The fracture toughness evaluation of the DCB specimens was determined using the modified beam theory (MBT) [168].

Figure 6-8 : Quasi static test set-up for delamination test

6.3.2 Mode I fatigue delamination

The mode I fatigue disbonding tests were performed on a 20 kN DMG hydraulic machine fitted with a 20 kN load cell. A pin and clevises system together with loading blocks was used to introduce the load/displacement into the specimens. All the test were performed at a frequency of 1 Hz. Displacement control was used rather than load control as it proved to be a more stable mean of applying the load. In fact load control would results either in a premature failure of the specimen with not enough data-points to establish the fatigue crack growth rate or a disbond arrest as described in [169]. Prior to the fatigue test, it was necessary to grow the crack for approximately 5 mm in order to pre-crack the specimen.

This was performed according to the quasi-static protocol described before. This initial step was used in order to get an evaluation of the fracture toughness of the specimen. Moreover, this first step was necessary in order to evaluate the load to use for the fatigue test. In fact, the last load recorded during the pre-crack was used as the load that will define the maximum displacement of the specimen.

Load (maximum and minimum), displacement, crack length and cycles number were recorded all over the test at regular intervals. An optical travelling microscope was used in order to locate the position of the crack tip with the help of the scale drawn on the specimen. The test was stopped once the fatigue crack growth rates reached values of 10^{-9} m/cycles or once the crack had reached a total length of 100 mm (50 mm from the crack starter).

The MBT procedure was used in order to analyse the strain energy release rate during the fatigue test. The strain energy release rate can be calculated at the maximum and minimum loads. Hence, when considering the evolution of the crack growth rate, the results can be represented as a function of the maximum strain energy release rate G_{Imax} as well as the $\Delta G = G_{Imax}-G_{Imin}$ **(6-1)**. Some authors [171] also use the expression $\left(\sqrt{G_{Imax}}-\sqrt{G_{Imin}}\right)^2$ **(6-2)** as an alternative. In the present case, G_{Imax} was employed to characterize the delamination data.

The data reduction techniques in ASTM E647 [159] can also be applied in the present study. In the present case, the slope of the linear regression through 7 points was used in order to evaluate the fatigue crack growth rates and the strain energy release rate averaged over these 7 points was associated to that fatigue crack growth rates.

6.3.3 Mode II fatigue delamination

There are various mode II delamination test that can be used to describe the fatigue disbonding of adhesives such as the 3 point bend end notched flexure (ENF), the stabilised end notched flexure, the 4 point bend end notched flexure and the end-loaded split (ELS) Figure 6-9.

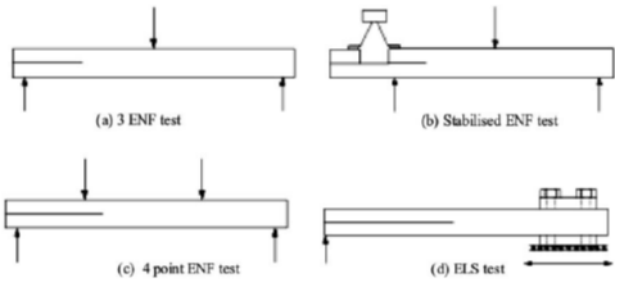

Figure 6-9: 4 types of mode II delamination test methods [170]

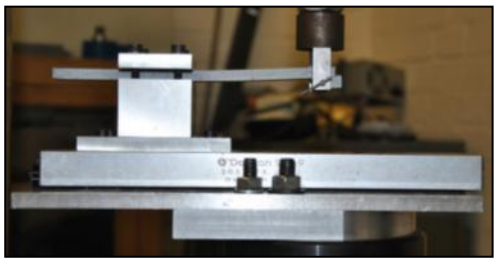

Figure 6-10: Mode II fatigue test set-up

While mode I delamination testing has reach a standardization level [168], no standard has been established for the determination of mode II delamination in adhesive either for static or fatigue analysis [170]. Hence the present test was based on a quasi-static protocols for mode II delamination that are aiming to a standardization of the method [171] . The choice was made to perform the test using the ELS test configuration. This was performed following an ESIS TC4 protocol [172] that gives directions and details specific to that type of tests.

The ELS tests were performed on a 20 kN DMG hydraulic machine fitted with a 20 kN load cell. A pin and clevises system together with a loading block was used to introduce the load/displacement into the specimens. The test set-up is shown in Figure 6-10. All the tests were performed in displacement control at a displacement ratio of R = 0.1 and a frequency of 1 Hz. The tests were stopped when the crack was 5 mm from the clamped area. The crack length was monitored at regular intervals using a travelling microscope. The load was also recorded during the test in order to calculate the SERR. The Experimental Compliance method was used to calculate the SERR.

6.3.4 Mixed mode fatigue delamination

The mixed mode fatigue delamination tests were based on the standard test method ASTM D6671/D6671M – 06 [173] using the test jig shown in Figure 6-11. The proportions of mode I and mode II are adjusted by changing the distance between the loading point and the “mid-point’’ of the test jig. The ratio of mode is defined through the following equation:

$$\frac{G_{II}}{G_{Tot}} = \frac{G_{II}}{G_I + G_{II}} = \frac{3(e+L)^2}{3(e+L)^2 + 4(3e-L)^2} \quad \textbf{(6-3)}$$

As the distance L is kept constant, the distance e can be changed in order to vary the mode ratio. The mode ratio is independent of the crack length. The test specimens have the same configuration as the DCB and ELS. Test machine and monitoring systems were identical to mode I and mode II tests. The superposition of mode I and mode II is explained in Figure 6-12.

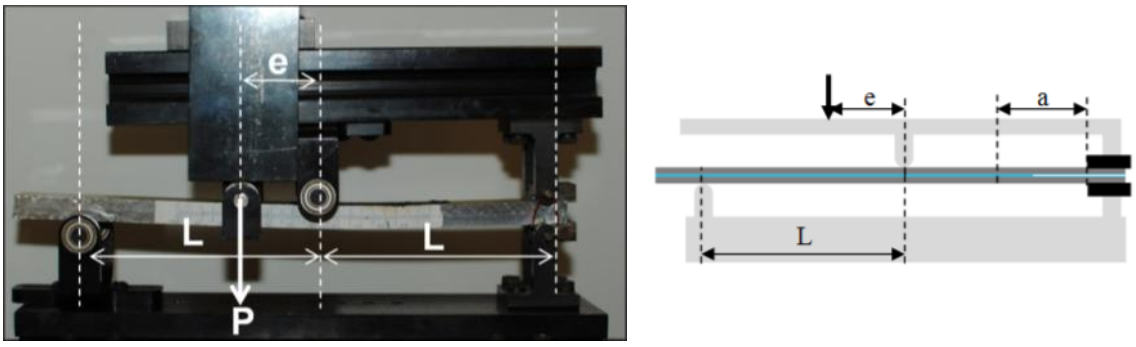

Figure 6-11 : Mixed mode test jig

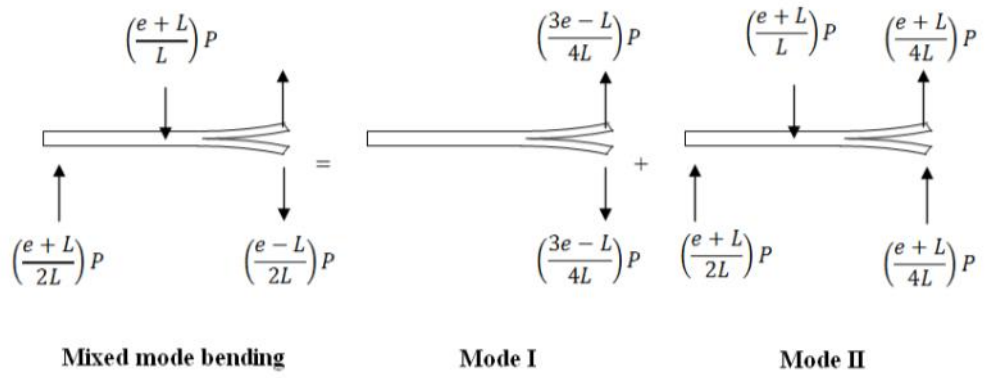

Figure 6-12 : Superposition of modes on the MMB specimen

The loading for each individual mode can be divided into two components P_I and P_{II} respectively associated to mode I loading and mode II loading which have the expression $P_I = \left(\frac{3e-L}{4L}\right)P$ **(6-4)** and $P_{II} = \left(\frac{e+L}{L}\right)P$ **(6-5)** where P is the loading applied in the MMB case. As the simple beam theory of a DCB specimen gives the expression of the mode I strain energy release rate $G_I = \frac{12a^2P_I^2}{b^2h^3E_{11}}$ **(6-6)**, by substitution of P_I into that expression, one can obtain the

contribution to mode I strain energy release rate in the mixed mode bending case, $G_I = \frac{3a^2P^2}{4b^2h^3L^2E_{11}}(3e-L)^2$ **(6-7)**. The same applies to the expression of G_{II} for the ENF specimen, $G_{II} = \frac{9a^2{P_{II}}^2}{16b^2h^3E_{11}}$ **(6-8)**. Substituting P_{II} by its expression in the case of MMB gives the contribution of mode II to the MMB test, $G_{II} = \frac{9a^2P^2}{16b^2h^3L^2E_{11}}(e+L)^2$ **(6-9)**.

Hence the total strain energy release rate for the MMB tests is

$$G = \frac{3a^2P^2}{16b^2h^3L^2E_{11}}[4(3e-L)^2 + 3(e+L)^2] \quad \textbf{(6-10)}$$

Note: In all expression given above, the constant are described as follows:

- a = disbonding length (m)
- e and L, tests parameters as described (m) as described in Figure 6-12
- h = thickness of specimens arms (m)

Further data processing techniques that include correction to the previous expression are developed in [173], [174].

6.4 Delamination test results

6.4.1 FM94/S2-prepreg static toughness tests

This section outlines the results of the specimens that used the FM94/S2-prepreg as an adhesive system. The results are summarized in Table 6-5.

Table 6-5 : FM94/S2-prepreg test specimen fracture toughness results

Batch	Designation	Adhesive	Interface	G_{IC} (J/m^2)	Type of failure	Average	Standard deviation	CoV
#1 Alcoa specimens	DCB#1-1-S	FM94-S2	prepreg/prepreg	2450	Cohesive	1825	555	30%
	DCB#2-1-S			1900	Cohesive			
	DCB#3-1-S			1850	Mixed			
	DCB#4-1-S			1100	Mixed			
	DCB#5-1-S		substrate/prepreg	950	Adhesive	1150	344	30%
	DCB#6-1-S			1650	Adhesive			
	DCB#7-1-S			900	Adhesive			
	DCB#8-1-S			1100	Adhesive			
#2 Cranfield specimens	DCB#1-2-S		prepreg/prepreg	1400	Adhesive	1825	601	33%
	DCB#2-2-S			2250	Cohesive			
	DCB#3-2-S		substrate/prepreg	1300	Adhesive	1250	71	6%
	DCB#4-2-S			1200	Adhesive			
#3 Glare	DCB#1-3-S		substrate/prepreg	1775	Adhesive	1613	230	14%
	DCB#2-3-S			1450	Adhesive			

The FM94/S2-prepreg for the batch #1 showed an average G_{IC} of 1825 J/m^2 for the prepreg/prepreg interface and 1150 J/m^2 for the substrate/prepreg interface. Both interface showed scatter – a usual observation for this type of tests. Batch #2 resulted in averages of 1825 J/m^2 for the prepreg/prepreg interface and 1250 J/m^2 for the substrate/prepreg interface. In both case, there was greater G_{IC} for the prepreg/prepreg interface than the substrate/prepreg interface. Cohesive failure and a mixture of cohesive and adhesive were generally observed for the prepreg/prepreg interface while adhesive failure was always observed for the substrate/prepreg interface. In batch #1 in particular, the interface moved from cohesive to adhesive during the tests for specimens DCB#3-1-S and DCB#4-1-S as illustrated in Figure 6-13.

In batch #3 cases, the average G_{IC} is 1613 J/m^2. Multiple sites of delamination were observed with the initial front moving to a different interface as the crack was propagating. The toughness values were slightly smaller than the other batches.

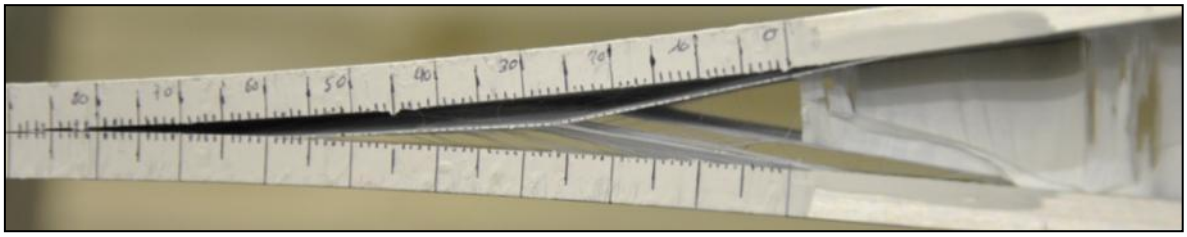

Figure 6-13 : DCB#3-1-S after testing showing the delamination front that moved from a cohesive failure to and adhesive one.

The results demonstrate a coefficient of variation (CoV) of up to 33 % for the delamination investigation of the FM94-S2 adhesive system. There are no obvious correlation between the type of interface studied and the CoV.

It is important to note that the relationship between the G_{IC} and K_{IC} is dependent of the square of K_{IC} ($G_{IC} \sim K_{IC}^2$). Hence any change in the fracture mechanics behaviour of the coupons will largely impact the G_{IC} results, hence raise the variability in the results.

In addition, the large CoV observed in this case can be explained by the following factors.

- Fibre bridging due to the Glass fibre in the adhesive system was observed during testing (Figure 6-13) which may affect the result as multiple crack path were generated in that case; there was no longer one single crack path.
- The CoV are calculated on small families with only 4 specimens per CoV. Hence the use of a larger number of coupons for statistical analysis may reduce the CoV.
- Large variation for this type of test is not uncommon as highlighted in the literature [175], [176].

6.4.2 G_{IC} values for specimens bonded with FM94

This section outlines the results of the specimens that used the FM94 as an adhesive system. The results are summarized in Table 6-6.

Table 6-6 : FM94 quasi static disbonding results

Batch	Designation	Adhesive	Interface	G_{IC} (J/m^2)	Type of failure	Average	Standard deviation	CoV
#4 Cranfield specimens	DCB#1-4-S	FM94	N/A	750	Cohesive	1601	411	26%
	DCB#2-4-S			1000	Cohesive			
	DCB#3-4-S			1850	Cohesive			
	DCB#4-4-S			1800	Cohesive			
	DCB#5-4-S			1950	Cohesive			
	DCB#6-4-S			2150	Cohesive			
	DCB#7-4-S			1400	Cohesive			
	DCB#8-4-S			1700	Cohesive			
	DCB#9-4-S			1750	Cohesive			
	DCB#10-4-S			1670	Cohesive			
	DCB#11-4-S			1590	Cohesive			

The average toughness value is 1600 J/m^2 with a large scatter. The failures were all cohesive in nature. The overall average value for the FM94/S2-prepreg was lower with 1512 J/m^2 without considering the Glare specimens.

Although the number of coupons in the family is larger than the previous results, the G_{IC} values here also demonstrate quite a large CoV. It is likely that the number of specimens is still too small, considering the large variation in results that can be observed for this type of tests as outlined in the previous section.

6.4.3 FM94 fatigue delamination crack growth - Mode I

This section gives the results of the test performed under mode I conditions. It shows the results for the test conducted on the FM94 (DCB#3, DCB#4). Figure 6-14 shows the results of the fatigue tests with the delamination growth rates given as functions of the strain energy release rate at maximum load (maximum displacement).

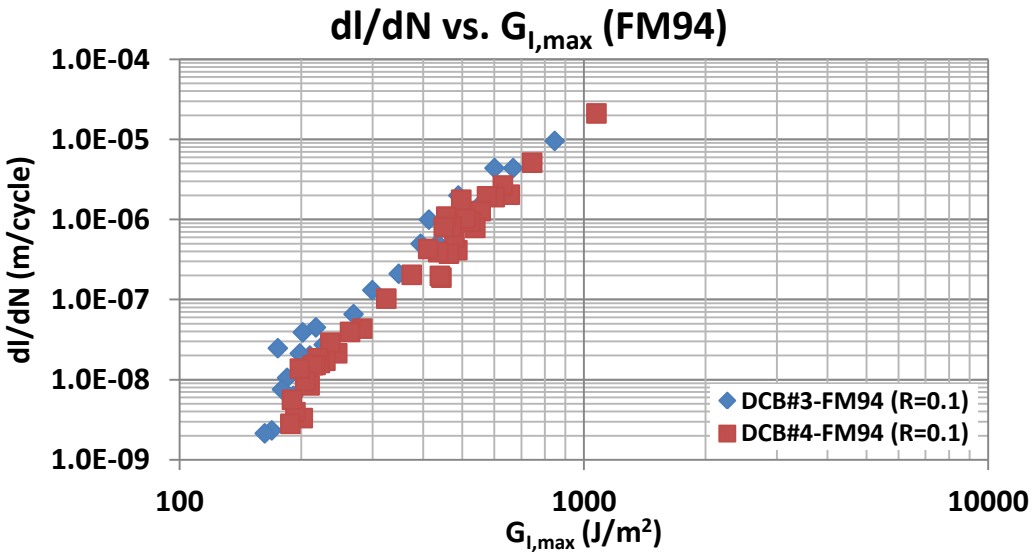

Figure 6-14 : Mode I fatigue delamination growth rates for FM94

The test results show very similar results in the two samples with little scatter. The test data show the fatigue crack growth rate for a range of strain energy release rate from 170 J/m^2 to 1100 J/m^2 with a delamination growth rate varying from 2.3x10^{-9} m/cycle to 2.1x10^{-5} m/cycle. The crack growth rate tends to a possible fatigue delamination growth threshold at G_{max} = 200 J/m^2.

6.4.4 FM94 fatigue delamination crack growth - Mode II-ELS samples

Three test samples were used for mode II test at R = 0.1. ELS#1 was tested with a starting load of 1000 N. ELS#2 was tested with initial maximum loads of 800 N, 700 N, 600 N and 500 N. ELS#3 was tested with an initial maximum load of 800 N. Figure 6-15 shows the test results. It gives the disbonding growth rate as a function of the total maximum strain energy release rate $G_{II,max}$.

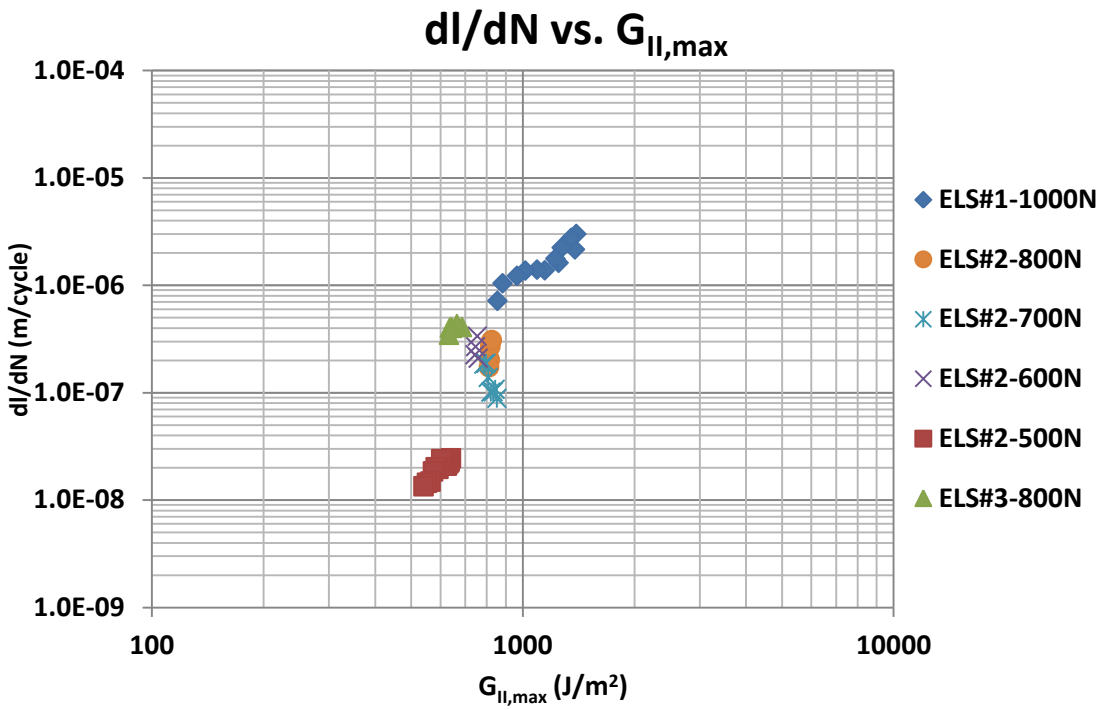

Figure 6-15 : 100% mode II fatigue disbonding growth rates for FM94 adhesive

During the test, it was difficult to keep a regular crack growth rate as the crack grew fast or not at all. This is why there are only a few data points in some parts of the curve in Figure 6-15. Growth rates were slower for the same value of G than for the Mode I tests.

6.4.5 FM94 fatigue delamination crack growth - mixed mode

5 tests were conducted under mixed mode conditions, with one sample in 100% mode II, two samples with 75% Mode II; one sample with 50% mode II and one with 25% Mode II. All the specimens used the FM94 adhesive and were tested with an R-ratio of 0.1 (displacement ratio).

- **100% Mode II – mixed mode**

Different configurations were used during the test in order to cover a wider range of strain energy release rate and crack length. Hence the test was first started with the parameters e = 21.1 mm and L = 65 mm with a test performed under load control at respectively maximum loads of 1000 N and 800 N. The jig parameters were then changed to e = 31.1 mm and L =95 mm in order to cover a larger crack length, using load control with a maximum load of 800 N and

1000 N. In order to cover a larger range of strain energy release rate, it was then decided to perform the tests in displacement control with corresponding starting loads of 1000 N and 800 N. One final test consisted of using parameters e = 33 mm and L = 100 mm in order to accommodate more crack length. All the variants were conducted on the same specimen. Figure 6-16 gives the results for the 100% mode II loading on the mixed mode jig. It gives the disbonding growth rate as a function of the total maximum strain energy release rate $G_{tot,max} = G_{I,max} + G_{II,max}$ **(6-11)**.

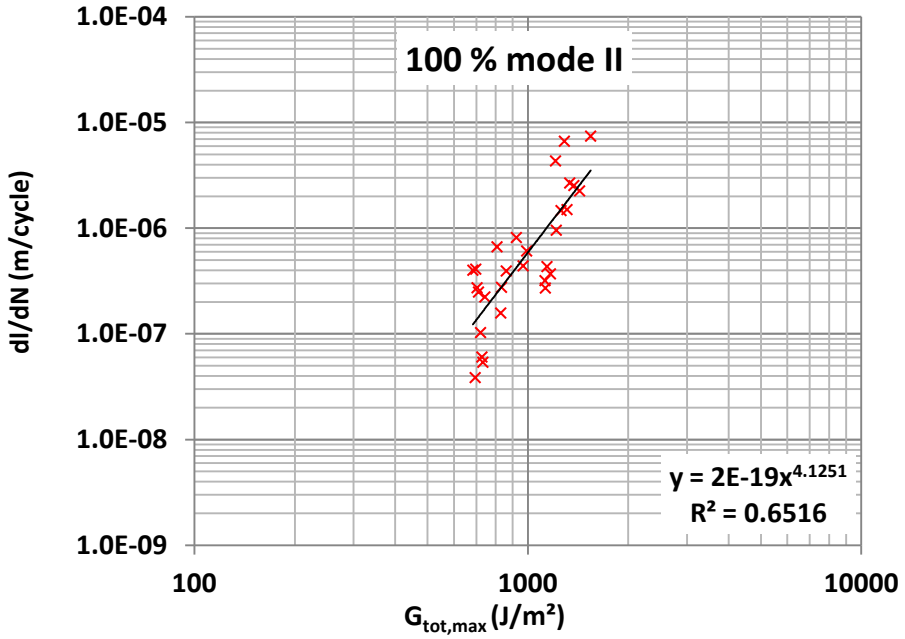

Figure 6-16 : Pure mode II mixed mode bending delamination growth rates (R = 0.1)

The data show some scatter, with crack growth rates between $2.0x10^{-8}$ m/cycles and up to $8.0x10^{-6}$ m/cycle covering a range of strain energy release rate between 700 J/m^2 and 1500 J/m^2. There is good agreement with growth rates obtained in Mode II using the ENF sample geometry.

- **75% mode II/25%mode I – Mixed mode**

Two specimens were tested with 75% mode II and 25% mode I. The test parameters used were e = 60 mm and L = 100 mm. Figure 6-17 gives the results for this configuration. It shows delamination growth rate as a function of the total maximum strain energy release rate ($=G_{I,max} + G_{II,max}$) for tests MMB#2 and MMB#3.

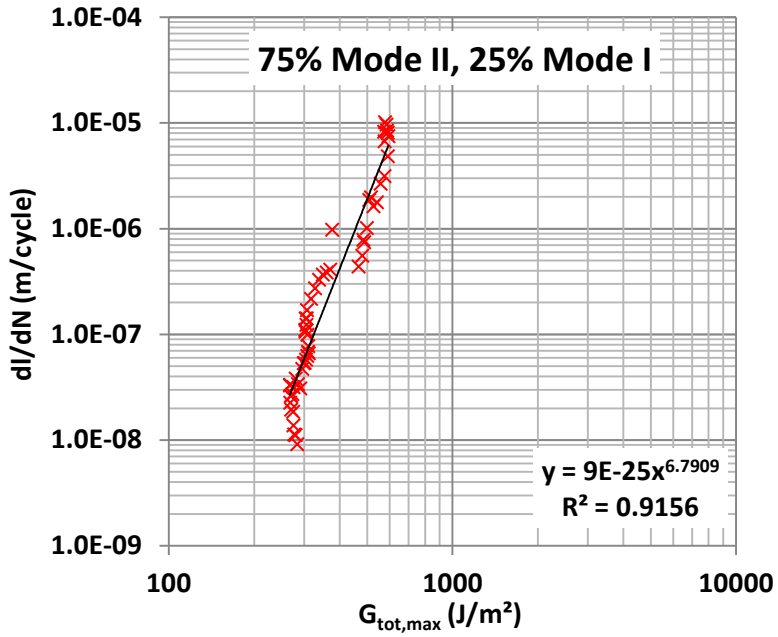

Figure 6-17 : Mixed mode bending delamination growth rates with 75% Mode II/ 25% Mode I (R = 0.1)

The data show reduced scatter in comparison to the previous test, with crack growth rates measured between $9.0x10^{-9}$ m/cycles and up to $1.0x10^{-5}$ m/cycle covering a range of total strain energy release rate between 250 J/m^2 and 600 J/m^2. The data show a steep gradient which means that a small change in the value of the total strain energy release rate will result in a large difference in delamination growth rate.

- **50% Mode II/50% Mode I – Mixed mode**

One specimen was tested with 50% Mode II and 50% Mode I (Figure 6-18). Two test parameters were used in order to cover a larger range of delamination length with e = 87.4 mm, L = 100 mm and e = 96 mm, L = 110 mm.

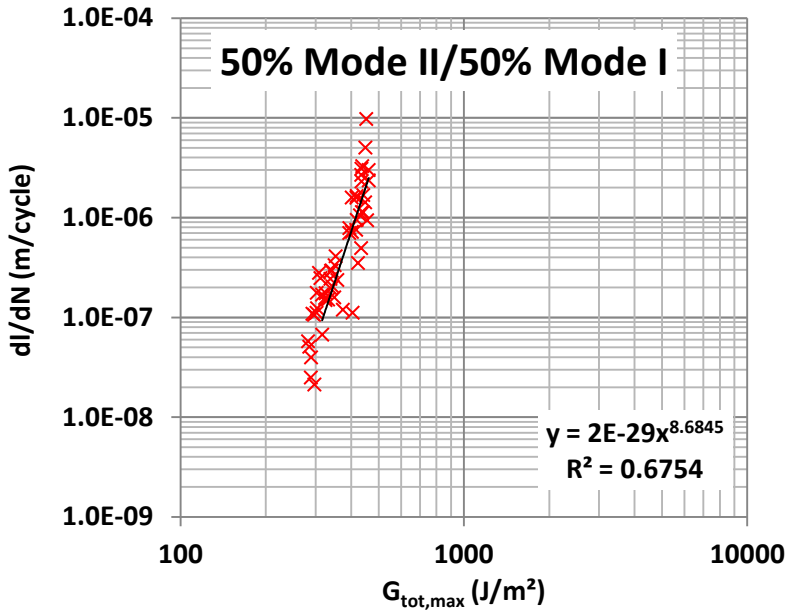

Figure 6-18 : Mixed mode bending delamination growth rates with ratio = 0.5 (R = 0.1)

The data show a reduced amount of scatter in comparison to the first test, with crack growth rates measured between 2.1×10^{-8} m/cycles and up to 9.7×10^{-6} m/cycle covering a range of total strain energy release rate between 280 J/m^2 and 450 J/m^2. As for the 0.75 ratio the set of data shows a steep gradient.

- **25% Mode II/75% Mode I**

Two specimens were tested with 25% Mode II. The test parameters used were e = 183 mm, L = 110 mm for both specimens. Figure 6-19 shows the results. The delamination growth rate is shown as a function of the total maximum strain energy release rate $G_{tot,max} = G_{I,max} + G_{II,max}$.

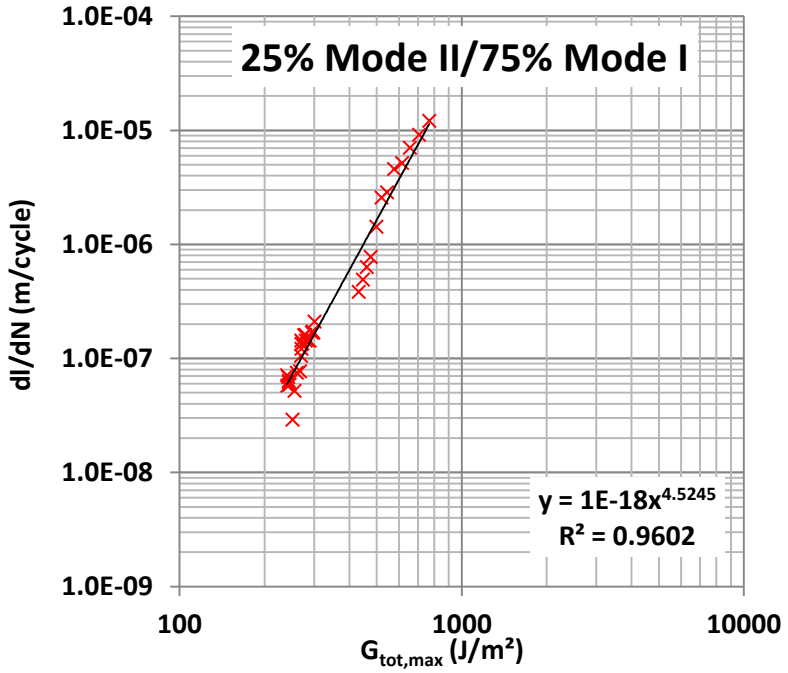

Figure 6-19 : Mixed mode bending delamination growth rates with ratio = 0.25

The data show a reduced amount of scatter in comparison to the first test, with crack growth rates measured between 2.9×10^{-8} m/cycles and up to 1.2×10^{-5} m/cycle covering a range of total strain energy release rate between 250 J/m^2 and 750 J/m^2.

6.5 Summary and conclusions

6.5.1 Static toughness G_{IC} – choice of adhesive

The mode I toughness tests summarized in Table 6-7 explored the influence of a number of variables on the values obtained.

(a) **Location of the pre-crack :** On the substrate interface or within the adhesive FM94/S2-prepreg, tests showed that failure within the adhesive gave greater toughness (mean of 1825 J/m^2) than failure at the substrate interface (mean of 1337 J/m^2), a 36% difference.

(b) **Location of sample manufacture :** FM94/S2-prepreg samples manufactured by Alcoa and by Cranfield, both tested at Cranfield showed no significant difference in toughness.

(c) **Comparison of FM94/S2-prepreg and FM94 toughness :** Average FM94 adhesive toughness was 1601 J/m^2; that of FM94/S2-prepreg was 1512 J/m^2; a 5% difference.

Table 6-7 : Mode I quasi static test summary of results

Batch	Adhesive	Interface	Avg G_{IC} (J/m^2)
#1	FM94-S2	prepreg/prepreg	1825
		substrate/prepreg	1150
#2		prepreg/prepreg	1825
		substrate/prepreg	1250
#3		substrate/prepreg	1613
#4	FM94	N/A	1601

Average values of Mode I G_{IC} measured in this work were consistently about 60% (1600 - 1800 J/m^2) of values reported in previous work and in published literature (up to 3,000 J/m^2). The FM94/S2-prepreg toughness never reached the value of 3,000 J/m^2 observed on tests by Politechnico di Milano [158]. In those tests, the delamination was grown within a GLARE 3/2 laminate bonded between aluminium plates, rather than directly between two plates bonded with FM94/S2-prepreg. The observation that delamination growing between two plates bonded with FM94/S2-prepreg have a G_{IC} value of 1300 J/m^2 (average of substrate/prepreg interface) whereas if the delamination was growing within GLARE a value of 3,000 J/m^2 would be obtained, suggested that if AIRSTREAM used the FM94/S2-prepreg to bond the crack retarders rather than FM94, inferior crack retardation would result. Laine Pearce in his investigation of fatigue crack growth rates in M(T) samples with bonded straps [116] found much inferior BCR performance when using FM94/S2-prepreg than was found in the first BCR project which used FM 94 where the delamination crack grew in the GLARE.

Because FM94 had greater toughness than FM94/S2-prepreg, the former was chosen for sample manufacture in the rest of the project.

6.5.2 Effect of mixed mode loading on delamination crack growth rates for FM94

Figure 6-20 illustrates the combined results obtained from mode I, 100% mode II tests and all mixed mode tests with 25, 50 and 75% Mode II loading.

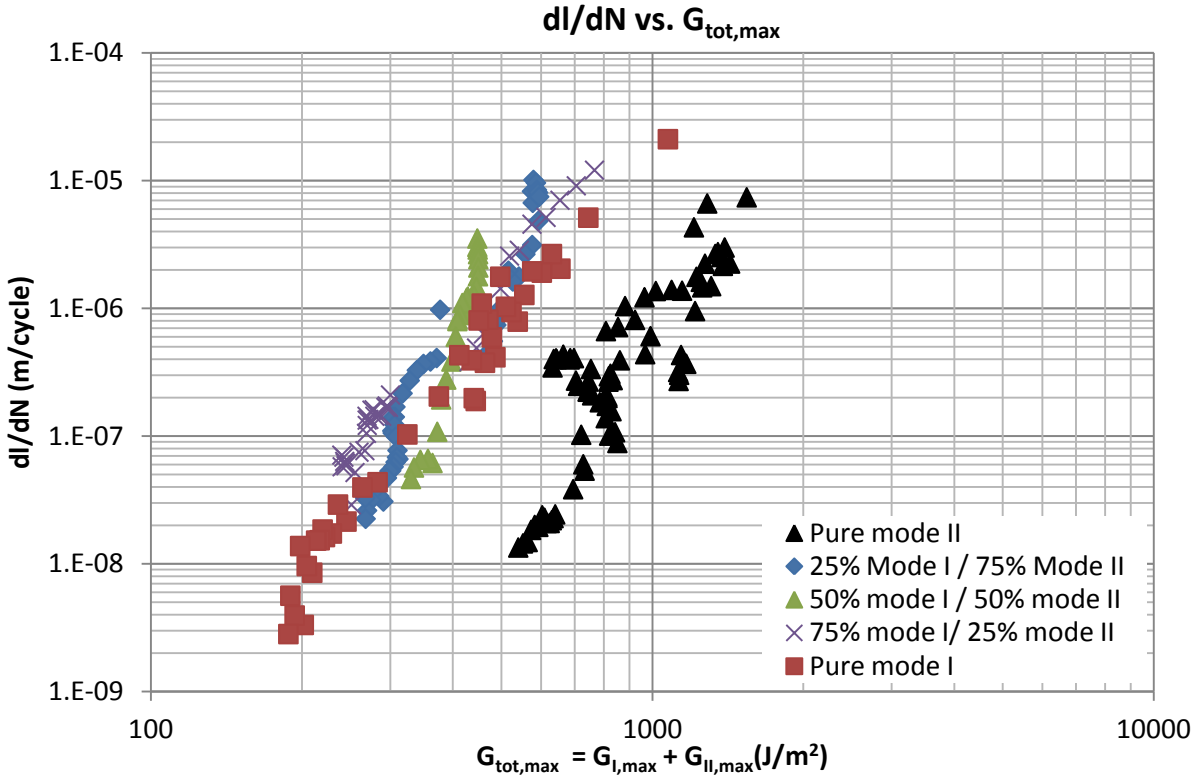

Figure 6-20 : FM94 (new) combined results

There are two groups of data in this chart. The first group comprises mode I and all mixed mode apart from the 100% mode II. The other group is the 100% mode II data. The first group has delamination growth rates that are 50% greater than the 100% mode II for the same values of $G_{tot,max}$ $(=G_{I,max}+G_{II,max})$. One interesting observation is that mixed mode (Modes I/II) tests containing 25,50 and 75% of Mode II have similar growth rates to those found in tests using 100% mode I, when expressed in terms of maximum SERR, $G_{tot,max}$ $=G_{I,max}+G_{II,max}$.

The data obtained from this test are directly used for the calculation of the delamination advance of BCR structures, as outlined in the next sections.

6.5.3 Study of the crack growth rates and comparison to other data

- **Comparison Mode I/Mode II**

Figure 6-21 presents the results of pure mode I and pure mode II. It shows that the results for Mode I demonstrate lower values of SERR than the mode II SERR under the same R-ratio of 0.1 at equivalent crack growth rate. It was also observed in past studies [5] that the fracture toughness for FM94 epoxy adhesive was higher for mode II than mode I, with G_{IC} = 3000 J/m^2 and G_{IIC} = 9000 J/m^2 which qualitatively correlates with the results shown here. As a consequence, for a same level of strain energy release rate, delamination is faster for mode I than mode II. The difference in crack growth rates may also be attributed to the fact that during mode II propagation, friction will reduce the disbond propagation hence making it more difficult for the crack to propagate as suggested in [177].

Figure 6-22 to Figure 6-24 are data obtained from the literature on the study of fatigue delamination under mixed mode conditions in different composite laminates. Data have been re-plotted in order to use similar expression of strain energy release rate as the one used in Figure 6-21. The linear regression obtained from the data is used here for means of comparison. The trend is similar to the one found with the FM94 adhesive with a specific distribution of mode I and mode II.

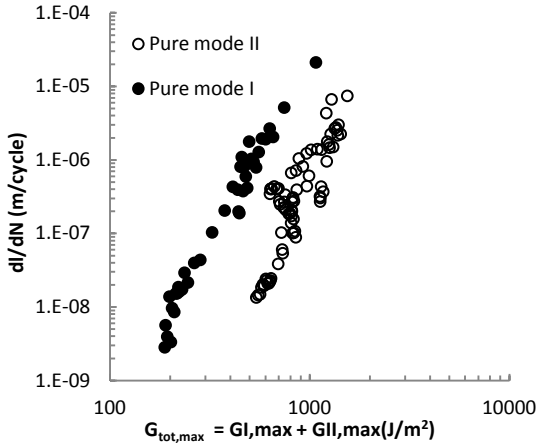

Figure 6-21 : Delamination growth rate, versus total SERR(max) for FM94 epoxy adhesive – Mode I and mode II cases

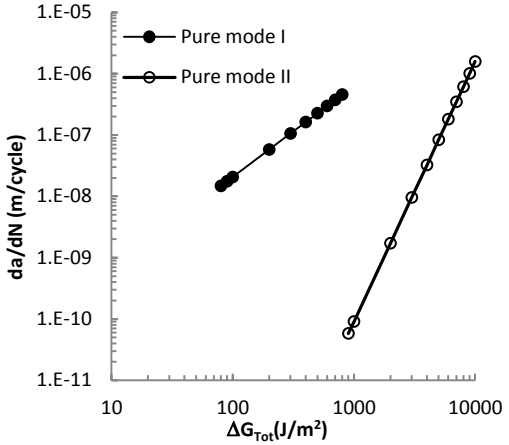

Figure 6-22 : Delamination growth rate, versus range of SERR for unidirectional glass/epoxy laminates (E-glass fibre/M10 epoxy resin - VICOTEX) – Mode I and mode II cases –[174]

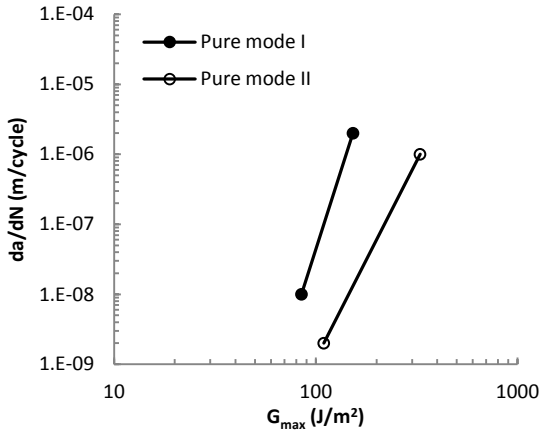

Figure 6-23 : Delamination growth rate, versus SERR(max) for T300/#3100 – Mode I and mode II cases –[178]

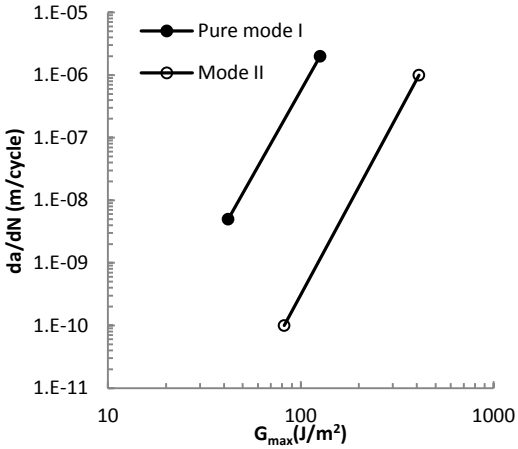

Figure 6-24 : Delamination growth rate, versus SERR(max) for T800H/#3631 – Mode I and mode II cases – [178]

- **Mixed mode cases**

The analysis of mixed mode delamination shows that the mixed mode cases are all in the same data range as the pure mode I in terms of level of SERR and crack growth rates, with lower levels of SERR as opposed to the pure mode II. Figure 6-25 shows the results of the single mode (I and II) and mixed mode as reported earlier. Figure 6-26 to Figure 6-28 show the results of fatigue crack growth delamination obtained for 3 different composite laminates under mixed mode conditions of delamination.

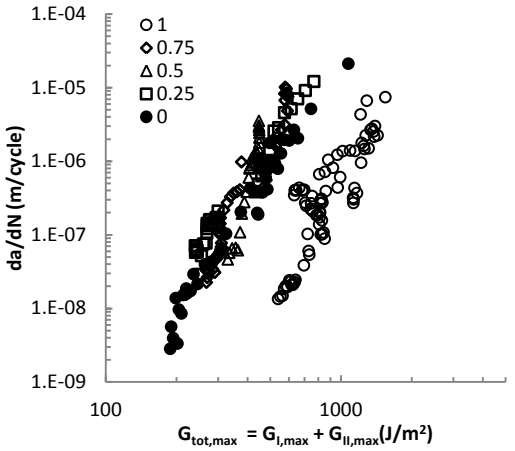

Figure 6-25 : Delamination growth rate, versus total SERR(max) for FM94 epoxy adhesive – Mixed Mode cases

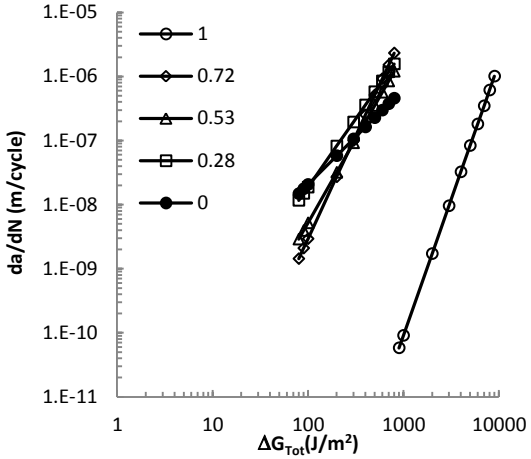

Figure 6-26 : Delamination growth rate, versus range of SERR for unidirectional glass/epoxy laminates (E-glass fibre/M10 epoxy resin - VICOTEX) – Mixed Mode cases [174]

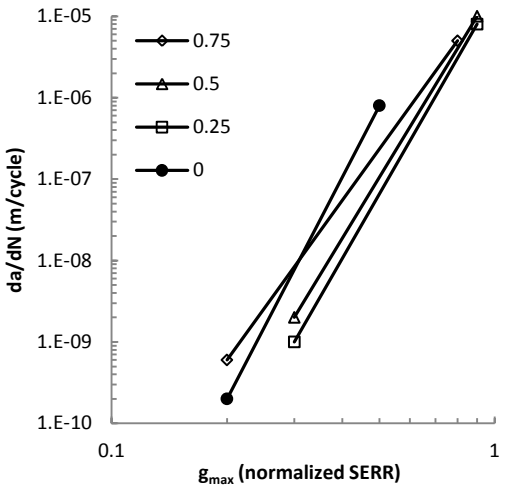

Figure 6-27 : Delamination growth rate, versus range of SERR for T700/QY811carbon/bismaleimide composite– Mixed Mode cases [179]

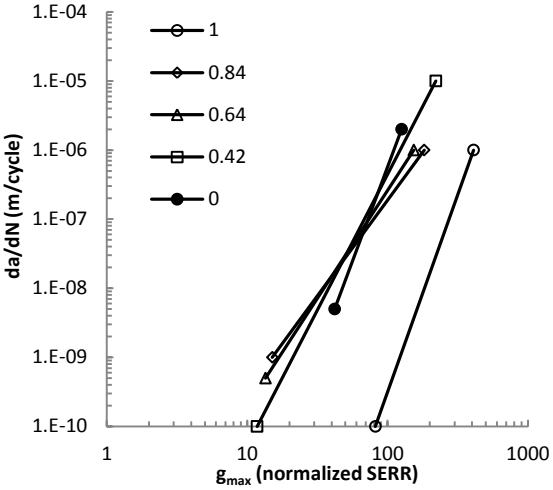

Figure 6-28 : Delamination growth rate, versus range of SERR for T800/#3631carbon/bismaleimide composite– Mixed Mode cases [178]

They demonstrate the same behaviour as the one obtained for the FM94 adhesive with mixed mode fatigue crack growth data embedded into the pure mode I ranges of SERR and crack growth rates but with a well-marked difference with pure mode II results.

In particular, one can observe in Figure 6-28 that with a mixed ratio of 84%, the results are unchanged. Hence even with a small amount of Mode I (16%) in a mixed mode case, the results tend towards a mode I behaviour.

Figure 6-29 illustrates the distribution of the fracture toughness for several mixture ratios from pure mode I to pure mode II for an IM7/E7T1 graphite epoxy. In that case, it shows fewer variations from 0 to 0.5 mixtures than above 0.5 with a non-monotonic behaviour. Hence this may explain the critical contribution played by mode I in the delamination mechanism.

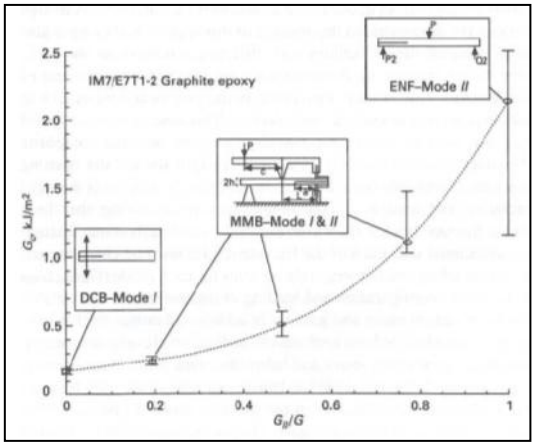

Figure 6-29 : Mixed mode I and II delamination criterion [180]

This behaviour can be explained by the role played by friction for mode II delamination. In fact the mode II mechanisms is controlled by the shear stresses at the interface between the two adherents and the compression state between the two adherent increases the friction which results in a larger amount of energy required to propagate the delamination. This was demonstrated in [177] and Blackman [181] also commented on the fact that friction will oppose to the shear displacement. Hence in the case of mixed mode delamination with low amounts of mode I, the friction is mainly reduced which makes it easier for the delamination to propagate due to the slight amount of opening mode (mode I) that reduces the compression between the two adherents.

Chapitre 7 : Calculation of substrate K values in structures containing BCR

The present chapter describes the modelling techniques used to study BCRs and to develop a design tool for fatigue life prediction.

7.1 Mechanisms operating when a fatigue crack encounters a BCR

One of the difficulties in modelling bonded crack retarders is to include the different mechanisms that are operating and also that all these mechanisms interact with each other. Figure 7-1 shows a reinforced coupon with the substrate lead crack, disbonding and the crack bridging effect.

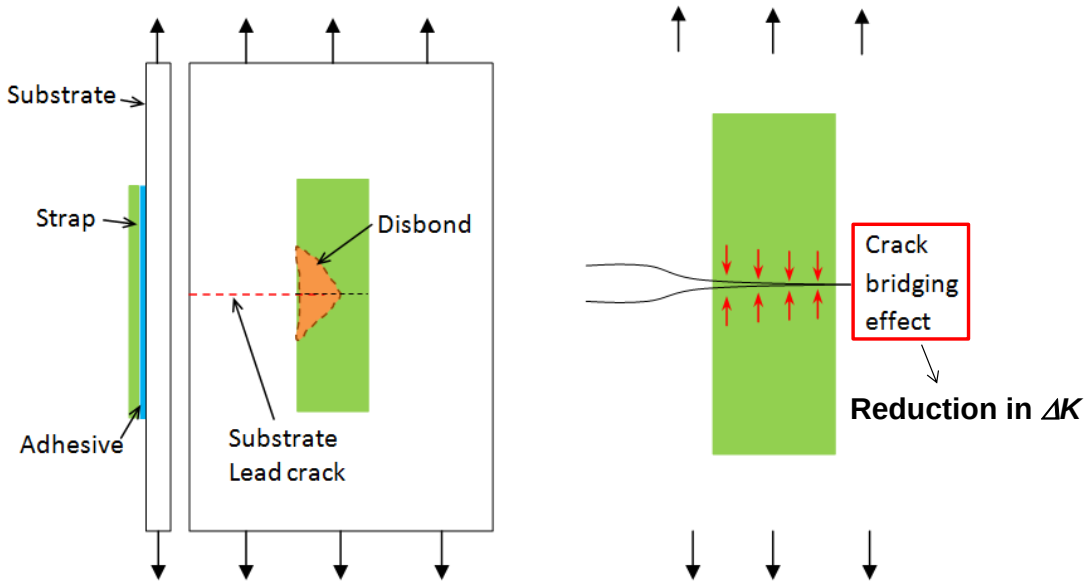

Figure 7-1 : BCR mechanisms (view of half M(T) specimen)

Lead crack in substrate: This is the main damage form.

Secondary bending: The reinforcement is applied on one side of the sample only. Hence the neutral axis of the specimen is no longer at the mid-plane of the substrate but is shifted towards the reinforcement. When the specimen is loaded the plate tries to get back to its neutral axis creating out of plane bending (Figure 7-2). This effect needs to be taken into account in the calculation of the stress intensity factor either through the use of 3D elements or by using a

specific formulation as developed by Boscolo in [103], [104] when using 2D elements.

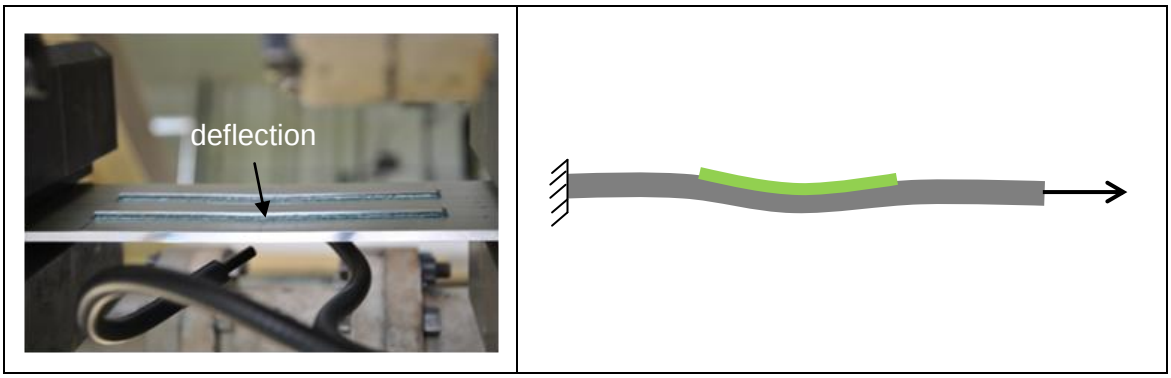

Figure 7-2: Secondary bending mechanism

Thermal residual stresses (TRS): Bonding straps at elevated temperature will result in residual stresses in the substrate and strap at room temperature, since the substrate and strap materials have different coefficients of thermal expansion (Figure 7-3). Residual stress magnitude and distribution will change during the crack propagation. The residual stresses will influence fatigue crack growth rates.

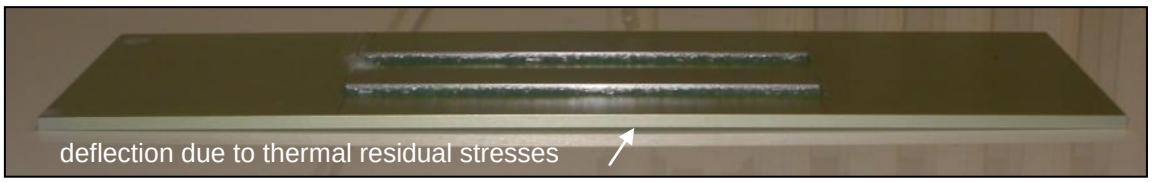

Figure 7-3: Specimen after curing -Thermal residual stresses effect with out-of-plane bending

According to the measurements performed by Syed in [163] and illustrated in Figure 7-4, the longitudinal residual stresses are low tensile residual stresses, of ~ 20 MPa in the substrate with no significant variation through the thickness and across the width of the specimen.

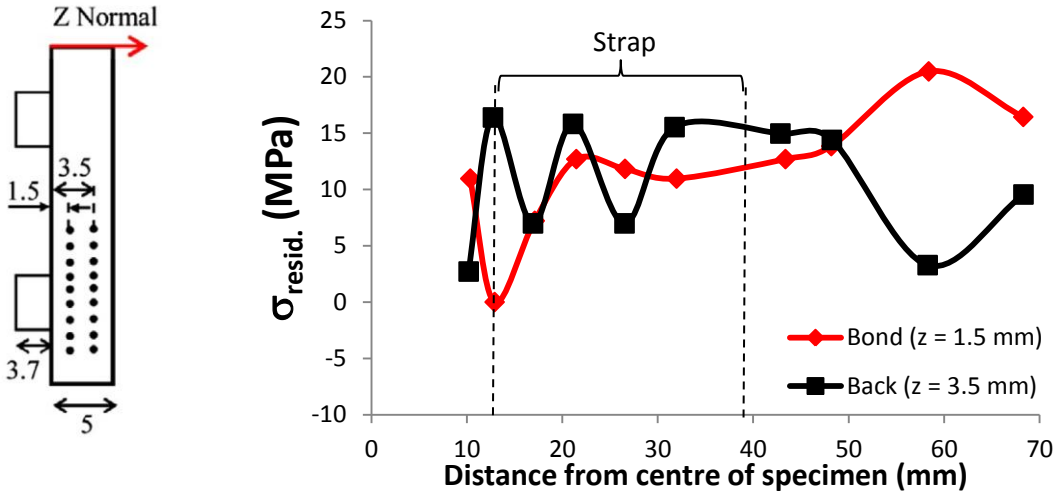

Figure 7-4 : Longitudinal residual stress measurement on M(T) specimen at z = 1.5 mm and z = 3.5 mm through specimen thickness

Crack bridging effect: The strap will limit the substrate crack opening displacement under cyclic loading, resulting in reduction in the stress intensity factor and consequently the fatigue crack growth rate.

Disbonding of adhesive layer: While the substrate crack develops underneath the strap, fatigue delamination is observed in the adhesive layer [7]. The delamination may reduce the effectiveness of the crack bridging and hence increase K value (Figure 7-5).

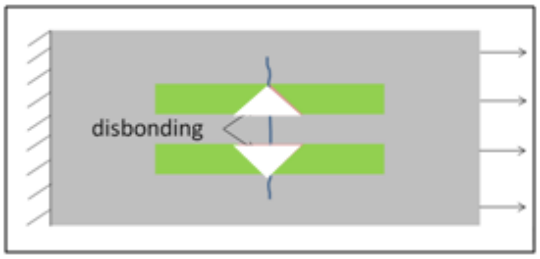

Figure 7-5 : Schematic delamination shape

Sample gripping: During fatigue tests, each end of the substrate were clamped in the gripping system restricting the out of plane secondary bending (**Erreur ! Source du renvoi introuvable.**).

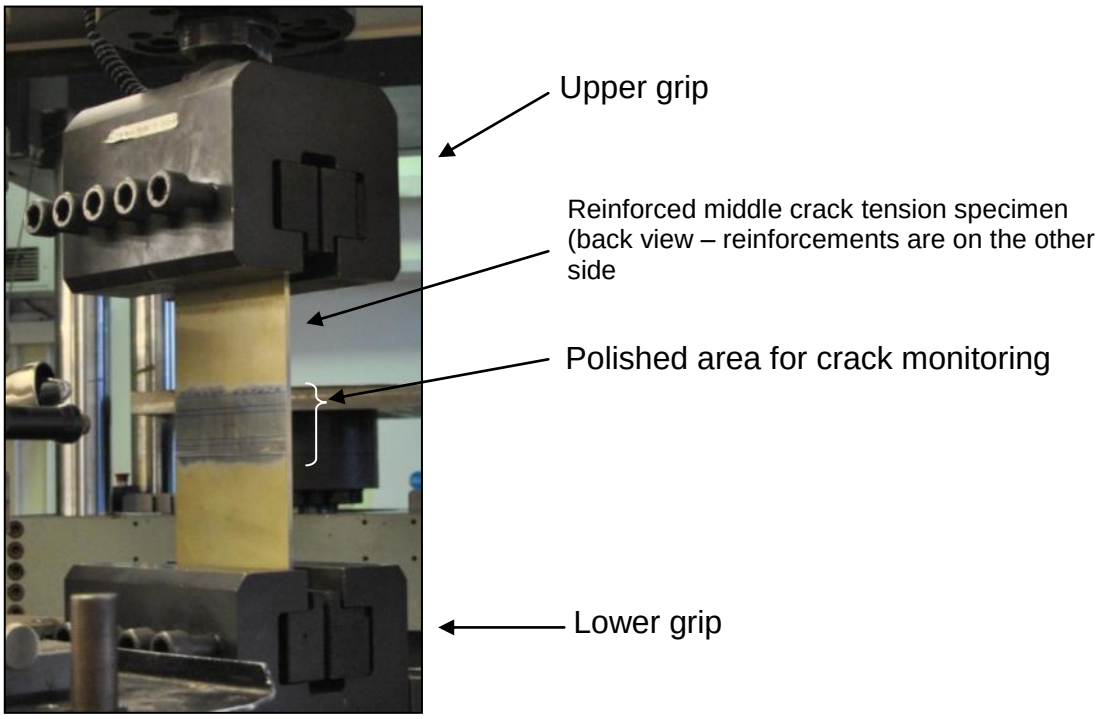

Figure 7-6 : Back view of sample gripping system showing boundary condition over specimen during testing

7.2 Assumptions used in construction of FE and fatigue crack models

- Strap behaviour

No damage or delamination within the strap is considered in the FE model. It is assumed that the straps stay undamaged and disbonding only occurs at the interface between the strap and the substrate.

- Substrate crack profile

In a sample with a bonded strap, if the test sample is sufficiently thick, the substrate crack front will be an asymmetric curved shape through the thickness

with a longer crack length on the back side than on the retarded reinforced side (Figure 7-7).

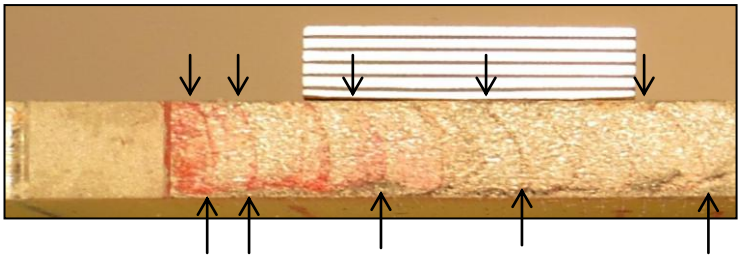

Figure 7-7: Substrate crack curved crack profile for reinforced M(T) specimen MTR1

Since the model uses only one element through the substrate thickness, the substrate crack length was assumed the same on the reinforced and on the back side.

- Disbonding at strap/substrate interface

The model was constructed with three parts representing the substrate, adhesive layer and strap. Hence two disbonding interfaces were possible, either between the substrate and the adhesive or between the adhesive and the strap. A choice was made to have disbond located at the interface between the substrate and adhesive (Figure 7-8).

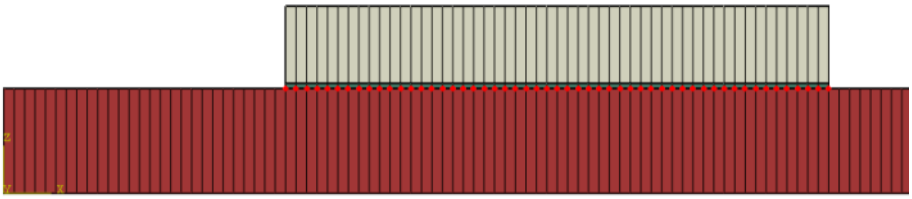

Figure 7-8 : definition of disbonding interface (between substrate and adhesive layer)

- Disbonding restrictions

Based on observations made during testing of M(T) coupons [116], [161] it was assumed that the disbonded area had the same length as the substrate crack and was behind the substrate crack tip. It was assumed that disbonding will only extend at the maximum cyclic load and calculation of the incremental increase was performed at maximum load.

The increment was calculated based on the number of cycles required to grow the bonded side substrate crack. Further details of the calculation are given in Chapter 8.

- Out-of-plane bending and crack bridging effect

The out-of-plane bending and crack bridging effects were incorporated in the FE model by means of realistic boundary conditions and the choice of elements (3D elements).

7.3 Finite element model by ABAQUS

Commercial finite element software ABAQUS version 6.12-2 was used for the modelling work. The model is of a reinforced M(T) specimen shown in Figure 7-9. The model consist of three layers of continuum shell elements representing the substrate, adhesive layer and strap, which are linked together with constraint and contact conditions to simulate the bonding between the different layers and the possible disbonding created between those layers.

Due to the double axial symmetries (X and Y) only one quarter of the specimen was modelled. That implies the application of specific boundary conditions given later.

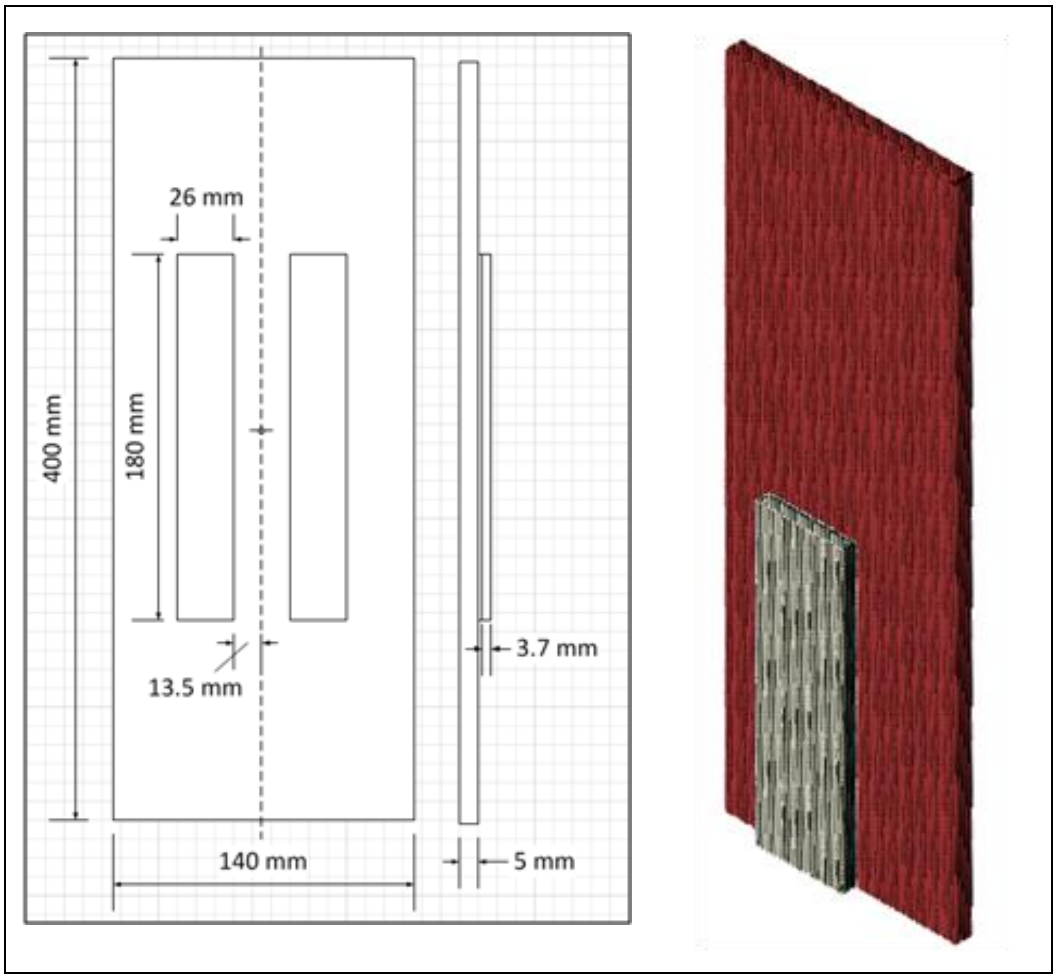

Figure 7-9: M(T) specimen, geometry and FE model

7.3.1 Finite element types

3D analysis was chosen to simulate the BCR design using 8-noded hexahedron continuum shell elements (designated as SC8R in ABAQUS), and general purpose finite membrane strain elements [145]. These elements defined the initial geometry of the surface by discretization of the three dimensional structure of the specimen (each layer in the case of M(T) specimens) in the same way as 3D solid elements. The advantage of such elements is that only one element through the thickness needs to be used for each layer of the assembly because there are no restrictions on the aspect ratio. Hence all layers (substrate, strap and adhesive) used these continuum shell elements – SC8R – for each discretized part of the specimens. The bonding between each part was then modelled through the use of tie constraint or specific contact constraint to allow for delamination to propagate. No specific elements such as cohesive

elements of X-fem solution was used in the current model. All models used the element quoted above.

7.3.2 Interaction properties

One of the main difficulties in this case is to model the interaction between all surfaces. As mentioned earlier, it is assumed that a disbond will only propagate at the interface between the strap and the substrate. Hence the disbond is modelled in the adhesive layer.

Every layer of material was represented in the model with one layer for the substrate, one for the adhesive and one for the reinforcement. The disbond was assumed to be an adhesive failure.

- **Interface with no delamination: “Tie” constraint.**

This constraint was defined at the interface between the strap and the adhesive. The tie constraint is a surface based constraint that ties two surfaces together so that the nodes of the respective surfaces have coupled behaviour with identical motion.

- **Interface of disbond: “Disbond” option.**

For the disbond, a contact interaction is defined. This is a surface-to-surface definition of a contact that can be restricted to a certain area defined by the node bonded to a surface in that particular area. This contact is associated with a contact interaction property for which details are given in Table 7-1.

Table 7-1: Contact properties for disbond simulation

Tangential behaviour:	Friction formulation =	Penalty
	Friction =	Friction coef. = 0
Normal behaviour:	Pressure Overclosure =	“Hard” Contact
	Constraint enforcement method =	Default
Geometric properties	(left to default)	

When defining the contact interaction it is necessary to select the property previously defined. It is also required in the “*Bonding*” menu to select the option “*Limit bonding to slave nodes in subset*” and select here the subset that correspond to the bonded area. This is an important step in the definition of the model as this will restrict the bonding to a certain area and will allow for the calculation of further disbond in the model as the crack is advancing into the substrate.

Abaqus includes a module that offers the possibility to specify the crack/disbond propagation between two surfaces that are initially partially bonded through the “*Disbond’’ option based on the virtual crack closure technique (VCCT).

In order to use the “*Disbond’’ option, the user needs to specify a “*Fracture criterion”. Reeder’s criterion [199] was used in the model with artificially high critical value of parameters in order to prevent the static delamination and allow for the design tool to automatically calculate the fatigue disbonding. The Reeder law is defined by G_{IC}, G_{IIC}, G_{IIIC} and η. These parameters are directly entered in the Abaqus code of the input file (file that defines the whole analysis). Detail of that code is given in Figure 7-10.

```
*debond, slave=Adhesive-BOT, master=Substrate-top, OUTPUT=both
*FRACTURE CRITERION,TYPE=VCCT,MIXED MODE BEHAVIOR=REEDER,TOLERANCE=0.1
3000, 3000, 3000, 1.75
```

G_{IC} G_{IIC} G_{IIIC} η

Figure 7-10 : Input file code

In the present model, this option was used to evaluate the Strain Energy Release Rate (SERR) at the delamination front as the VCCT is directly embedded in Abaqus code. The value of the SERR was then used to calculate

the disbond growth rate using the adhesive fatigue crack growth rates obtained from fatigue delamination data given in Chapter 6.

7.3.3 Material models

All the materials in the model were modelled as linear elastic. The adhesive and the aluminium substrate have isotropic properties whereas the Glare fibre metal laminate has orthotropic properties.

The Glare was modelled through the composite layup option available in Abaqus, in the Property module. The user can define a composite material through the definition of its different layers. The orthotropic definition of Glare comes from the S2-prepreg layers which are glass fibre reinforced epoxy adhesive layer. They were defined in the model through the ‘’Lamina’’ data detailed in Table 7-2.

Table 7-2 : Lamina mechanical properties of S2-prepreg [156]

Material	E_1 (MPa)	E_2 (MPa)	ν_{12}	G_{12} (MPa)	G_{13} (MPa)	G_{23} (MPa)
S2-prepreg	50300	5500	0.31	1995	1995	2099

Material	$CTE_{11}(°C^{-1})$	$CTE_{22}(°C^{-1})$	$CTE_{33}(°C^{-1})$
S2-prepreg	$2.88x10^{-6}$	$4.03x10^{-5}$	$4.03\ x10^{-5}$

Abaqus gives a schematic representation of the composite layup shown in Figure 7-11. This allows checking the orientation of any layers.

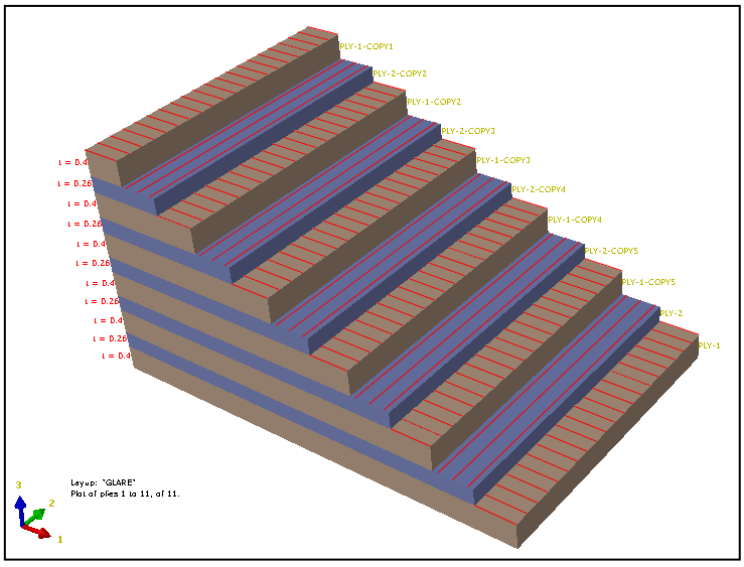

Figure 7-11 : Composite layup representation (Abaqus)

7.3.4 Thermal residual stresses

The thermal residual stress distribution was calculated by FE analysis. In order to take into account the residual stresses generated during the curing process, a ‘’predefined field” of temperature ΔT was applied to the structure that simulated the drop of temperature associated with the curing process.

The curing temperature recommended by the manufacturer for FM94 is T_c = 120°C [162]. Assuming a room temperature of T_c = 20°C, the temperature difference is: ΔT = 20 - 120 = -100°C. The values used for the simulation are given in (Table 7-3)

Table 7-3 : Thermal expansion coefficients

Material	**Coefficient of Thermal Expansion (m/m/°C)**
2624 -T351 [152]	2.32×10^{-5}
FM94 [162]	0
FM94/S2-prepreg [166]	$\alpha_{11} = 2.88 \times 10^{-6}$
	$\alpha_{22} = 4.03 \times 10^{-5}$
	$\alpha_{33} = 4.03 \times 10^{-5}$
2024 -T3 [156]	2.32×10^{-5}

As the crack propagates in the substrate, the substrate residual stresses will redistribute. That is why the predefined temperature field must be kept in both

steps in order to make sure that the residual stresses are taken into account during the simulation of the loading process.

In the present case of AA2624-T351 reinforced with Glare 2A 6/5 (0.4), as the substrate coefficient of thermal expansion is higher than that of Glare, the substrate will expand more during the curing process. Hence it will be restricted by the Glare strap when returning to the room temperature resulting in tensile residuals stresses in the substrate as illustrated in Figure 7-4. Those tensile residual stresses will promote crack opening and consequently increase the crack propagation rate.

When simulating the residual stresses, particular care must be taken in the definition of the boundary conditions as the specimen is not restricted during the curing process while it is constrained by the test machine during the loading process. Details of the boundary conditions used in the analysis are given in the next section.

7.3.5 Analysis steps, loading and boundary conditions

Two major stages need to be modelled in order to simulate accurately the testing of the reinforced specimens. The first stage is the curing process which is described in the previous section. The second is the mechanical loading process. For each stage, specific boundary conditions are applied.

- **Boundary Condition Set 1: Curing process**

During the curing process the reinforced specimen is simply supported by a table placed in the autoclave. After curing the specimen will have thermal residual stresses due to the mismatch of the thermal expansion coefficients and the elastic modulus. Hence the first set of boundary conditions has the double symmetry boundary conditions applied to the specimen due to the modelling of only one quarter of the specimens.

- **Set 2: mechanical loading process**

During the second step of the analysis, the previous set of boundary conditions is kept. The clamping conditions applied during testing (**Erreur ! Source du**

renvoi introuvable.) need to be simulated to restrict the specimen movement over a clamp length of 50 mm. This is defined through a node set that encloses the top and bottom surfaces of the substrate over a length of 50 mm. Two boundary conditions are applied to the previously defined node set, to constrain the movement of the specimen to a longitudinal movement only – no rotation allowed. The boundary conditions on the substrate section that simulates the crack path will be changed by node release during modelling of the crack advancement.

A loading condition is then applied to the specimen top section in order to simulate the maximum and minimum loads applied to the coupon. All these boundary conditions are illustrated in Figure 7-12.

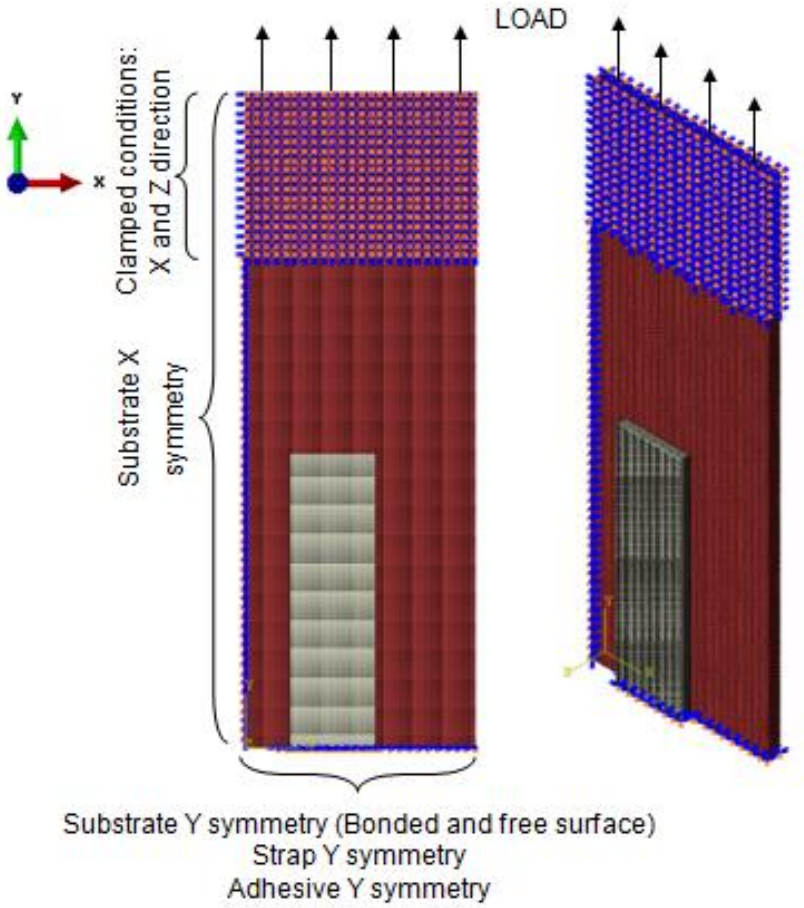

Figure 7-12 : Boundary conditions for quarter of reinforced M(T) specimen

When solving the problem above, geometrical non-linearity must be used to calculate the solution. This is due to the presence of the strap causing nonlinear behaviour of the assembly.

7.4 Determination of stress intensity factor K

The Modified Virtual Crack Closure Technique (MVCCT) also referred to as the VCCT in its earlier versions, is used in this work.

The Virtual Crack Closure Technique (VCCT) [42], or modified version (MVCCT), is based on Irwin's crack closure integral method [25] that states that the strain energy released when a crack is extended to a certain amount Δa is the same as to close that crack by Δa. The drawback of the crack extension method is that two finite element calculations are required in order to obtain the strain energy release rate (SERR) at the crack front. This was later simplified through the Modified Virtual Crack Closure Technique that showed that the state of the crack tip from $a+\Delta a$ to $a+2\Delta a$ (2 analysis) is not significantly changed. Hence, only one analysis is required.

The general expression of the mode I strain energy release rate is the following one, as illustrated in Figure 7-13.

$$G_I = -\frac{1}{2\Delta A} F(w_1 - w_2) \quad \textbf{(7-1)}$$

where F is the reaction force at the crack tip node, w_1 and w_2 are the displacement on each side of the crack as shown in Figure 7-13, $\Delta A = \Delta a \times b$ **(7-2)** is the area virtually closed with Δa corresponding to the length of the crack increment (= finite element length) and b corresponding to the width of the elements.

As the specimen studied in this research have a symmetric configuration, w1 = -w2. The expression of the mode I SERR can then be re-written as:

$$G_I = -\frac{1}{\Delta A} Fw \quad \textbf{(7-3)}$$

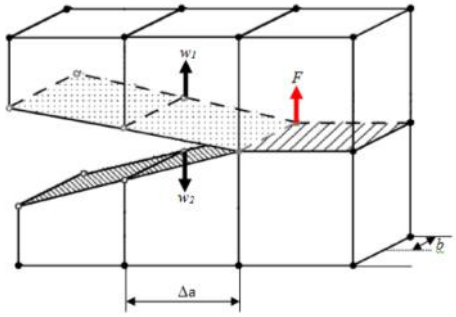

Figure 7-13: VCCT for 8 nodes continuum shell elements (SC8R) – Through thickness view

Assuming the plane stress condition, the stress intensity factor is then calculated using the expression:

$$K_I = \sqrt{E.G_I} \quad \textbf{(7-4)}$$

where E is the Young's modulus of the material used for the substrate.

One of the advantages of this technique is that it is not highly mesh size dependent, hence the mesh defined at the crack tip does not need to be refined to the smallest size like the displacement method.

In the present case, force and displacement are directly obtained from the output database file. The geometric factor β is then obtained using the relationship $K = \beta\sigma\sqrt{\pi a}$ **(7-5)** which gives $= \frac{K}{\sigma\sqrt{\pi a}}$ **(7-6)**. Further details of the calculation are outlined in the next chapter.

- **Thickness considerations**

For single sided reinforced coupons stress intensity factors are calculated for the bond side K_{bond} and the back side K_{back}, for a symmetric crack front (Figure 7-14). Loads and displacements necessary for the calculation are extracted from the crack tip nodes respectively located on each side, as illustrated in Figure 7-14.

Load	Displacement
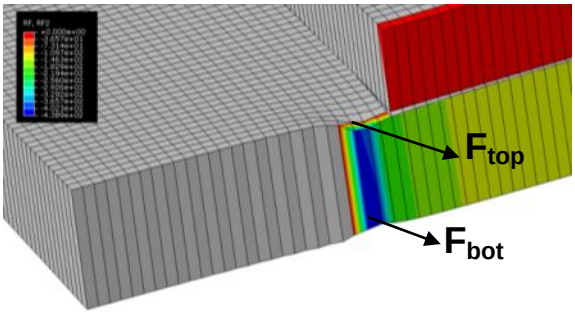	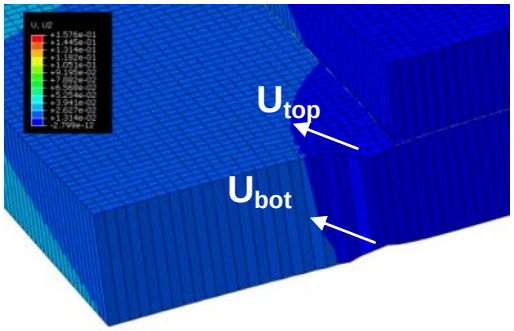

Figure 7-14 : Load and displacement extraction from FE model

The MVCCT formulation described in the previous section is then used in order to calculate the stress intensity factor for bond and back faces.

Chapitre 8 : Fatigue Life Improvement Calculation

The fatigue life of bonded samples can be calculated by integration of crack growth rate data once the relation between ΔK and crack length is known. One of the necessary steps is to calculate the stress intensity factor coefficient β (normalized stress intensity factor) as a function of crack length for the relevant bonded coupon or structural geometry.

The approach used in this research was to incorporate the effect of all major interacting parameters such as thermal residual stresses, secondary bending and delamination into the value of β. A scripted calculation routine entitled ReSLIC was developed in order to calculate the evolution of β with crack length in bonded samples. Calculation assumptions were the following ones.

- **Secondary bending** is considered through the choice of a 3D model with 3D elements.

- **Thermal residual stresses** are introduced by the use of a curing step in the analysis and consideration of thermal residual stresses for the post-processing of the FE results (incorporation of residual stress into ΔK_{eff}).

- **Distribution of stress through the thickness** is calculated through a weighted method as developed by Boscolo [50]

- **Disbonding** is evaluated during the crack growth iterations.

- **Non linearity** is considered through the solver solution that takes into account the geometric non-linearity of the problem.

All other mechanism such as gripping, crack bridging effect and lead crack growth were taken into account by definition of boundary conditions, interface definition in the model and iterative calculation.

The last step in the fatigue life prediction is the integration of the material fatigue crack growth law. In the present work, the computer code AFGROW was used to perform the material law integration.

8.1 ReSLIC methodology

The computer code ReSLIC developed during the course of this study is a computer script written in object oriented language Python to manage the calculation of the residual stress and stress intensity factor (SIF, K) and the SIF coefficient β together with the calculation of the disbonding growth. ReSLIC general approach is illustrated in Figure 8-1.

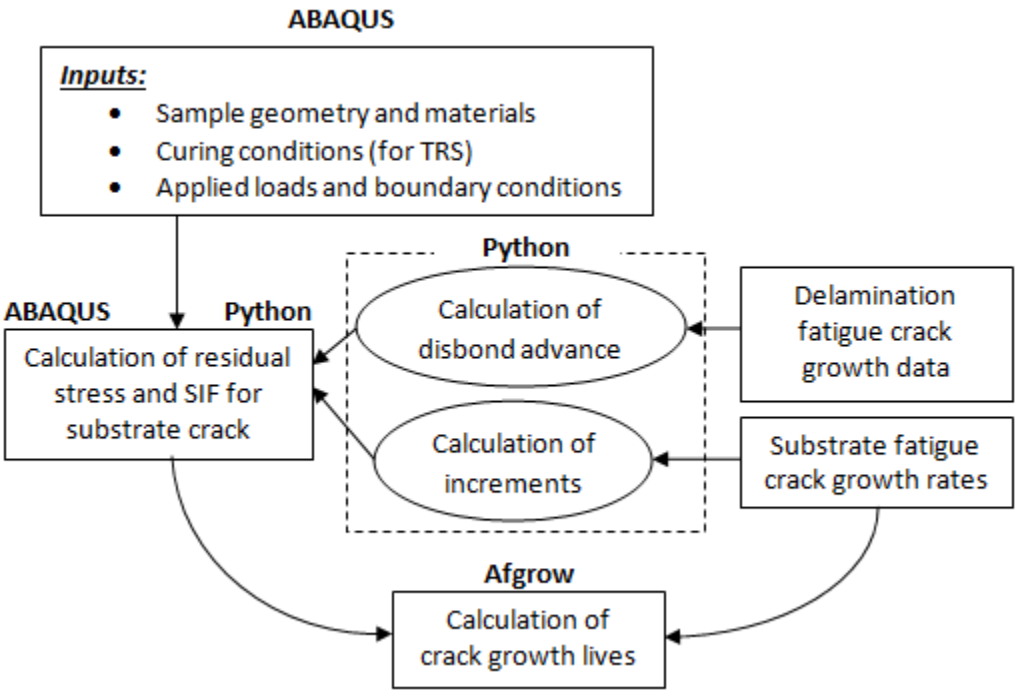

Figure 8-1 : ReSLIC approach

The first step of the calculation was to calculate the stress intensity factor under maximum applied stress σ_{max} and the associated disbond advance. Then the results of the disbond advance were used for the calculation under minimum applied stress σ_{min}.

Details of the crack advance calculation procedure and the associated disbonding are given in the following sections.

8.1.1 Extension of substrate crack

The extension of the lead substrate crack in ReSLIC is based on the mesh size of the model. If the mesh size of the model is Δe (Figure 8-2), then Δe was the

crack increment. For a crack length $a_{i,}$ then $a_{i+1} = a_i + \Delta e$ for the bond and back faces.

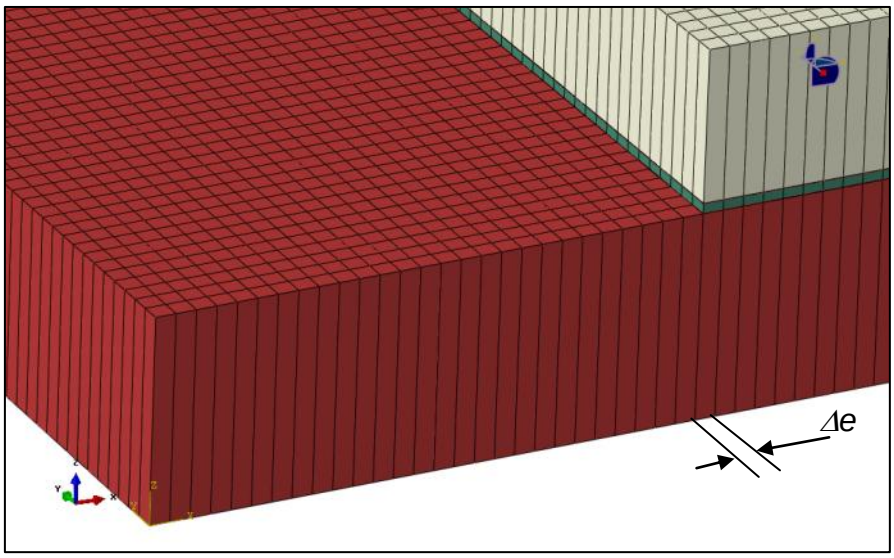

Figure 8-2 : Mesh size details

ReSLIC calculates the values of K_{max} and K_{min} at the substrate bond surface and the back surface of the specimen under maximum and minimum cyclic stress (σ_{max} and σ_{min}).

This step is repeated for each increment until the crack has reached a final length. ReSLIC will release only one node at the crack front on both the bond and back faces, which results in a straight crack front for the entire crack propagation.

8.1.2 Extension of associated interface disbond

In parallel to the substrate crack advance calculation, the disbond extension was implemented into the script using a fracture mechanics approach. Disbond advance was calculated under maximum applied stress and the disbond front shape was then used for minimum applied stress simulations. This assumes that disbond only grows under maximum applied stress. It was assumed that the disbond will start when the substrate crack tip enters the strap covered area (Figure 8-3). The first step is to release the first corner node of the bonded interface.

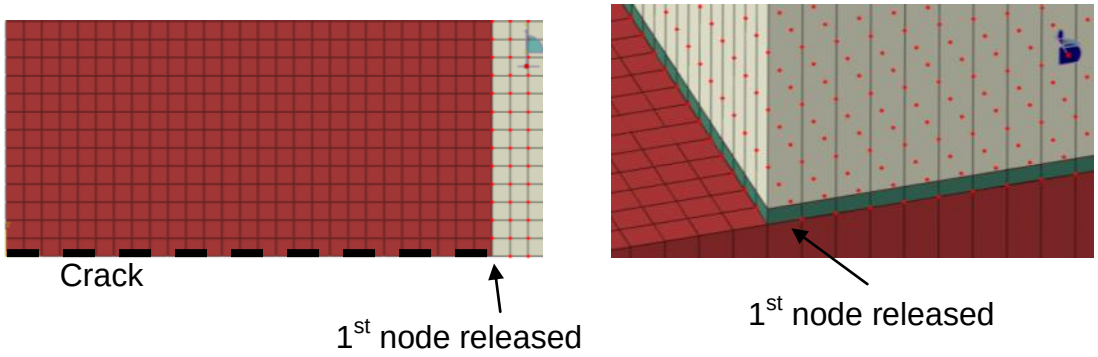

Figure 8-3 : First node release as crack is entering in the bonded area

As the substrate crack advances, the “Disbond” option is then used to get the strain energy release rate (SERR) at the disbonding front. For each crack increment, Abaqus outputs mode I, II and III strain energy release rates [145] for each nodes of the disbond front. In the present case, it was assumed that only mode I and mode II were relevant (Figure 8-4).

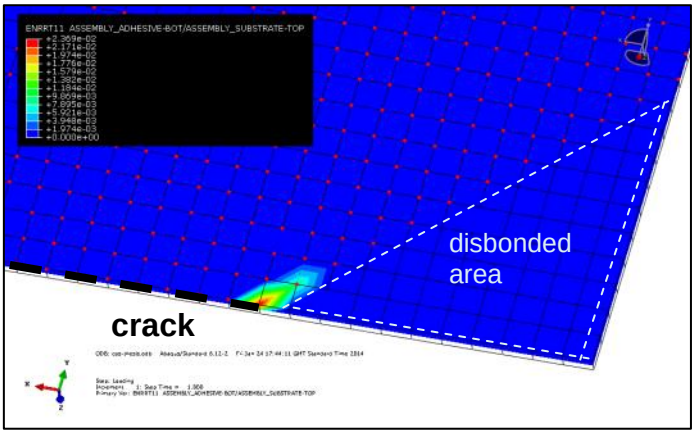

Figure 8-4 : Example of mode I SERR at disbonding front (back view of adhesive layer) showing the higher values of SERR near the crack front.

These values of strain energy release rate were then used to calculate delamination advance at the disbond front, based on the calculated mode I to mode II ratio and the overall value of total SERR. Figure 8-5 gives an illustration of the extraction of mode I and mode II SERR together with the calculation of the mode ratio. The ratio is defined as : mode ratio = $G_{II}/(G_I+G_{II})$ **(8-1)**. The series of fatigue delamination tests reported in Chapter 6 are used here in the calculation of delamination advance.

Mode I SERR extraction	Mode II SERR extraction
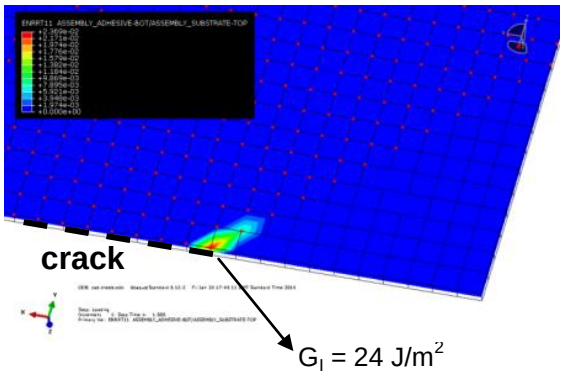	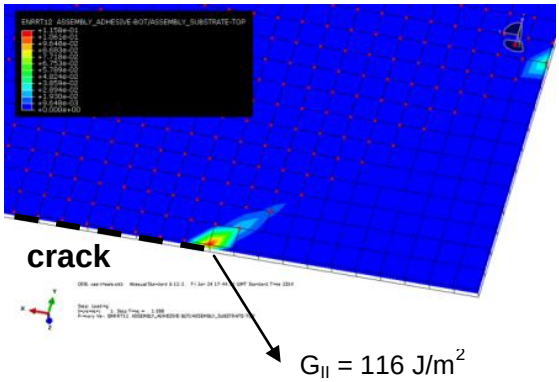

$$Mode\ ratio = \frac{G_{II}}{G_I + G_{II}} = \frac{116}{24 + 116} = 0.83$$

Figure 8-5 : Example of ‘’extraction’’ of SERR in mode I and mode II for calculation of mode ratio – case of a 19 mm substrate crack and triangular delamination

Calculation of the disbond growth rate was simplified to facilitate automation of ReSLIC. Five mode ratios were considered with 0 (pure mode I), 0.25, 0.5, 0.75 and 1 (pure mode II). However, the actual mode ratio of a node of the disbonding front may not correspond to one of these ratios. Hence, an approximation of the values is selected as illustrated in Table 8-1. A range of a particular ratio was associated to the calculated value and the disbond growth rate corresponding to that range was used to calculate the disbond advance (for example, growth rate of mixed mode ratio 0.75 covers a range of mixture ratio from 0.625 to 0.875).

Table 8-1 : Ratio range and corresponding tests results for mode mixture

Ratio range (calculated)	Ratio to use (from test)
0 Pure mode I → 0.125	0 (Pure mode I)
0.125 → 0.375	0.25
0.375 →0.625	0.5
0.625 → 0.875	0.75
0.875 → 1	1 (Pure mode II)

From the mode ratio of disbond and the total SERR, it is possible to approximate a disbond increment for each node of the disbond front. The

disbond increment is calculated according to the number of cycles ΔN necessary to grow the substrate crack of an increment $\Delta e = \Delta a_i$ on the bond face for maximum applied stresses.

In order to get an approximation of the number of cycles ΔN_i, one uses the value of K_{max} on the bond face that is directly calculated within ReSLIC. Assuming that $K_{min} = R \times K_{max}$ **(8-2)** with, in the current case R=0.1, ΔK is calculated. From that value of ΔK, the crack growth rate is extracted from the data at R = 0.1 for the substrate material. The number of cycles is then given by: $f(\Delta K) = \frac{da}{dN}\Big)_i = \frac{\Delta a_i}{\Delta N_i}$ **(8-3)** which gives, $\Delta N_i = {\Delta a_i}\Big/{\frac{da}{dN}\Big)_i}$ **(8-4)**. This approximated value of ΔN_i is then used for calculating the disbond extension.

Given a total SERR at maximum load, $G_{tot,max} = G_I + G_{II}$ **(8-5)**, and the associated mode ratio = $G_{II} / (G_I+G_{II})$, the disbond growth rate is then calculated. In fact, the results of the fatigue disbonding tests (Chapter 6) for each mixed-mode ratio can be represented by a Paris-law like relationship such as $\frac{dl}{dN}\Big)_i = A(G_{tot,max,i})^b$ **(8-6)**, with A and b being two constants that depend on the calculated mode ratio (Table 8-2).

For each node i of the disbond front, the total SERR, $G_{tot,max,i}$ is associated to a mode ratio (Table 8-1) – that corresponds to a defined Paris-law like expression – that returns a disbond growth rate $\frac{dl}{dN}\Big)_i = A(G_{tot,max,i})^b$. Hence the following relationship can be written for small increment of disbond advance:

$\frac{dl}{dN}\Big)_i = \frac{\Delta l}{\Delta N}\Big)_i \rightarrow \Delta l_i = \frac{dl}{dN}\Big)_i \times \Delta N_i$, **(8-7)** with ΔN_i calculated from the substrate crack advance on the bond face.

Table 8-2 : Fatigue disbonding growth rate parameter (Paris like parameters) obtained through fatigue disbonding tests (Chapter 6)

Mode ratio used	A	b
0 (Pure mode I)	3.0×10^{-20}	4.94
0.25	1.0×10^{-18}	4.52
0.5	2.0×10^{-29}	8.68
0.75	9.0×10^{-25}	6.79
1 (Pure mode II)	2.0×10^{-19}	4.12

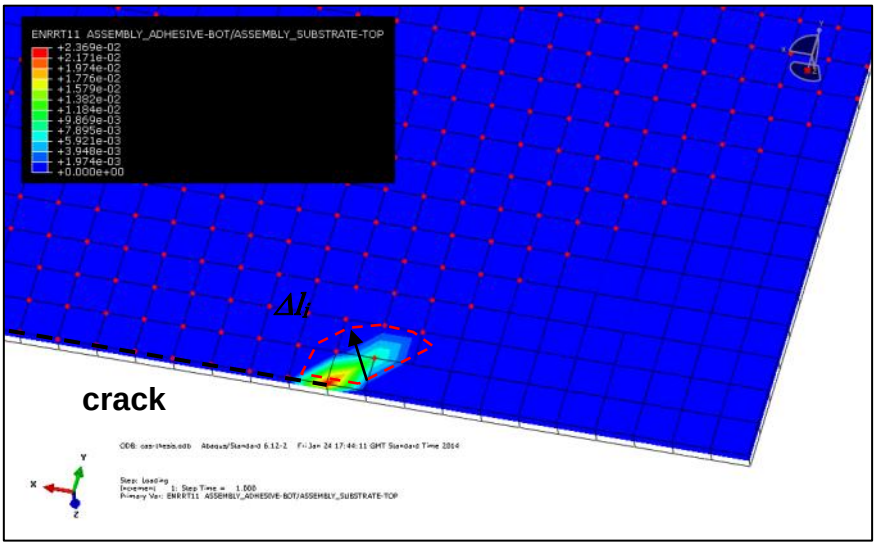

Figure 8-6 : Disbond advance showing increments of delamination for 1 node of the disbond front – here the node near the crack front will see the largest disbond increment with an increment Δl_i

The disbond increment is then compared to the element size (Δ_e) in order to determine whether or not the node belonging to the disbonding front should be released or not. If $\Delta_l > \Delta_e$, then the node becomes unbonded and if $\Delta_l < \Delta_e$, the node stays bonded (Figure 8-6).

Once all the nodes on the disbond front have been evaluated, the calculation goes to the next step iteration with an increment of the substrate crack length.

Note: the disbond advance is always based on the values of SERR at the maximum load levels as it is assumed that disbond only propagates at the maximum load.

8.2 Algorithm

The algorithm of ReSLIC is illustrated in Figure 8-7. It is defined through the following steps:

Step 1: Build the FE model: This is all performed automatically through the script. The user defines the geometry, materials and analysis parameters of the specimen.

Step2: Write the input file: Once the model is built, the input file is automatically created.

Step3: Launch the iterative calculation: ReSLIC will go through the following steps, repetitively.

1. Edit the input file with the right parameters. This edits sets of nodes that are necessary for the post-processing of the data file from the calculation. It is a necessary step for the calculation of the substrate crack stress intensity factor.
2. Submit the analysis. ReSLIC launches the calculation and waits for its completion.
3. Extract the necessary data and calculate the SIF K using the MVCCT. The loads and displacements are extracted from the substrate crack stress intensity factor using the sets previously defined and the MVCCT calculation incorporated into ReSLIC script.
4. Check whether the disbonding front should be modified or not. This goes through all nodes of the disbond front and checks for increments of the disbond front based on the levels of strain energy release rate and mode ratio as defined above.
5. Once all calculation of SIF and disbond advance are completed, the substrate crack length is incremented of one element as defined above.
6. Go back to 1.

The script will automatically stop once it has reached a certain crack length defined by the user during the early stage of the program. By the end of the calculation, it will have created two output text file giving the profile of K_{max} and

K_{min} for maximum and minimum applied stresses on both the bond face and the back face for all substrate crack length increment. All input files that contain the definition of the model and in particular the disbond front will be kept during the calculation in order to be able to monitor the disbond advance.

Note: It is assumed that prior to the computation, details of the substrate material crack growth rate and the fatigue disbond growth rate data are input (updated) into the script by the user.

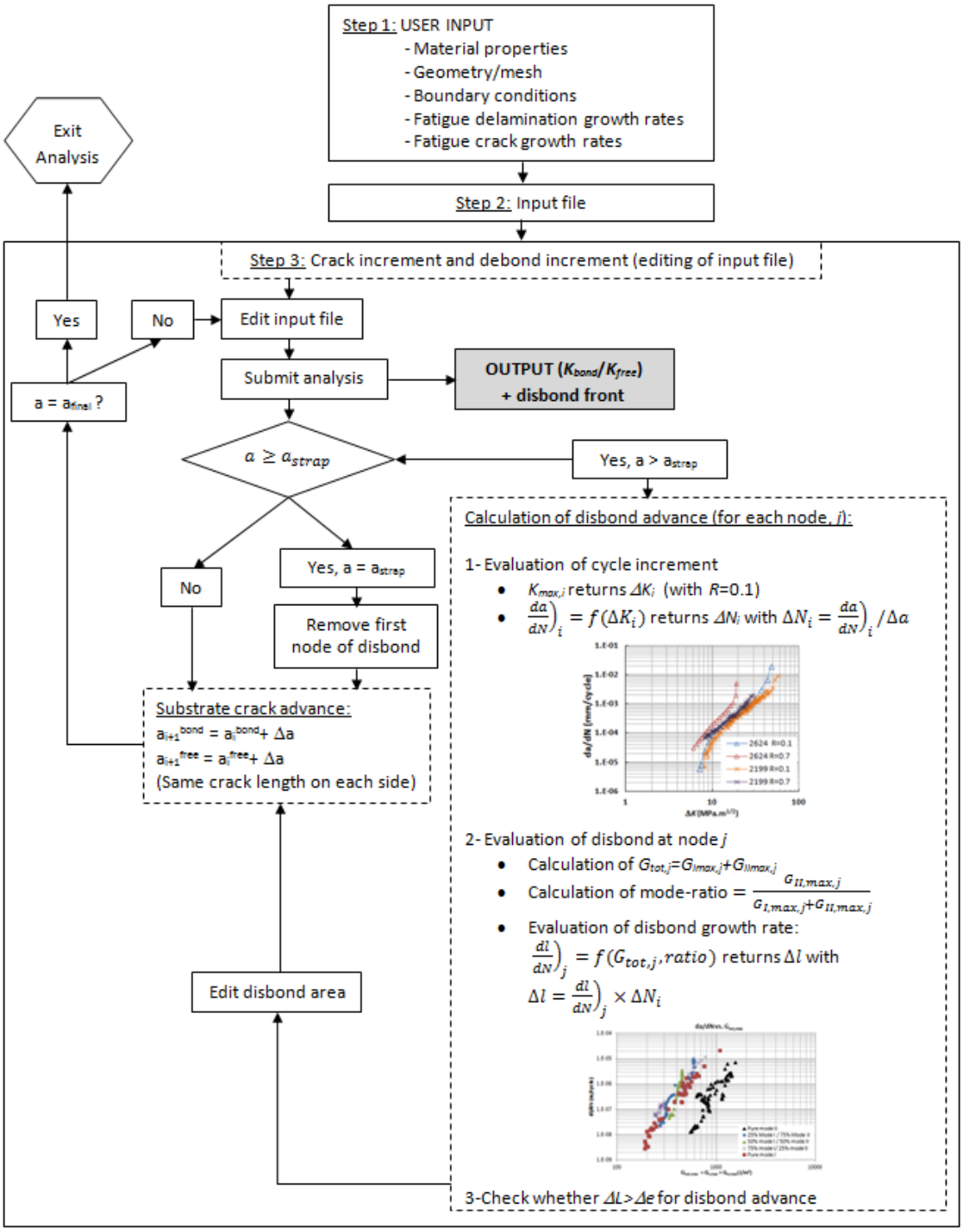

Figure 8-7 : ReSLIC algorithm

8.3 Modules

In order to complete the different steps described above, it was necessary to create different script modules allocated to a particular task of calculation as described hereafter:

- *ReSLIC.py* → main script, calls other scripts and implements the iterative calculation
- *userinput.py* → gets input of geometry, material and load conditions from the user
- *scripttobuilt.py* → computes the input file
- *calculK.py* → calculates SIF (K) by the MVCCT
- *dadNcalculation.py* → evaluates load cycle increment ΔN required for disbond advancement
- *delam.py* → calculates whether or not the disbond front will advance (contains fatigue disbond growth data obtained by tests)
- *remnode.py* → deletes the node at the disbond front if a fracture condition is satisfied

Figure 8-8 outlines the aim of each module by illustrating where each module is used in the calculation approach that was presented in Figure 8-1.

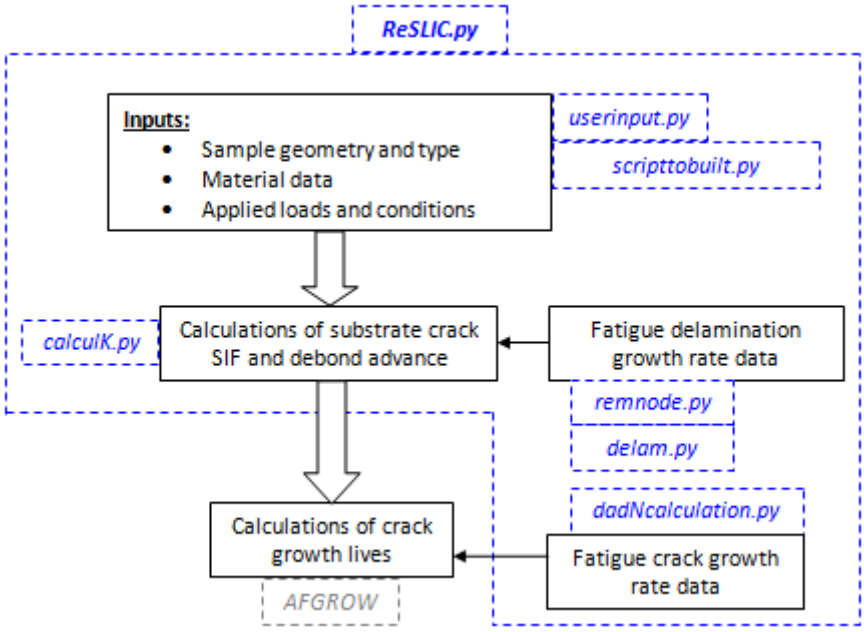

Figure 8-8: Module allocation

8.4 Outputs

The script calculates the K_{max} and K_{min} values for both the bond and back faces. Hence, one of the major outputs of this script is the *K* vs. crack length relation under maximum and minimum applied stresses. The *K* values at maximum and minimum loads determine the geometrical factor β for the particular specimen studied, including the effect of the strap as described earlier. The β factor can then be used to obtain the stress intensity factor and then evaluate the fatigue crack growth life. These results are given in the Output_'name of the specimen'.txt file that is automatically created by ReSLIC.

The user can monitor disbond growth as the substrate crack is advanced. Only the input files of the iterative calculations are kept in order to save memory. Nevertheless, it is possible to rerun any input file in case more details of the analysis are required.

8.5 Life prediction techniques

8.5.1 Fatigue life computation : AFGROW

Two methods can be used for the computation of a specimen fatigue life depending on whether the specimen is loaded under constant amplitude or variable amplitude. In the case of constant amplitude, this can be done by the integration of the material crack growth data using the stress intensity factor range ΔK and the stress ratio *R*.

For any step *i* of the integration the crack length is a_i and the stress intensity factor is $\Delta K_i = \beta_i \Delta\sigma\sqrt{\pi a_i}$ **(8-8)** with β_i the stress intensity factor coefficient than can be obtained either through an analytical solution or through finite element modeling.

For each value of ΔK_i is associated a crack growth rate $\left.{da}/{dN}\right)_i$ for a certain R-ratio, $R = \frac{\sigma_{min}}{\sigma_{max}}$ **(8-9)** according to the material law (Figure 8-9).

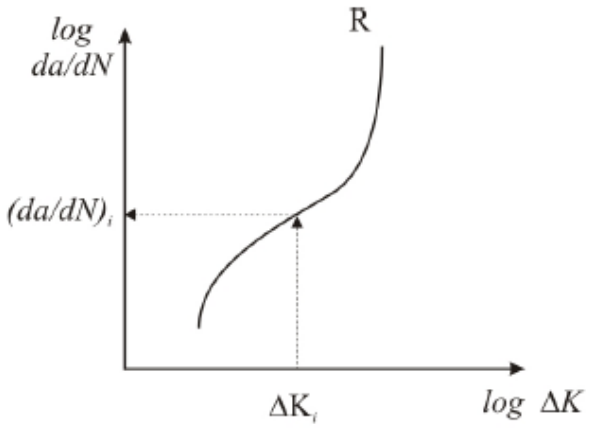

Figure 8-9 : Material law for the determination of the crack growth rate [243]

The integration step is defined as a certain number of cycles ΔN. Considering a small cycle increment, the stress intensity factor is assumed to stay constant during that increment which leads to:

$$\frac{\Delta a_i}{\Delta N} = \frac{da}{dN}\Big)_i \text{ hence } \Delta a_i = \frac{da}{dN}\Big)_i \Delta N \quad \textbf{(8-9)}$$

This leads to an increment in crack length and the total number of cycles with:

$$a_{i+1} = a_i + \Delta a_i \quad \textbf{(8-10)} \text{ and } N_{i+1} = N_i + \Delta N \quad \textbf{(8-11)}$$

The integration is finished when the structure has reached a failure condition that can be either fracture or net section yield. The integration then gives the life of the structure as *a* vs. *N* as well as *da/dN* vs *a*.

For the case of variable amplitude, AFGROW software package is used in order to compute the fatigue life of the specimen over the spectrum.

AFGROW is a commercial product that performs cycle by cycle computation of the fatigue life of a specimen. It can be used for both pre-defined geometries as well as calculated solution when the geometry is not found in the cases library. It features several material models for the description of the fatigue laws as well as several retardation models.

AFGROW offers different solutions to characterise material crack growth data. The first is the Forman equation [46], [47]. The equation parameters are defined

by the user (C and m are parameters found from curve fitting). The crack growth data can be described with up to 3 segments.

$$\frac{da}{dN} = \frac{C\Delta K^m}{(1-R)K_C - \Delta K} \textbf{ (8-12)}$$

A second option is through the Harter T-method [49]. In that case a series of crack growth rates are chosen by the user in a tabular database and the Harter T-method is then used for data interpolation.

The Walker equation is another material model [45] where n represents the slope of the crack growth rate data and m is a non-dimensional constant with no physical meaning.

$$\frac{da}{dN} = C\left[\Delta K(1-R)^{(m-1)}\right]^n \textbf{ (8-13)}$$

It controls the shift of the crack growth rate depending on the R-ratio of the data. The Walker equation is used to represent the R-ratio effect and to interpolate or extrapolate any missing data.

The third equation is the NASGRO equation [46], [48]. A materials database with NASGRO equation constants is directly available and the user has the possibility to modify the parameters that define the NASGRO equation. Details of that equation were outlined in paragraph **2.3.3.** .

$$\frac{da}{dN} = C\left[\left(\frac{1-f}{1-R}\right)\Delta K\right]^n \frac{\left(1-\frac{\Delta K_{th}}{\Delta K}\right)^p}{\left(1-\frac{K_{max}}{K_{crit}}\right)^q} \textbf{ (8-14)}$$

Fatigue crack growth data can also be entered using the Tabular Look-Up method.

In the present case, AFGROW code was used for both constant and variable amplitude load case with the Tabular Look-Up material model. Two data-set of the 2024 HDT material for R = 0.1 and R = 0.5 were used. Because BCR geometries are not within AFGROW's geometry library, the stress intensity factor coefficient β has to be input for 25 crack length cases (limit of 25 input

values). All influences of the strap are incorporated into the β values, such as the out-of-plane bending effect and the stiffness ratio. Despite one single value of b through the thickness (2D approach), this incorporates all 3D effect as the non-symmetry of the β values from the reinforced side and the free one are considered in those single values. Other inputs are the equivalent residual stress intensity factor $K_{res,eq}$, R-ratio and applied stresses. AFGROW then performs the integration of the material model chosen, based on β values and fatigue crack growth rates values.

8.5.2 Non-linear effects

As stated above, AFGROW deduces the stress intensity factor range ΔK necessary to the calculation of the fatigue life from the stress intensity factor coefficient β it is given as well as the other inputs. Hence one of the difficulties is to define these values of β for each single value of crack lengths.

In cases where the behaviour is **geometrically linear**, only one calculation is necessary in order to calculate the β factors i.e. at maximum load. The stress intensity factor range is then deduced using the R-ratio applied by $\Delta K = (1 - R)K_{max}$ **(8-15)** with R defined as $R = \frac{\sigma_{min}}{\sigma_{max}} = \frac{K_{min}}{K_{max}}$ **(8-16)**. The β factors can then be used in AFGROW.

In cases where the behaviour is **geometrically non-linear**, the relations are no longer valid, $R = \frac{\sigma_{min}}{\sigma_{max}} \neq \frac{K_{min}}{K_{max}}$. Hence the calculations need to be performed at both maximum and minimum loads in order to deduce the R-ratio for individual crack lengths as well as ΔK that will give the β coefficient.

Due to the secondary bending caused by the single sided reinforcement, the bonded crack retarder configuration is geometrically non-linear. In addition, the main difficulty for single sided reinforcement as found in BCR is the fact that this values of K_{max} and K_{min} are obtained for the bond face and the back face of the substrate crack as follows:

$$K_{bond,max} = K_{bond,applied\ load\ (Fmax)} + K_{bond,Residual\ stresses} \quad \textbf{(8-17)}$$

$$K_{bond,min} = K_{bond,applied\ load\ (Fmin)} + K_{bond,Residual\ stresses}$$ **(8-18)**

$$K_{back,max} = K_{back,applied\ load\ (Fmax)} + K_{back,Residual\ stresses}$$ **(8-19)**

$$K_{back,min} = K_{back,applied\ load\ (Fmin)} + K_{back,Residual\ stresses}$$ **(8-20)**

Hence, one needs to derive one single value of β out of these 4 values of stress intensity factor and extract the equivalent residual stress intensity factor $K_{res,eq}$.

8.5.3 Derivation of β values for BCR

The solutions that can be considered in order to calculate a single value of β are the mean value, $\beta_{mean} = \frac{(\beta_{bond}+\beta_{back})}{2}$ **(8-21)** or the root mean square, $\beta_{RMS} = \sqrt{\frac{\beta_{bond}^2+\beta_{back}^2}{2}}$ **(8-22)**. Nevertheless, those solutions will not consider the effect that the single sided reinforcement has on the crack front, with the crack growing faster on one side than the other [5]. Also, it will be difficult to consider the non-linearity of the current problem. The method adopted here in order to calculate a single value of β through the thickness uses the "alternate analysis" described in [50], [103], [104] as well as the weighted average as described by Hosseini-Toudeshky [90]. The stages of the method are described here:

Stage 1:

The 3D quasi-static FE calculations are performed at maximum and minimum load with both taking into account the residual stresses due to the bonding process. This is performed through ReSLIC iterative calculations. The results obtained from this first stage are the 4 values of stress intensity factors, two for the bond face (max and min loads) and two for the back face (max and min loads) as defined above.

The alternative solution uses a weighted average between the bond face and the back face as the one developed by Hosseini-Toudeshky et Al. [90]. In their work, they studied the effects of 3D simulations of the crack front between a curved crack front and a straight one. They showed that the curved crack front could be approximated with a straight crack front using one single value of the

stress intensity factor at a particular position across the thickness of the specimen. For thin plates, $\frac{t_p}{2W} < 0.05$ (t_p being the reinforced plate thickness and w the width of the reinforced specimen), they showed that this particular position was given by $\frac{Z_e}{t_p} = \left[0.0166 \times \left(\frac{E_{Al}}{Ereinf.}\right) + 0.3453\right]$ **(8-23)**, with Z_e, the position across the plate thickness, from the back side, E_{Al}, the plate Young's modulus and $E_{reinf.}$ the reinforcement Young's modulus. This gives a ratio of 0.36 in the case studied here, which means that the most representative value of the stress intensity factor is closer to the back side. That is why the proportion of each side has been distributed as 36% from the bond side and 64% from the back side. Hence their formulation takes into account the imbalance of stress intensity factor from the bond face to the back face due to the presence of the strap and reduces it to one single value.

Hence, for the present case, the weighted value of the stress intensity factor coefficient is given by $\beta_{weighted} = 0.36 \times \beta_{bond} + 0.64 \times \beta_{back}$ **(8-24)** or in terms of stress intensity factors, $K_{weighted} = 0.36 \times K_{bond} + 0.64 \times K_{back}$ **(8-25)** and that for maximum and minimum loads.

Using Hosseini-Toudeshky formulation, it is then possible to deduce a weighted value of the stress intensity factor for both applied load case. In fact, the value of $K_{max}$and K_{min} given above can be obtained for the bond face and the back face as illustrated here after.

	Max stress	**Min stress**
Bond face	$K_{bond,max}$	$K_{bond,min}$
Back face	$K_{back,max}$	$K_{back,min}$
Weighted value	$K_{max,weighted} = 0.36 \times K_{bond,max} + 0.64 \times K_{back,max}$ **(8-26)**	$K_{min,weighted} = 0.36 \times K_{bond,min} + 0.64 \times K_{back,min}$ **(8-27)**

Hence $K_{max,weighted}$ and $K_{min,weighted}$ can be directly calculated from the results of the simulation at maximum and minimum loads as performed through ReSLIC.

Stage 2:

An effective stress intensity factor range and an effective R-ratio are then deduced from these two values of stress intensity factor at maximum and minimum stress:

$\Delta K_{eff} = K_{max,weighted} - K_{min,weighted}$ **(8-28)** and $R_{eff} = \frac{K_{min}}{K_{max}} \neq \frac{\sigma_{min}}{\sigma_{max}}$ **(8-29)**

Stage 3:

A single value of β, parameter necessary for the AFGROW computation is deduced from the previous expressions with: $\beta_{eff} = \frac{\Delta K_{eff}}{\Delta\sigma\sqrt{\pi a}}$ **(8-30)**.

This represents a weighted effective stress intensity factor coefficient that takes into account the geometrical non-linearity of the problem as well as the asymmetry of the crack front.

AFGROW does not allow the direct input of the effective R-ratio, R_{eff}. An alternative solution is the input of an equivalent residual stress intensity factor K_{eq}^{res} which is defined as $K_{eq}^{res} = \frac{\frac{\Delta K}{1-R}\left(R_{eff}-R\right)}{1-R_{eff}}$ **(8-31)** where $\Delta K = K_{applied\ load\ (Fmax)} - K_{applied\ load\ (Fmin)}$ **(8-32)**, $R_{eff} = \frac{K_{min}}{K_{max}}$ **(8-33)** with K_{max} and K_{min} defined above and $R = \frac{K_{applied\ load\ (Fmin)}}{K_{applied\ load\ (Fmax)}}$ **(8-34)** with $K_{applied\ load\ (Fmax)}$ and $K_{applied\ load\ (Fmax)}$ the stress intensity factors for the applied loads only. Details of the calculation of K_{eq}^{res} are given in **Appendix B**. By its definition, K_{eq}^{res} considers both the effect of thermal residual stresses and non-linearity.

Hence, the calculation of β is derived from the ReSLIC computation that returns the value of $K_{bond,max}$, $K_{bond,min}$, $K_{back,max}$ and $K_{back,min}$

The life prediction is then calculated from the integration of the material data performed directly in AFGROW for the constant and variable amplitude cases. The parameters that are required in AFGROW are the geometry of the specimen, the stress intensity factor coefficients β, the equivalent residual stress intensity factors and the loading spectrum. In the case of variable amplitude, parameters corresponding to the retardation effects can also be implemented in the code.

Chapitre 9 : ReSLIC validation

9.1 Mesh convergence study

A mesh convergence study on a non-reinforced M(T) specimen was performed.

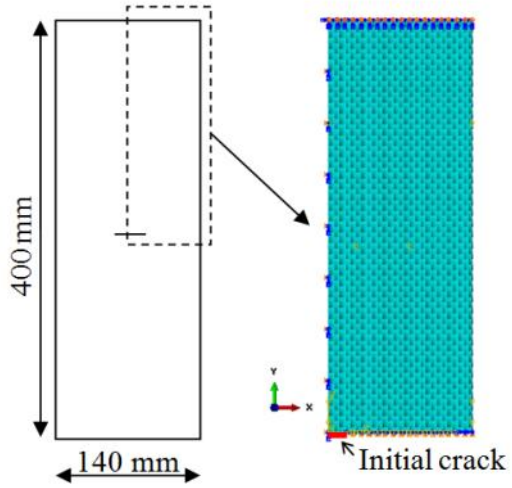

Figure 9-1 : Plain sample geometry and ¼ of model

The convergence M(T) sample was 400 mm long, 140 mm wide and 5 mm thick. 3D continuum shell elements (SC8R) were used to model a quarter of the specimen, using the appropriate boundary conditions (Figure 9-1). A regular mesh was used over the whole ¼ specimen. 4 mesh sizes were studied with 5 mm, 2.5 mm, 1 mm and 0.5 mm. There was only one element through the thickness. 12 half crack lengths cases from 10 mm to 65 mm were used.

The MVCCT [42] was used to calculate the stress intensity factor and then used to estimate the stress intensity factor coefficient β. Results of the FE analysis were compared to the analytical solution of the stress intensity factor coefficient given by $\beta = \frac{1}{\sqrt{cos\left(\frac{\pi a}{2b}\right)}}$ **(9-1)** for a plain M(T) specimen.

Figure 9-2 shows the results of the stress intensity factor coefficient β obtained for 4 different mesh sizes comparing them to the analytical solution.

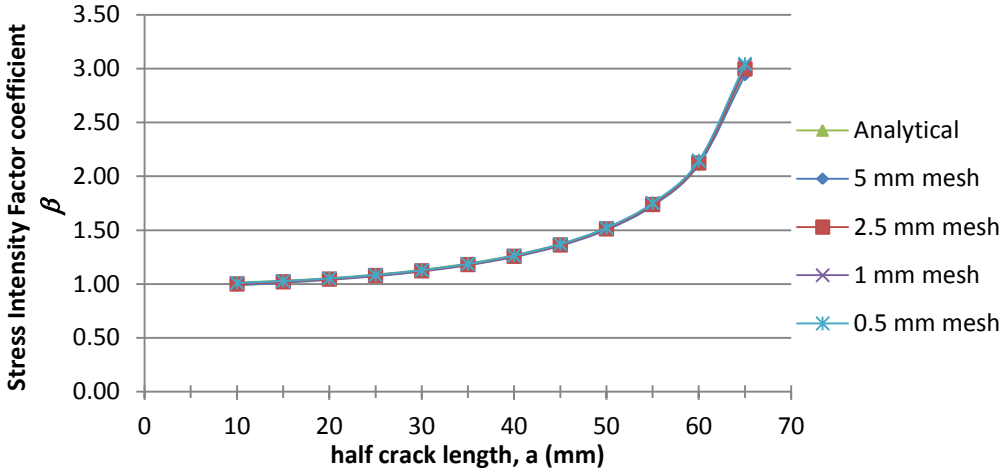

Figure 9-2 : Mesh convergence for β solution – Unreinforced M(T)

Figure 9-3 shows the error in the β solution compared to the analytical solution. The error is defined as: $error = \frac{FEM-analytical}{FEM}$ **(9-2)**.

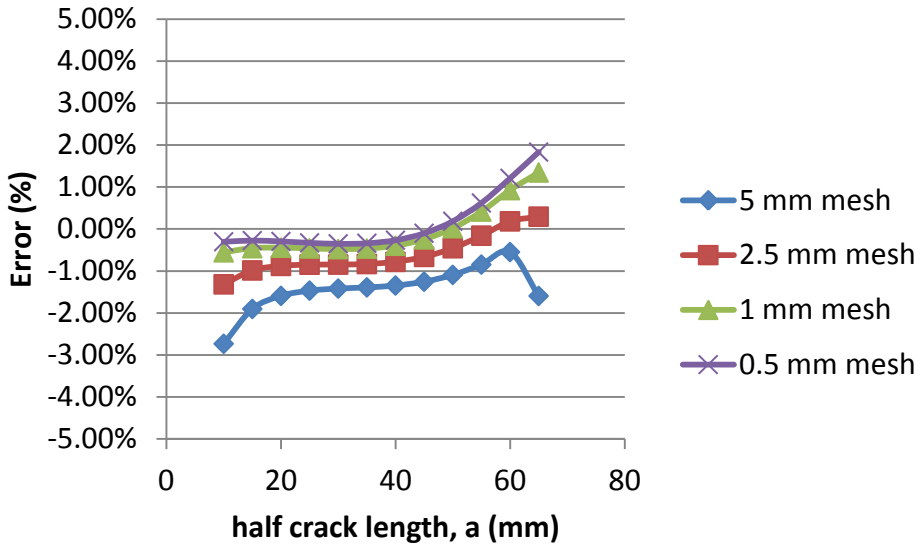

Figure 9-3 : Prediction error for stress intensity factor β

The model is not highly mesh dependent as the error for all four mesh sizes was less than 3%. For half crack length from 10 to 50 mm, the error is minimal for the 0.5 mm mesh with less than 1%. A mesh size of 0.5 mm was used for all the analyses.

9.2 Fatigue life prediction using ReSLIC : comparison with experimental data

The ReSLIC finite element package was used to calculate the stress intensity factor (SIF) solution at maximum (K_{max}) and minimum loads (K_{min}) for different M(T) test coupon designs, followed by life prediction. The life prediction is first given for a baseline M(T) specimen and then for two reinforced coupons.

9.2.1 Unreinforced M(T) specimen

This case considers a non-reinforced M(T) coupon made of aluminium 2624-T351, tested under constant amplitude loading. The results of the stress intensity computation are shown in figure 9-2 above. Figure 9-4 shows the result of the AFGROW life calculation together with data from experiments.

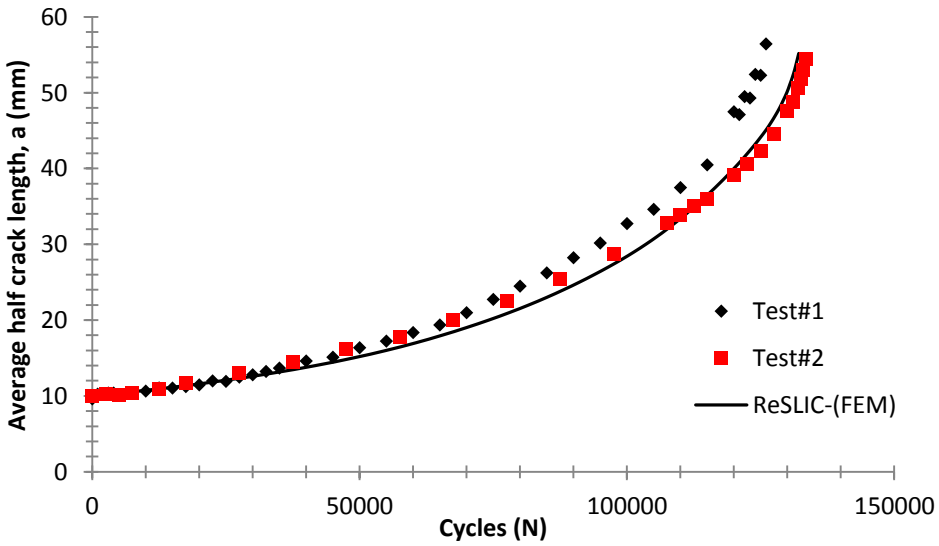

Figure 9-4 : Fatigue life prediction for unreinforced specimen

It shows a very good agreement between the test and the prediction. Table 9-1 shows the quantitative data together with the error $= [N_{FEM}-N_{test}]/N_{test}$ **(9-3)**.

Table 9-1 : Prediction error for fatigue life of plain specimen

Specimen	Life	Error
Test#1	126000	N/A
Test#2	133861	N/A
Prediction - plain	132145	1.70%

Hence there is good agreement between predicted values and measured one for the method employed here in terms of prediction of the fatigue life as the error between, the prediction and the test (average of two tests considered) is 1.70%.

9.2.2 AIRstream reinforced M(T) coupons

The AIRstream reinforced M(T) coupons were described in detail in Chapter 0. The simulations were run with a maximum stress of 60 MPa in the total cross section (substrate + reinforcement).

Figure 9-5 illustrates ΔK_{eff} as a function of half crack length *a* for the bond face and back face of the sample. Stress intensity factor ranges for an unstrapped sample are also shown (*baseline*) for comparison.

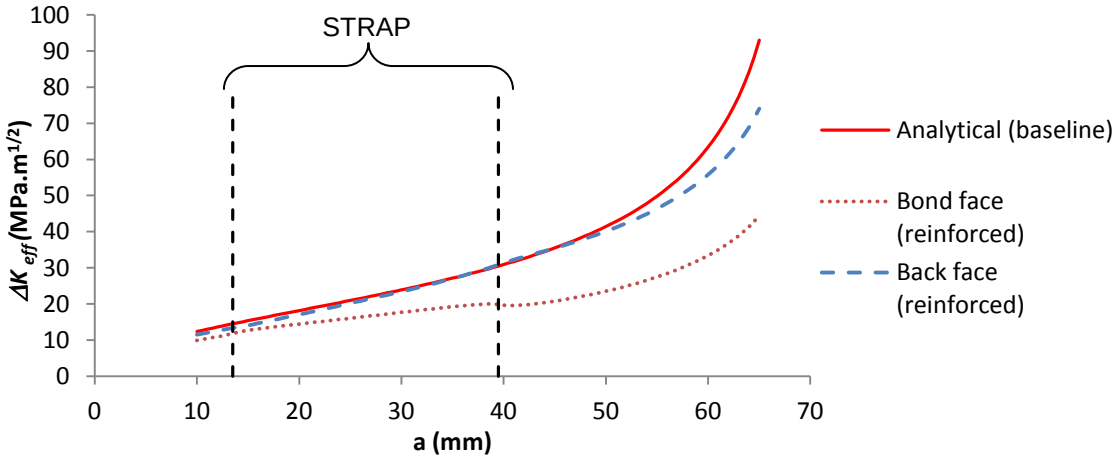

Figure 9-5 : Bond and back face effective stress intensity range for AIRstream reinforced M(T) specimen under an external stress of 60 MPa on full cross section

Figure 9-5 shows the ΔK_{eff} values on the bond side are always lower than the baseline unstrapped value. This is the effect of bridging reducing crack opening on that side. On the back side, the values of ΔK_{eff} are smaller than the ones for the unstrapped sample up to a crack length of approximately 25 mm where the values become equal and larger than the baseline solution. This is attributed to the secondary bending (due to a shift in neutral axis) promoting crack opening on the back side. It then becomes smaller than the baseline solution for an

approximate crack length of 48 mm. A change in ΔK_{eff} on the bond side is observed as the crack exits the strapped area.

The difference in ΔK_{eff} between the two sides is partly attributed to the secondary bending that increases the stresses on the back side and lowers them on the bond side relative to the nominal stresses (a detailed analysis of that phenomenon is highlighted in the next chapter). As the difference in ΔK_{eff} values increases with the crack length, this indicates that the secondary bending effect increases with the crack length. The difference is also due to the crack bridging effect due to the presence of the strap.

As explained in Chapter 8, only one value of ΔK_{eff} is used in order to get the β_{eff} function of the specimen that is then used in AFGROW. This was produced by the weighted average of the bond and back face values at maximum ($K_{max,weighted} = 0.36 \times K_{bond,max} + 0.64 \times K_{back,max}$) **(9-4)** and minimum ($K_{min,weighted} = 0.36 \times K_{bond,min} + 0.64 \times K_{back,min}$) **(9-5)** stress levels and then computing the range of these averages in order to obtain a weighted effective value of the stress intensity factor range ΔK_{eff} ($\Delta K_{eff} = K_{max,weighted} - K_{min,weighted}$) **(9-6)**. β_{eff} is then deduced from that value. Figure 9-6 shows the results of that calculation with the values of ΔK_{eff} for the un-strapped case.

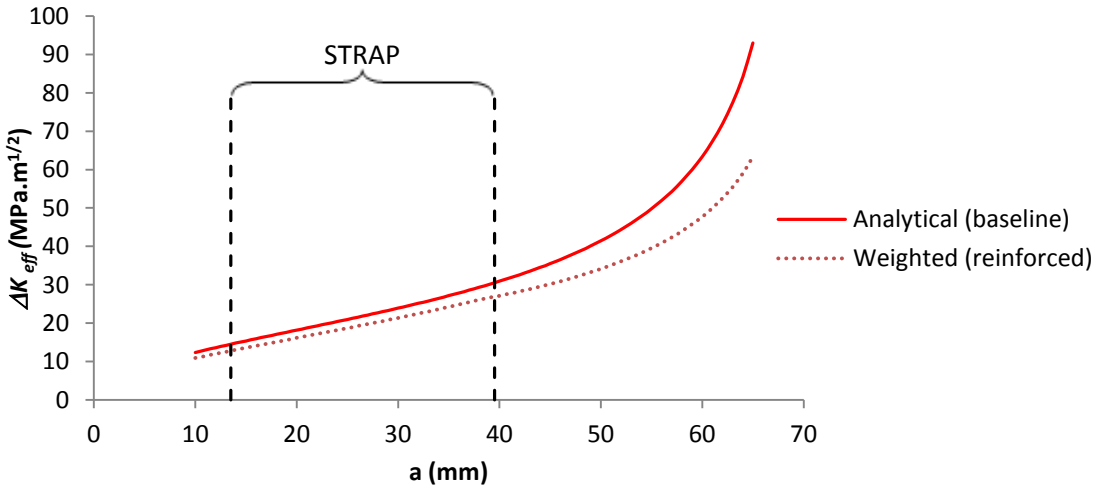

Figure 9-6 : Weighted average solution for ΔK_{eff} in AIRstream reinforced M(T) specimen

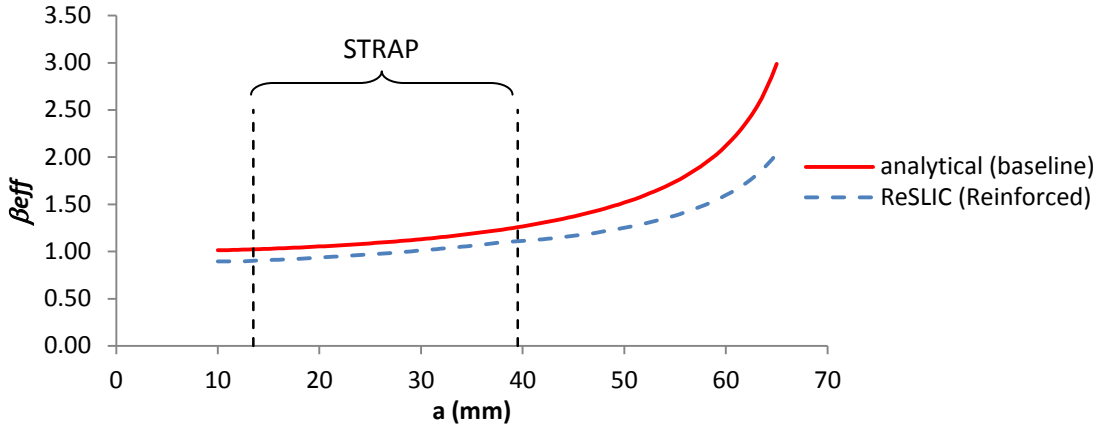

Figure 9-7 : Weighted Average for βeff in AIRstream reinforced M(T) specimen

Figure 9-6 and Figure 9-7 show that the weighted values of ΔK_{eff} and β_{eff} at all crack length are lower than the baseline solution due to the effect of the strap. In order to run the predictions in AFGROW, 25 values of β_{eff} are extracted from Figure 9-7 together with the corresponding values of K_{eq}^{res}.

- Adhesive disbonding advance

The simulation showed no disbond between the strap and the substrate as illustrated in Figure 9-8. The disbond was restricted to the 1 element disbond as imposed during the simulation that ought to reproduce the effect of the disbond initiation as well as the advance of the substrate crack at the interface.

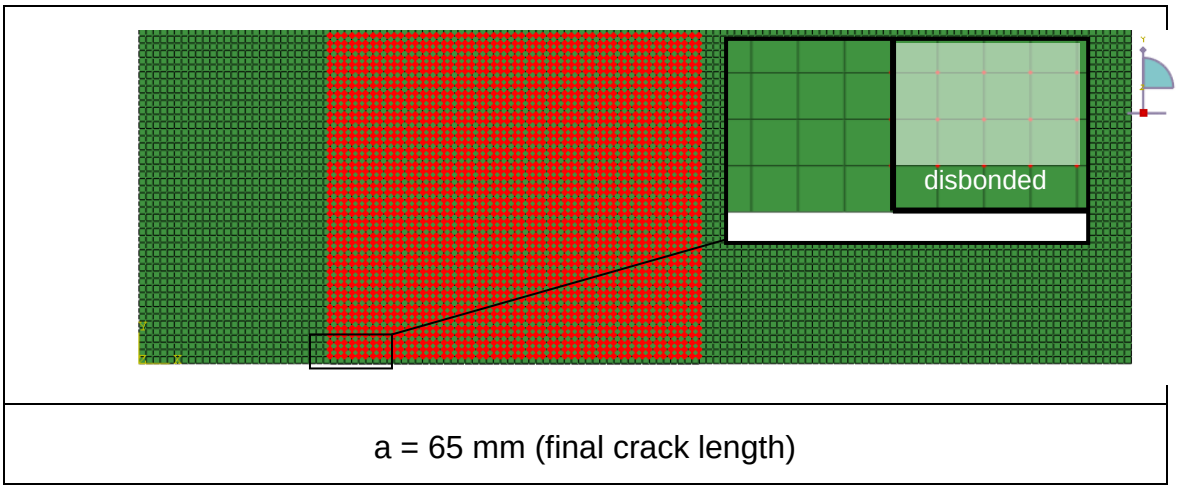

Figure 9-8 : Fatigue disbonding advance for AIRstream reinforced M(T) specimen – top view of model for final crack of 65 mm

The reasons for the disbond not to progress can be explained by the values of strain energy release rate at the early stage of disbonding and in the one

element initial delamination that are much smaller than what is required to grow the delamination. In fact, the mode I strain energy release rate calculated was of the order of 10 to 20 J/m^2 and for the mode II they were of the order of 100 J/m^2, which is much smaller than what has been measured during the fatigue delamination tests (minimum of 200 J/m^2 for mode I and 600 J/m^2 for mode II). Hence the levels of strain energy release rate are too small for disbond propagation based on this initiation criterion.

Figure 9-9 shows the C-scan of sample MTR2 reported in Chapter 5 - and simulated here - after fatigue testing under constant amplitude loading (124,651 cycles) showing no disbond. Yellow areas near the strap are resin-rich areas.

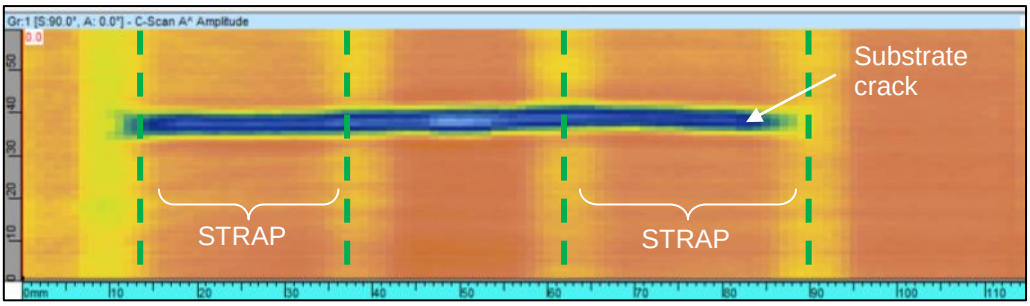

Figure 9-9 : Ultrasound C-SCAN of AIRstream reinforced M(T) specimen during testing under constant amplitude loading (a =37 mm) showing no disbond.

Hence the FE computations showed the same results as the tests with no disbonding observed.

Using the β_{eff} factors shown in Figure 9-7, the life of the M(T) specimens tested was predicted using the AFGROW package for a constant amplitude case with a nominal stress of 60 MPa and a R-ratio of 0.1.

- Fatigue Life predictions under **constant amplitude loading**

The simulation used the weighted stress intensity factor coefficient β_{eff} as illustrated in Figure 9-7 . Figure 9-10 and Figure 9-11 illustrates the values of the effective R-ratio and the equivalent residual stress obtained through the ReSLIC computation. $K_{res,eq}$ is directly input into AFGROW as a mean to take into account the effective R-ratio [50].

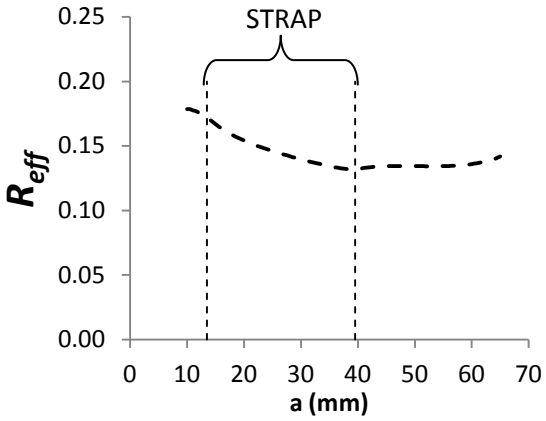

Figure 9-10 : Effective stress ratio

$R_{eff} = K_{max,weighted}/K_{min,\ weighted}$

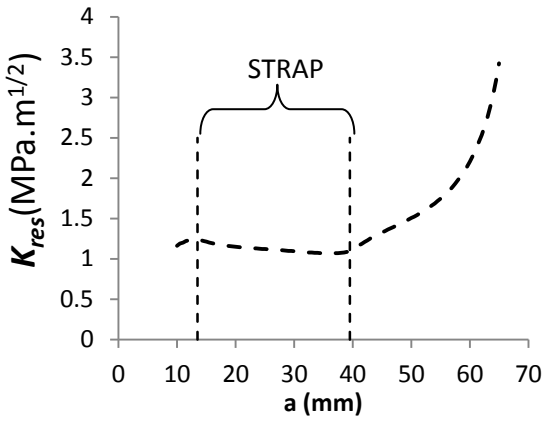

Figure 9-11 : Equivalent residual stress intensity factor (calculated)

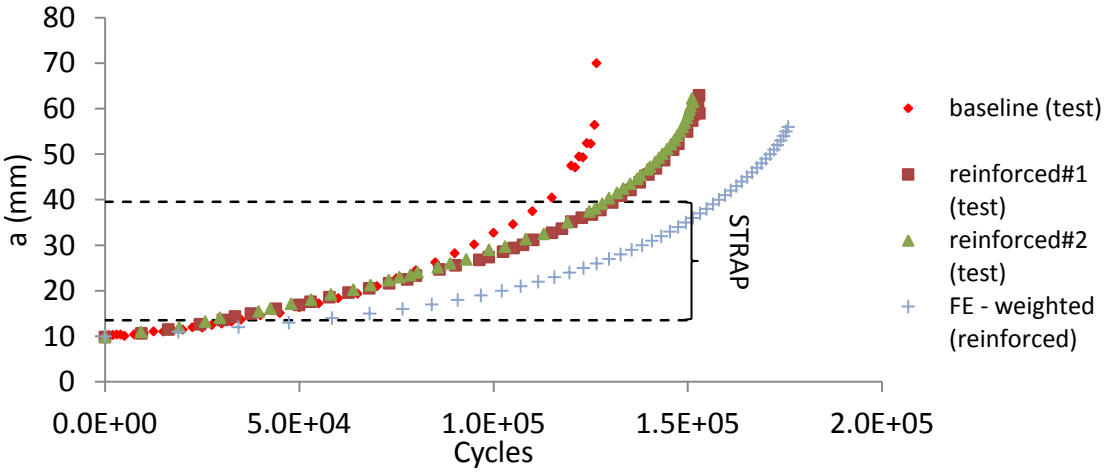

Figure 9-12 : Fatigue life prediction for CONSTANT AMPLITUDE test – AIRstream reinforced M(T) specimen - σ_{max} = 60 MPa (nominal), R = 0.1

Table 9-2 : Error on calculation of life – constant amplitude life predictions

Specimen/Simulation	Number of cycles	Error (%) for simulation
Test – reinforced#1	151,500	+16%
Test – reinforced#2	152,990	+15%
Weighted value simulation	175,839	N/A

Figure 9-12 shows the predicted crack length vs. cycles curve for the strapped sample under constant amplitude loading with a final life of 175,839 cycles for

the reinforced M(T) sample. The error, as reported in Table 9-2 is within 16%. The results show that the prediction is always lower in terms of the crack length for a given number of cycles and the difference appears very early in the predictions before the crack has entered the strapped area.

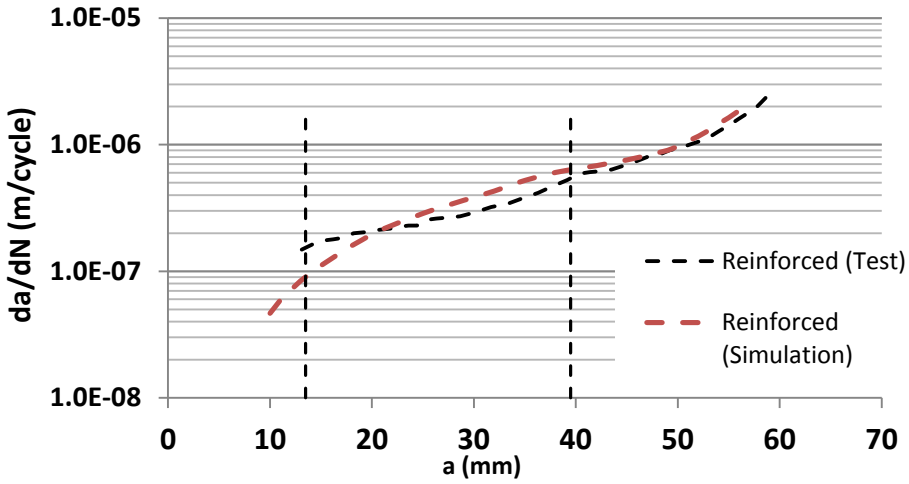

Figure 9-13 : Fatigue crack growth rate prediction for CONSTANT AMPLITUDE test – AIRstream reinforced M(T) specimens - σ_{max} = 60 MPa (nominal), R = 0.1

Figure 9-13 shows the predicted fatigue crack growth rate in comparison with the fatigue crack growth rate obtained from experiment. There is good agreement between the two. From 10 mm up to 20 mm, the predicted growth rate is lower than the measured one. Past the crack length of 20 mm the prediction is faster than the measure data.

9.2.3 BCR M(T) coupons

- Geometry and material

Specimens from the earlier BCR programme were made of aluminium 7085 – T7651 substrate reinforced with Glare1-3/2 (0.4) straps. The substrate was 400 mm long, 140 mm wide and 10 mm thick. The straps were 180 mm long, 20 mm wide and each strap consisted of two straps of GLARE 3/2 bonded together to reach a total thickness of 3.6 mm (= 2 x 1.8 mm). They were located 13.5 mm from the centre of the specimen. The straps were bonded to the substrate using FM94 epoxy adhesive (Figure 9-14). The initial crack length was 8 mm. The coupon was tested with a maximum applied stress of 60 MPa on the total cross section. The sample geometry is shown in Figure 9-14.

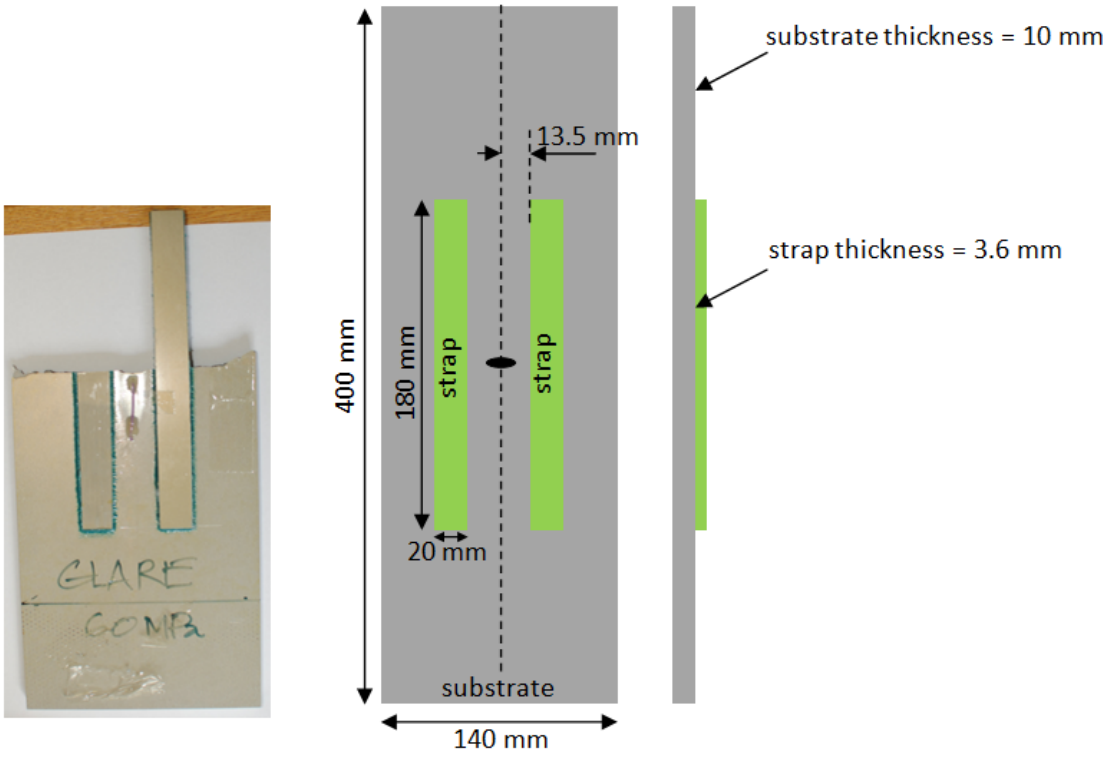

Figure 9-14 : Reinforced M(T) specimen from the BCR programme showing specimen after failure and geometry

- Stress intensity calculations for the strapped BCR sample

Figure 9-15 illustrates the variation of ΔK_{eff} as a function of half crack length *a* for the bond face and back face of the sample. Stress intensity ranges for an unstrapped sample is also shown (*baseline*) for means of comparison.

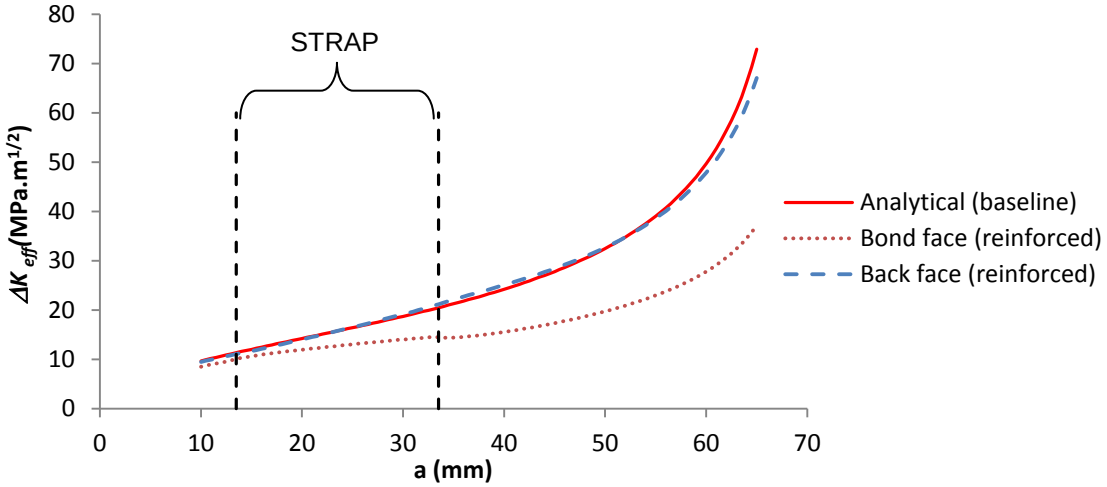

Figure 9-15 : Bond and back face effective stress intensity range for BCR reinforced M(T) specimen under an external stress range of 60 MPa on substrate section

The ΔK_{eff} values on the back side are almost the same as the non-reinforced case. On the bond side the values of ΔK_{eff} are significantly reduced compared with the baseline and the back face ΔK_{eff} values. The reduction in ΔK_{eff} is attributed to the effect of the strap.

Figure 9-16 gives the results for a weighted value of ΔK_{eff} as described in the previous example. These values are then normalized in order to get the stress intensity factor coefficient β_{eff} that is used in AFGROW. The weighted values of ΔK_{eff} show reduced values when compared to the baseline. The normalized values of β_{eff} used in AFGROW are shown in Figure 9-17.

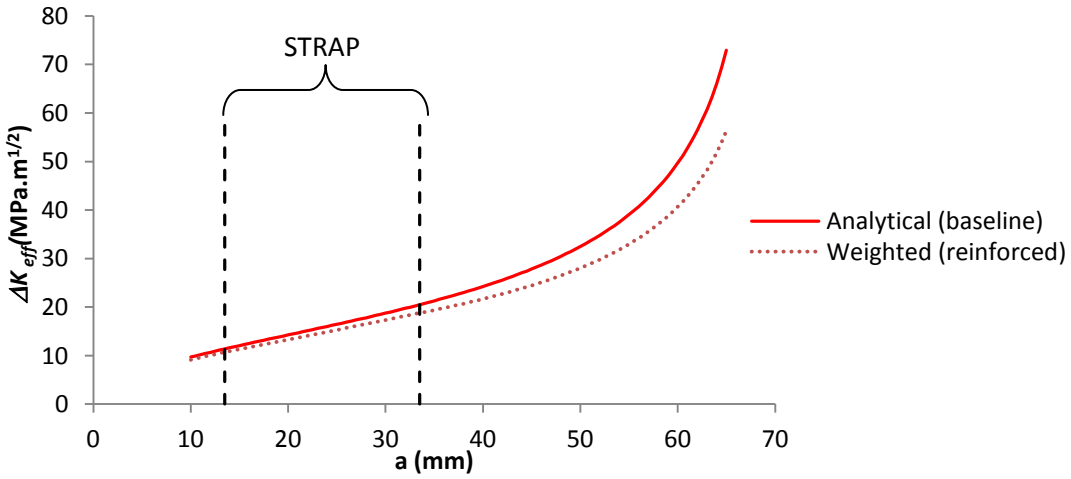

Figure 9-16 : Weighted average solution for ΔK_{eff} in BCR reinforced M(T) specimen

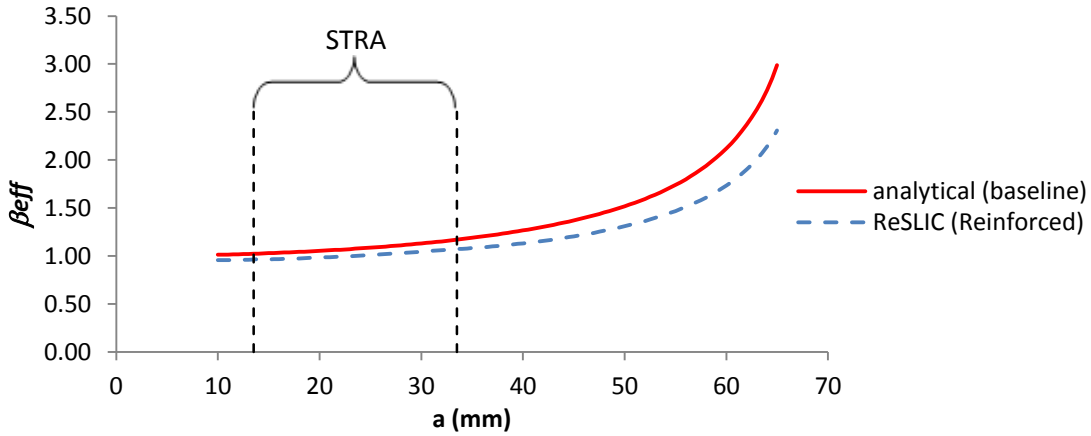

Figure 9-17 : Weighted Average for β_{eff} in BCR reinforced M(T) specimen

- Adhesive disbonding advance

Figure 9-18 shows that no disbonding was predicted in the calculation. The disbonding is restricted to one element in size and corresponds to the assumed disbonding for initiation.

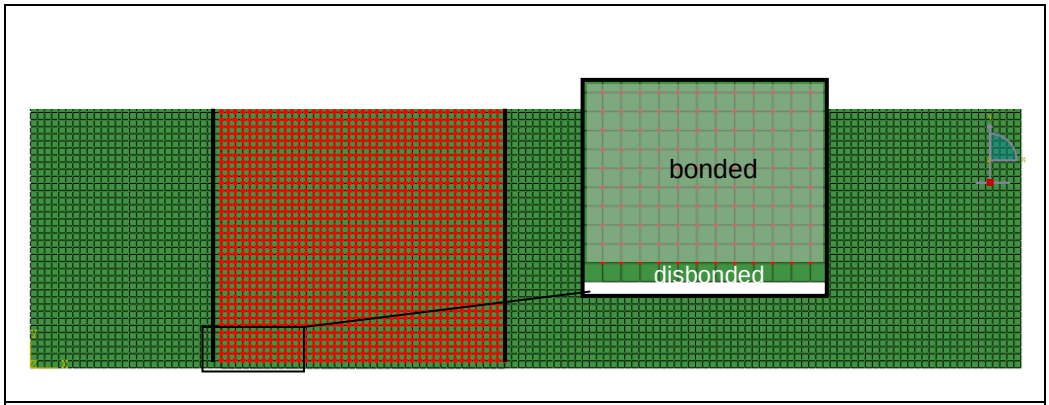

Figure 9-18 : Fatigue disbonding advance for BCR reinforced M(T) specimen – top view of model for final crack of 65 mm

No data was available to make a comparison for this specific type of specimen.

- Life predictions

The life prediction for the BCR geometries obtained from the AFGROW computation using ReSLIC β_{eff} results is compared to the test results reported in [5]. The stress used for the simulation was 54.4 MPa as the stress used for the

BCR tests was 60 MPa but with no consideration of the additional cross section due to the presence of the straps.

As for the AIRstream case, the simulation used the equivalent residual stresses. Figure 9-19 and Figure 9-20 describe the effective R-ratio and the equivalent residual stresses. K_{res} is directly input into AFGROW as a mean to take into account the effective R-ratio [50].

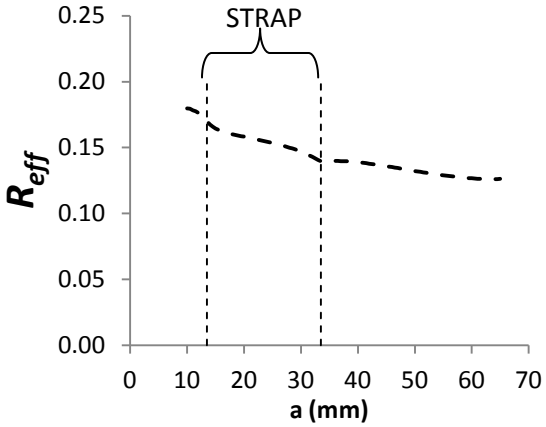

Figure 9-19 : Effective stress ratio

$R_{eff} = K_{max,weighted}/K_{min,\ weighted}$

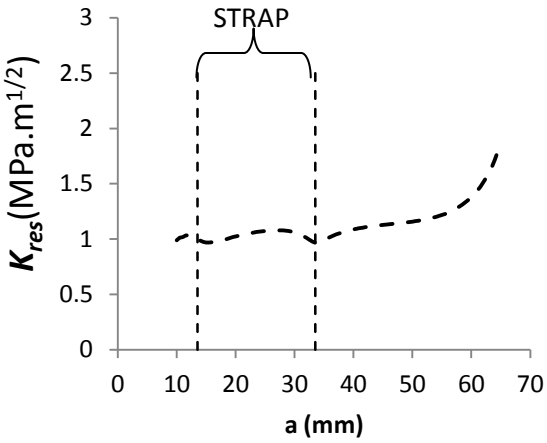

Figure 9-20 : Equivalent residual stress intensity factor

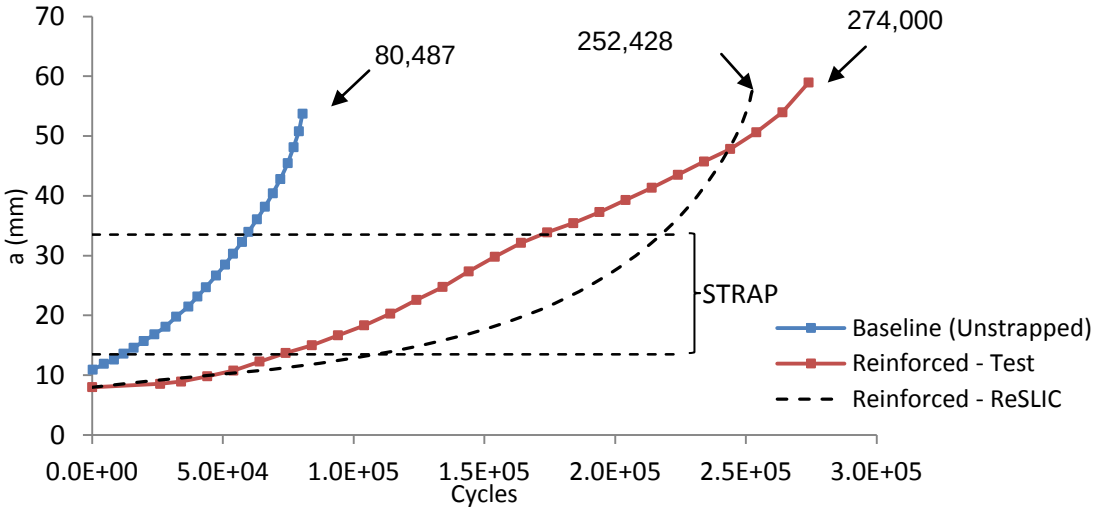

Figure 9-21 : Fatigue crack length vs. cycles prediction for CONSTANT AMPLITUDE test – BCR reinforced M(T) specimen - σ_{max} = 54.4 MPa, R = 0.1

Table 9-3 : Error on calculation of life – constant amplitude life predictions

Specimen/Simulation	Number of cycles	Error (%) for simulation
BCR1-BASELINE	80,487	N/A
BCR1-REINFORCED	274,000	N/A
BCR1-ReSLIC (reinforced)	252,428	-8%

Figure 9-21 shows that ReSLIC under predicts life in comparison to the tests. It predicted a life of 252,428 cycles while the test lasted 274,000 cycles. The prediction error is 8% (Table 9-3). The trend of the predicted life demonstrates large differences from the test.

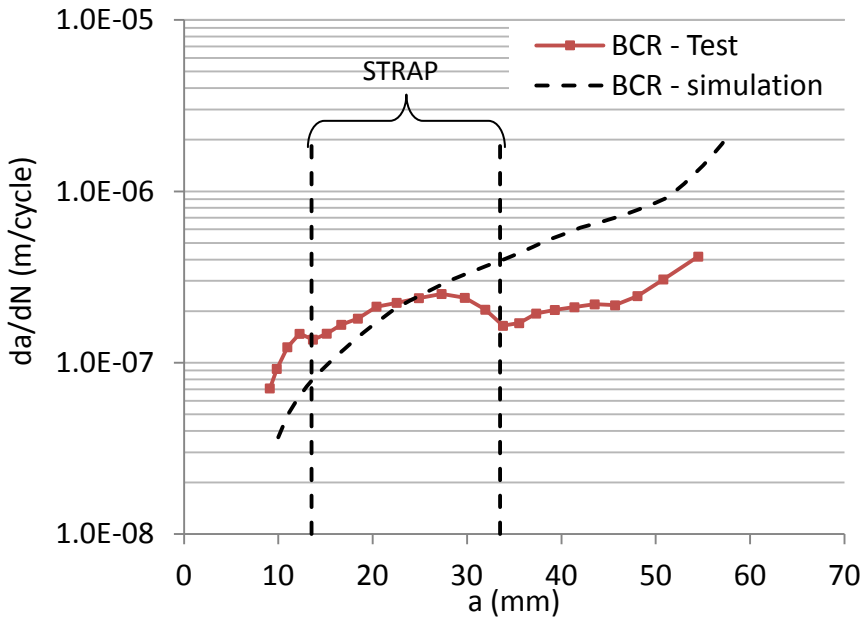

Figure 9-22 : Fatigue crack growth rate prediction for CONSTANT AMPLITUDE test – BCR reinforced M(T) specimens - σ_{max} = 60 MPa, R = 0.1

Figure 9-22 shows the predicted fatigue crack growth rates obtained from AFGROW compared with test results [5]. There is good agreement up to a crack length of 25 mm. Past that crack length the predictions are faster than the measured growth rates.

9.2.4 Summary

- For constant amplitude loading, RESLIC predicts with an error of +16% and -8% the fatigue life of the specimens as well as the fatigue crack growth rate for the AIRstream case and the BCR case.
- For both geometries, ReSLIC predicted no disbond growth as the calculated G values were too small. This is in agreement with experimental observations for MT samples. This will be further reviewed in the discussion chapter.

9.2.5 Source of errors

The error on life prediction reported here only reflects the difference between the life as predicted from AFGROW integration on material law and the life as obtained from the tests. Hence the error may be first coming from the error found in the testing results. In fact, the crack, as measured from the test is read on the unbounded side and not the reinforced one, hence it does not reflect the possible curvature of the crack length. The difference in crack length interpretation may contribute to the observed error. In addition, the experimental life is based on a couple of tests and the variation commonly observed in fatigue test will be present due to the reduced number of test results. On the other hand the calculation does consider the curvature of the crack length through the use of the equivalent crack length methodology as developed by Hosseini-Toudeshky [200] but with a certain approximation.

From a modelling point of few, the Hosseini-Toudeshky method [200] that reduces the solution to a single value of stress intensity factor through the thickness also brings some error in the crack length calculation as it defines with a 2D result a mechanism that is actually a 3D one due to the crack curvature through the thickness.

The integration of the fatigue crack growth data may also introduce a certain level of error in the model prediction as it uses an equivalent residual stress intensity factor to take into account the change in R-ratio due to residual stresses. Also the use of the tabular look-up method for the introduction of crack

growth rate data implies that interpolation and extrapolation are necessary in order to calculate the fatigue life which may introduce some errors in the life prediction.

In summary, errors can be identified for every step of the life calculation, starting from the evaluation of the stress intensity factor up to the life calculation in AFGROW. In additions, the error notified here is linked to the variability in life cycles encountered with fatigue tests specimens. Table 9-4 lists the type of errors for each step of the analysis.

Table 9-4 : Possible sources of the observed error, from the modelling, life integration and testing point of views

Model	Life calculation (AFGROW)	Testing
Approximation of residual stress effect (K_{eq}^{res})	Residual stress effects introduced through (K_{eq}^{res})	Reading of crack length on unbounded side only
3D behaviour of substrate main crack reduced to a 2D model	Interpolation/extrapolation of fatigue crack growth data using Tabular Look-Up material model	Reduced number of data for comparison considering large variation for fatigue results
No plastic deformation in material model	AFGROW intrinsic errors	

Chapitre 10 : Parametric study of factors influencing crack growth life

This chapter will look at the sensitivity of parameters changing the fatigue behaviour of the reinforced structure with:

1- The effect of specimen definition with the Airstream configuration compared to the BCR one.
2- The effect of disbond.
3- The effect of strap geometry with the same stiffness ratio of $\mu = 0.2$.
4- The effect of the substrate thickness with the same stiffness ratio $\mu = 0.2$.
5- The effect of strap material (keeping the same stiffness ratio $\mu = 0.2$)

While the first study made use of the FE model developed in Chapter 07 in order to conduct the comparative study, all other parametric studies were performed using ReSLIC design tool to calculate fatigue lives. All calculations were geometrically non-linear. The simulations were run at maximum and minimum loads for a σ_{max} = 60 MPa and an R-ratio = 0.1 (σ_{min} = 6 MPa).

All parametric cases are compared to the reinforced M(T) specimen results that were given in the previous chapter. The comparisons will look at both the bonded side and the back side with comparisons of the effective stress intensity factors. The fatigue lives and fatigue crack growth rates will also be compared.

10.1 Stress analysis for two geometries: BCR-1 and AIRstream

Constant amplitude fatigue tests of reinforced M(T) coupons using the AIRstream geometry showed reduced crack retardation in comparison to the test performed on M(T) samples of similar geometry and stresses in the earlier BCR programme. A life improvement factor of 1.17 was obtained in Airstream (Chapter 04) compared to 2.7 in the earlier project. In addition a change in disbond path under the strap was observed. In the BCR case, disbonding was observed between the outer layer of aluminium of the Glare strap and the rest of the strap, while in the AIRstream samples, disbonding - not confirmed –

appeared to be in the adhesive layer (Figure 10-1 and Figure 10-2). This section calculates the stress field differences in the two samples, which had significant difference in substrate thickness and stiffness ratio.

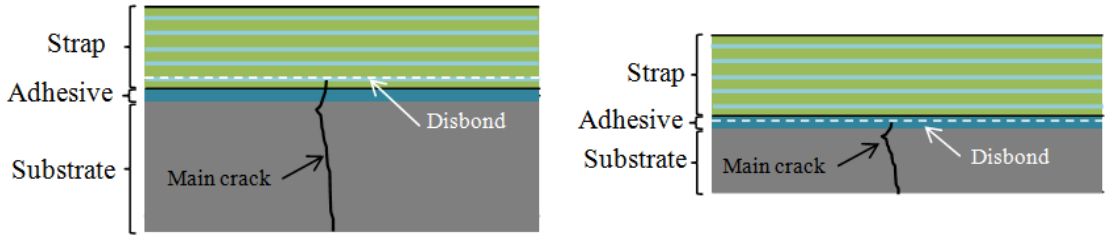

(a) BCR configuration (b) AIRstream configuration

Figure 10-1 : Disbond location in BCR and Airstream M(T) samples (Not to scale)

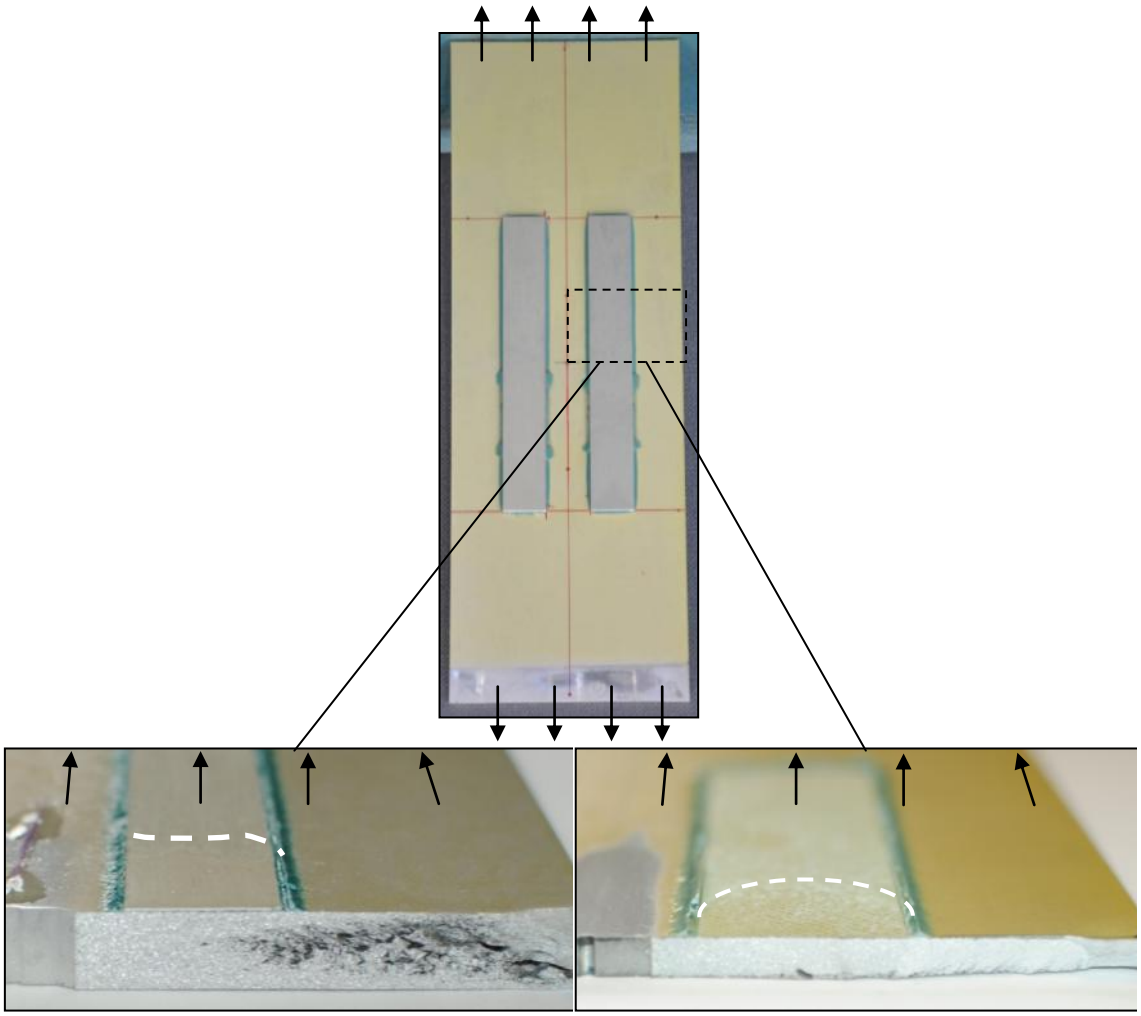

(a) BCR configuration (b) AIRstream configuration

Figure 10-2: Comparison of fracture surface after fatigue tensile testing – View of BCR and AIRstream specimen after complete failure of the specimen (cross section views)

10.1.1 BCR-1 Geometry

The BCR-1 specimens were of aluminium 7085-T7651 substrate reinforced with Glare1-3/2 (0.4) straps. The geometry of the sample is shown in Figure 10-3. The substrate was 400 mm long, 140 mm wide and 10 mm thick. The straps were 180 mm long, 20 mm wide and each strap consisted of two straps of GLARE 3/2 bonded together to reach a total thickness of 3.6 mm (= 2 x 1.8 mm). They were located 13.5 mm from the centre of the specimen. The straps were bonded to the substrate using FM94 epoxy adhesive. The stiffness ratio (μ) for the BCR configuration was 0.09.

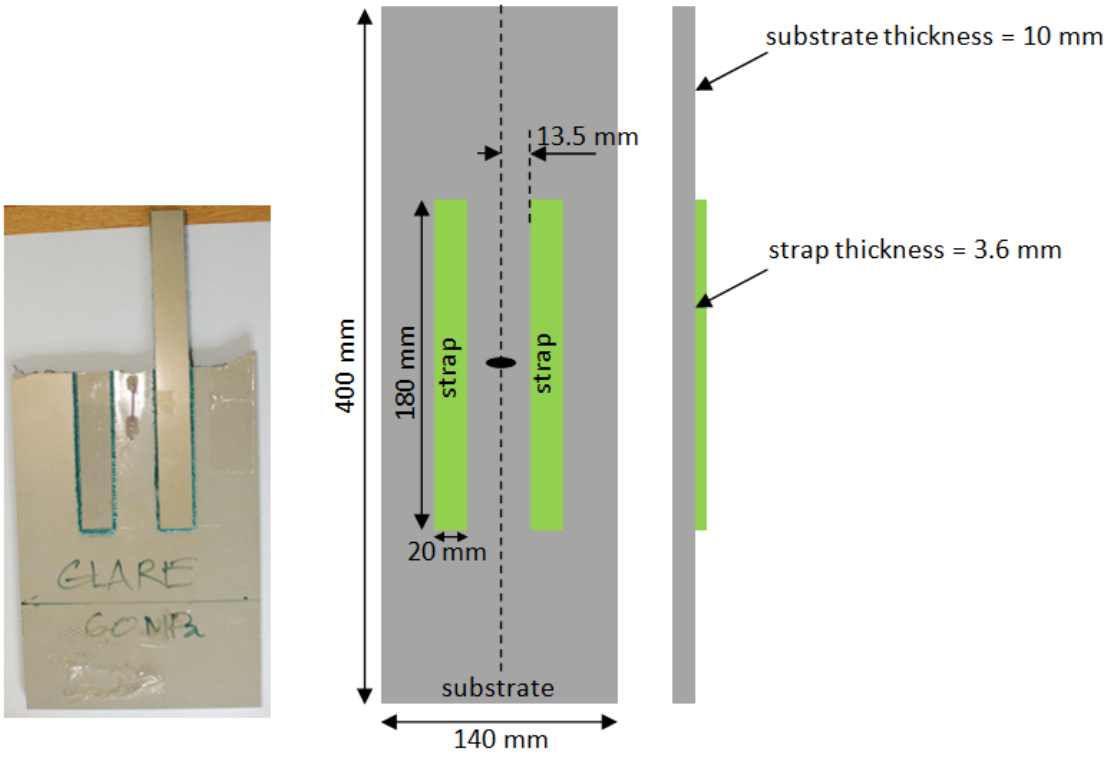

Figure 10-3 : Geometry of test samples used in earlier BCR research project [5] **– referred to as 'BCR' coupons (all dimensions in mm) – μ = 0.09.**

10.1.2 Finite element models

The finite element models represent one quarter of the specimen. Some changes have been made in order to reproduce the changes in the location of the disbond interface. While the model defined earlier has three parts for strap, substrate and adhesive, the model considered here increased this level of detail

with the adhesive modelled with two individual layers and the Glare strap with details of the first aluminium layer; and the first S2-prepreg layer of the strap. This was applied to both AIRstream and BCR models (Figure 10-4). This gives a more realistic model of what is observed during testing as outlined earlier.

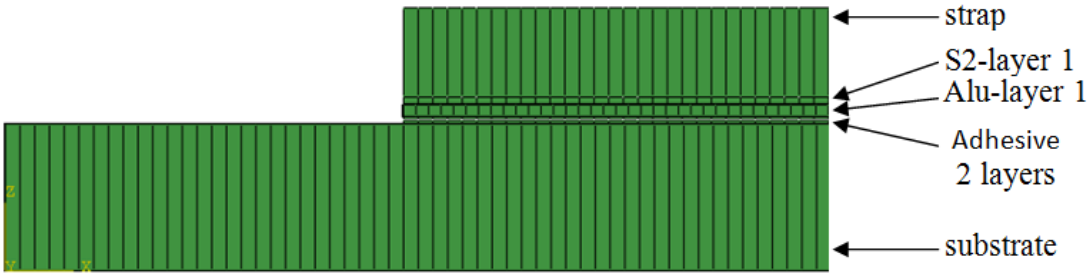

Figure 10-4 : FE section – layers definition – AIRstream case

All parts were modelled using continuum shell elements SC8R with one element through the thickness and an element size of 0.5 mm. Tie interaction properties were used between each part.

10.1.3 Results

- **Substrate longitudinal stresses**

This section shows longitudinal stresses perpendicular to the substrate crack plane (Figure 10-5), along the crack path. The stress values shown in Figure 10-6 are located at the bonded interface and the back (unbonded) surface together with the respective mean and bending stresses for an initial crack length of 10 mm.

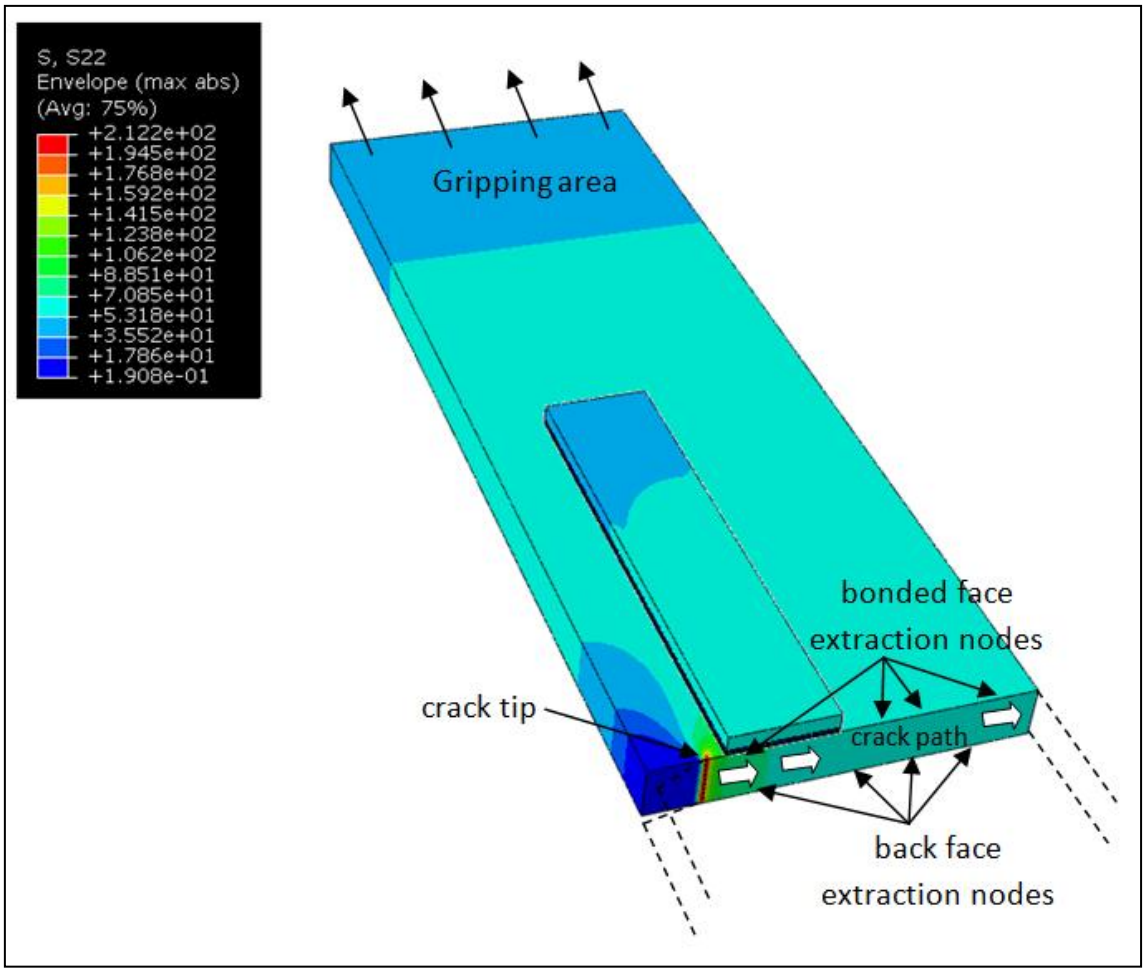

Figure 10-5 : Envelope results of S22 longitudinal stresses at crack path – BCR case ¼ specimen model for 10 mm crack – definition of bonded and back side nodes of extraction

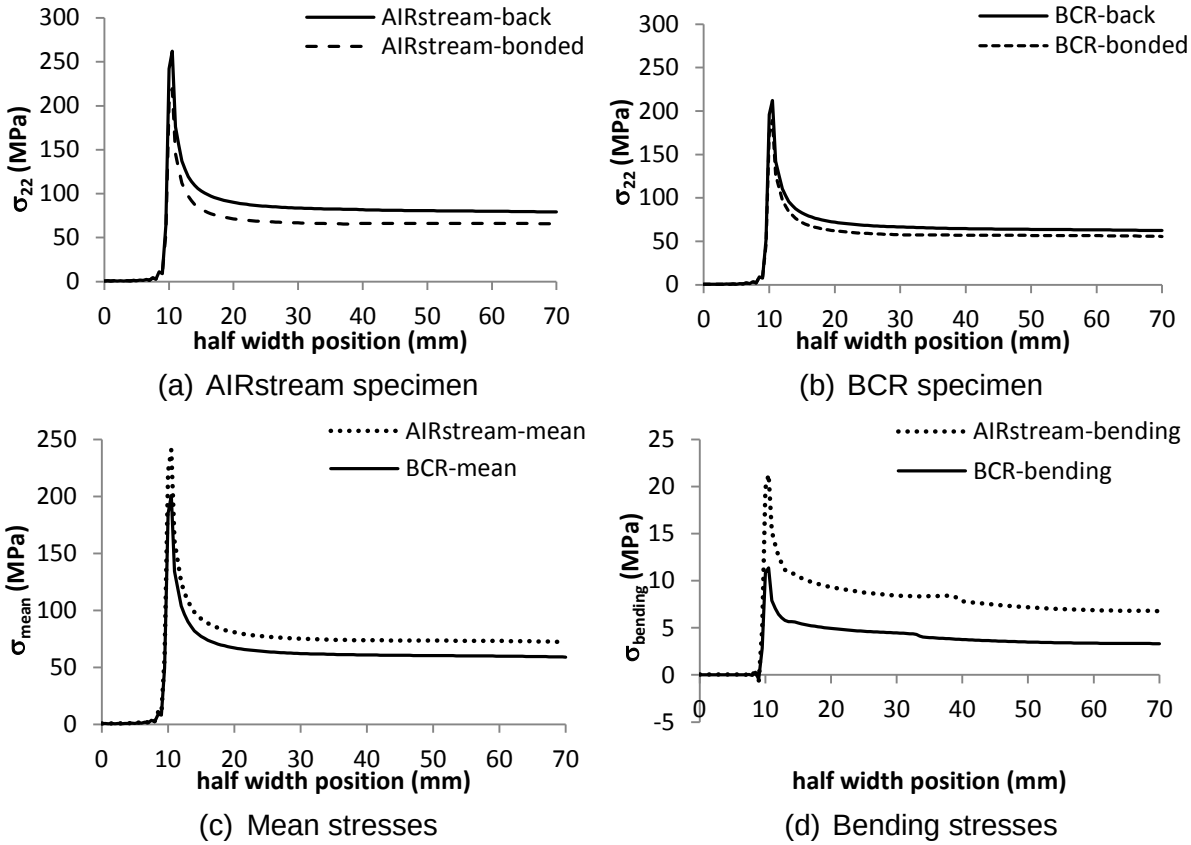

(a) AIRstream specimen (b) BCR specimen

(c) Mean stresses (d) Bending stresses

Figure 10-6 : Plot of longitudinal stress along half width of substrate (on bonded and back faces) for the two sample types (10 mm crack length case) – Applied stresses were 54 MPa for BCR and 60 MPa for AIRstream

Figure 10-6 shows a difference in stresses between the bond face and the back face that is greater for the AIRstream sample than for the BCR one. It demonstrates a greater amount of bending for the AIRstream case than for the BCR case (4 - 5 MPa in difference) with bending stresses up to 10 MPa for the Airstream case and 5 MPa for the BCR case. The AIRstream case also has greater mean stresses than the BCR case.

The higher mean stresses coupled to the larger bending for the AIRstream case means that the longitudinal stresses will be greater than the BCR case along the crack path. This will result in a larger stress intensity factor as demonstrated in the next paragraph. Hence the crack growth rates will be faster for the AIRstream case which means reduced fatigue retardation.

- **Longitudinal stresses along strap length**

This section compares the longitudinal stresses along the strap length. The stresses are provided at the bonded interface and at the free surface (Figure 10-7) together with the respective mean and bending stresses for an initial crack length of 10 mm. The stresses at the bonded interface are extracted from the first aluminium layer.

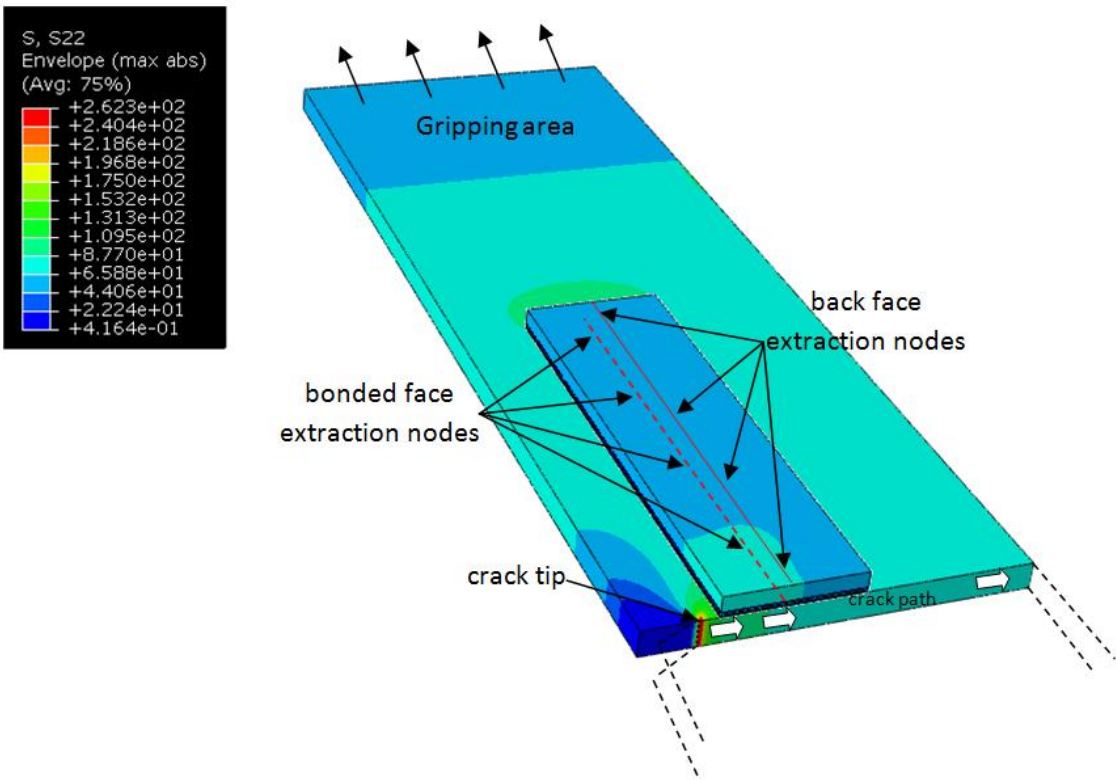

Figure 10-7 : Envelope results of S22 longitudinal stresses along strap half length– AIRstream case ¼ specimen model for 10 mm crack – definition of bonded and back side nodes of extraction

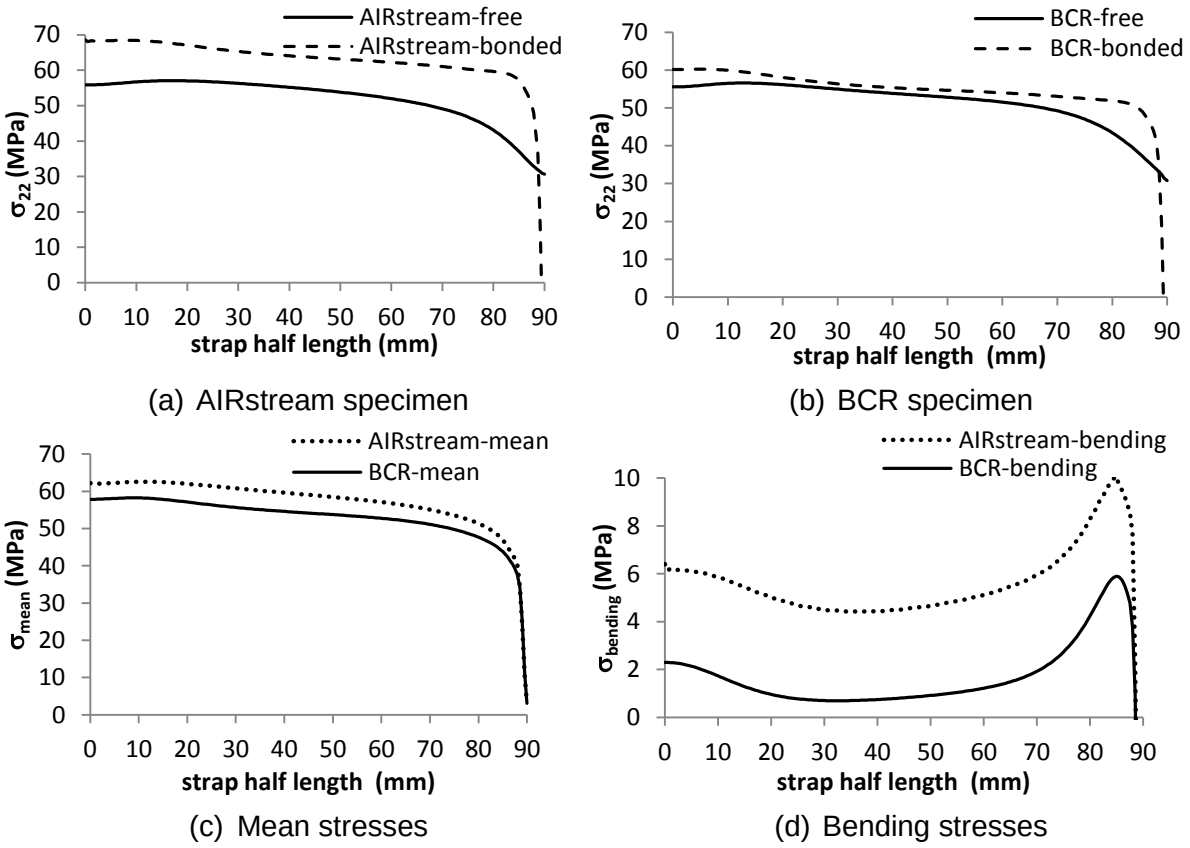

(a) AIRstream specimen

(b) BCR specimen

(c) Mean stresses

(d) Bending stresses

Figure 10-8 : Plot of longitudinal stress vs. half-length in strap for the two sample types on bonded and back faces (10 mm crack length) – Applied stresses were 54 MPa for BCR and 60 MPa for AIRstream

The analysis demonstrates that the difference in stresses between the bonded surface and the free (unbonded) surface of the strap is greater for the AIRstream case than for the BCR one. There is more bending in the strap for the AIRstream case than for the BCR case as illustrated in Figure 10-8. The mean longitudinal stresses carried by the AIRstream strap are greater than the BCR one.

- **Stress intensity factor (SIF)**

The stress intensity factor at the substrate crack front for the bonded and back surfaces as well as the weighted values are represented hereafter.

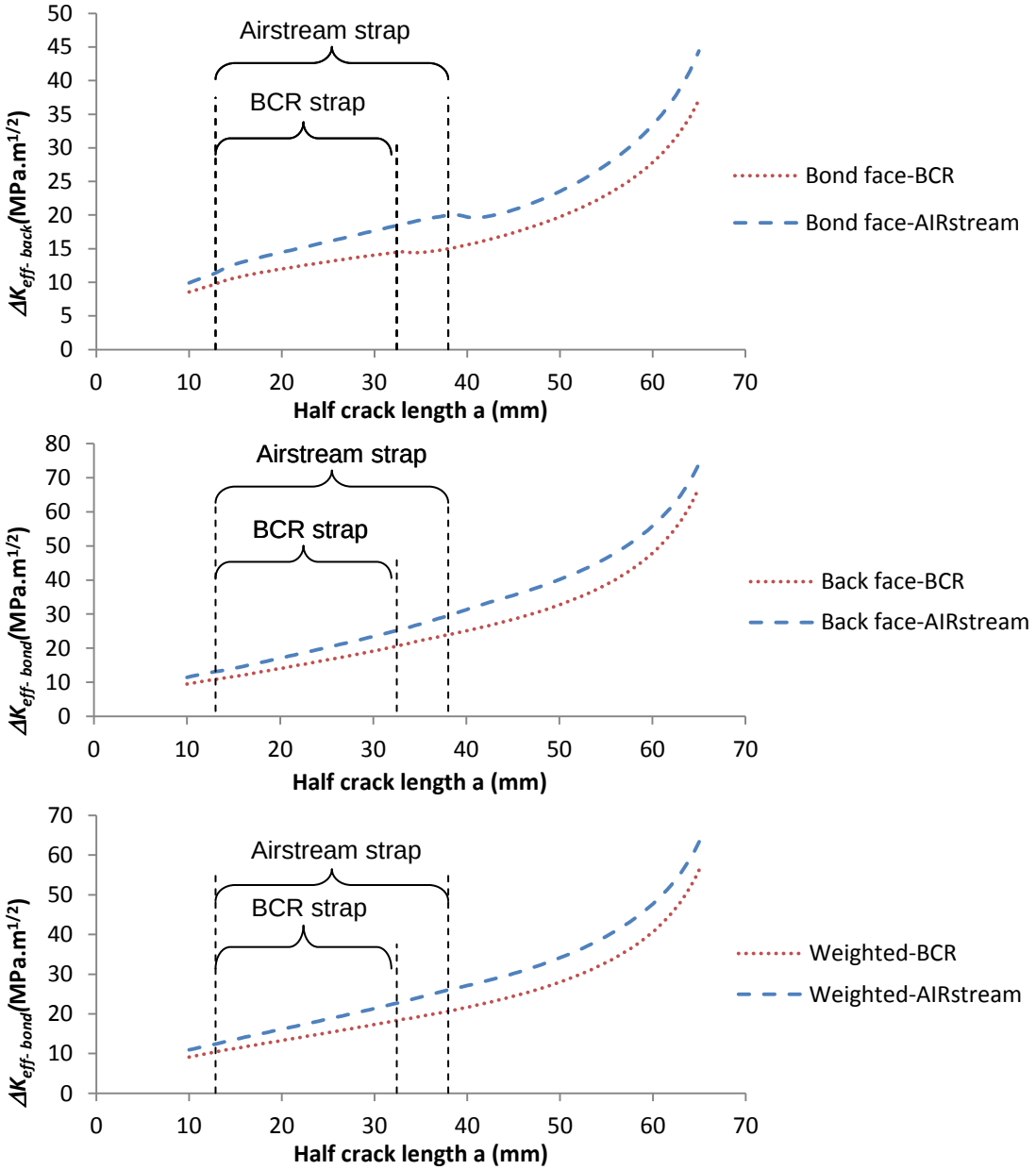

Figure 10-9 : SIF for AIRstream and BCR coupons showing back face and bond face and weighted values for growing crack length

Stress intensity factor variations at the crack front are greater for the AIRstream case than for the BCR one for all three results given here (bond, back and weighted, Figure 10-9). This is due to the larger secondary bending observed in AIRstream specimens with 10 MPa instead of 5 MPa. This will results in faster crack growth rates for the AIRstream case than the BCR one and consequently, shorter fatigue lives.

- **Deflection comparison**

Figure 10-10 shows the Airstream sample under load, with a visible deflection. Table 10-1 gives the deflection obtained at the reference point for the BCR and AIRstream cases for the 3 different crack lengths.

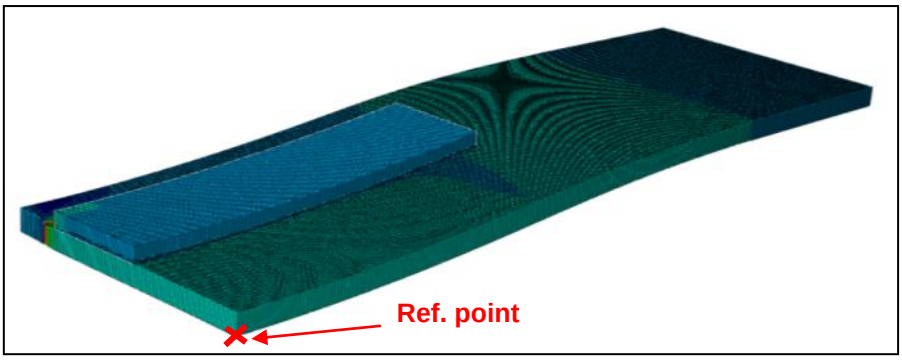

Figure 10-10 : Deflection reference point

Table 10-1 : Deflection at reference point for both cases

Crack case	AIRstream – δ (mm)	BCR – δ (mm)
Before (10 mm)	0.20	0.04
Middle of strap (26.5/23.5 mm)	0.29	0.07
Past strap (43 mm)	0.49	0.20

The deflection is always greater for the AIRstream case than for the BCR case which is a direct consequence of the increased amount of secondary bending from one coupon design to the other. This applies to all crack length cases.

10.2 Study of the effect of disbond size

This section looks at two cases of disbond. The first one is the one that has been reported in the previous chapter for the reinforced M(T) specimen in the AIRstream configuration with the disbond limited to one element. It will be referred to as “NO disbond”. The second case is a large triangular shape disbond as observed in [161]. It is a triangle that covers the width of the specimen as illustrated in Figure 10-11. It is 26 mm wide over a length of 52 mm. It will be referred to as “FULL disbond”.

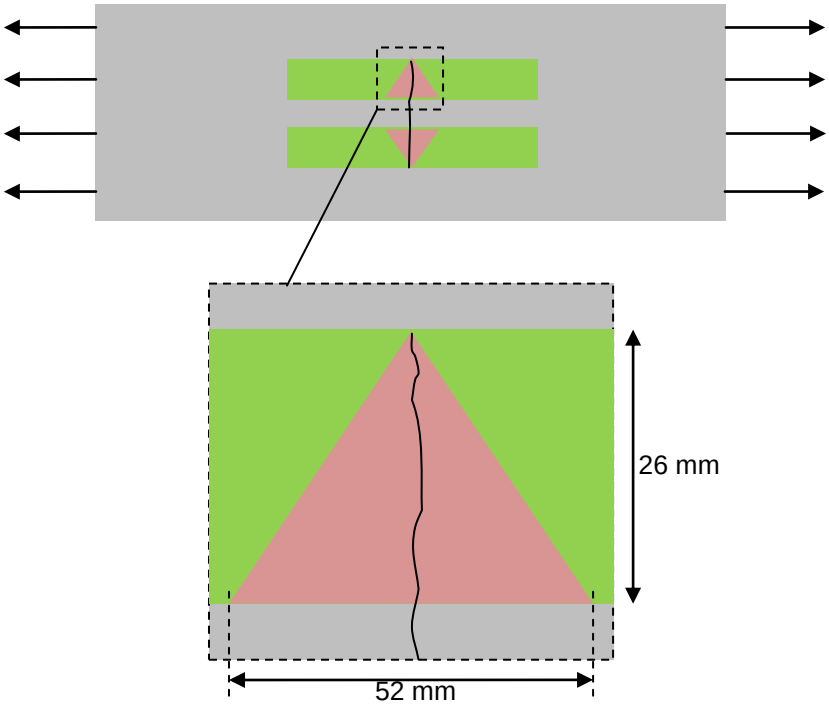

Figure 10-11 : “FULL disbond” MT specimen case

10.2.1 Disbond profiles

Figure 10-12 and Figure 10-13 show the disbond profile for the two cases for 4 crack length cases.

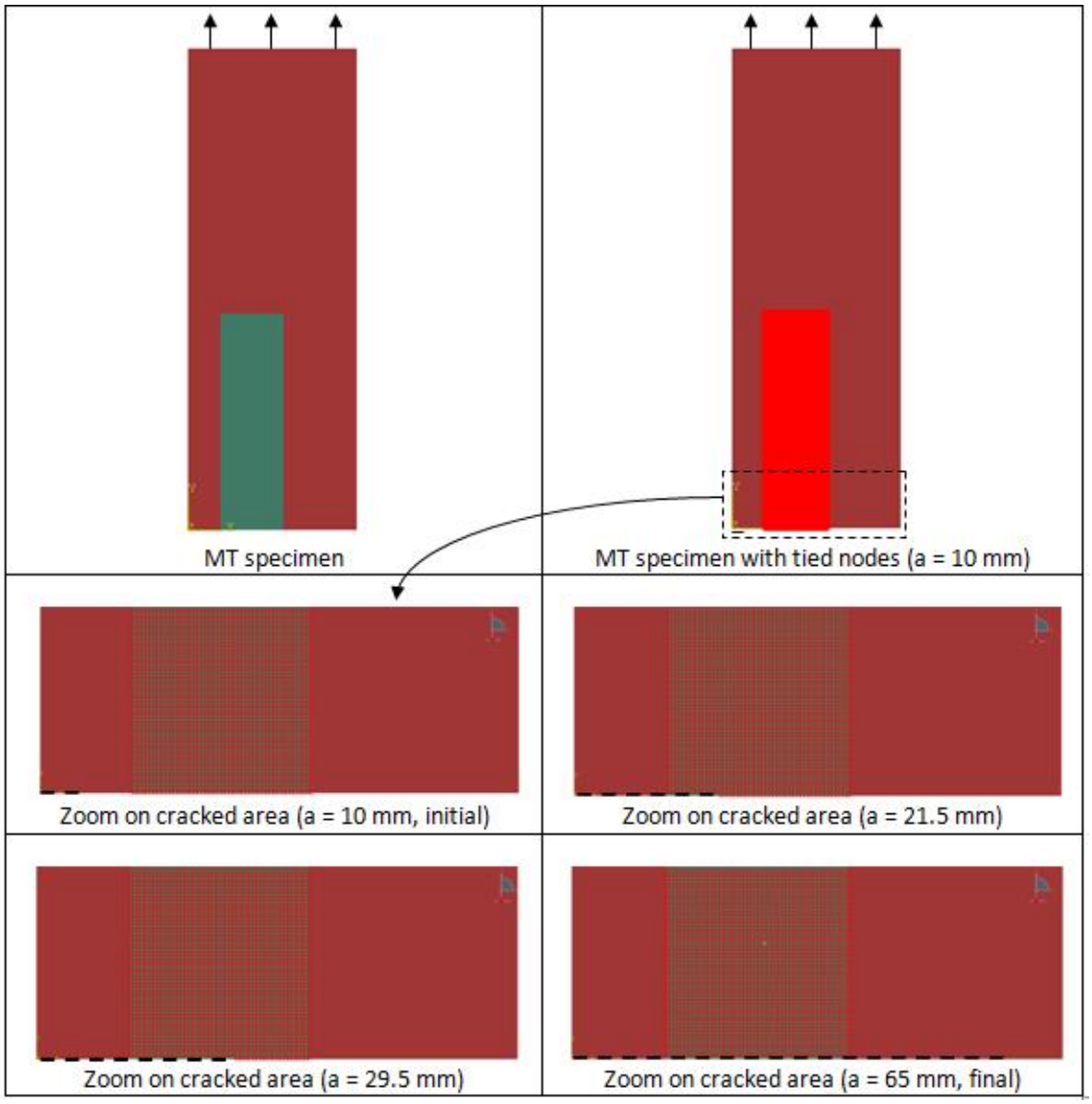

Figure 10-12 : FE disbond advance for AIRstream reinforced M(T) specimen – NO disbond

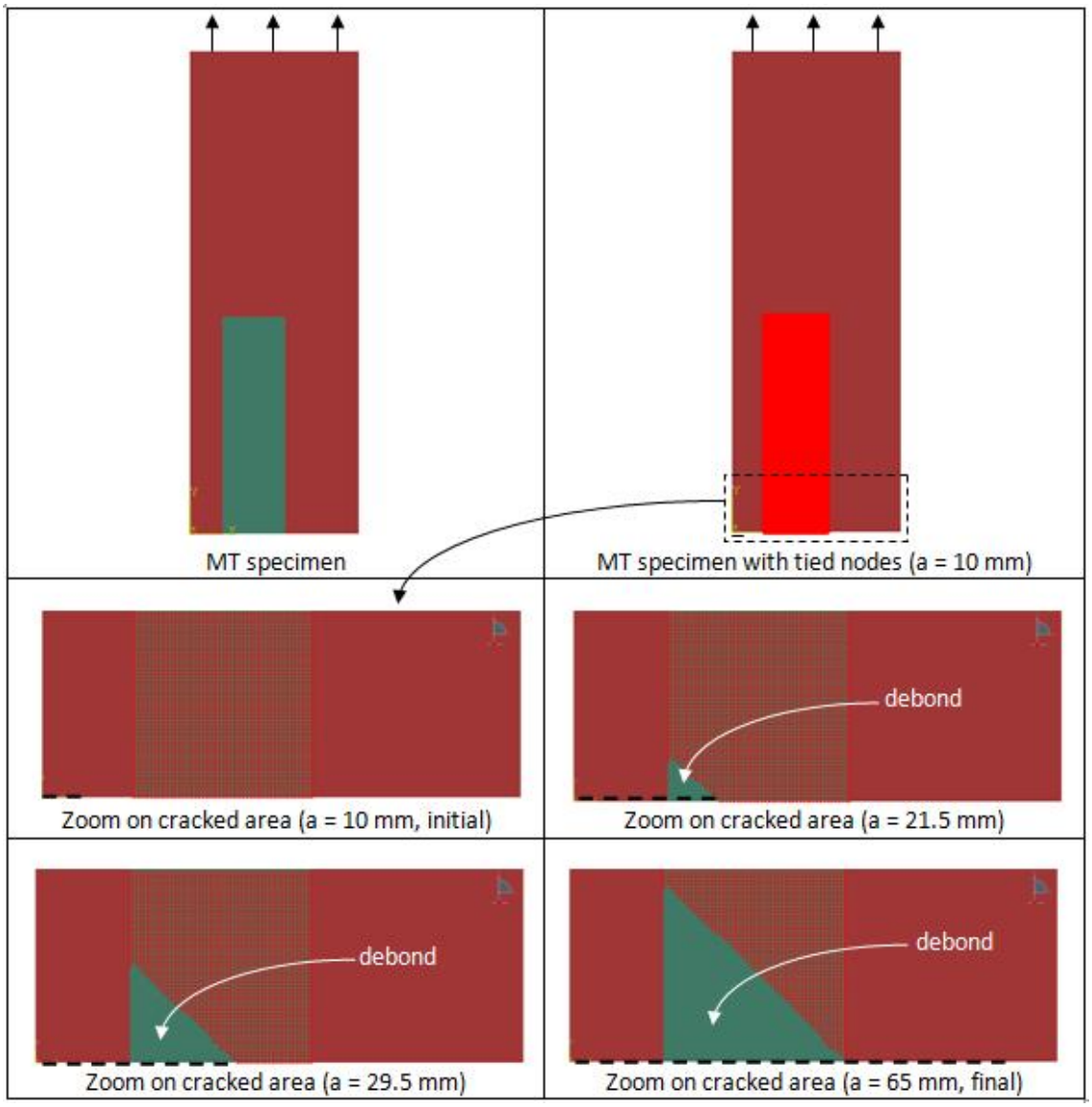

Figure 10-13 : FE disbond advance for AIRstream reinforced M(T) specimen – FULL disbond – shows the evolution of a triangular disbond.

For the first case of “NO disbond” only one element of disbond is visible. It corresponds to the initiation of disbond as implemented in ReSLIC and is advancing with the substrate crack as illustrated in Figure 10-12.

In the second case (Figure 10-13) the calculation was set in order to have a large disbonded area with a triangular shape and straight crack front.

10.2.2 Effect of disbond on stress intensity factor range

The calculation compares the stress intensity in the substrate with the full disbond to the NO disbond case and calculates the variation defined as:

$$Variation = \left[\Delta K_{eff}^{debond} - \Delta K_{eff}^{NO\ debond}\right] / \Delta K_{eff}^{NO\ debond} \quad \textbf{(10-1)}$$

- FULL disbond

Figure 10-14 and Figure 10-15 show ΔK_{eff} for the bond face and back face for the full disbond and for the NO disbond cases.

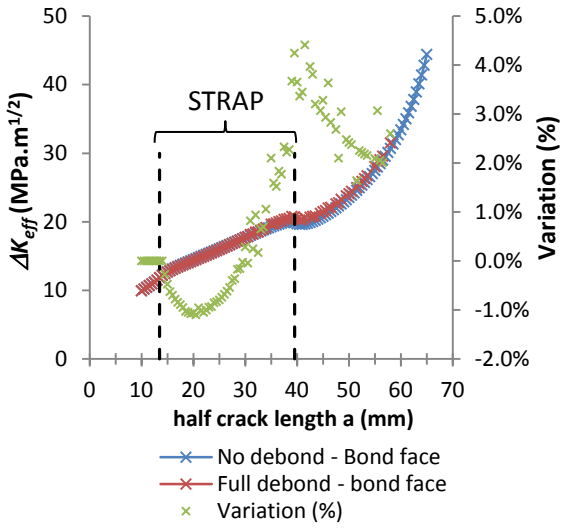

Figure 10-14 : ΔK_{eff} for bonded face – FULL disbond – applied stress = 60 MPa

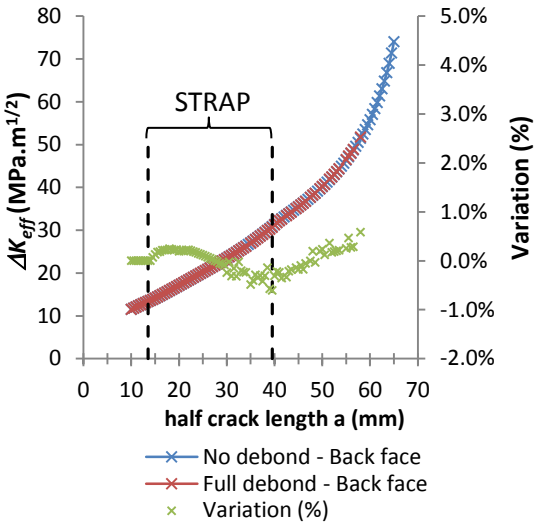

Figure 10-15 : ΔK_{eff} for back face – FULL disbond – applied stress = 60 MPa

Figure 10-14 shows that there is a small difference caused by a disbond of this size compared with the situation without. The curves are very similar and the difference reaches a maximum of 5%. The variation is mainly negative in the reinforced area up to 2/3 of the width indicating smaller values for the disbonded case than the bonded one. It then increases on exiting the reinforced area. On the back face there is little effect of the disbond with a variation of less than 1% between the case with and the one without.

10.2.3 Life prediction changes with disbond

The fatigue life was predicted using AFGROW tool, assuming a substrate made of 2624-T351 aluminium alloy for the material data and using the same

approximation and the same calculation techniques as the ones described earlier.

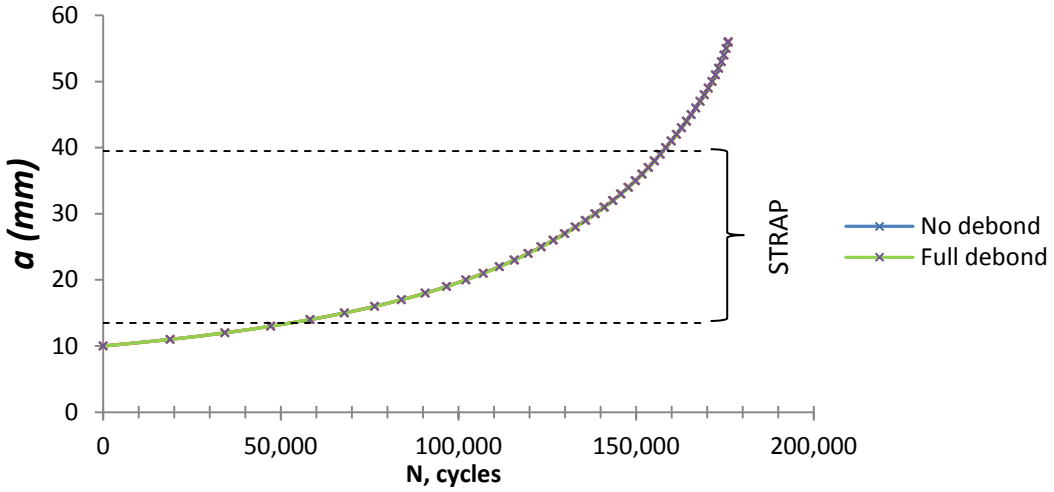

Figure 10-16 : Predicted fatigue lives in different cases of disbond

Figure 10-16 illustrates the fatigue life obtained from the AFGROW computation. As a consequence of the similar stress intensity factor coefficient, there is little change in life.

10.2.4 Conclusions

The cases of disbond reported here showed that disbond of triangular shape and with a size of 26 mm by 52 mm had no effect on the fatigue life of the reinforced M(T) specimen by comparison with a pristine case (no disbond). Nevertheless, a larger disbond may results in an increase of the stress intensity factor which will reduce the life of the specimens. This is due to the reduced bridging effect as there is less load transfer between the strap and the substrate due to the reduced surface of interaction between the two.

While the variation stayed small in the case presented here, it is possible that a larger amount of disbond - say 1/3 of total area covering the specimen – may have a larger influence on the stress intensity factor and significantly change the fatigue life. This will require further investigation but may not reflect what has been observed during the fatigue tests where very small disbond was observed at the interface between the strap and the substrate.

10.3 Study of the effect of strap width

The effect of the strap width on stress intensity was studied through the case of a strap with a width of 54 mm and a thickness reduced to 1.8 mm to keep the stiffness ratio to μ = 0.2. This will correspond to the use of a Glare 2A (3/2) material. This case is compared to the AIRstream reinforced M(T) specimens described in Chapter 08 & 09, 26 mm wide and 3.6 mm thick. There was no disbond in the calculations. The applied nominal stress was 60 MPa as for the Airstream case. Details of the wide strap geometry and model are given in Figure 10-17.

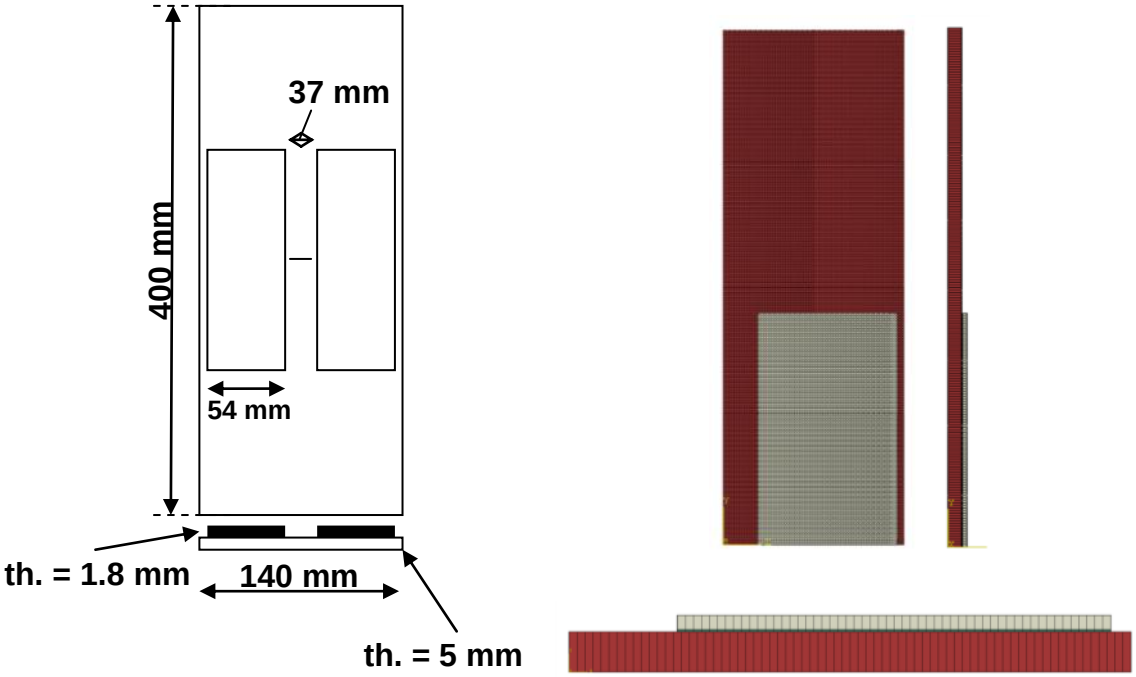

(a) Geometry (b) Model

Figure 10-17 : Details of (a) geometry and (b) mesh of the reinforced M(T) specimen with large strap (width = 54 mm) – applied nominal stress = 60 MPa

10.3.1 Effect of strap width on the stress intensity factor range

Figure 10-18 and Figure 10-19 show plots of ΔK_{eff} vs crack length on the bond face and the back face for the cases of narrow and wide straps. The variation between wide and narrow is defined as:

$$Variation = \left[\Delta K_{eff}^{wide} - \Delta K_{eff}^{narrow}\right] / \Delta K_{eff}^{narrow} \quad \textbf{(10-2)}$$

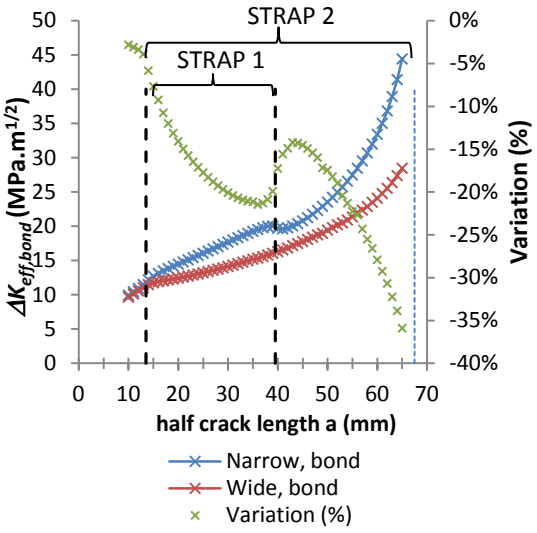

Figure 10-18 : ΔK_{eff} on bond face for narrow and wide strap; μ = 0.2 – Applied stress = 60 MPa

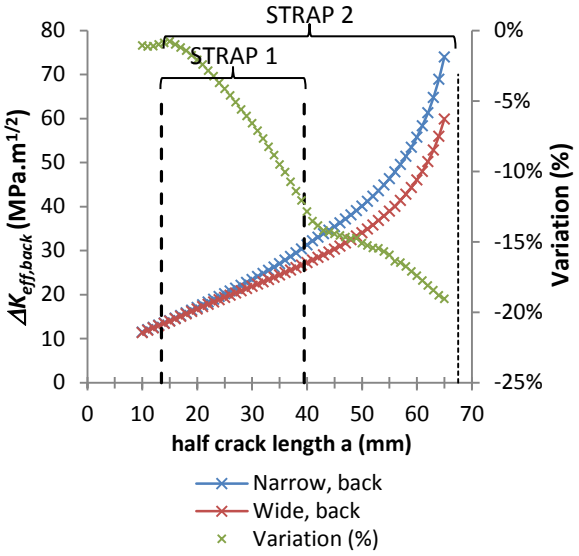

Figure 10-19 : ΔK_{eff} on back face for narrow and wide strap; μ = 0.2 – applied stress = 60 MPa

Figure 10-18 and Figure 10-19 show that ΔK_{eff} for the wide strap is smaller than the narrow strap for both faces. On the bond side, the effect of the larger strap appears immediately at the beginning of the strapped area. It decreases up to -20% before rising to - 15% due to the singularity of the narrow strap and then decreases up to -35% for the final crack length. On the back side, the beneficial effect of the wide strap appears later in the strapped area and the effect is reduced with a variation that reaches a minimum of -20% towards the final crack length.

Figure 10-20 gives the results for the weighted effective stress intensity factor range.

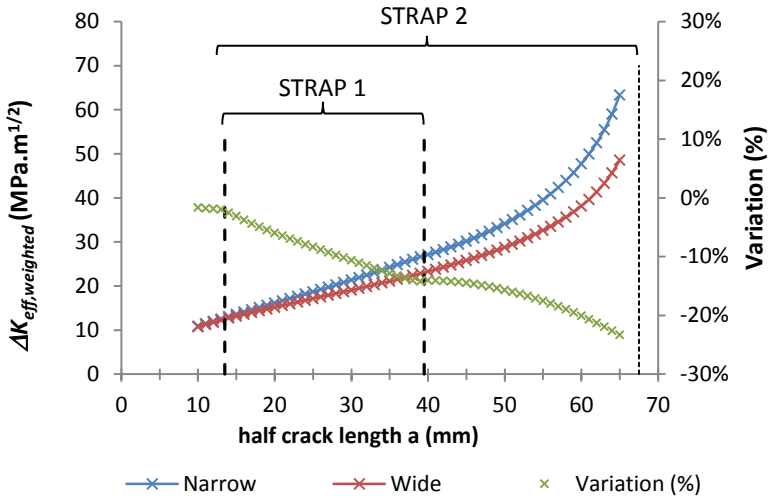

Figure 10-20 : Weighted Stress intensity factor for narrow and wide strap with associated variation; $\mu = 0.2$

The weighted stress intensity factor range results plotted in Figure 10-20 demonstrate that the wide strap has reduced stress intensity compared with the narrow one with an effect that starts early in the reinforced area. The variation decreases up to -15% with a steady rate in the narrow reinforced area and it decreases up to - 25% for the final crack length for the wide strap configuration. Hence the use of a wider strap is beneficial.

The results could be interpreted in terms of the effect of strap thickness as well as strap width. Thickness may be more appropriate than width, as the data show an effect on ΔK_{eff} even at crack lengths smaller than the narrowest strap. The local effects of thickness may be the dominant influence in this region, with reduced thickness at the same μ value having beneficial effects.

This beneficial effect of the wide strap can also be explained by the effect of secondary bending. Figure 10-21 and Figure 10-22 illustrate the longitudinal normal stresses and bending stresses in both specimen configurations with a crack length of a/2 = 10 mm and under applied nominal stresses of 60 MPa.

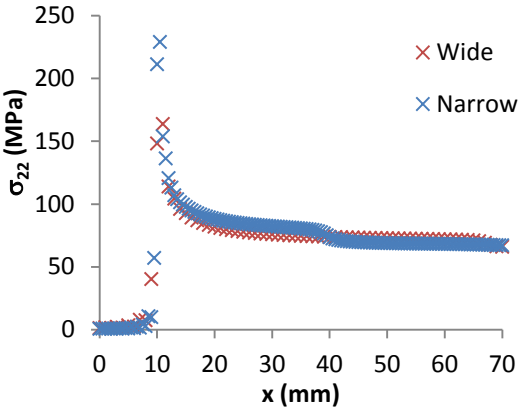

Figure 10-21 : Longitudinal normal stress for wide and narrow straps – applied stress = 60 MPa

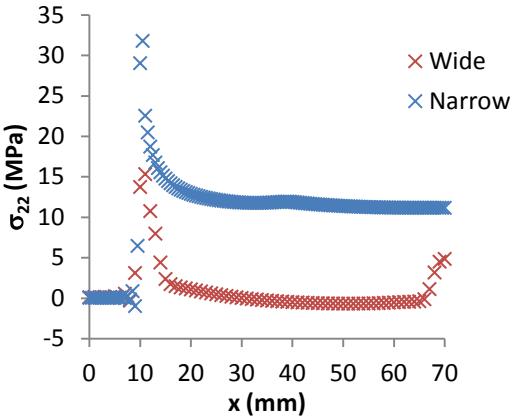

Figure 10-22: Longitudinal bending stress for wide and narrow straps – applied stress = 60 MPa

The normal stresses appear to be 5-10% higher for the narrow strap for the substrate length between 10 mm and 40 mm (end of the narrow strapped area) compared to the wide strap. This is reversed after 40 mm. Hence there appears to be a larger bridging effect for the wide strap than the narrow one at lower crack length which may explain the difference in ΔK_{eff} observed. This effect for small crack length is beneficial in terms of fatigue lives as small crack length changes are more beneficial than larger crack length changes.

Bending stresses may be the major explanation to the difference observed between the narrow strap and the large one as bending stresses appear to be much larger for the narrow strap than the wide one with a difference of approximately 10 MPa. These will increase the value of the stress intensity factors for the narrow straps while there are almost no bending stresses for the wide one.

10.3.2 Effect of strap width on fatigue life

Using the weighted value of the effective stress intensity factor range shown in Figure 10-20, the stress intensity factor coefficient β were calculated and used for the evaluation of the fatigue lives.

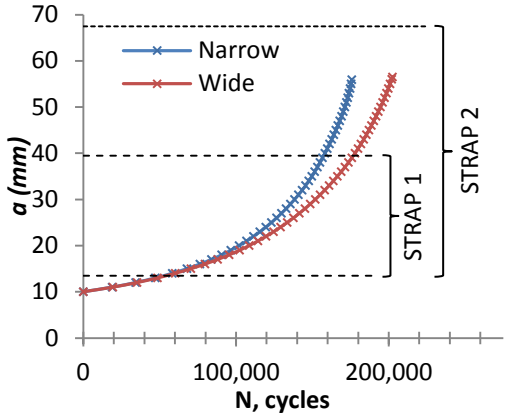

Figure 10-23 : Predicted fatigue lives for narrow and wide straps; μ = 0.2 – applied stress = 60 MPa

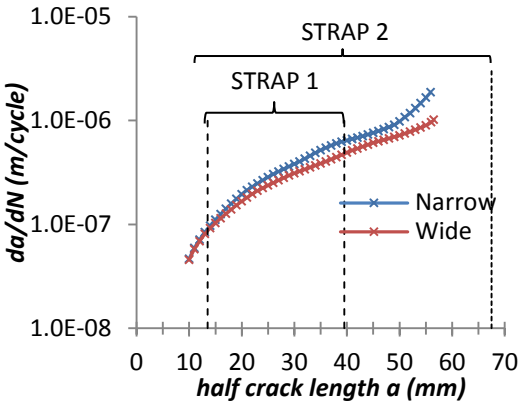

Figure 10-24 : Predicted crack growth rate for narrow and wide straps; μ = 0.2 – applied stress = 60 MPa

The calculated fatigue lives for the narrow and wide straps are respectively **175,868** and **202,499** cycles demonstrating an increase of 15% in fatigue life for the wide strap. The fatigue crack growth rates illustrated in Figure 10-24 show lower values for the wide strap than the narrow case with a difference that increases with crack length. The two curves separate shortly after the crack has entered the strapped area.

10.4 The effect of substrate thickness

The effect of the substrate thickness was studied through the case of a 10 mm thick substrate. To keep a stiffness ratio of μ = 0.2, a larger Glare 2A-6/5- strap 52 mm X 3.7 mm was used. Results were compared to those obtained for the AIRstream reinforced M(T) specimens illustrated in the previous chapter. No disbond was considered.

Details of the specimen geometry and model are given in Figure 10-25.

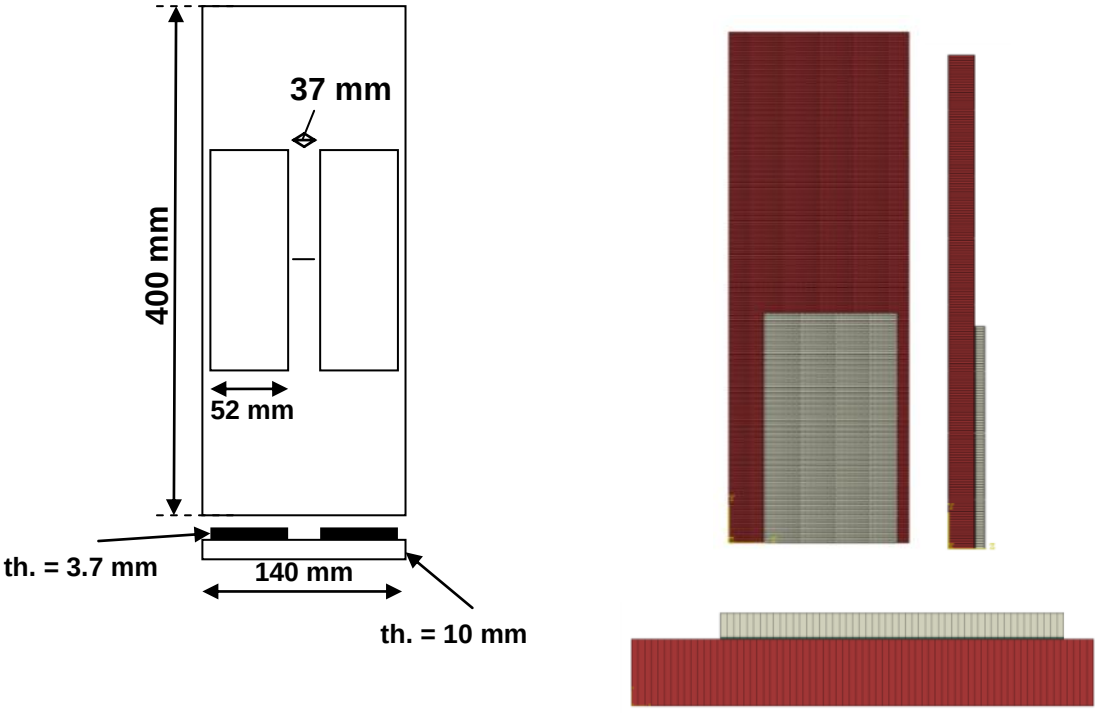

(a) Geometry (b) Model

Figure 10-25 : Details of (a) geometry and (b) mesh of the reinforced M(T) specimen with large strap (width = 54 mm)

10.4.1 Effect on the stress intensity factor range

Figure 10-26 and Figure 10-27 show the effective stress intensity factor range on the bond face and the back face for thin and thick substrates. STRAP 1 corresponds to the thin substrate case while STRAP 2 corresponds to the thick substrate case. The variation for both faces is defined as:

$$Variation = \left[\Delta K_{eff}^{thick} - \Delta K_{eff}^{thin}\right]/\Delta K_{eff}^{thin} \quad \textbf{(10-3)}$$

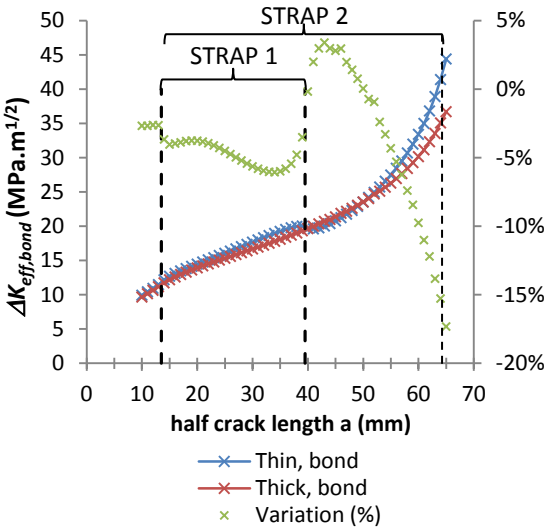

Figure 10-26 : ΔK_{eff} on bond face for thin and thick substrate; μ = 0.2 – applied stress = 60 MPa

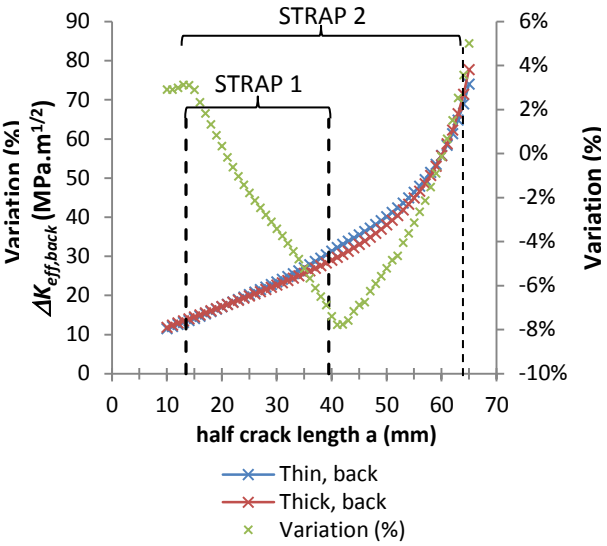

Figure 10-27 : ΔK_{eff} on back face for thin and thick substrate; μ = 0.2 – applied stress = 60 MPa

ΔK_{eff} for the bond side shows slightly reduced values for the thick substrate than the thin one in the strapped area with a variation around -5%. Once past the strap the values become similar with a positive variation up to 3.5%, after a crack length of 50 mm, this variation becomes negative, reaching -17% for the final crack length.

On the back side (Figure 10-27), the values of the effective stress intensity factor range start higher for the thicker substrate but decrease quickly on entering the strapped area. The variation is up to -8% in the strapped area but then increases up to 5% for the final crack length.

Figure 10-28 gives the results for the weighted effective stress intensity factor range.

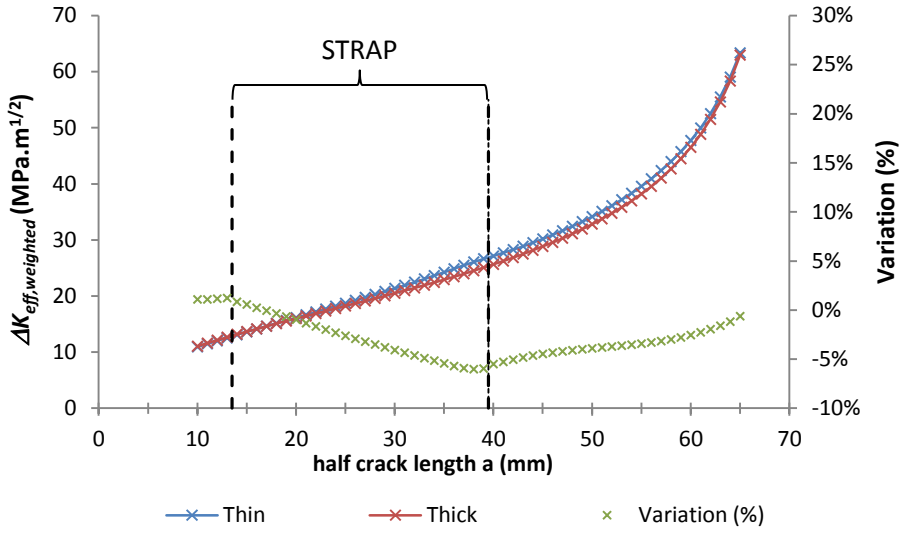

Figure 10-28 : Weighted Stress intensity factor for thin and thick substrate with associated variation; μ = 0.2

The weighted stress intensity factor range results plotted in Figure 10-28 demonstrate that overall, the use of a thick substrate has little effect. The variation starts with a value of 1% but then decreases in the strapped area up to -5%. It then increases for the remaining substrate crack lengths but stays with a negative value, indicating an improvement.

These results consider not only a thicker substrate but also a wider strap. Hence the improvement may be attributed to the presence of a wider strap rather than a thicker substrate. Using the same stiffness ratio for the reinforcement, a thicker substrate gives slightly reduced ΔK_{eff} than a thin one.

10.4.2 Effect on fatigue life

Using the weighted value of the effective stress intensity factor range shown in Figure 10-28, the stress intensity factor coefficient β were calculated and used to calculate fatigue lives.

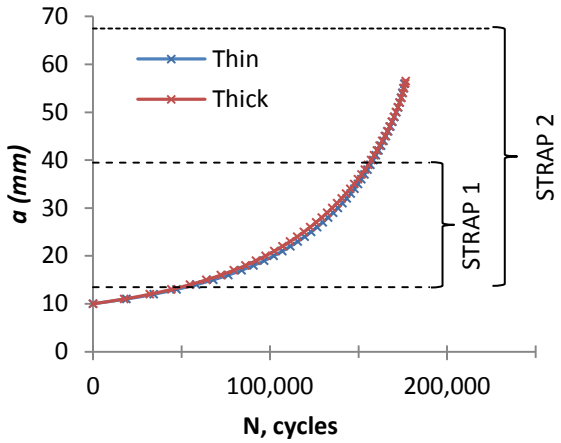

Figure 10-29 : Predicted fatigue lives for thin and thick substrates; $\mu = 0.2$

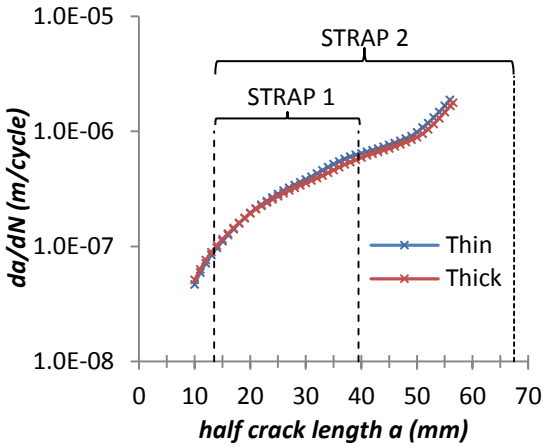

Figure 10-30 : Predicted crack growth rate for thin and thick substrates; $\mu = 0.2$

The calculated fatigue lives for the thin and thick substrates are respectively **175,868** and **176,629** cycles which demonstrate an increase of less than 1% in the fatigue life. There is also little effect of substrate thickness on crack growth rates.

10.5 The effect of strap material

A parametric study was conducted with different strap materials. The sample geometry used was the reinforced AIRstream M(T) specimen 400 mm X 140 mm X 5 mm thick. The strap thickness values were chosen to keep the stiffness ratio μ = 0.2 constant with a width of 26 mm. In all cases, the straps were placed 13.5 mm from the centre of the specimen. Strap materials were modelled as linear elastic with isotropic properties. The applied nominal stress for all cases was 60 MPa. Geometry and material details are given in Table 10-2.

Table 10-2: Strap geometry and material details

Strap	Thickness (mm)	E (MPa)	ν	α (CTE) (mm/mm/°C)	*density (g/cm^3)*
Glare	3.7	65,000	0.33	1.63×10^{-5}	2.5
Aluminium	3.4	71,000	0.33	2.32×10^{-5}	2.7
CFRP	1.8	135,000	0.3	-0.3×10^{-6}	1.8
GFRP	5.2	46,000	0.28	7.0×10^{-6}	2.0
Titanium	2.1	113,800	0.342	8.60×10^{-6}	4.5

No disbonding was allowed in this study. Thermal residual stresses were considered through the simulation of the curing process hence the effects observed here are the results of the combined effects of strap stiffness and TRS.

10.5.1 Effect of strap material on stress intensity factor range

Figure 10-31 to Figure 10-38 illustrate the stress intensity factors for the bond and back faces for all the materials considered above. All values are compared to the Glare case together with the variation between the two.

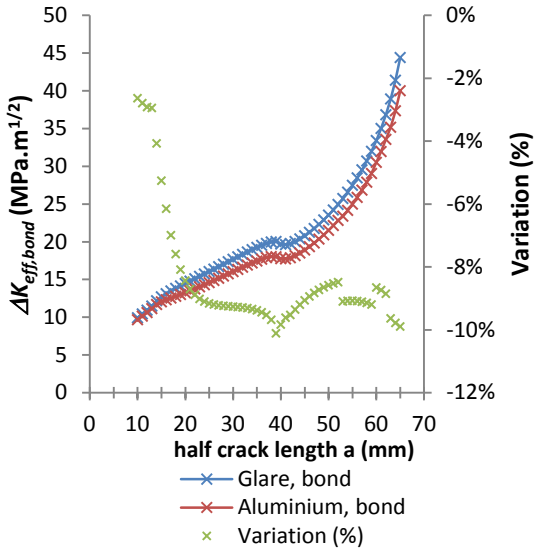

Figure 10-31 : ΔK_{eff} on bond face for Glare and Aluminium straps; μ = 0.2 – applied stress = 60 MPa

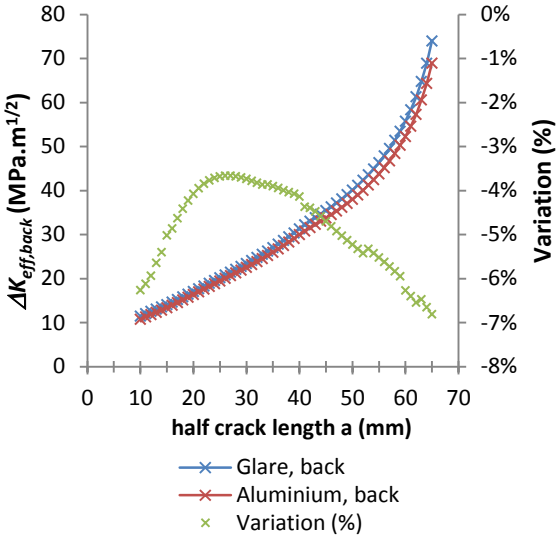

Figure 10-32 : ΔK_{eff} on back face for Glare and Aluminium straps; μ = 0.2 – applied stress = 60 MPa

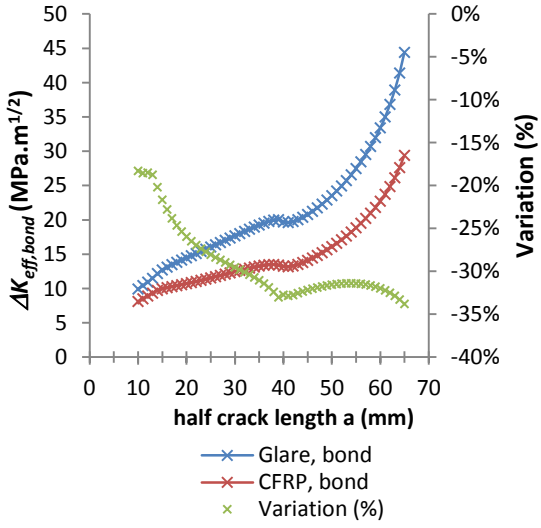

Figure 10-33 : ΔK_{eff} on bond face for Glare and CFRP straps; μ = 0.2 – applied stress = 60 MPa

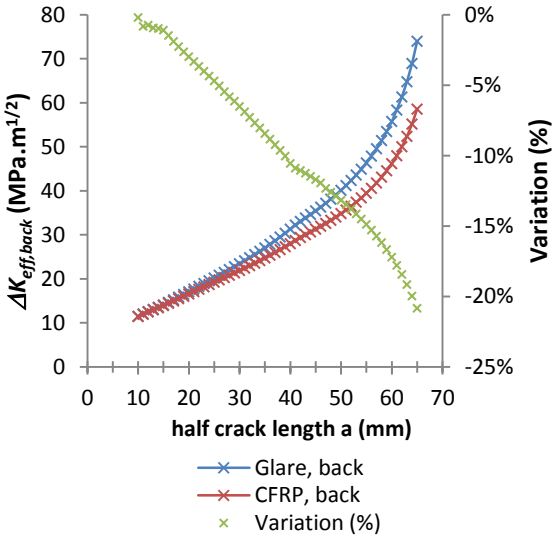

Figure 10-34 : ΔK_{eff} on back face for Glare and CFRP straps; μ = 0.2 – applied stress = 60 MPa

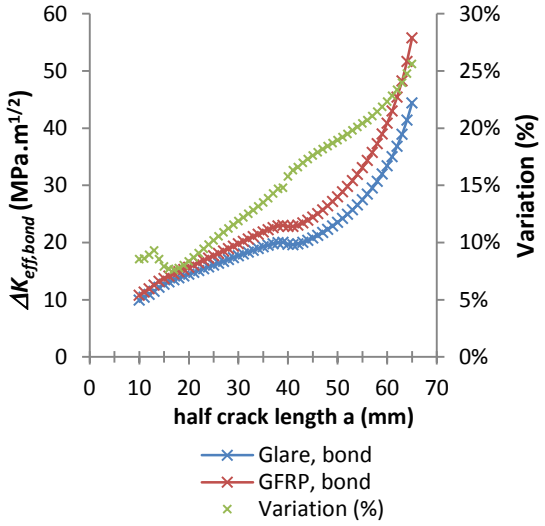

Figure 10-35 : ΔK_{eff} on bond face for Glare and GFRP straps; μ = 0.2 – applied stress = 60 MPa

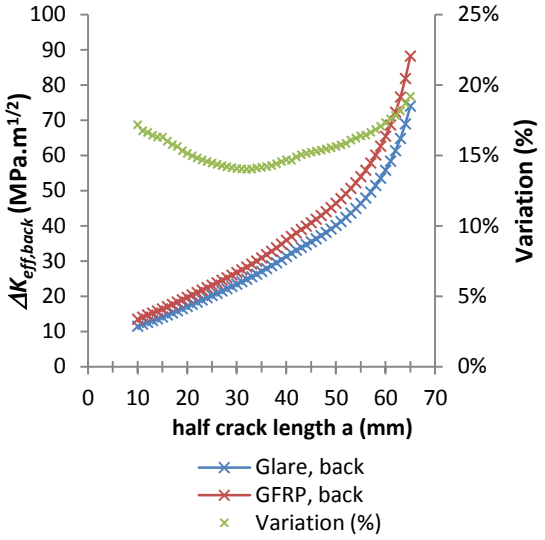

Figure 10-36 : ΔK_{eff} on back face for Glare and GFRP straps; μ = 0.2 – applied stress = 60 MPa

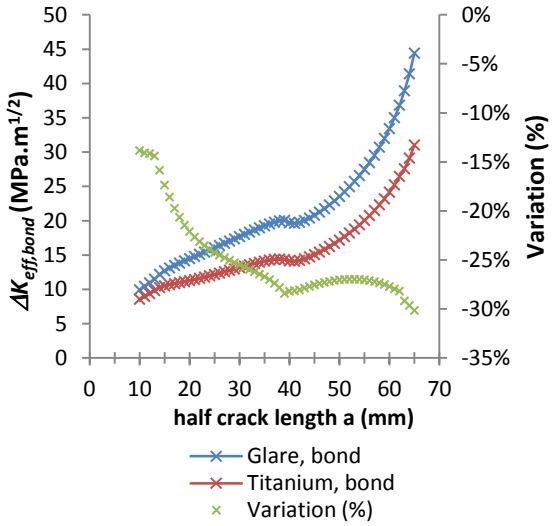

Figure 10-37 : ΔK_{eff} on bond face for Glare and Titanium straps; μ = 0.2 – applied stress = 60 MPa

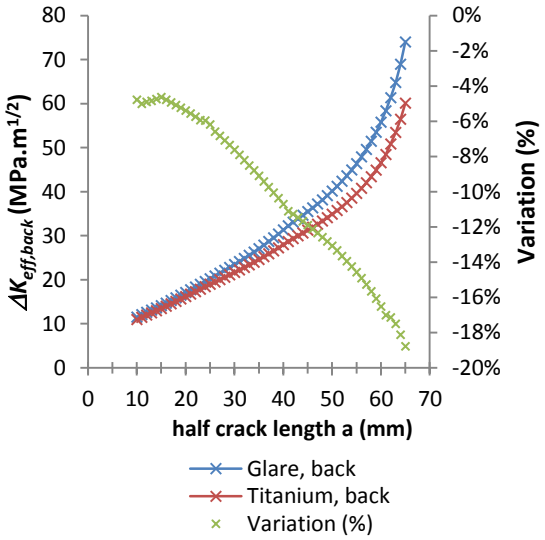

Figure 10-38 : ΔK_{eff} on back face for Glare and Titanium straps; μ = 0.2 – applied stress = 60 MPa

On the bond face, the largest improvement – largest variation – is observed for the CFRP strap. Titanium is second best followed by the aluminium strap. On the other hand, GFRP does not demonstrate an improvement compared to the Glare. As concerns the back side, the improvements are similar to the bond side, but the variations are reduced by a factor of 5-10%. Again, GFRP does not

demonstrate any improvement over Glare. **Figure 10-39** illustrates the weighted stress intensity factor range for each case of strap stiffness as a function of the crack length.

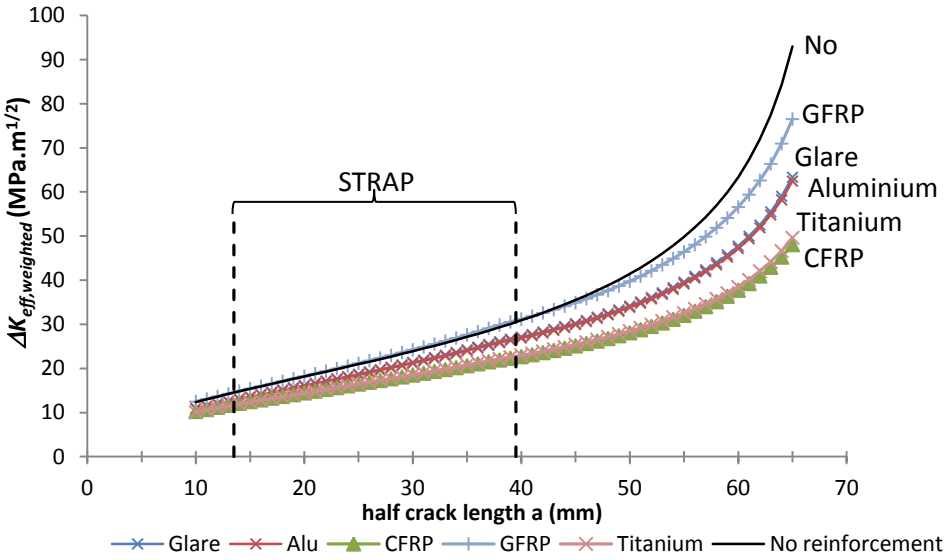

Figure 10-39 : Weighted stress intensity factor range for different strap stiffness

Figure 10-39 demonstrates that the different strap stiffness values result in similar overall behaviour but with different levels of reduction in $\Delta K_{eff,weighted}$. The smallest reduction relative to the no-reinforcement case was the GFRP strap that demonstrates no improvement compared to Glare. The largest reduction was in the CFRP strap. Table 10-1 shows that the ranking of the strap materials in $\Delta K_{eff,weighted}$ reduction is the same as the E value ranking, with CFRP the stiffest at 1.35 X 10^5 MPa and GFRP the least stiff at 0.46 X 10^5 MPa. This is also the ranking of strap thickness with CFRP the thinnest and GFRP the thickest.

10.5.2 Secondary bending stresses

Figure 10-40 to Figure 10-43 illustrate the bending stresses for all materials described above for an initial substrate crack length of 10 mm. For each case the bending stresses are calculated between the back face and the bond face under the maximum applied stress of 60 MPa. All results are compared to the Glare strap case.

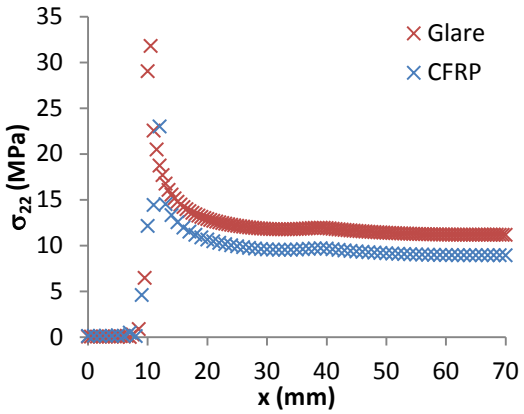

Figure 10-40 : Longitudinal bending stresses for CFRP strap

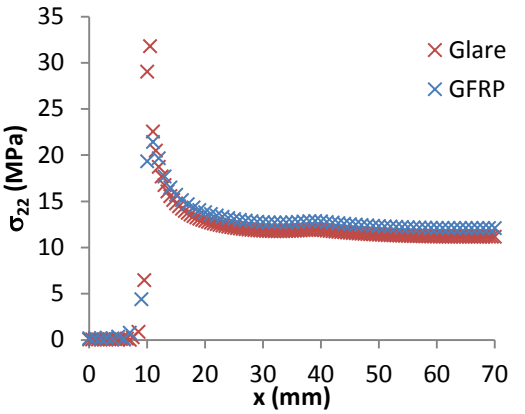

Figure 10-41 : Longitudinal bending stresses for GFRP strap

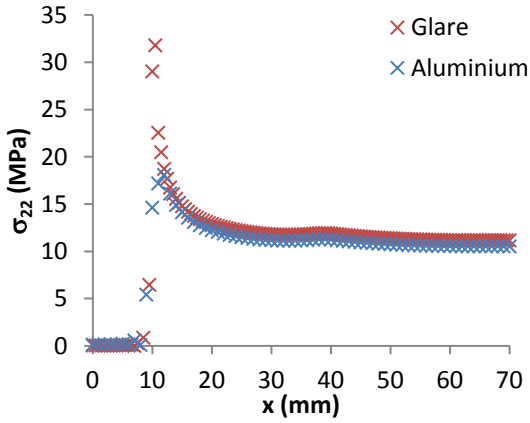

Figure 10-42 : Longitudinal bending stresses for Aluminium strap

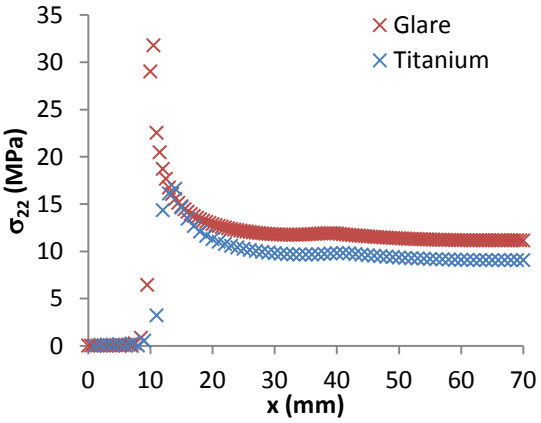

Figure 10-43 : Longitudinal bending stresses for Titanium strap

For all strap material case, the variation in bending stresses is less than 5 MPa compared to Glare. The bending is higher for the GFRP case while it is lower for CFRP, aluminium and titanium. Aluminium has got very similar bending stresses to Glare which may be explained by the fact that the thickness of the two straps are close and their modulus are close as well. GFRP values are slightly higher (1 MPa) which may be explained by the fact that the thickness is much higher than the Glare one (5.2 mm). Titanium and CFRP have got reduced stresses with difference of 3 to 5 MPa. These lower stresses may also be explained by the differences in thickness, which are reduced compared to Glare (2.1 and 1.8 mm). Hence these results suggest that the use of a thinner strap is better than a thick one in terms of secondary bending effects.

10.5.3 Thermal residual stresses

Figure 10-44 illustrates the substrate longitudinal thermal residual stresses as calculated from the FE analysis for each material case. This is obtained from the first step in the calculation that simulates the autoclave cure.

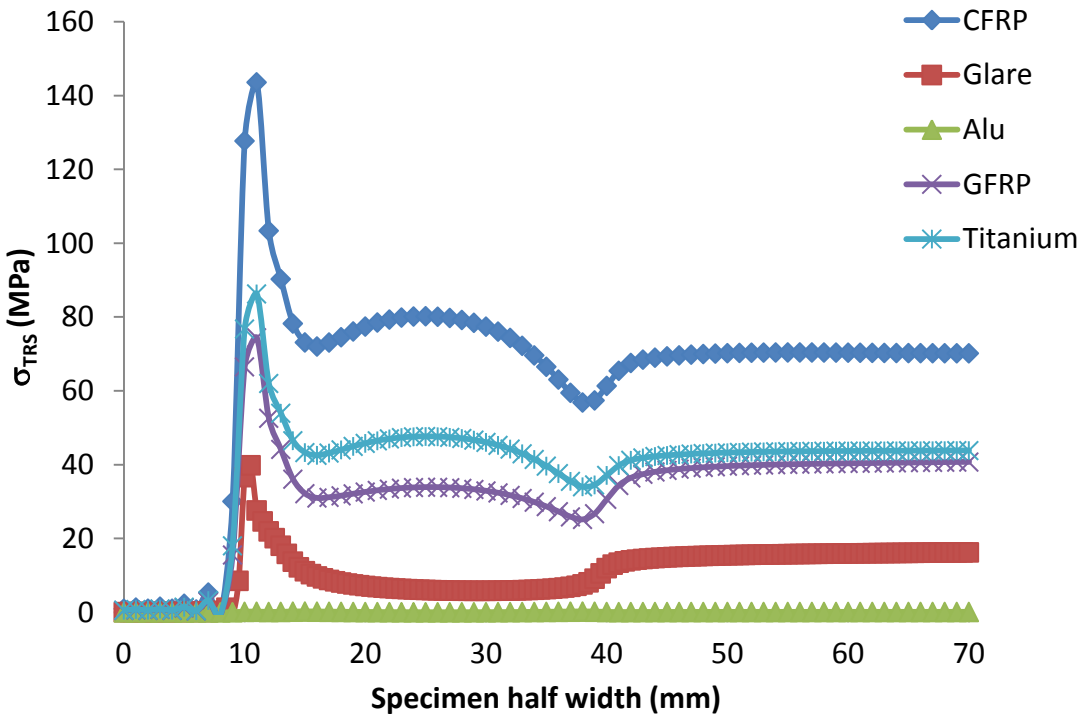

Figure 10-44 : Thermal residual stresses in substrate (longitudinal) for different strap materials.

It shows that CFRP has got the highest thermal residual stresses while Aluminium has got the lowest. The low values observed for aluminium is due to the fact that strap and substrate expand of the same amount during the curing process, hence there is no thermal residual stresses after curing. On the other hand, CFRP contracts (negative coefficient of thermal expansion) while the aluminium substrate expands. Hence when returning to room temperature, the strap and substrate tend to go in reverses directions which creates higher residual stresses compared to the other strap materials. Glare is the second lowest with thermal residual stresses of approximately 5-10 MPa as Glare contains layers of aluminium which limits its expansion. GFRP and titanium demonstrate higher thermal residual stresses than Glare with a range between 25 and 50 MPa.

As described in Chapter 08, the thermal residual stresses are taken into account in the calculation of the fatigue life through the equivalent stress intensity factor for residual stresses, $K_{res,equivalent}$.

10.5.4 Effect on fatigue lives

Using the weighted value of the effective stress intensity factor range shown in Figure 10-39, the stress intensity factor coefficient β were calculated and used for the evaluation of the fatigue lives. They are illustrated in Figure 10-45. The equivalent stress intensity factor for residual stresses, $K_{res,equivalent}$ – as defined in chapter 8 – that were also used for the calculation are illustrated in Figure 10-46.

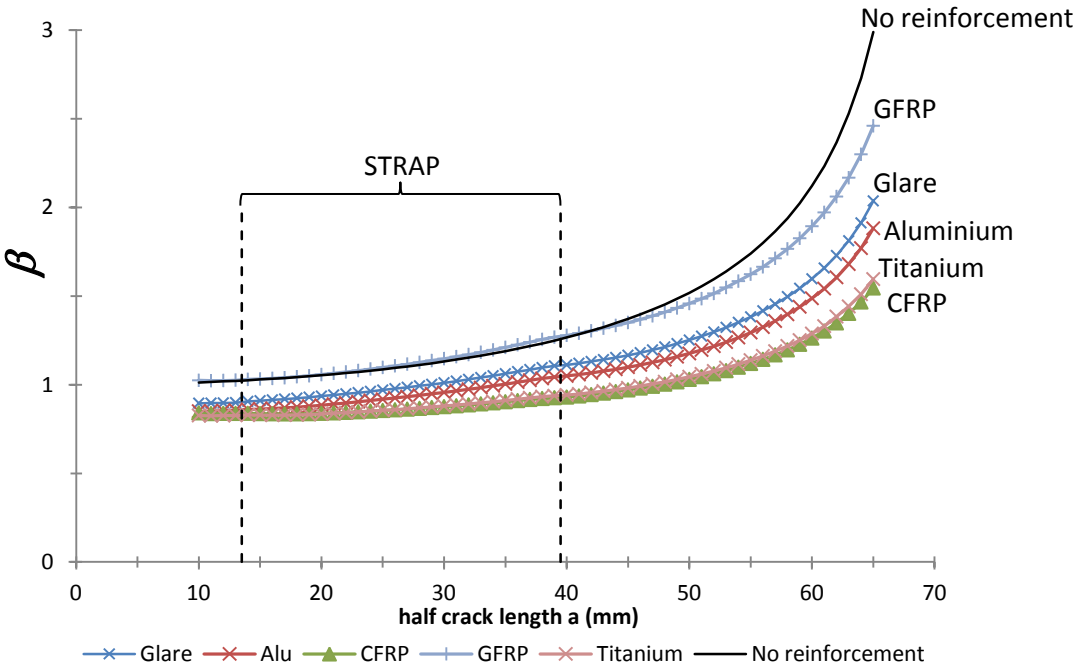

Figure 10-45 : Effective stress intensity factor coefficient for different material used for the strap

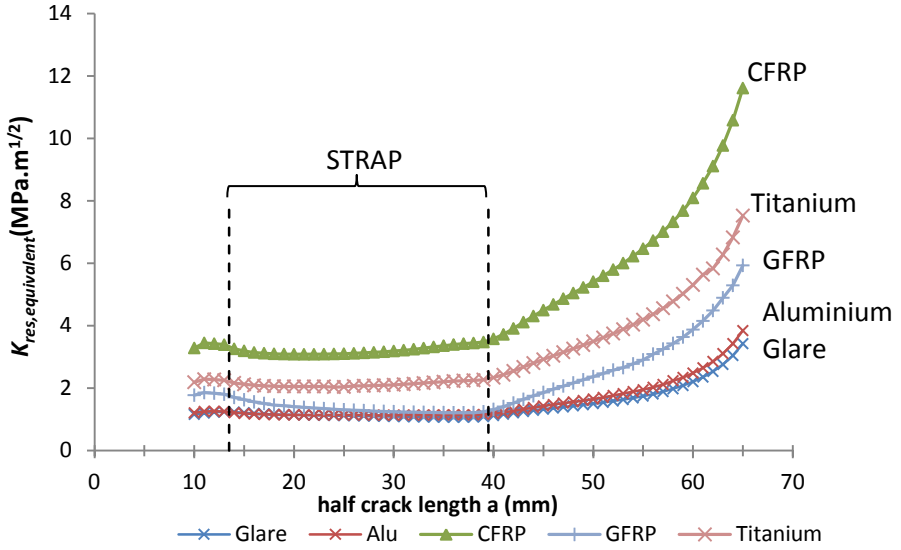

Figure 10-46 : Equivalent residual stresses for different material used for the strap

The values of $K_{res,equivalent}$ are minimal for the straps made of aluminium and Glare. The values are smaller than 5 MPa in the reinforced area but then quickly increase in the non-reinforced area.

Based on the values of β and $K_{res,equivalent}$, the fatigue lives are calculated using AFGROW. The results are illustrated in Figure 10-47.

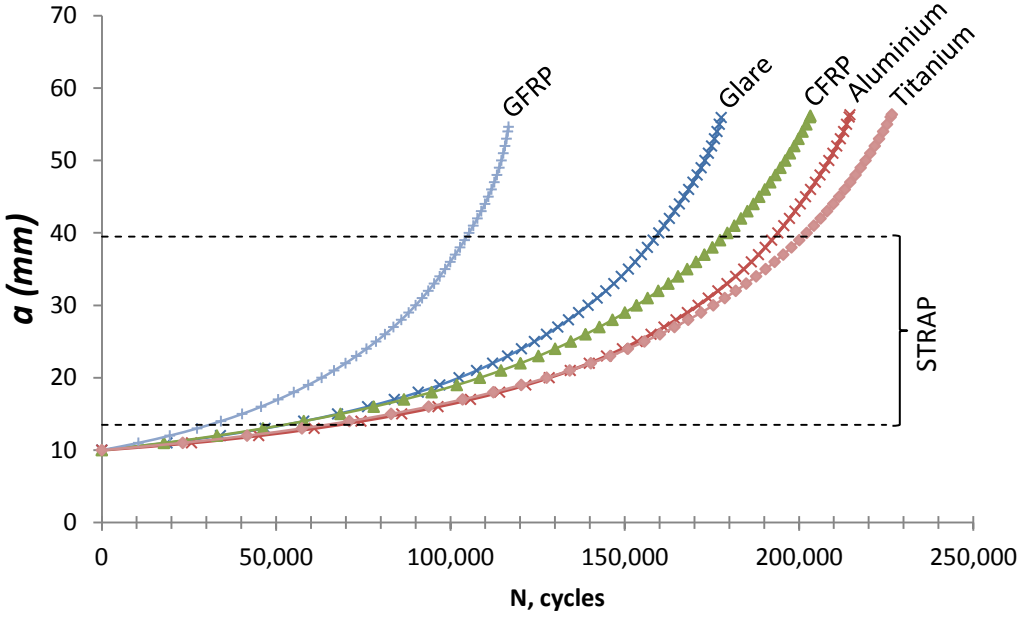

Figure 10-47 : Predicted fatigue lives for different strap materials

Table 10-3 : Fatigue lives obtained for strap material parametric study

Strap material	Life	α (CTE) (mm/mm/°C)	E (MPa)
Glare	177,686	1.63×10^{-5}	65,000
Aluminium	214,610	2.32×10^{-5}	71,000
CFRP	203,279	-0.3×10^{-6}	135,000
GFRP	116,668	7.0×10^{-6}	46,000
Titanium	226,629	8.60×10^{-6}	113,800

Titanium straps show the largest fatigue life with 226,629 cycles; an increase of 28% in comparison to the Glare straps. The shortest life is calculated for the GFRP strap with 116,668 cycles which is a decrease of -34%. CFRP and Aluminium straps also demonstrate larger lives compare to the Glare configuration with respectively 203,279 and 214,610 cycles.

The fatigue lives results can be explained as a combination of the stress intensity factor and the residual stresses. In fact, while CFRP demonstrated the largest improvement in terms of stress intensity factor reduction, the life is reduced compared to the other materials due to the presence of higher residual stresses. The GFRP life is smallest as would be expected from figures 10-20 and Figure 10-45.

Hence, the fatigue life results from a combination of residual stresses and secondary bending effects which are directly linked to the thickness of the strap. Both effects balance each other as demonstrated from the graphs above.

10.6 Summary

- A triangular disbond of size up to 26 mm by 52 mm changes ΔK_{eff} by only a few percent (less than 5%) and consequently does not influence fatigue life significantly.

- The effect of changing strap width and thickness at constant μ of 0.2 was investigated. The use of a wider, thinner strap proved beneficial, with a 15 to 25% reduction of the stress intensity factors and consequently an increase in the fatigue lives of 15%. Both increased width and decreased thickness may play a role.
- Changing the thickness of the substrate from 5 mm to 10 mm, keeping the same stiffness ratio of 0.2 and having a wider strap with 3.7 mm thickness did not have a significant effect on ΔK_{eff} The fatigue life was increased by less than 1%.
- The effect of strap materials with different stiffness (E) values was investigated. Straps of Glare, Aluminium, Titanium, CFRP and GFRP were modelled, and strap thickness changed to keep stiffness ratio constant at 0.2. The greatest reduction in ΔK_{eff} was in the CFRP strap, and the least in GFRP. The ranking of the strap materials was in the order of their stiffness (CFRP greatest at 1.35×10^5 MPa, and GFRP the least at 0.44×10^5 MPa) and their strap thickness (CFRP the thinnest and GFRP the thickest). When calculating fatigue lives where values of ΔK_{eff}, and $K_{res,equivalent}$ are used, titanium strap samples had the longest life and GFRP the smallest.

The results of the calculations of the fatigue lives are summarised in Table 10-4.

Table 10-4 : Results of fatigue lives for parametric study using ReSLIC

Specimen type	Fatigue life (nb, cycles)	Variation in fatigue life (%) (= [ref – case]/ref)
AIRstream M(T) – ref. coupon	**175,868**	N/A
Small disbond	175,931	< 1%
Large disbond	176,024	< 1%
Full disbond	175,918	< 1%
Wide strap; μ = 0.2	202,499	+ 15%
Thick substrate; μ = 0.2	176,629	< 1%
Aluminium strap	214,610	+ 22%
CFRP strap	203,279	+ 16%
GFRP strap	116,668	**- 34%**
Titanium strap	226,629	**29%**

Chapitre 11 : Discussions

11.1 Introduction

This discussion is a critical review of the parameters that are affecting the efficiency of the BCR technology. It is built in two levels. The first level is an analysis at the coupons scale, discussing the results previously developed in Chapter 10 together with other studies conducted on the BCR technology. The second level of these discussions is at the panel level where it studies the effect of a greater scale on the BCR technology. For both levels, the influence on the stress intensity factor and the fatigue life will be outlined.

11.2 Coupons level

11.2.1 Influence of geometry, materials and mechanical interaction in BCR

The tests reported in Chapter 4 showed a life improvement ratio of 1.17 which was much smaller than the life improvement of 2.7 obtained previously in the BCR samples [5]. This change is directly related to the changes in crack growth rate in the two samples as illustrated in Figure 11-1.

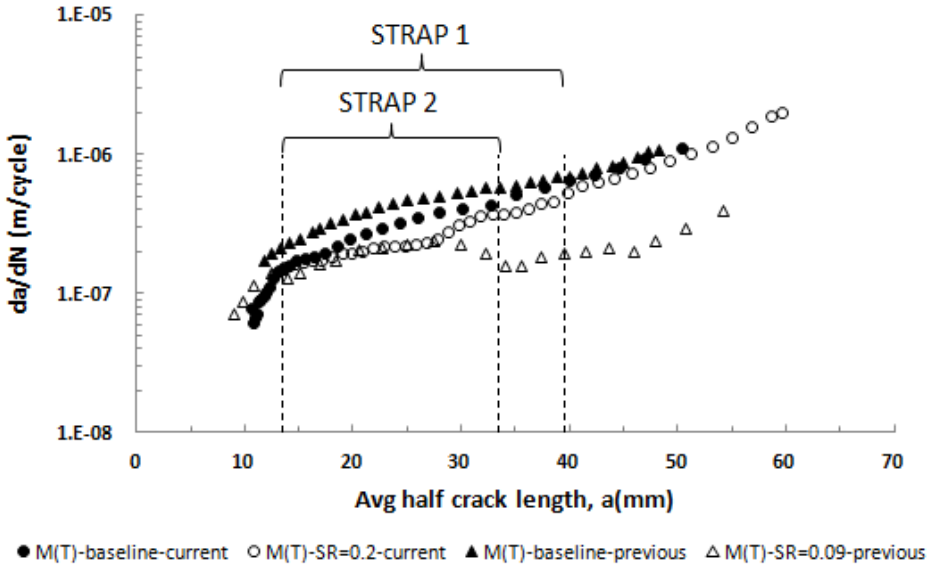

Figure 11-1 : Fatigue crack growth rates for M(T) specimens under loading of σ_{max} = 60 MPa and R = 0.1 for current design (μ = 0.2) and previous design (μ = 0.09)

The difference in crack growth rate between the baseline and the reinforced case was of one order of magnitude (10^{-7} m/cycle) for the AIRstream specimen while the reduction was 2-3 times greater in the BCR case. These changes in crack growth rates are directly related to changes in stress intensity factors at the substrate crack front. The comparative FE analysis conducted in Chapter 10 that looked at the differences between the two specimens pointed out that the stress intensity factor values for the AIRstream case were higher than the one of the BCR geometry. It was attributed to the difference in secondary bending that was higher for the AIRstream case than the BCR one.

Because many parameters were changed between the AIRstream design and the BCR one, it is difficult to draw a conclusion on a single parameter that contributed to a reduction in secondary bending in the BCR case. There is an interaction between the geometry, material and mechanisms; the question is how they affect the ΔK_{eff} of the substrate crack front? The next sections will review each parameters and mechanisms individually.

11.2.2 Effect of substrate thickness on stress intensity factor

The $\Delta K_{eff,weighted}$ (Chapter 8) can be reduced if a thicker substrate is used with a stiffness ratio of 0.09 as illustrated in the previous section (substrate of 10 mm opposed to substrate of 5 mm with different stiffness ratio). However, in the analysis conducted in Chapter 10, there was little change in $\Delta K_{eff,weighted}$ with substrates of 5 and 10 mm in thickness using the same stiffness ratio of 0.2. Hence this analysis suggested as a first rule that using a thicker substrate and a reduced stiffness ratio gives more reduction than a thicker substrate at the same stiffness ratio. Nevertheless, these effects are not solely responsible for a change in $\Delta K_{eff,weighted}$ and the effects of the strap geometry must also be considered.

11.2.3 Effect of strap width

Past studies conducted on panels [5] showed that wide, thin straps had longer lives than thick, narrow ones. This was also demonstrated in chapter 10 with a reduction of $\Delta K_{eff,weighted}$ for wide, thin straps. The FE analysis conducted in

Chapter 10 showed reductions for wide thin strap of up to 35% on the bond side and 20% on the back side in comparison to the narrow, thick one. This resulted in a reduction of fatigue crack growth rates and increased life.

This was also verified through experiments with tests conducted by Scott in [201] where two reinforced specimen with a stiffness ratio of 0.134 were tested. The thick and narrow strap was made of Glare 2A-6/5 (0.4), 16 mm wide while the wide and narrow one was made of Glare 1-3/2 (0.4), 32 mm wide. The narrow strap showed almost no sign of retardation while the wide one demonstrated an improvement ratio of 1.09.

Hence the change in retardation effect for the wide strap may be attributed to a longer crack bridging effect due to the wider reinforced section, which results in a reduced stress intensity factor. This is confirmed in Figure 10-20 where under the same applied stress, the weighted stress intensity factor appears lower for the wide strap than for the narrow one from an early stage of the substrate crack length, approximately 17 mm. One of the major contributors to that change, as illustrated in Chapter 10 is the effect of secondary bending that is larger for the narrow strap than the wide one.

11.2.4 Effect of strap position

No calculations have been performed here on the effect on the stress intensity factor of the position of the BCR from the initial substrate crack. Nevertheless, it was proved in [202] that the best position is closer to the crack tip in the coupon case. In fact this will cause a reduction in fatigue crack growth rate in the early stages of the crack propagation which will increase the overall fatigue life of the specimen as early stage retardation are preferable to later stage retardation.

11.2.5 Effect of strap material on stress intensity factor

Several strap materials have been investigated through FE analysis in the current project under the condition that the stiffness ratio was kept at 0.2. It showed that with no disbonding, the effect of materials on the stress intensity factor was very variable with titanium and CFRP showing the best reduction of the stress intensity factor (Figure 10-45). Glare only resulted in a lesser

reduction of $\Delta K_{eff,weighted}$ with a similar reduction to aluminium. Figure 11-2 illustrates the value $\Delta K_{eff,weighted}$ for a half crack length of 30 mm for all material cases that have been studied as a function of strap thickness.

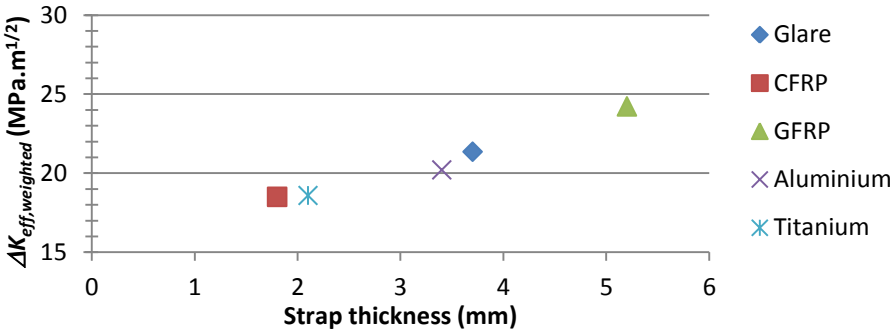

Figure 11-2 : Stress intensity factor as a function of thickness for different strap material under the same reinforcement ratio of μ = 0.2.

It shows that the stress intensity factor is reduced for thinner straps. This was explained in Chapter 10 through the effect of secondary bending. Hence this suggests that thinner is better.

Because the effect cannot be reduced to the thickness only under the condition that μ = 0.2 for all strap materials, the results are also linked to the stiffness of the strap. Figure 11-3 illustrates the value $\Delta K_{eff,weighted}$ for a crack length of 30 mm for all material cases that have been studied as a function of strap modulus.

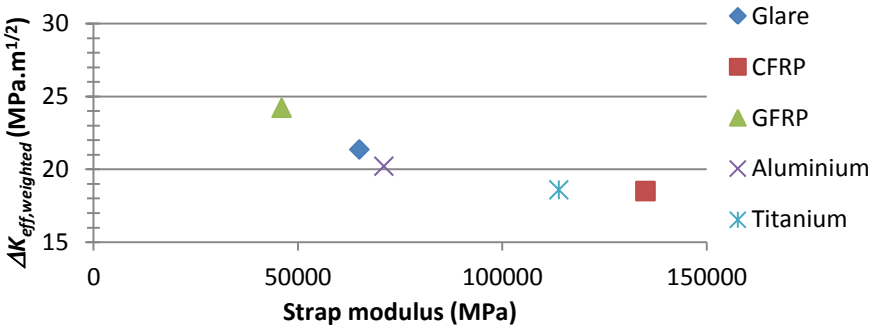

Figure 11-3 : Stress intensity factor as a function of stiffness for different strap material under the same reinforcement ratio of μ = 0.2.

It shows that the stress intensity factor is reduced for stiffer straps with a reduced stress intensity factor for CFRP and titanium. Hence the results

summarized here show that under the same stiffness ratio (0.2 here), using a thinner and stiffer strap results in lower values of the stress intensity factor.

11.2.6 Effect of disbond on stress intensity factor

Disbonding showed no effect on the stress intensity factor when limited to a small amount of the interface such as 14% as illustrate in Chapter 10. The restriction to a limited triangular area of 52 by 26 mm may explain the absence of changes on $\Delta K_{eff,weighted}$ as the disbonding is not significant enough to affect the results. Nevertheless, a larger amount of disbonding may affect the results.

This was suggested by the modelling in ReSLIC of the delamination found in SENT specimens, a geometry that had been tested during the course of the project [163]. Details of the geometry of the specimen are given in Figure 11-4. This specimen was also made of a 2024-T351 aluminium alloy substrate measuring 400 mm by 140 mm and 5 mm thick with a Glare 2A-6/5 (0.4) reinforcing strap measuring 100 mm wide by 200 mm long.

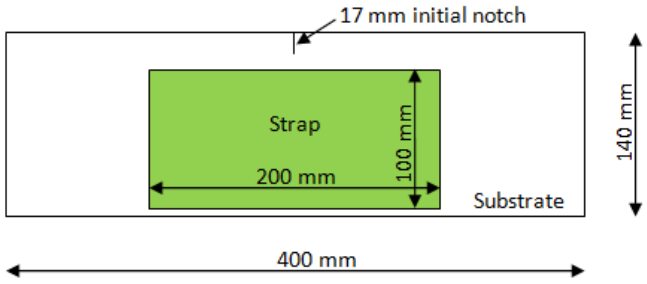

Figure 11-4 : Reinforced SENT specimen geometry

Constant amplitude fatigue tests carried out on these specimens [163] demonstrated larger amounts of disbond compared to the reinforced M(T) specimens as illustrated in Figure 11-5 with almost half of the reinforced area disbonded.

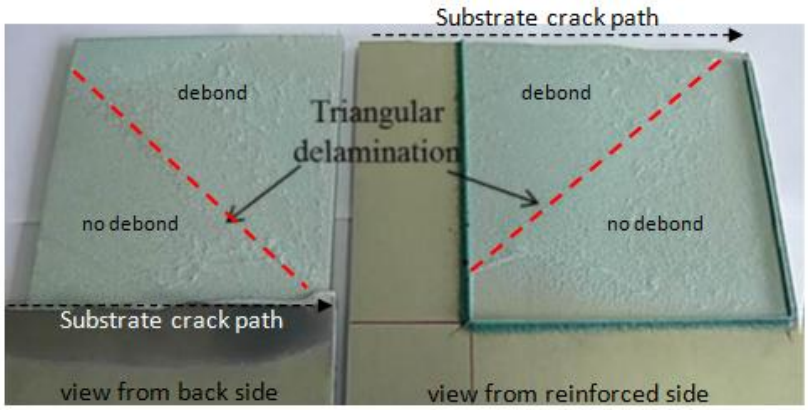

(Debond is triangular in shape and covers almost half of the reinforced area as shown in the schematic representation below)

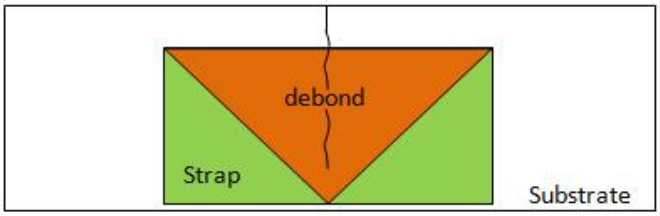

Figure 11-5 : Disbond characteristics for SENT specimen

This was confirmed by NDT inspection of the specimen after completion of the test that demonstrated a triangular like shape of disbonding through C-scanning of the coupon (Figure 11-6)

ReSLIC modelling results showed the same amount of disbonding resulting in an increase of the stress intensity factor as illustrated in Figure 11-8. The value given here is the weighted stress intensity factor range. The difference with a case with no disbonding is starting very early with a crack length of approximately 50 mm and increases as the crack grows with a very well-marked effect of disbonding passed 80 mm where the difference in stress intensity factor becomes larger than 40 MPa.$m^{1/2}$.

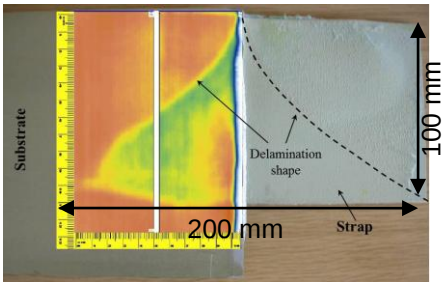

Figure 11-6 : Experimental evidence of disbonding for reinforced SENT specimen [163]

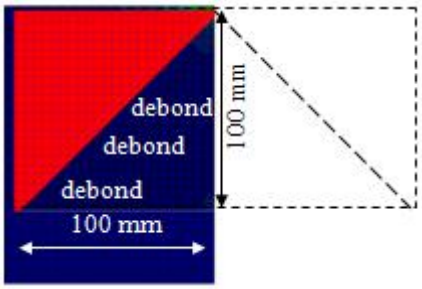

Figure 11-7 : Disbond model for reinforced SENT specimen (showing half specimen)

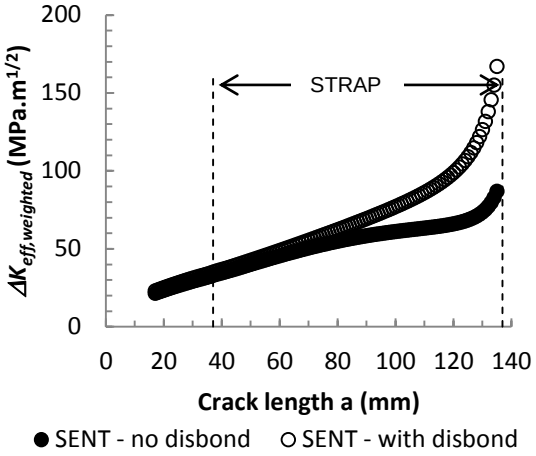

Figure 11-8 : Effect of disbonding on weighted stress intensity factor for reinforced SENT specimen

Hence, while 14% aerial delamination showed limited effect in the stress intensity factors, 50% showed a much larger effect on the stress intensity factor. This different effect on the stress intensity factor may be attributed to the difference in specimen geometries between the M(T) specimen and the SEN(T) specimen where delamination is more likely to develop in the SEN(T) case than the M(T) case.

In order to understand the reasons for the larger amount of disbond in SENT as opposed to the reinforced M(T) specimens, the level of strain energy release rate in the SENT specimen were investigated using the results from ReSLIC that returns the values of the strain energy release rate along the delamination front.

For a 38 mm crack length there are G values of **0 J/m^2** and **463 J/m^2** for mode I and mode II for the SEN(T) specimen while for the reinforced M(T) specimen they are respectively **0 J/m^2** and **25 J/m^2** for a similar crack case (values given

here are maximum values along the crack front). Hence the difference in delamination advance can be explained by the level of SERR that are quite different from one geometry to the other (factor of almost 20 for mode II).

11.2.7 Effect of thermal residuals stresses

In the case of Glare straps used in the Airstream geometry, residual stresses are tensile [163] of the order of 15 to 20 MPa on the reinforced side and with reduced stresses of 10 to 15 MPa on the back side. The tensile nature of these residuals stresses will reduce the retardation effect as they will contribute to higher values of stress intensity factors. The parametric study conducted in Chapter 10 also showed reduced residual stresses for Glare that are similar to aluminium and much reduced compared to CFRP, titanium and GFRP. Hence this effect, coupled to the effect of secondary bending reported in the previous chapters will affect the stress intensity factor ΔK_{eff}.

No investigation has been carried out regarding the effect of the strap geometry on the TRS in the current work, but Boscolo [50] conducted an analysis using titanium straps. Under equivalent cross section (same stiffness ratio μ), it showed that the wider and thinner the strap, the lower the residual stresses, and in consequence the residual stress intensity factor was reduced. If the strap thickness was kept constant and the width increased, the TRS increased. Considering the same width and increasing the thickness resulted in higher TRS, with a factor of 1.5 for a thickness increased from 2 to 6 mm (width was 20 mm).

11.3 Panels level

11.3.1 Effect of substrate material on retardation

In addition to the use of BCR, the life of a structure can be improved with the use of a material that present reduced crack growth rates. Brick [203] and Demri [161] studied crack propagation in non-reinforced M(T) coupons made of 2199 Al-Li and 2024 HDT respectively for a case of variable amplitude loading. Figure 11-9 is a comparison of the fatigue life data. Each coupon was tested under the same variable amplitude spectrum, clipped at 101 MPa and gated at 25 MPa. It shows a better result for the 2199 al-lith with a fatigue life of 269,824 cycles compared to 222,788 cycles for the 2024 HDT case. This is explained by the difference in crack growth rates illustrated in Figure 11-10. It shows the constant amplitude fatigue crack growth data for 2024 HDT (data provided by Alcoa) and 2199 Al-Li (data collected at Cranfield on C(T) specimens [204]) under R = 0.1 and R = 0.7. The crack growth rates for the 2024 HDT material are greater than the 2199 Al-Li, especially at the largest values of ΔK. Hence specimen made of a material that present reduced fatigue crack growth rate properties will exhibit a longer crack growth life.

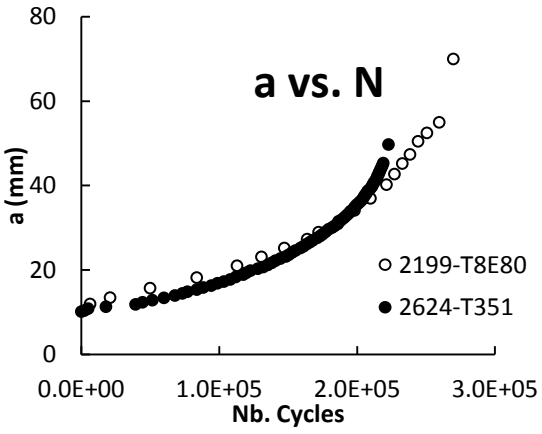

Figure 11-9 : a vs. N for M (T) baseline specimens (2199 and 2624) under spectrum loading with maximum spectrum stress of 101 MPa.

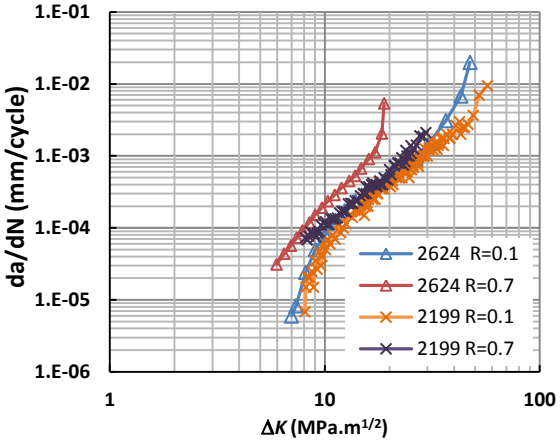

Figure 11-10 : Constant amplitude fatigue crack growth rate for 2624-T351 and 2199-T8E80 at R = 0.1 and R = 0.7

Despite the comments made above, this was not verified for the panel tests. As outlined in the panel chapter, 2024 HDT skins were used as well as 2199 al-lith. The baseline 2024 HDT panel performed better than the 2199 al-lith one with respective fatigue lives of 69,000 and 61,000 cycles for a crack length of 110 mm. The overall life was also better for the 2024 HDT baseline panel with 231,938 cycles as opposed to 206,694 cycles for the 2199 al-lith baseline panel (Figure 11-11). The crack growth rates illustrated in Figure 11-12 show higher crack growth rates for the 2199 al-lith panel compared to the 2624 HDT panel. Those results could be explained by the fact that the 2024 HDT baseline panel was tested at slightly higher stresses than the 2199 al-lith baseline panel, 2% higher. This could be responsible for a larger plastic zone when the peak loads are applied to the panel which could increase the retardation effect. It was also noted during preparation of the 2199 panel that there were local variations in skin thickness caused by the machining process. It is possible that the skin of the 2199 was locally reduced in thickness. This would promote a temporary enhancement in local stress, and hence in local ΔK, causing increased crack growth rates.

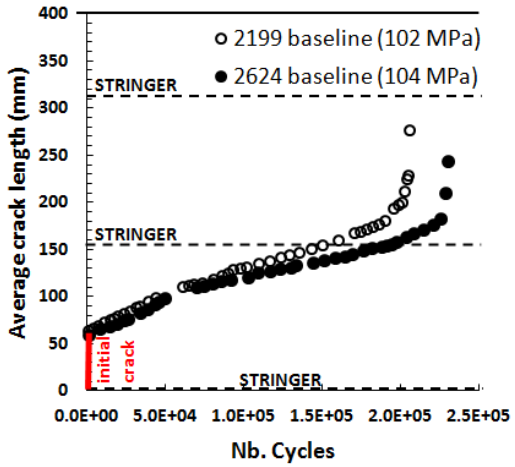

Figure 11-11 : Fatigue crack growth life for 2199 al-lith and 2024 HDT panels

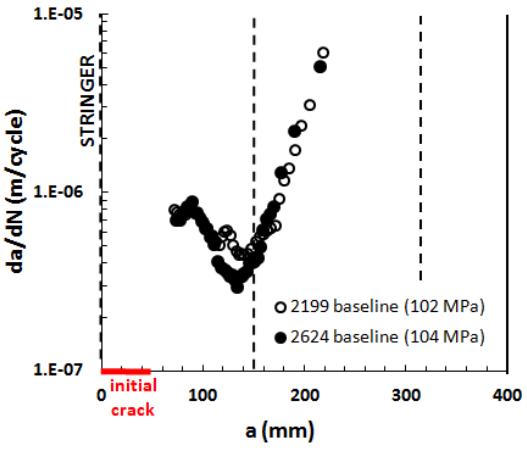

Figure 11-12 : Fatigue crack growth rates results for 2199 al-lith. baseline and 2024HDT baseline panels

Different results were observed for the reinforced panels with similar crack growth rates for the 2024 HDT panel and the 2199 al-lith one (Figure 11-13),

but with a slightly longer life for the 2199 al-lith panel compared to the 2024 HDT one, at equivalent crack length (Figure 11-14).

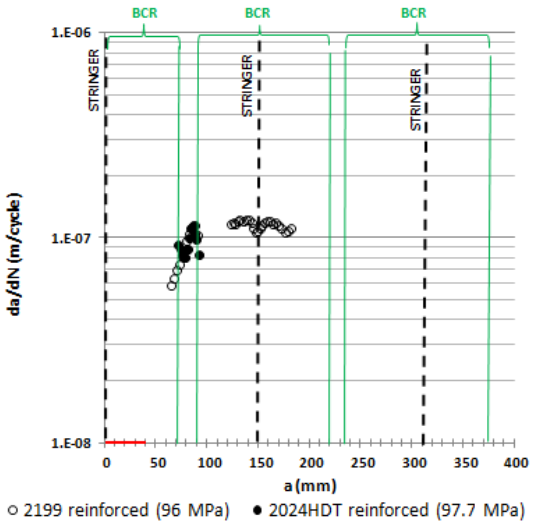

Figure 11-13 : Fatigue crack growth rates results for 2199 al-lith. and 2024HDT reinforced panels

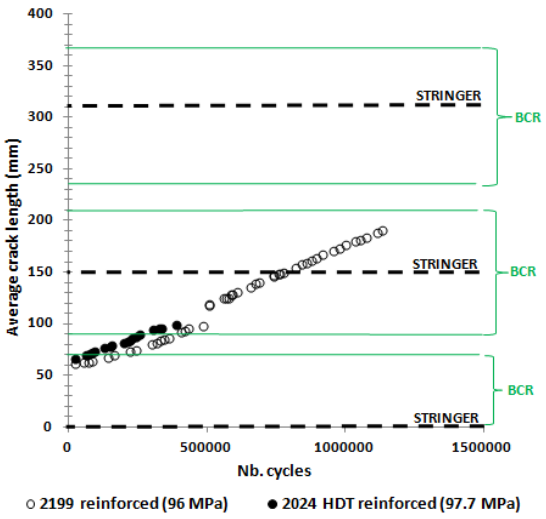

Figure 11-14 : Fatigue crack growth life results for reinforced 2199 al-lith. and reinforced 2024HDT panels

11.3.2 Panel design vs. coupons design

As developed in Chapter 10, secondary bending reduces the overall effect of BCR with an increase of the stress intensity factor weighted average. This was demonstrated at the coupons level with the difference observed between the Airstream coupons and the BCR one as well as through the parametric study of strap width and strap material. At the coupons level, this can be seen as a lack of stiffness of the overall coupon that does not limit the bending. In the case of skin-stringer panels, the stringers will limit the bending. Comparisons of the reinforced coupons and the reinforced panels tested under variable amplitude fatigue show large differences in the life improvement ratio with 1.24 for the coupons [161] and more than 5 for the panels. Using the strain gauge measurements from the calibration, Table 11-1 illustrates the amount of secondary bending obtained for the panels.

Table 11-1: Calculated secondary bending for baseline and reinforced panel based on strain gauge readings from calibration – comparison to coupons

Panel	Skin	BCR	Stress outer skin (MPa)	Stress inner skin (MPa)	Bending stress (MPa)	Bending %
P_COU_01	2024HDT	No	111	108	+1.5	1.5%
P_COU_02	2024HDT	Yes	93.5	90.6	+1.45	1.5%
P_ALC_01	2199 Al-lith	No	97.6	109	**-5.7**	**5.6%**
P_ALC_02	2199 Al-lith	Yes	89.0	98.4	-4.7	4.9%
P_COU_03	2099 - T81	Yes	115	117	-1	1%
M(T) Airstream design (current)		Yes	87	68.6	**9.2**	**15.3%**
M(T) BCR design (former)		Yes	68.8	59.5	4.7	7.8%

Table 11-1 demonstrates that the amount of bending is fairly small in the panels with an absolute maximum of 5.7 MPa for the al.-lith. baseline panel while bending stresses of up to 9 MPa were calculated on the M(T) specimens. Hence there is 5.6% of bending in the panels as opposed to 15.3% for the specimens (% of bending = bending stress/applied stress), a ratio of more than 2 between these two configurations. It shows that the panels are less subjected to secondary bending due to the presence of the stringer. This was confirmed by Demri [161], where measurements showed up to 20% of bending in the reinforced M(T) coupons for an applied stress of 101 MPa. Hence these measures confirmed the detrimental effect of secondary bending.

11.3.3 Geometry effect: ISP vs. bolted panels

Two designs were tested during the panel tests; bolted and integrally machined. An ISP design might be preferred in a real structure as the reduced number of

rivet hole reduces the possible sites of crack initiation. However the bolted design is likely to have increased damage tolerance [7].

As no baseline was tested for the ISP panel no comparison in improvement ratio can be made. Nevertheless crack growth behaviour and crack growth rates for the 3 reinforced panels can be compared. Figure 11-15 shows the fatigue life of these three panels and Figure 11-16 shows the associated crack growth rates.

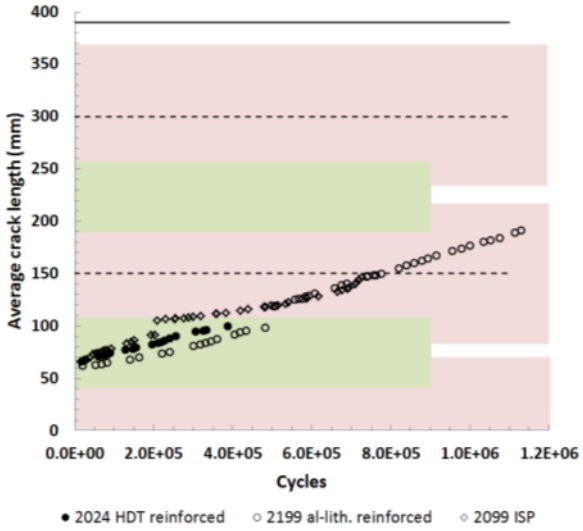

Figure 11-15 : Fatigue life for 2024 HDT reinforced, 2199 al-lith reinforced and 2099 ISP reinforced panels

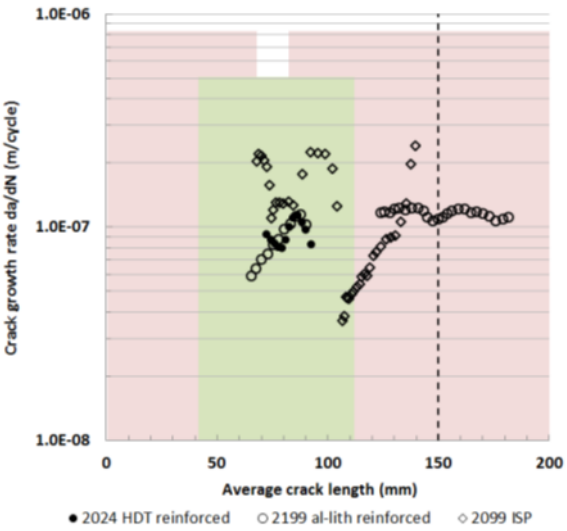

Figure 11-16 : Fatigue crack growth rates for 2024 HDT reinforced, 2199 al-lith reinforced and 2099 ISP reinforced panels

Very similar behaviour is observed for the 2 bolted panels with a longer life for the 2199 panel that can be attributed to the fact that the re-initiation was not successful in the 2024 HDT panel. Crack growth rates are also similar. The ISP panel has a shorter life at equivalent crack length – 100 mm – and higher crack growth rates as illustrated in Figure 11-16. The 2199 panel clearly demonstrates the effect of strap for crack lengths between 130 and 180 mm with an almost constant crack growth rate. This was not observed in the ISP panel. Hence those results suggest that the effects of BCR are more beneficial in the case of the bolted panel than the ISP one. It is also interesting to notice the load re-distribution in the two configurations that lead to different failure in unexpected

areas. Those were areas of stress concentration as well as areas of possible tensile residual stresses due to friction stir welding (ISP panel).

Nevertheless, the stiffness ratio μ is different between the ISP and the bolted panel with respectively 0.12 and 0.26. Hence it shows a lower level of reinforcement for the ISP panel which may explain the reduced life and the reduced effect of the BCR. The strap loading system is also different with directly loaded strap (straps loaded through the gripping system) for the bolted panel and shear loaded straps for the ISP (straps are not loaded in the gripping system). Hence less stress is transferred to the straps for the ISP panel as opposed to the bolted configuration.

Chapitre 12 : Conclusions

A comprehensive analysis of the use of Bonded Crack Retarders for lower wing applications has been successfully conducted through testing and finite element analysis. It contributed to a better understanding of the interaction of all parameters and mechanisms of BCR, hence allowing the designer to make the right choice regarding the design of the crack retarder.

1- Fatigue tests performed on reinforced M(T) coupons with a substrate 5 mm thick and a stiffness ratio of 0.2 demonstrated a life improvement of **17%.** This was a much lower improvement compared to **170%** that was obtained in the first project for 10 mm substrate with a reinforcement ratio of 0.09.
2- Skin-stringer panel tests demonstrated fatigue crack growth rates reduced by a factor of **up to 5-6** from the baseline with a life improvement of **more than 5** for the bolted reinforced panels. The reinforced ISP panel did not show a larger life compared to the reinforced bolted one (730,000 vs. $1.13x10^6$ cycles) but it demonstrated the smallest reduction in crack growth rate in the reinforced area.
3- A series of static and fatigue tests were performed in order to characterize the behaviour of the adhesive system employed. These data were used in a design tool to calculate the delamination progress.
4- A finite element design tool was developed in order to get a better understanding of the interacting mechanisms present in BCR and to conduct a parametric study. Thermal residual stresses, disbonding, nonlinear mechanisms and crack front asymmetry were considered in the model.
5- The finite element design tool was validated through a comparison with fatigue tests. The constant amplitude fatigue lives were predicted with an **error of 16%**.
6- Previous studies as well as use of the design tool to conduct a parametric analysis showed that :

– Disbonding has **no effect** on the substrate crack stress intensity factor for the M(T) case. For SEN(T) specimen, this effect is **well marked**.

- A wider strap is preferred to a narrow one – at equivalent stiffness ratio – with an **increase of 15% on fatigue life** that is attributed to a longer effect of the crack bridging mechanism. This was demonstrated through experimental results as well.
- A thicker substrate – at equivalent stiffness ratio – showed **no change** in improvement. With a thicker substrate and a reduced stiffness ratio, there is a major improvement as shown by the BCR case.
- Analysis of the stress intensity factor showed **reduced K values** for Aluminium, titanium and CFRP as opposed to Glare (up to 15 $MPa.m^{1/2}$). GFRP showed **higher values** (up to 10 $MPa.m^{1/2}$). This was verified in terms of fatigue lives with changes in the improvement ratios due to thermal residual stresses. Also, because of the stiffness ratio kept constant, the influence of strap thickness was verified with the conclusion that thinner is better due to a reduction in secondary bending effect for thinner straps.

7- It was demonstrated throughout the study that secondary bending is one of the major mechanisms defining the effect of BCR. Increase in secondary bending for the Airstream coupons geometry demonstrated a reduction in fatigue life improvement. This was proven through testing and FE analysis. That is why reducing the secondary bending effect is beneficial to fatigue life, as proven during the panel tests where bending was reduced due to the presence of the stiffeners (reduction of up to 10%).

Chapitre 13 : Future work

13.1 Application of ReSLIC to panel cases

ReSLIC, in its current version, was defined in order to conduct a parametric analysis at a coupons level in order to understand what would be the best BCR configuration. To that end it was developed such that a user could enter any geometry of an M(T) or SENT specimen associated to a rectangular shape BCR patch and ReSLIC will return delamination propagation and the stress intensity factor K as a function of crack length, allowing for the post-processing of fatigue life and crack growth rate. Hence, the geometry of the substrate is a limitation of ReSLIC and applying ReSLIC to a panel case would not be possible directly.

Nevertheless, some of the modules that define ReSLIC could be used for panel applications, and in particular the delamination module that calculates whether or not delamination progresses. In fact the calculation is based on the coordinate system of the BCR patch and if this are well defined initially, it will then be possible to use the *delam.py* script for delamination propagation. One requirement would be the definition of delamination initiation that could be either implemented as it is currently in ReSLIC, with delamination propagating when the main crack enter the strap or, one addition to the current calculation would be to base it on the evaluation of the adhesive through thickness stresses and in plane shear stresses. Use of that method will assume that delamination takes place at the interface between the strap and the skin substrate and this will need to be confirmed through NDT or cross section analysis of the current panels that have been tested.

In addition to the location and initiation of delamination, other assumptions that were considered for the coupons case were the absence of damage on the strap and the use of a straight main crack through the substrate thickness. Regarding the damage of the strap, this assumption could also be considered for the panel modelling as no damage were observed on the reinforcements. Regarding the straight crack front, this assumption could be kept as is for the bolted panel, but it will need to be revised for the ISP cases as curvature of the

crack front is observed in that case and needs to be considered for life calculations (Figure 13-1).

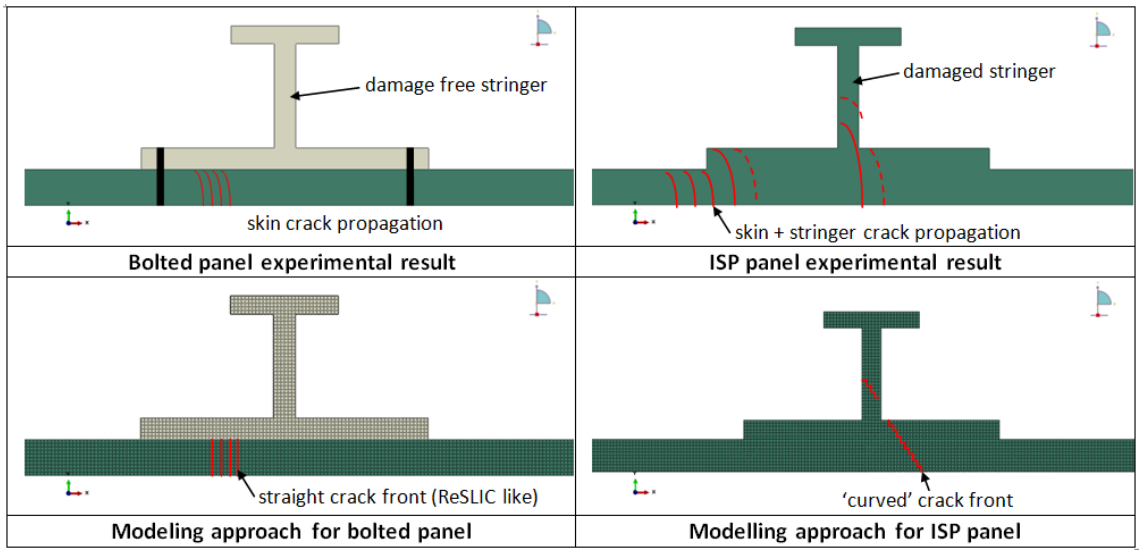

Figure 13-1 : Modelling approaches for bolted panels and integrally machined panels

The current method used in ReSLIC could be adapted to any node in the midline cross section of the panel where the crack is propagating. Otherwise, one method that could be used to calculate the curved crack front and that was suggested earlier in the thesis would be Hosseini-Toudeshky's method [90]. Both methods will consider a crack front that propagates in line through the centreline of the panel.

Regarding the implementation of the calculation in an algorithm similar to ReSLIC, a two steps calculation may be necessary for the panel case with first a preparation of the CAD file of the panel and the meshing of the geometry by the user and then in a second time, once all the geometry has been meshed and the rivet have been defined through specific elements – truss and coupling for example – the mesh may be used to automate the crack and delamination propagation as illustrated below (Figure 13-2).

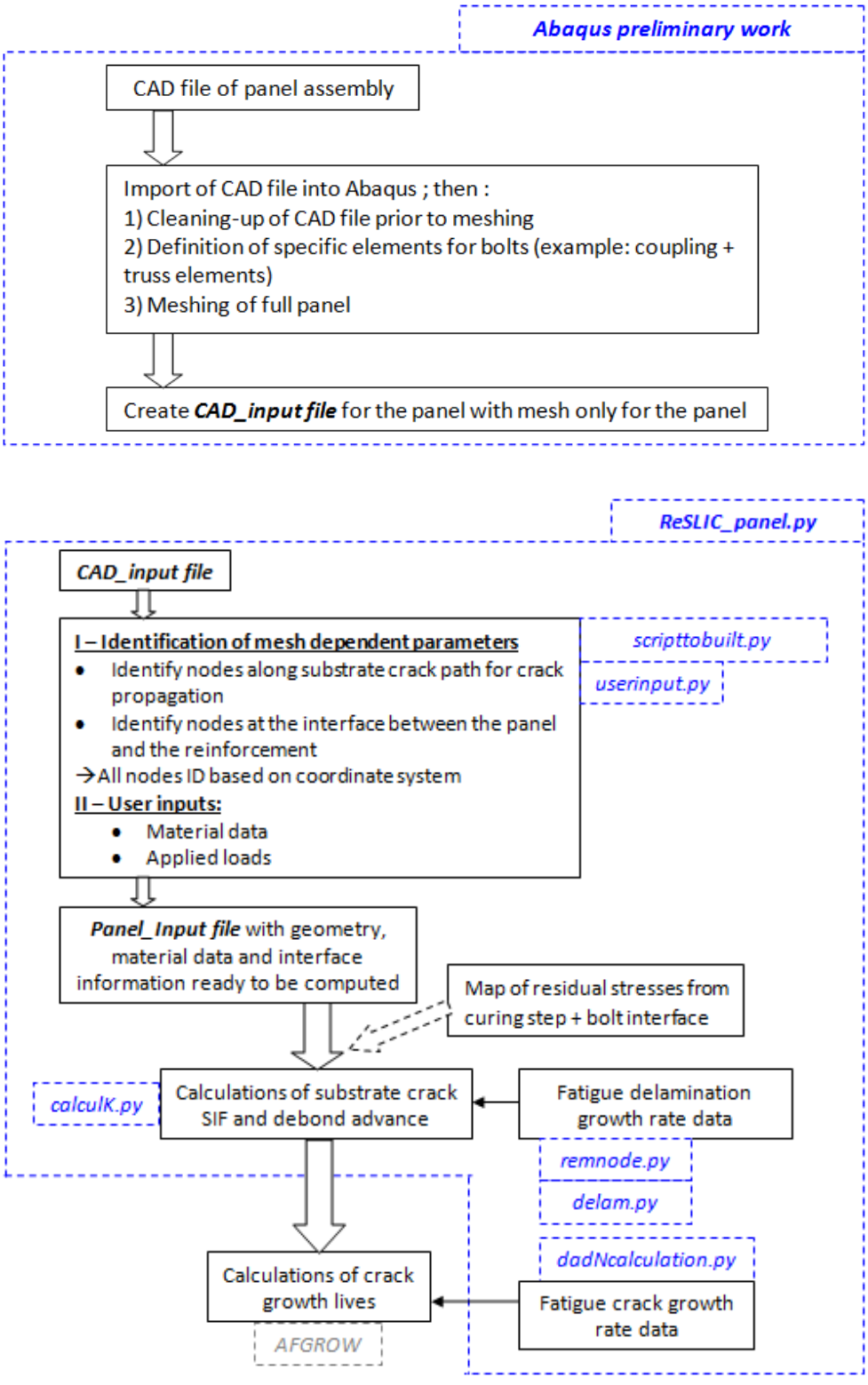

Figure 13-2 : Panel application of ReSLIC calculation

Figure 13-2 demonstrates that several modules of the coupons version of ReSLIC could be used for the panel case, under certain modification due to the complexity of the panel geometry. The crack advance and the delamination advance in that case will be based on preliminary identification of the nodes at the crack path and nodes at the delamination interface.

One key improvement that could be applied to the panel application of ReSLIC would be an independent calculation of the thermal residual stresses induced by the curing process in a separate model and then the use of output database as initial conditions in ReSLIC. This may reduce the calculation time and reduce the prediction errors.

Also one parameter that was not looked at on the coupons level because of their definition would be the residual stresses due to the presence of the bolts that will majorly change the stress distribution. In fact, this was highlighted for the ISP panel where the presence of the bolts may be responsible for a reduction of crack growth rates in the surroundings of the bolts due to compressive residual stresses. This will require additional modules for the panel calculation that considers the effect of bolts on the stress distribution.

One phenomenon that was not present for the coupons case is the damage initiation in the stringer, which was observed during the latest stage of fatigue crack growth in the panel. This will require further scripting to incorporate that calculation into the algorithm and is of importance as it will have a major effect on the load distribution in the panel.

If not using ReSLIC calculation algorithm directly, it appears that the sets of delamination data that were generated for FM94 are key data to calculate the delamination advance and those could be used through a different methodology that was quoted earlier in Chapter 3 such as the use of cohesive elements at the interface of delamination. In fact those data could be used for existing delamination codes [137].

In summary, ReSLIC would not be applicable directly to the panel case but additional scripting will be necessary as described above. Nevertheless, some

of the scripts used for crack advance and delamination propagation may be used for the panel case.

13.2 General items

One of the major limitations of the design tool is the lack of an initiation mechanism for delamination. This could be solved by exploring two methodologies which are the cohesive formulation or the enriched solution (X-FEM). It will also be interesting to evaluate the effect of larger amounts of delamination on the coupons and also verify the amount of delamination that was obtained through the panel tests and study the correlation with coupons tests.

Further work should be conducted on the coupons level with tests on reinforced coupons using substrates made out of aluminium Lithium 2199 material. This would validate the improvement found with baseline coupons that could not be confirmed with the panel tests.

The testing of a baseline ISP panel would demonstrate whether or not the use of BCR on an integrally machined structures results in the same level of retardation as a bolted one.

A wider range of mixed mode delamination test could be conducted in order to get further understanding on the effect of mode I for these tests with for example, levels of mode I of 5-10%. In addition, it would be interesting to conduct delamination fatigue test under variable amplitude loading condition.

REFERENCES

[1] M. Pacchione and J. Telgkamp, “Challenges of the metallic fuselage,” in *ICAS-Secretariat - 25th Congress of the International Council of the Aeronautical Sciences 2006*, 2006, vol. 4, pp. 2110–2121.

[2] T. Dursun and C. Soutis, “Recent developments in advanced aircraft aluminium alloys,” *Mater. Des.*, vol. 56, pp. 862–871, 2014.

[3] J. J. W. R. G. Pettit and C. Toh, “Validated Feasibility Study of Integrally Stiffened Metallic Fuselage Panels for Reducing Manufacturing Costs - The Boeing Company - 2000. NASA/CR-2000-209342.”

[4] F. A. R. part 25, “Airworthiness Standards: Transport Category Airplanes, Paragraph 25.571 Damage tolerance and fatigue evaluation of structure. Amendment 45.”

[5] P. E. Irving, X. Zhang, D. Figueroa-Gordon, M. Boscolo, and D. D. R. Cartie, “Bonded reinforcement and crack retarders in integral aluminium aircraft structures, Final Report,” *Cranf. Univ.*

[6] X. Zhang, M. Boscolo, D. Figueroa-Gordon, G. Allegri, and P. E. Irving, “Fail-safe design of integral metallic aircraft structures reinforced by bonded crack retarders,” *Eng. Fract. Mech.*, vol. 76, no. 1, pp. 114–133, 2009.

[7] X. Zhang, D. Figueroa-Gordon, M. Boscolo, G. Allegri, and P. E. Irving, “Improving fail-safety of aircraft integral structures throughthe use of bonded crack retarders,” *Proc. 24th Symp. Int. Comm. Aeronaut. Fatigue*, 2007.

[8] F. Bagnoli, M. Bernabei, D. Figueroa-Gordon, and P. E. Irving, “The response of aluminium/GLARE hybrid materials to impact and to in-plane fatigue,” *Mater. Sci. Eng. A*, vol. 523, no. 1–2, pp. 118–124, 2009.

[9] M. Colavita, A. Bowler, X. Zhang, and P. E. Irving, “Adhesively bonded CFRP straps as fatigue crack growth retarders on AA2024-T3,” in *International SAMPE Symposium and Exhibition (Proceedings)*, 2006, vol. 51.

[10] P. Colombi, A. Bassetti, and A. Nussbaumer, “Delamination effects on cracked steel members reinforced by prestressed composite patch,” *Theor. Appl. Fract. Mech.*, vol. 39, no. 1, pp. 61–71, 2003.

[11] J.-C. Ehrström, R. Muzzolini, S. Arsène, and S. Van Der Veen, “Improving damage tolerance of integrally machined panels,” *Proc. 23rd ICAF Symp.*, vol. 1, pp. 79–90, 2005.

[12] M. Heinimann, R. Bucci, M. Kulak, and M. Garratt, “Improving damage tolerance of aircraft structures through the use of selective reinforcement,” *Proc. 23rd ICAF Symp. Hambg.*, vol. 1, pp. 197–208, 2005.

[13] P. E. Irving, D. Figueroa-Gordon, X. Zhang, and M. Boscolo, “Bonded crack retarders for enhanced fail safety and damage tolerance in aircraft structures,” *Proc. 1st Int. Conf. Eng. against Fract.*, 2008.

[14] J. Schijve, “Crack stoppers and arall laminates,” *Eng. Fract. Mech.*, vol. 37, no. 2, pp. 405–421, 1990.

[15] Z. Sun and M. Huang, “Fatigue crack propagation of new aluminum lithium alloy bonded with titanium alloy strap,” *Chinese J. Aeronaut.*, vol. 26, no. 3, pp. 601–605, 2013.

[16] A. Brot, Y. Peleg-Wolfin, I. Kressel, and Z. Yosef, “The damage-tolerance behavior of integrally stiffened metallic structures,” in *Technion Israel Institute of Technology - 48th Israel Annual Conference on Aerospace Sciences 2008*, 2008, vol. 2, pp. 747–758.

[17] G. L. Farley, “Selective reinforcement to enhance the structural performance of metallic compression panels,” in *Collection of Technical Papers - AIAA/ASME/ASCE/AHS/ASC Structures, Structural Dynamics and Materials Conference*, 2004, vol. 7, pp. 5606–5615.

[18] H. Hosseini-Toudeshky, “Effects of composite patches on fatigue crack propagation of single-side repaired aluminum panels,” *Compos. Struct.*, vol. 76, no. 3, pp. 243–251, 2006.

[19] M. R. Lena, J. C. Klug, and C. T. Sun, “Composite patches as reinforcements and crack arrestors in aircraft structures,” *J. Aircr.*, vol. 35, no. 2, pp. 318–323, 1998.

[20] X. Z. J. Doucet P.E. Irving, “Application of advanced metallic technology to support life extension, Final report,” 2014.

[21] T. L. Anderson, *Fracture Mechanics, Fundamentals and Applications*, vol. Taylor & F. 2005.

[22] J. Schijve, “Fatigue of structures and materials,” *Fatigue of Structures and Materials*. pp. 1–622, 2009.

[23] D. Broek, *Elementary engineering fracture mechanics*. Springer, 1986.

[24] D. Broek, “The practical use of fracture mechanics.,” 1989.

[25] G. R. Irwin, “Analysis of Stresses and Strains Near the End of a Crack Traversing a Plate,” *J.Appl.Mech.*, 1957.

[26] H. M. Westergaard, “Bearing pressures and cracks,” *J. Appl. Mech.*, vol. 6, pp. 49–53, 1939.

[27] D. P. Rooke, D. J. Cartwright, and G. B. M. of D. P. Executive, *Compendium of Stress Intensity Factors*. Stationery Office, 1976.

[28] D. P. Rooke, F. I. Baratta, and D. J. Cartwright, “Simple methods of determining stress intensity factors,” *Eng. Fract. Mech.*, vol. 14, no. 2, pp. 397–426, 1981.

[29] W. D. Pilkey and D. F. Pilkey, *Peterson’s Stress Concentration Factors*. Wiley, 2008.

[30] D. R. J. Owen and A. J. Fawkes, *Engineering Fracture Mechanics: Numerical Methods and Applications*. Pineridge Press Limited, 1983.

[31] E. Byskov, “The calculation of stress intensity factors using the finite element method with cracked elements,” *Int. J. Fract. Mech.*, vol. 6, no. 2, pp. 159–167, Jan. 1970.

[32] R. S. Barsoum, “On the use of isoparametric finite elements in linear fracture mechanics,” *Int. J. Numer. Methods Eng.*, vol. 10, no. 1, pp. 25–37, 1976.

[33] R. D. Henshell and K. G. Shaw, “Crack tip finite elements are unnecessary,” *Int. J. Numer. Methods Eng.*, vol. 9, no. 3, pp. 495–507, 1975.

[34] C. F. Shih, H. G. Lorenzi, and M. D. German, “Crack extension modeling with singular quadratic isoparametric elements,” *Int. J. Fract.*, vol. 12, no. 4, pp. 647–651.

[35] W. X. Zhu and D. J. Smith, “On the use of displacement extrapolation to obtain crack tip singular stresses and stress intensity factors,” *Eng. Fract. Mech.*, vol. 51, no. 3, pp. 391–400, Jun. 1995.

[36] G. V. Guinea, J. Planas, and M. Elices, “KI evaluation by the displacement extrapolation technique,” *Eng. Fract. Mech.*, vol. 66, no. 3, pp. 243–255, Jun. 2000.

[37] W. C. Carpenter, “Extrapolation techniques for determining stress intensity factors,” *Eng. Fract. Mech.*, vol. 18, no. 2, pp. 325–332, Jan. 1983.

[38] R.H.Gallagher, “A review of finite element techniques in fracture mechanics,” in *Proc. 1st Int. Conference on Numerical Methods in Fracture Mechanics, University College Swansea*, 1978, p. pp. 1.

[39] S. K. Chan, I. S. Tuba, and W. K. Wilson, “On the finite element method in linear fracture mechanics,” *Eng. Fract. Mech.*, vol. 2, no. 1, pp. 1–17, Jul. 1970.

[40] T. K. Hellen, “On the method of virtual crack extensions,” *Int. J. Numer. Methods Eng.*, vol. 9, no. 1, pp. 187–207, 1975.

[41] E. F. Rybicki and M. F. Kanninen, “A finite element calculation of stress intensity factors by a modified crack closure integral,” *Eng. Fract. Mech.*, vol. 9, no. 4, pp. 931–938, Jan. 1977.

[42] R. Krueger, “Virtual crack closure technique: History, approach, and applications,” *Appl. Mech. Rev.*, vol. 57, no. 1–6, pp. 109–143, 2004.

[43] E. Wolf, “Fatigue crack closure under cyclic tension,” *Eng. Fract. Mech.*, vol. 2, no. 1, pp. 37–45, 1970.

[44] P. C. Paris and F. Erdogan, “ A Critical Analysis of Crack Propagation Laws.,” *J. Basic Eng.*, vol. 85, no. 4, pp. 528–534, 1960.

[45] K. Walker, “The Effect of Stress Ratio During Crack Propagation and Fatigue for 2024-T3 and 7075-T6 Aluminum,” *Effects of Environment and Complex Load History on Fatigue Life*. ASTM International, pp. 1–14, Jan-1970.

[46] R. G. Forman, V. E. Kearney, and R. M. Engle, “Numerical Analysis of Crack Propagation in Cyclic-Loaded Structures,” *J. Fluids Eng.*, vol. 89, no. 3, pp. 459–463, Jan. 1967.

[47] R. G. Forman, *Behavior of Surface and Corner Cracks Subjected to Tensile and Bending Loads in Ti-6Al-4V Alloy*. 1990.

[48] A. F. R. L. W.-P. A. F. B. O. H. A. V. Directorate and J. A. Harter, *AFGROW Users Guide and Technical Manual*. Storming Media, 1999.

[49] J. A. Harter, “MODGRO User’s Manual, Version 1.2,” DTIC Document, 1988.

[50] M. Boscolo, “A finite element analysis of bonded crack retarders for integral aircraft structures,” Cranfield University, 2009.

[51] S. Suresh, *Fatigue of Materials*. Cambridge University Press, 1998.

[52] R. J. Chester, K. F. Walker, and P. D. Chalkley, “Adhesively bonded repairs to primary aircraft structure,” *Int. J. Adhes. Adhes.*, vol. 19, no. 1, pp. 1–8, 1999.

[53] I. Meneghin, G. Molinari, G. Ivetic, and E. Troiani, “Damage tolerance of adhesive bonded stiffened panels: Experimental and analytical investigation of the fatigue crack propagation underneath the stringers,” in *ICAF 2011 Structural Integrity: Influence of Efficiency and Green Imperatives - Proceedings of the 26th Symposium of the International Committee on Aeronautical Fatigue*, 2011, pp. 771–783.

[54] I. Meneghin, M. Pacchione, and P. Vermeer, “Investigation on the design of bonded structures for increased damage tolerance,” in *ICAF 2009, Bridging the Gap Between Theory and Operational Practice - Proceedings of the 25th Symposium of the International Committee on Aeronautical Fatigue*, 2009, pp. 427–447.

[55] G. Molinari, I. Meneghin, M. Melega, and E. Troiani, “Parametric damage tolerance design of metallic aeronautical stiffened panels,” *Aeronaut. J.*, vol. 116, no. 1182, pp. 815–831, 2012.

[56] M. Plokker, D. Daverschot, and T. Beumler, “Hybrid structure solution for the A400M wing attachment frames,” in *ICAF 2009, Bridging the Gap Between Theory and Operational Practice - Proceedings of the 25th Symposium of the International Committee on Aeronautical Fatigue*, 2009, pp. 375–385.

[57] X.-L. Zhao and L. Zhang, “State-of-the-art review on FRP strengthened steel structures,” *Eng. Struct.*, vol. 29, no. 8, pp. 1808–1823, 2007.

[58] Y. E. Ma, H.-W. Hu, and P. Irving, “Damage tolerance of FSWed integral wing panel reinforced by bonded crack retarders,” *J. Aircr.*, vol. 50, no. 6, pp. 1880–1885, 2013.

[59] Y. E. Ma and P. F. Xu, “Effects of bonded crack retarders on fatigue parameters of FSWed integral panel,” *Advanced Materials Research*, vol. 891–892. pp. 627–632, 2014.

[60] J. G. Teng, T. Yu, and D. Fernando, “Strengthening of steel structures with fiber-reinforced polymer composites,” *J. Constr. Steel Res.*, vol. 78, pp. 131–143, 2012.

[61] H. B. Liu, X. L. Zhao, and R. Al-Mahaidi, “Effect of fatigue loading on bond strength between CFRP sheets and steel plates,” *Int. J. Struct. Stab. Dyn.*, vol. 10, no. 1, pp. 1–20, 2010.

[62] D. Quinn, A. Murphy, and L. Cervi, “Fatigue performance of aircraft panels with novel skin buckling containment features,” *Proc. Inst. Mech. Eng. Part G J. Aerosp. Eng.*, vol. 225, no. 7, pp. 791–806, 2011.

[63] T. Swift, “Fail-safe design requirements and features, regulatory requirements,” in *AIAA\ICAS International Air and Space Symposium and Exposition: The Next 100 Years*, 2003.

[64] T. Swift, “Damage tolerance capability,” *Int. J. Fatigue*, vol. 16, no. 1, pp. 75–94, 1994.

[65] D. F. O. Braga, S. M. O. Tavares, L. F. M. da Silva, P. M. G. P. Moreira, and P. M. S. T. de Castro, “Advanced design for lightweight structures: Review and prospects,” *Prog. Aerosp. Sci.*, 2014.

[66] Ž. Domazet, “Comparison of fatigue crack retardation methods,” *Eng. Fail. Anal.*, vol. 3, no. 2, pp. 137–147, 1996.

[67] M.-L. Pastor, X. Balandraud, M. Grédiac, and J.-L. Robert, “On the fatigue response of aluminium specimens reinforced with carbon–epoxy patches,” *Compos. Struct.*, vol. 83, no. 3, pp. 237–246, 2008.

[68] A. Vlot, J. M. A. Massar, C. B. Guijt, and S. Verhoeven, “Bonded aircraft repairs under variable amplitude fatigue loading and at low temperatures,” *Fatigue Fract. Eng. Mater. Struct.*, vol. 23, no. 1, pp. 9–18, 2000.

[69] F. I. C. a titan. Flightglobal., “No Title.” [Online]. Available: http://www.flightglobal.com/assets/getAsset.aspx?ItemID=9116.

[70] G. Vlot Ad and J. Willem, *Fibre Metal Laminates: an introduction.* Drodrecht, The Netherlands: Kluwer Academic Publishers, 2001.

[71] D. P. (D Rooke, *Compendium of stress intensity factors / by] D. P. Rooke, D. J. Cartwright : for the] Procurement Executive, Ministry of Defence*. London: H.M.S.O, 1976.

[72] M. M. Ratwani, “Analysis of Cracked, Adhesively Bonded Laminated Structures,” *AIAA J.*, vol. 17, no. 9, pp. 988–994, 1979.

[73] L. R. F. Rose, “An application of the inclusion analogy for bonded reinforcements,” *Int. J. Solids Struct.*, vol. 17, no. 8, pp. 827–838, 1981.

[74] L. R. F. Rose, “A cracked plate repaired by bonded reinforcements,” *Int. J. Fract.*, vol. 18, no. 2, pp. 135–144, Jan. 1982.

[75] A. A. Baker, L. R. F. Rose, and R. Jones, *Advances in the Bonded Composite Repair of Metallic Aircraft Structure*, no. vol. 1. Elsevier Science, 2003.

[76] W. and Rose, “On the design of bonded patches for one-sided repair.,” *Proc. 11th Int. Conf. Compos. Mater. Gold Coast, Aust.*, vol. 5, pp. 347–356, 1997.

[77] C. H. Wang, L. R. F. Rose, and R. Callinan, “Analysis of out-of-plane bending in one-sided bonded repair,” *Int. J. Solids Struct.*, vol. 35, no. 14, pp. 1653–1675, 1998.

[78] C. H. Wang and L. R. F. Rose, “A crack bridging model for bonded plates subjected to tension and bending,” *Int. J. Solids Struct.*, vol. 36, no. 13, pp. 1985–2014, Jan. 1999.

[79] Q. Q. Yu, T. Chen, X. L. Gu, X. L. Zhao, and Z. G. Xiao, “Fatigue behaviour of CFRP strengthened steel plates with different degrees of damage,” *Thin-Walled Struct.*, vol. 69, no. 0, pp. 10–17, 2013.

[80] J. H. Kim and S. B. Lee, “Calculation of stress intensity factor using weight function method for a patched crack with debonding region,” *Eng. Fract. Mech.*, vol. 67, no. 3, pp. 303–310, Jan. 2000.

[81] R. J. Clark and D. P. Romilly, “Linear coupled bending and extension of an unbalanced bonded repair,” *Int. J. Solids Struct.*, vol. 44, no. 10, pp. 3156–3176, 2007.

[82] J. S. Ahn, P. K. Basu, and K. S. Woo, “Analysis of cracked aluminum plates with one-sided patch repair using p-convergent layered model,” *Finite Elem. Anal. Des.*, vol. 46, no. 5, pp. 438–448, 2010.

[83] M. R. Ayatollahi and R. Hashemi, “Computation of stress intensity factors (< i> K</i>< sub> I</sub>,< i> K</i>< sub> II</sub>) and< i> T</i>-stress for cracks reinforced by composite patching,” *Compos. Struct.*, vol. 78, no. 4, pp. 602–609, 2007.

[84] A. Bassetti, P. Colombi, and A. Nussbaumer, “Finite element analysis of steel members repaired by prestressed composite patch,” *Proceedings of XV Congresso Nazionale del Gruppo Italiano Frattura IGF*. 2000.

[85] A. C. and S. C.T., “Bending effects of unsymmetric adhesively bonded composite repairs on cracked aluminum panels. In: May 4–6 Proc. FAA/NASA Int. Symp. on Advanced Structural Integrity Methods for Airframe Durability and Damage Tolerance,” in *Advanced Structural Integrity Methods for Airframe Durability and Damage Tolerance, Part 2*, 1994, vol. I, pp. 33–48.

[86] R. J. Callinan, L. R. F. Rose, and C. H. Wang, “Three dimensional stress analysis of crack patching,” in *ICF 9-Sydney, Australia-1997*, 2012.

[87] R. Chandra and K. Guruprasad, “Numerical estimation of stress intensity factors in patched cracked plates,” *Eng. Fract. Mech.*, vol. 27, no. 5, pp. 559–569, 1987.

[88] H. Errouane, Z. Sereir, and A. Chateauneuf, “Numerical model for optimal design of composite patch repair of cracked aluminum plates under tension,” *Int. J. Adhes. Adhes.*, vol. 49, no. 0, pp. 64–72, 2014.

[89] L. Gu, A. R. M. Kasavajhala, and S. Zhao, “Finite element analysis of cracks in aging aircraft structures with bonded composite-patch repairs,” *Compos. Part B Eng.*, vol. 42, no. 3, pp. 505–510, 2011.

[90] H. Hosseini-Toudeshky and B. Mohammadi, “A simple method to calculate the crack growth life of adhesively repaired aluminum panels,” *Compos. Struct.*, vol. 79, no. 2, pp. 234–241, 2007.

[91] H. Hosseini-Toudeshky, B. Mohammadi, G. Sadeghi, and H. R. Daghyani, “Numerical and experimental fatigue crack growth analysis in mode-I for repaired aluminum panels using composite material,” *Sel. Pap. from Jt. 8th Int. Conf. Deform. Fract. Compos. Exp. Tech. Des. Compos. Mater. held Univ. Sheffield, UK*, vol. 38, no. 4, pp. 1141–1148, 2007.

[92] H. Hosseini-Toudeshky, M. Saber, and B. Mohammadi, “Finite element crack propagation of adhesively bonded repaired panels in general mixed-mode conditions,” *Finite Elem. Anal. Des.*, vol. 45, no. 2, pp. 94–103, 2009.

[93] H. Hosseini-Toudeshky, M. Sadighi, and A. Vojdani, “Effects of curing thermal residual stresses on fatigue crack propagation of aluminum plates repaired by FML patches,” *Compos. Struct.*, vol. 100, no. 0, pp. 154–162, 2013.

[94] R. Jones and R. J. Callinan, “A design study in crack patching,” *Fibre Sci. Technol.*, vol. 14, no. 2, pp. 99–111, 1981.

[95] R. Jones and R. J. Callinan, “On the use of special crack tip elements in cracked elastic sheets,” *Int. J. Fract.*, vol. 13, no. 1, pp. 51–64, Jan. 1977.

[96] A. R. M. Kasavajhala and L. Gu, “Fracture analysis of Kevlar-49/epoxy and e-glass/epoxy doublers for reinforcement of cracked aluminum plates,” *Compos. Struct.*, vol. 93, no. 8, pp. 2090–2095, 2011.

[97] R. Kaye and M. Heller, “Finite element-based three-dimensional stress analysis of composite bonded repairs to metallic aircraft structure,” *Int. J. Adhes. Adhes.*, vol. 26, no. 4, pp. 261–273, 2006.

[98] J. Klug, S. Maley, and C. T. Sun, “Characterization of Fatigue Behavior of Bonded Composite Repairs,” *J. Aircr.*, vol. 36, no. 6, pp. 1016–1022, 1999.

[99] W.-Y. Lee and J.-J. Lee, “Fatigue behavior of composite patch repaired aluminum plate,” *J. Compos. Mater.*, vol. 39, no. 16, pp. 1449–1463, 2005.

[100] R. Krueger and P. J. Minguet, “Analysis of composite skin–stiffener debond specimens using a shell/3D modeling technique,” *Compos. Struct.*, vol. 81, no. 1, pp. 41–59, 2007.

[101] S. Giannis and R. H. Martin, “Skin-stringer separation in Glare composite aerospace panels,” in *ICCM International Conferences on Composite Materials*, 2009.

[102] S. Psarras, S. T. Pinho, and B. G. Falzon, “Damage-Tolerant Design of Stiffener Run-Outs: A Finite Element Approach,” 2012.

[103] M. Boscolo and X. Zhang, “A modelling technique for calculating stress intensity factors for structures reinforced by bonded straps. Part II: Validation,” *Eng. Fract. Mech.*, vol. 77, no. 6, pp. 896–907, 2010.

[104] M. Boscolo and X. Zhang, “A modelling technique for calculating stress intensity factors for structures reinforced by bonded straps. Part I: Mechanisms and formulation,” *Eng. Fract. Mech.*, vol. 77, no. 6, pp. 883–895, Apr. 2010.

[105] C. T. Sun, J. Klug, and C. Arendt, “Analysis of cracked aluminum plates repaired with bonded composite patches,” *AIAA J.*, vol. 34, no. 2, pp. 369–374, 1996.

[106] S. Naboulsi and S. Mall, “Modeling of a cracked metallic structure with bonded composite patch using the three layer technique,” *Compos. Struct.*, vol. 35, no. 3, pp. 295–308, 1996.

[107] D. Ouinas, B. B. Bouiadjra, B. Serier, and M. SaidBekkouche, “Comparison of the effectiveness of boron/epoxy and graphite/epoxy patches for repaired cracks emanating from a semicircular notch edge,” *Compos. Struct.*, vol. 80, no. 4, pp. 514–522, 2007.

[108] D. Ouinas, B. Bachir Bouiadjra, B. Achour, and N. Benderdouche, “Modelling of a cracked aluminium plate repaired with composite octagonal patch in mode I and mixed mode,” *Mater. Des.*, vol. 30, no. 3, pp. 590–595, 2009.

[109] V. Sabelkin, S. Mall, and J. B. Avram, “Fatigue crack growth analysis of stiffened cracked panel repaired with bonded composite patch,” *Eng. Fract. Mech.*, vol. 73, no. 11, pp. 1553–1567, 2006.

[110] V. Sabelkin, S. Mall, M. A. Hansen, R. M. Vandawaker, and M. Derriso, “Investigation into cracked aluminum plate repaired with bonded composite patch,” *Compos. Struct.*, vol. 79, no. 1, pp. 55–66, 2007.

[111] W.-Y. Lee and J.-J. Lee, “Successive 3D FE analysis technique for characterization of fatigue crack growth behavior in composite-repaired aluminum plate,” *Twelfth Int. Conf. Compos. Struct.*, vol. 66, no. 1–4, pp. 513–520, 2004.

[112] A. R. Maligno, C. Soutis, and V. V Silberschmidt, “An advanced numerical tool to study fatigue crack propagation in aluminium plates repaired with a composite patch,” *Eng. Fract. Mech.*, vol. 99, no. 0, pp. 62–78, 2013.

[113] T. V. R. S. Umamaheswar and R. Singh, “Modelling of a patch repair to a thin cracked sheet,” *Eng. Fract. Mech.*, vol. 62, no. 2–3, pp. 267–289, 1999.

[114] F. Ricci, F. Franco, and N. Montefusco, *Bonded Composite Patch Repairs on Cracked Aluminum Plates: Theory, Modeling and Experiments*. INTECH Open Access Publisher, 2011.

[115] A. S. McGee, “No Title,” *Numer. Study Optim. Parameters Bond. Compos. Repairs Crack. Alum.*, 2012.

[116] L. Pearce, “Crack Growth Retardation in Structures with Bonded Glare Straps,” Cranfield University.

[117] I. A. Ashcroft and A. D. Crocombe, “Modelling fatigue in adhesively bonded joints,” *Modeling of Adhesively Bonded Joints*. Springer Berlin Heidelberg, Affiliation: Wolfson School of Mechanical and Manufacturing Engineering, Loughborough University, Loughborough,Leicestershire, LE11 3TU, United Kingdom; Affiliation: Division of Mechanical, Medical and Aerospace Engineering, School of Engineering, Univers, pp. 183–223, 2008.

[118] J. Lemaitre, “How to use damage mechanics,” *Nucl. Eng. Des.*, vol. 80, no. 2, pp. 233–245, 1984.

[119] J. Lemaitre, “CONTINUOUS DAMAGE MECHANICS MODEL FOR DUCTILE FRACTURE.,” *J. Eng. Mater. Technol. Trans. ASME*, vol. 107, no. 1, pp. 83–89, 1985.

[120] L. M. Kachanov, “Introduction on continuum damage mechanics,” *Dordrenht*, 1986.

[121] C. Rans, R. Alderliesten, and R. Benedictus, “Misinterpreting the results: How similitude can improve our understanding of fatigue delamination growth,” *Compos. Sci. Technol.*, vol. 71, no. 2, pp. 230–238, 2011.

[122] M. Quaresimin and M. Ricotta, “Stress intensity factors and strain energy release rates in single lap bonded joints in composite materials,” *Compos. Sci. Technol.*, vol. 66, no. 5, pp. 647–656, 2006.

[123] R. Krueger, “Development of a benchmark example for delamination fatigue growth prediction,” in *25th Technical Conference of the American Society for Composites and 14th US-Japan Conference on Composite Materials 2010*, 2010, vol. 2, pp. 948–967.

[124] T. R. Brussat, S. T. Chiu, and S. Mostovoy, “Fracture mechanics for structural adhesives bonds,” *Fract. Mech. Struct. Adhes. Bond. - Final Rep.*, 1977.

[125] T. R. Brussat and S. T. Chiu, “Fatigue crack growth of bondline cracks in structural bonded joints,” *J. Eng. Mater. Technol. Trans. ASME*, vol. 100, no. 1, pp. 39–45, 1978.

[126] J. A. Pascoe, “Delamination of Bonded Repairs: A Damage Tolerance Approach,” Delft University of Technology, 2012.

[127] R. H. Martin, “Incorporating interlaminar fracture mechanics into design,” *Proc. Inst. Mech. Eng. Part L J. Mater. Des. Appl.*, vol. 214, no. 2, pp. 91–97, 2000.

[128] M. Quaresimin and M. Ricotta, “Life prediction of bonded joints in composite materials,” *Int. J. Fatigue*, vol. 28, no. 10 SPEC. ISS., pp. 1166–1176, 2006.

[129] D. M. Hoyt, S. H. Ward, and P. J. Minguet, “Strength and fatigue life modeling of bonded joints in composite structure,” *J. Compos. Technol. Res.*, vol. 24, no. 3, pp. 188–208, 2002.

[130] D. Xie and S. B. Biggers Jr., “Strain energy release rate calculation for a moving delamination front of arbitrary shape based on the virtual crack closure technique. Part I: Formulation and validation,” *Eng. Fract. Mech.*, vol. 73, no. 6, pp. 771–785, 2006.

[131] D. S. Dugdale, “Yielding of steel sheets containing slits,” *J. Mech. Phys. Solids*, vol. 8, no. 2, pp. 100–104, 1960.

[132] G. I. Barenblatt, “Mathematical theory of equilibrium cracks,” *Adv. Appl. Mech.*, vol. 7, pp. 56–129, 1962.

[133] P. P. Camanho, C. G. Dávila, and M. F. De Moura, “Numerical simulation of mixed-mode progressive delamination in composite materials,” *J. Compos. Mater.*, vol. 37, no. 16, pp. 1415–1438, 2003.

[134] J. W. Foulk III, D. H. Allen, and K. L. E. Helms, “A model for predicting the damage and environmental degradation dependent life of SCS-6/Timetal®21S [0]4 metal matrix composite,” *Mech. Mater.*, vol. 29, no. 1, pp. 53–68, 1998.

[135] M. L. Benzeggagh and M. Kenane, “Measurement of mixed-mode delamination fracture toughness of unidirectional glass/epoxy composites with mixed-mode bending apparatus,” *Compos. Sci. Technol.*, vol. 56, no. 4, pp. 439–449, 1996.

[136] P. Robinson, U. Galvanetto, D. Tumino, G. Bellucci, and D. Violeau, “Numerical simulation of fatigue-driven delamination using interface elements,” *Int. J. Numer. Methods Eng.*, vol. 63, no. 13, pp. 1824–1848, 2005.

[137] P. W. Harper and S. R. Hallett, “A fatigue degradation law for cohesive interface elements - Development and application to composite materials,” *Int. J. Fatigue*, vol. 32, no. 11, pp. 1774–1787, 2010.

[138] N. Blanco, E. K. Gamstedt, L. E. Asp, and J. Costa, “Mixed-mode delamination growth in carbon-fibre composite laminates under cyclic loading,” *Int. J. Solids Struct.*, vol. 41, no. 15, pp. 4219–4235, 2004.

[139] A. Turon, J. Costa, P. P. Camanho, and C. G. Dávila, “Simulation of delamination in composites under high-cycle fatigue,” *Compos. Part A Appl. Sci. Manuf.*, vol. 38, no. 11, pp. 2270–2282, 2007.

[140] M. May, R. Pullin, M. Eaton, C. Featherston, and S. R. Hallett, “An advanced model for initiation and propagation of damage under fatigue loading - part II: Matrix cracking validation cases,” *Compos. Struct.*

[141] M. May and S. R. Hallett, “A combined model for initiation and propagation of damage under fatigue loading for cohesive interface elements -- Printed,” *Compos. Part A Appl. Sci. Manuf.*, vol. 41, no. 12, pp. 1787–1796, 2010.

[142] J. A. Pascoe, R. C. Alderliesten, and R. Benedictus, “Methods for the prediction of fatigue delamination growth in composites and adhesive bonds - A critical review,” *Eng. Fract. Mech.*, vol. 112–113, pp. 72–96, 2013.

[143] B. Landry and G. LaPlante, “Modeling delamination growth in composites under fatigue loadings of varying amplitudes,” *Compos. Part B Eng.*, vol. 43, no. 2, pp. 533–541, 2012.

[144] H. Khoramishad, A. D. Crocombe, K. B. Katnam, and I. A. Ashcroft, “Predicting fatigue damage in adhesively bonded joints using a cohesive zone model,” *Int. J. Fatigue*, vol. 32, no. 7, pp. 1146–1158, 2010.

[145] A. 6. 1. online documentation, “Modeling discontinuities as an enriched feature using the extended finite element method,” 2014. [Online]. Available: http://50.16.176.52/v6.13/books/usb/default.php.

[146] T. Belytschko and T. Black, “Elastic crack growth in finite elements with minimal remeshing,” *Int. J. Numer. Methods Eng.*, vol. 45, no. 5, pp. 601–620, 1999.

[147] D. B. P. Huynh and T. Belytschko, “The extended finite element method for fracture in composite materials,” *Int. J. Numer. Methods Eng.*, vol. 77, no. 2, pp. 214–239, 2009.

[148] R. D. S. G. Campilho, M. D. Banea, F. J. P. Chaves, and L. F. M. D. Silva, “EXtended Finite Element Method for fracture characterization of adhesive joints in pure mode i,” *Comput. Mater. Sci.*, vol. 50, no. 4, pp. 1543–1549, 2011.

[149] J. L. Curiel Sosa and N. Karapurath, “Delamination modelling of GLARE using the extended finite element method,” *Compos. Sci. Technol.*, vol. 72, no. 7, pp. 788–791, 2012.

[150] O. Bacarreza and M. H. Aliabadi, “A novel methodology for fatigue delamination growth analysis of composites,” *Key Engng Mater*, pp. 488–489, 2012.

[151] F. G. Alcoa Inc. (private communication), “Chemical composition of AL 2624.” 2014.

[152] A. I. (private communication), “Alcoa_2024HDT-T351_plate.” 2011.

[153] N/A, “Military Handbook - MIL-HDBK-5H: Metallic Materials and Elements for Aerospace Vehicle Structures (Knovel Interactive Edition).” U.S. Department of Defense.

[154] D. Figueroa-Gordon, “Bonded crack retarders internal reports and documentations.” Cranfield University, 2008.

[155] A. I. (private communication), “Glare / FML machining recommendations.” .

[156] A. I. (private communication), “Glare Constituent Material Properties.” 2010.

[157] R. C. Alderliesten, “Fatigue crack propagation and delamination growth in Glare,” Delft University Press, 2005.

[158] A. Airoldi, M. Vesco, S. Van Der Zwaag, A. Baldi, and G. Sala, “Damage in GLARE laminates under indentation loads: Experimental and numerical

results," in *ICCM International Conferences on Composite Materials*, 2009.

[159] *ASTM E647-05 Standard Test Method for Measurement of Fatigue Crack Growth Rates*. ASTM International, 2008.

[160] A. I. (private communication), "Autoclave Bonding Guidelines." 2011.

[161] S. DEMRI, "BONDED CRACK RETARDERS (BCR) FOR IMPROVED FATIGUE LIFE OF AIRCRAFT WINGS," Cranfield University, 2013.

[162] C. E. M. (CEM), "FM94 ADHESIVE FILM, Technical Data Sheet." .

[163] A. K. Syed, M. E. Fitzpatrick, and J. E. Moffatt, "Evolution of residual stress during fatigue crack growth in an aluminium specimen with a bonded crack retarder," *Compos. Struct.*, vol. 117, no. 0, pp. 12–16, 2014.

[164] A. K. Syed, "Durability of bonded crack retarders for aerospace," Open University, 2014.

[165] S. Peyron, "Finite element modelling of crack growth retardation in integral structures reinforced by Bonded Crack Retarders (BCR)," Cranfield University - School of Engineering, 2013.

[166] C. E. M. (CEM), "FM 94 - S2 UD Glass Tape, Technical Data Sheet." .

[167] "BS ISO 15024:2001 - Fibre-reinforced plastic composites. Determination of mode I interlaminar fracture toughness, Gic, for unidirectionally reinforced materials." 2002.

[168] "BS 7991 - Determination of the mode I adhesive fracture energy, GIC, of structural adhesives using the double cantilever beam (DCB) and tapered double cantilever beam (TDCB) specimens." 2001.

[169] A. J. Brunner, N. Murphy, and G. Pinter, "Development of a standardized procedure for the characterization of interlaminar delamination propagation in advanced composites under fatigue mode I loading conditions," *Eng. Fract. Mech.*, vol. 76, no. 18, pp. 2678–2689, 2009.

[170] A. J. Brunner and J. G. Williams, "Mode II fracture testing of composites: a new look at an old problem," *Eng. Fract. Mech.*, vol. 73, no. 16, pp. 2443–2455, 2006.

[171] A. J. Brunner, S. Stelzer, G. Pinter, and G. P. Terrasi, "Mode II fatigue delamination resistance of advanced fiber-reinforced polymer-matrix laminates: Towards the development of a standardized test procedure," *Int. J. Fatigue*, vol. 50, pp. 57–62, 2013.

[172] “ESIS TC4: Fibre Composites - The determination of the mode II fracture resistance, GIIC, of unidirectional fibre-composites using the calibrated end loaded split (C-ELS) test and an effective crack length approach.” .

[173] “D6671_D6671M |Test Method for Mixed Mode I-Mode II Interlaminar Fracture Toughness of Unidirectional Fiber Reinforced Polymer Matrix Composites.” ASTM International, 2001.

[174] M. Kenane and M. L. Benzeggagh, “Mixed-mode delamination fracture toughness of unidirectional glass/epoxy composites under fatigue loading,” *Compos. Sci. Technol.*, vol. 57, no. 5, pp. 597–605, 1997.

[175] P. Davies, “Round Robin analysis of GIc interlaminar fracture test,” *Appl. Compos. Mater.*, vol. 3, no. 3, pp. 135–140, 1996.

[176] P. Davies, B. R. K. Blackman, and A. J. Brunner, “Standard Test Methods for Delamination Resistance of Composite Materials: Current Status,” *Appl. Compos. Mater.*, vol. 5, no. 6, pp. 345–364, Jan. 1998.

[177] F. Parrinello, G. Marannano, G. Borino, and A. Pasta, “Frictional effect in mode II delamination: Experimental test and numerical simulation,” *Eng. Fract. Mech.*, vol. 110, no. 0, pp. 258–269, 2013.

[178] G. Allegri, M. I. Jones, M. R. Wisnom, and S. R. Hallett, “A new semi-empirical model for stress ratio effect on mode II fatigue delamination growth,” *Compos. Part A Appl. Sci. Manuf.*, vol. 42, no. 7, pp. 733–740, 2011.

[179] J. Zhang, L. Peng, L. Zhao, and B. Fei, “Fatigue delamination growth rates and thresholds of composite laminates under mixed mode loading,” *Int. J. Fatigue*, vol. 40, pp. 7–15, 2012.

[180] I. S. Raju and T. K. O’brien, “1 - Fracture mechanics concepts, stress fields, strain energy release rates, delamination initiation and growth criteria,” in *Delamination Behaviour of Composites*, S. Sridharan, Ed. Woodhead Publishing, 2008, pp. 3–27.

[181] B. R. K. Blackman, “16 - Delamination in adhesively bonded joints,” in *Delamination Behaviour of Composites*, S. Sridharan, Ed. Woodhead Publishing, 2008, pp. 458–484.

[182] S. Stelzer, A. J. Brunner, A. Argüelles, N. Murphy, and G. Pinter, “Mode I delamination fatigue crack growth in unidirectional fiber reinforced composites: Development of a standardized test procedure,” *Recent Adv. Deform. Fract. Compos. Exp. Anal.*, vol. 72, no. 10, pp. 1102–1107, Aug. 2012.

[183] I. A. Ashcroft and S. J. Shaw, “Mode I fracture of epoxy bonded composite joints 2. Fatigue loading,” *Int. J. Adhes. Adhes.*, vol. 22, no. 2, pp. 151–167, 2002.

[184] Y. Shindo, A. Inamoto, F. Narita, and K. Horiguchi, “Mode I fatigue delamination growth in GFRP woven laminates at low temperatures,” *Eng. Fract. Mech.*, vol. 73, no. 14, pp. 2080–2090, 2006.

[185] M. Hojo, T. Ando, M. Tanaka, T. Adachi, S. Ochiai, and Y. Endo, “Modes I and II interlaminar fracture toughness and fatigue delamination of CF/epoxy laminates with self-same epoxy interleaf,” *Third Int. Conf. Fatigue Compos. Third Int. Conf. Fatigue Compos.*, vol. 28, no. 10, pp. 1154–1165, 2006.

[186] “ASTM D5528-01 : StandardTest Method for Mode I Interlaminar Fracture Toughness of Unidirectional Fiber-Reinforced Polymer Matrix Composites.” ASTM International, 2007.

[187] “Test Method for Mode I Fatigue Delamination Growth Onset of Unidirectional Fiber-Reinforced Polymer Matrix Composites.” ASTM International, 2011.

[188] T. E. Tay, “Characterization and analysis of delamination fracture in composites: An overview of developments from 1990 to 2001,” *Appl. Mech. Rev.*, vol. 56, no. 1, pp. 1–32, 2003.

[189] A. J. Brunner, B. R. K. Blackman, and P. Davies, “A status report on delamination resistance testing of polymer–matrix composites,” *Fract. Compos. Mater.*, vol. 75, no. 9, pp. 2779–2794, 2008.

[190] M. Hojo, K. Tanaka, C. G. Gustafson, and R. Hayashi, “Effect of stress ratio on near-threshold propagation of delimination fatigue cracks in unidirectional CFRP,” *Compos. Sci. Technol.*, vol. 29, no. 4, pp. 273–292, 1987.

[191] H. Masaki, O. Shojiro, C.-G. Gustafson, and T. Keisuke, “Effect of matrix resin on delamination fatigue crack growth in CFRP laminates,” *Eng. Fract. Mech.*, vol. 49, no. 1, pp. 35–47, 1994.

[192] J. Andersons, M. Hojo, and S. Ochiai, “Empirical model for stress ratio effect on fatigue delamination growth rate in composite laminates,” *Int. J. Fatigue*, vol. 26, no. 6, pp. 597–604, 2004.

[193] T. K. O’brien, “Characterization of delamination onset and growth in a composite laminate,” *Damage Compos. Mater. ASTM STP*, vol. 775, no. 2, pp. 140–167, 1982.

[194] R. H. Martin and G. B. Murri, “Characterization of mode I and mode II delamination growth and thresholds in graphite/peek composites,” *ASTM STP*, vol. 1059, pp. 251–270, 1988.

[195] L. E. Asp, A. Sjögren, and E. S. Greenhalgh, “Delamination Growth and Thresholds in a Carbon/Epoxy Composite under Fatigue Loading,” *J. Compos. Technol. Res.*, vol. 23, no. 2, pp. 55–68, 2001.

[196] K. Shivakumar, H. Chen, F. Abali, D. Le, and C. Davis, “A total fatigue life model for mode I delaminated composite laminates,” *Int. J. Fatigue*, vol. 28, no. 1, pp. 33–42, 2006.

[197] A. Argüelles, J. Viña, A. F. Canteli, M. A. Castrillo, and J. Bonhomme, “Interlaminar crack initiation and growth rate in a carbon-fibre epoxy composite under mode-I fatigue loading,” *Deform. Fract. Compos. Anal. Numer. Exp. Tech. with Regul. Pap.*, vol. 68, no. 12, pp. 2325–2331, 2008.

[198] J. R. Reeder and J. H. REWS, “Mixed-mode bending method for delamination testing,” *AIAA J.*, vol. 28, no. 7, pp. 1270–1276, 1990.

[199] J. R. Reeder, K. Song, and P. Chunchu, “Postbuckling and growth of delaminations in composite plates subjected to axial compression,” 2002.

[200] H. Hosseini-Toudeshky, A. Jasemzadeh, and B. Mohammadi, “Fatigue debonding analysis of repaired aluminium panels by composite patch using interface elements,” *Appl. Compos. Mater.*, vol. 18, no. 6, pp. 571–584, 2011.

[201] K. Scott, “An investigation into the geometric effects of Glare BCRs,” Cranfield University - School of Engineering, 2013.

[202] M. Boscolo, G. Allegri, and X. Zhang, “Design and modeling of selective reinforcements for integral aircraft structures,” *AIAA J.*, vol. 46, no. 9, pp. 2323–2331, 2008.

[203] G. Brick, “Predicting crack growth life in Al-Li alloy 2199-T8E80 under spectrum loading,” Cranfield University - School of Engineering, 2012.

[204] R. T. Walker, “Measurement of fatigue crack growth rate in Al-Li alloy 2199-T8E80,” Cranfield University - School of Engineering, 2011.

Bibliography

[1] P.E. Irving, X. Zhang, **J. Doucet**, D. Figueroa-Gordon, M. Boscolo, M.B. Heinimann, G. Shepard, M.E. Fitzpatrick, D. Liljedahl, "*Life Extension Techniques for Aircraft Structures – Extending Durability and Promoting Damage Tolerance through Bonded Crack Retarders''*, ICAF Symposium, 2011

[2] **Jeremy Doucet** , Xiang Zhang , Philip Irving , (2013) "Fatigue modelling of aluminium plates reinforced with bonded fibre metal laminates", International Journal of Structural Integrity, Vol. 4 Iss: 4, pp.416 – 428

[3] **J. Doucet**, X. Zhang, P. E. Irving, "Modelling Fatigue Crack Growth Rates in Aluminium Plates Reinforced by Bonded Fibre-Metal Laminates for Fatigue Life Extension", Advanced Materials Research, Vols. 891-892, pp. 1803-1809, 2014

[4] M. B. Heinimann, R. Maziarz, L. Castelletti, V. Naik, P. E. Irving, D. Figueroa, **J. Doucet**, X. Zhang, M. Boscolo, M. E Fitzpatrick, A. K. Syed, J. E. Moffatt, C. D. M. Liljedahl, Use of Bonded Crack Retarders to Improve Damage Tolerance of Wing Covers, AEROMAT 25-The Latest World in Aerospace Materials, Orlando, Florida, 16-19 June, 2014

[5] Abdul Khadar Syed, Michael E. Fitzpatrick, James E. Moffatt, **Jeremy Doucet**, Isidro Durazo-Cardenas, Effect of impact damage on fatigue performance of structures reinforced with GLARE bonded crack retarders, International Journal of Fatigue, Volume 80, November 2015, Pages 231-237.

APPENDICES

Appendix A Spectrum manipulations

This appendix presents the results of the manipulation performed on the variable amplitude loading spectrum (2144) provided by our partner, AIRBUS. The load capacity of the testing machine being 800 kN modification of the spectrum was necessary through clipping of the original spectrum. In order to reduce the duration of the test, a gating manipulation that consists of removing the cycles smaller than a given range was also performed. The effects of these manipulations were evaluated through a series of life calculation simulation using a baseline middle crack tension coupon.

A.1 Original spectrum: Spectrum 2144 – Bottom Cover Panel test

The spectrum, as received, consisted of a sequence of 4,800 blocks with 21 different blocks in the sequence. There was a maximum of 573 turning points per block. As the spectrum was received as a sequence of blocks it needed to be concatenated. Once concatenated using a macro in Microsoft Excel, the sequence of 4,800 blocks consisted of a spectrum with 276,461 turning points and 138,230 cycles. The first 2000 turning points are presented in Figure A-1.

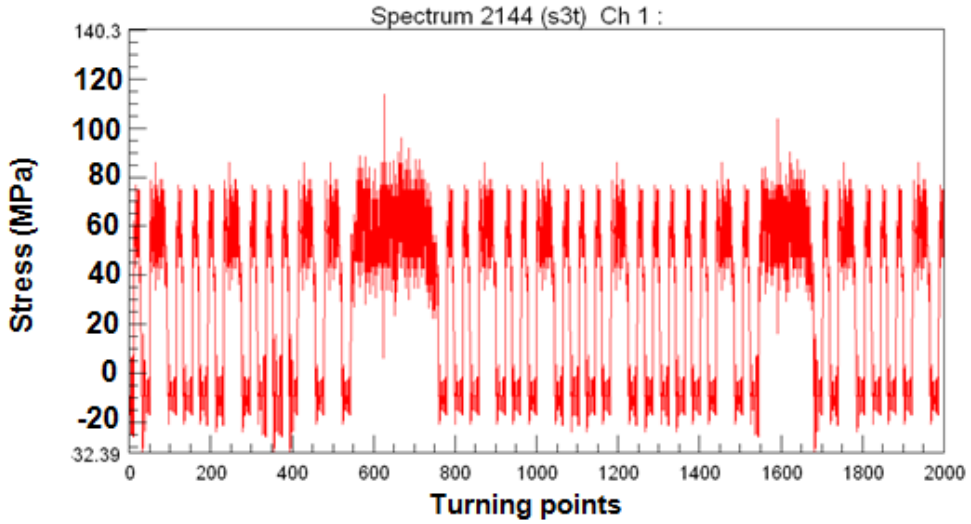

Figure A-1: First 2000 turning points of original loading spectrum 2144

The maximum stress is 140.3 MPa and the minimum stress, -32.39 MPa.

The software nCode was used to perform a rain flow cycle count of the original spectrum in order to see the distribution of the cycles. The result of this rain flow cycle count is shown as a range/mean histogram representation of the number of cycles (Figure A-2).

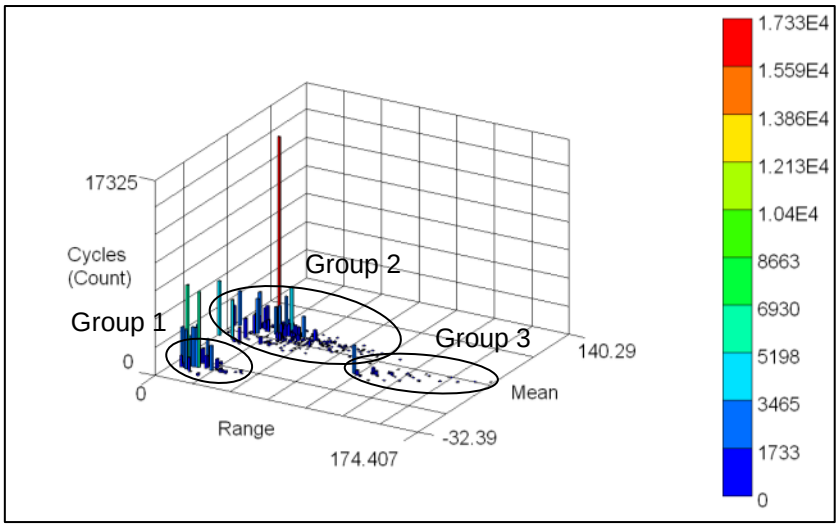

Figure A-2 : Histogram of cycle counting for original spectrum

The histogram above gives the number of cycles depending on the stress range (MPa) and the mean stress (MPa) of these cycles.

Three groups clearly appeared in this rain flow cycle count. The first one (Group 1) is made of a large number of cycles with a range lower than 15 MPa and a negative mean between -10 MPa and -20 MPa. These cycles appear clearly on the spectrum in Figure A-1 as the small cycles in the lower part of the spectrum. The second group (Group 2) has a much larger number of cycles with a range mainly between 25 MPa and 50 MPa and a mean stress around 60 MPa. These cycles also appear clearly on the spectrum part shown in Figure A-1 as the bigger cycles in the upper part of the spectrum. The last group (Group 3), with fewer cycles than the two other groups is the one with a mean stress around 20 MPa and a range above 100 MPa. These cycles correspond to the takeoff and landing cycles.

A.2 Spectrum modification

The maximum capacity of 800 kN of the test machine meant that the spectrum had to be modified in order to fit to that limit. Table- A-1 hereafter gives the cross section of the different panels that were being tested together with the loads necessary to reach the maximum and minimum stresses corresponding to the **original spectrum**.

Table- A-1 Panels cross section and corresponding test loads.

Panel	Cross section (mm^2)	σ_{max} (MPa)	σ_{min} (MPa)	F_{max} (N)	F_{min} (N)
Bolted panel, Unreinforced	5,701	140.3	-32.4	799,811	-184,646
Bolted panel, Reinforced	7,919	140.3	-32.4	1,111,102	-256,511
Integrally Stiffened Panel (ISP), reinforced	6,547	140.3	-32.4	918,555	-212,059

The panels were being tested on a 1MN Instron loading machine restricted to loads of **800,000 N** in tension and **150,000 N** in compression. Hence, from the results above it appeared that the loading spectrum had to be modified. As the maximum cross section of the series of 3 panels was 7,919 mm^2 for the reinforced bolted panel, the maximum stress achievable with the machine was σ_{max} **= 101 MPa** and σ_{min} **= -19 MPa**.

In order to reduce the maximum and minimum values of the spectrum, two methods were possible. The first method, **clipping** consists in lowering all values above 101 MPa to 101 MPa and respectively all values below -19 MPa to -19 MPa. The second method, **linear reduction** consists in applying a factor to the whole spectrum (different for positive and negative loads) in order to reduce the maximum stress of the spectrum and consequently all stresses in the spectrum. Nevertheless, the second method was not chosen for manipulating the spectrum as it would have modified the whole content of the spectrum rather than just modify the upper and lower limits of the spectrum.

Instead, the clipping method was selected. The first 2000 turning points of the clipped spectrum are given in Figure A-3 and the rain flow histogram is represented in Figure A-4.

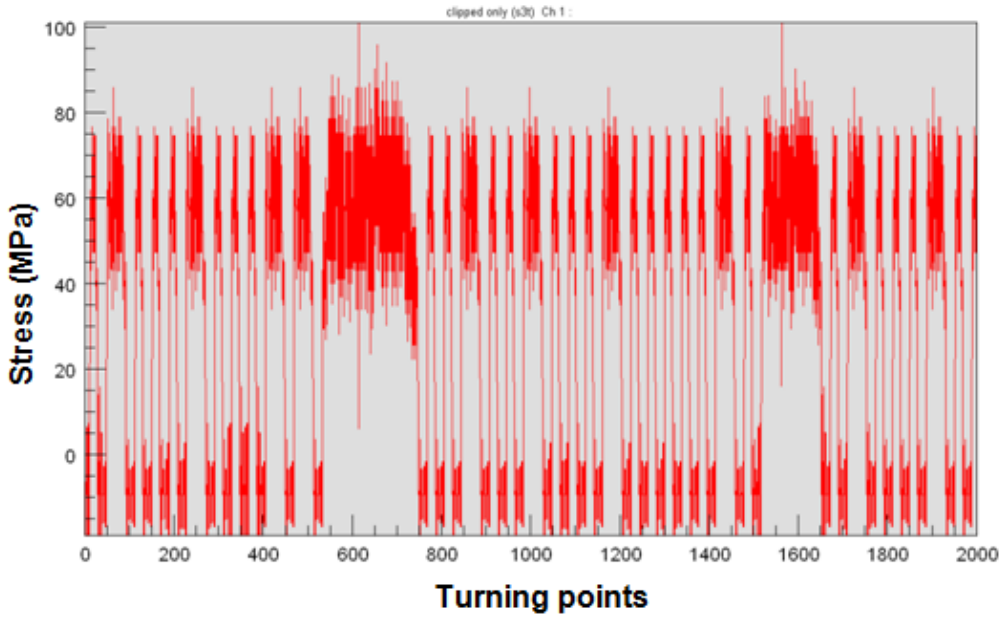

Figure A-3 : First 2000 turning points of clipped spectrum (no gating)

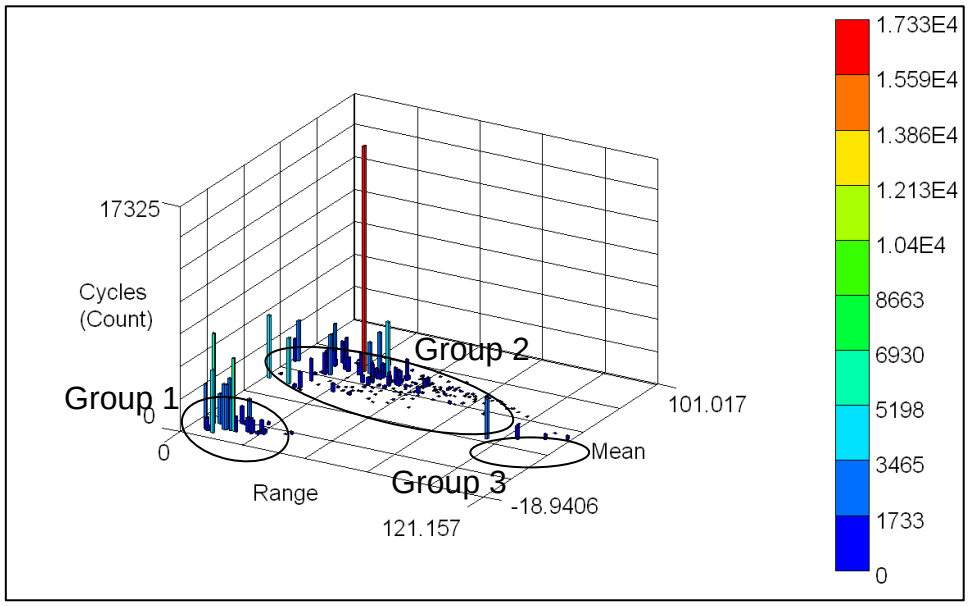

Figure A-4: Histogram of cycle counting for clipped spectrum (No gate)

As expected, one can observe that after clipping the spectrum the upper and lower limits have changed and reached values within the allowable interval of the machine. The cycles distribution (Figure A-4), has slightly changed but the

cycles distribution remained the same with a large amount of small cycles having a negative mean between -10 MPa and -20 MPa (group 1), larger cycles with a positive mean around 60 MPa (group 2) and the take-off and landing cycles (group 3).

The second manipulation concerns the number of cycles in the spectrum. In fact, as received the spectrum consists of 138,230 cycles. If the whole spectrum had been tested, this would have resulted in a very large amount of time for testing as many small cycles will be non-damaging. The solution was then to reduce the number of cycles in the spectrum in order to reduce the time of testing by a gating method. This method consists of removing the cycles that have a range lower than an amount determined by the user. Nevertheless, one must be careful when removing the low range cycles as it could change the results in terms of the damage content of the spectrum. Four gate levels were initially chosen, 10 MPa, 15 MPa, 20 MPa and 25 MPa. As shown by the rain-flow count of the original spectrum, there were a large number of cycles with a negative mean stress and a range lower than 15 MPa. Hence it was chosen to apply gates of 10 MPa and 15 MPa on the original spectrum. Moreover, as there were also a large number of cycles with a positive mean stress and a range lower than 25 MPa it was chosen to apply gates of 20 MPa and 25 MPa. The first 2000 turning points of the clipped and gated (25 MPa) spectrum are given in Figure A-5.

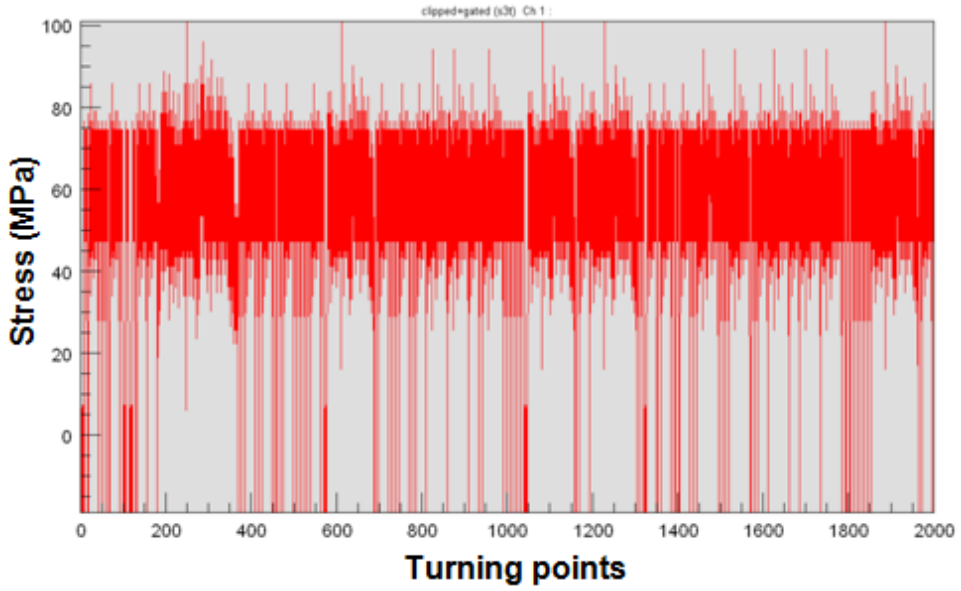

Figure A-5: First 2000 turning points of clipped and gated spectrum (25 MPa gate)

A.3 Modified spectrum

The modified spectra are given in terms of turning points and number of cycles in the next paragraphs. The modified spectrum rain-flow histograms are also given for means of comparison with the original spectrum.

A.3.1 Scenario 1: Gated original spectrum

Table A-2 : Modified original spectrum turning points and cycles number

	Gate level	Nb. Turning points	Nb. cycles
Original spectrum	No gate	276,461	138,230
	10 MPa	215,169	107,584
	15 MPa	177,343	88,671
	20 MPa	133,117	66,558
	25 MPa	116,407	58,203

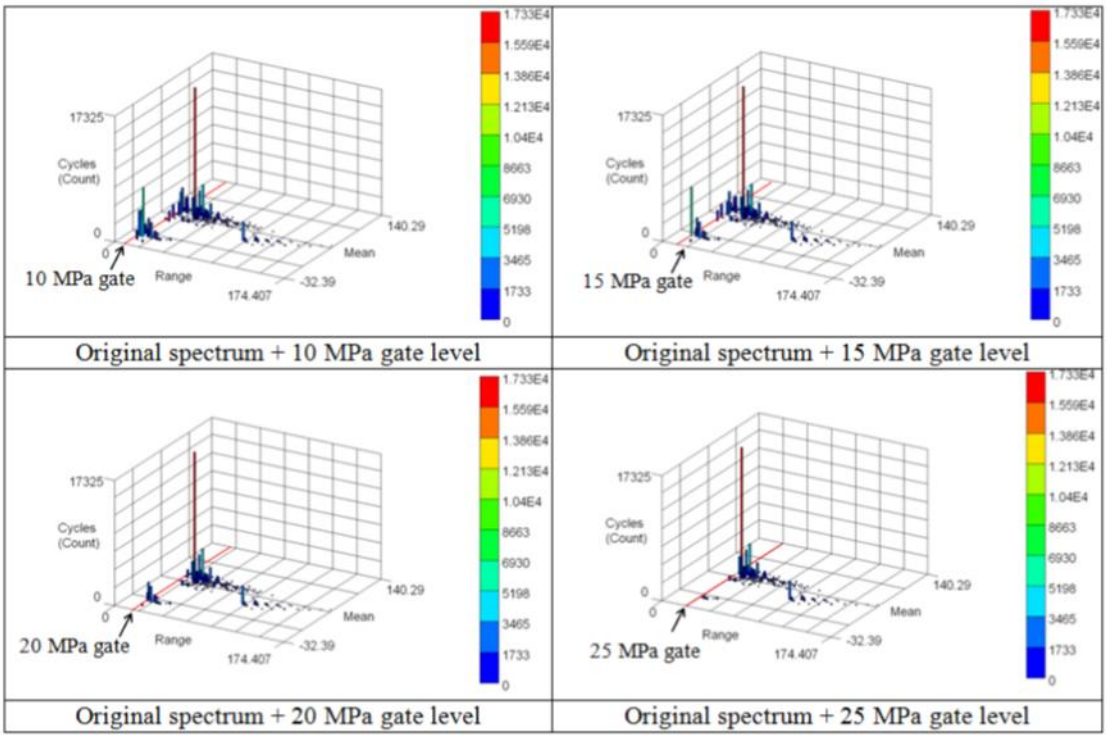

Figure A-6 : Rain flow histogram for original and gated spectra (10 MPa, 15 MPa, 20 MPa and 25 MPa gate levels)

As defined, applying a gate to a spectrum meant removing all the cycles that had a range lower than the gate level used. If the rain-flow histogram of the spectrum gated to a level of 10 MPa, respectively 15 MPa, 20 MPa and 25 MPa is compare to the rain-flow histogram of the full spectrum (Figure A-2) one can see that all the cycles with a range lower than 10 MPa respectively 15 MPa, 20 MPa and 25 MPa do not appear as they have been removed from the spectrum during the rain-flow counting as pointed out on Figure A-6. Moreover the three groups that have been described in Figure A-2 are still present with the number of cycles in group 1 (negative low range cycles) mainly reduced due to a large gate level.

A.3.2 Scenario 2: Gated and clipped spectrum

The clipped and gated spectra are given in terms of turning points and number of cycles (Table A-3). The modified spectrum rain-flow histograms are also given for comparison with the original spectrum (Figure A-7).

Table A-3 : Modified clipped spectrum turning points and cycles number

	Gate level	Nb. Turning points	Nb. cycles
Clipped spectrum	No gate	276,461	138,230
	10 MPa	212,469	106,234
	15 MPa	176,959	88,479
	20 MPa	132,733	66,366
	25 MPa	116,021	58,010

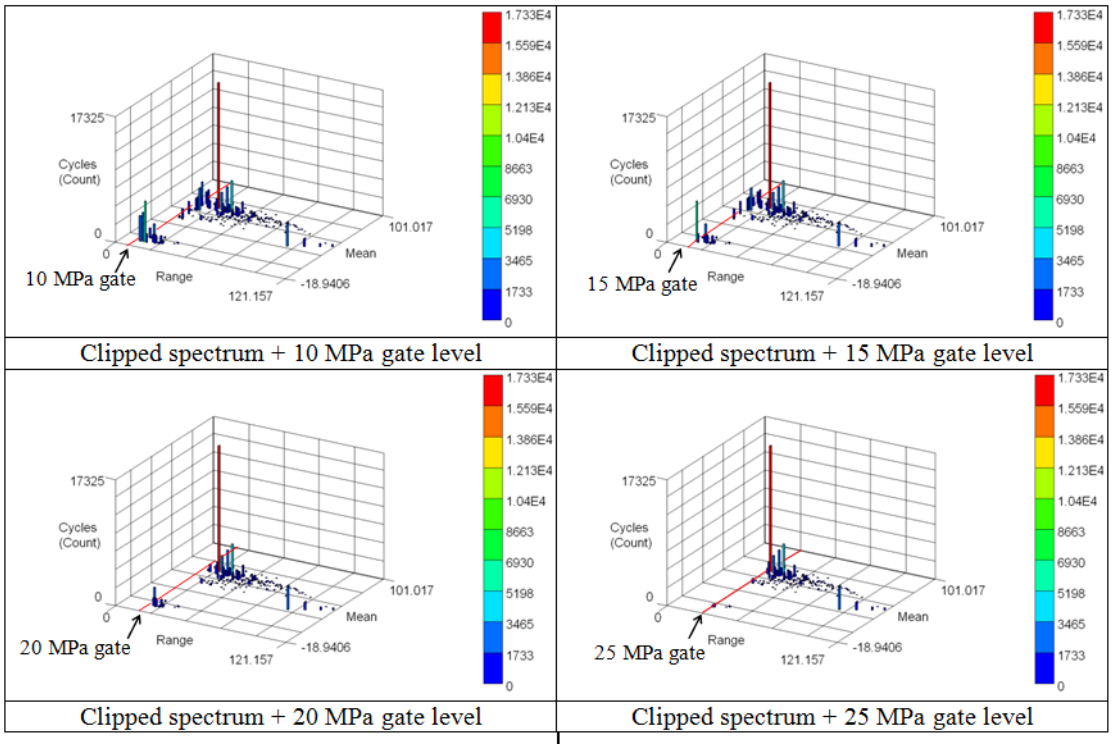

Clipped spectrum + 10 MPa gate level | Clipped spectrum + 15 MPa gate level

Clipped spectrum + 20 MPa gate level | Clipped spectrum + 25 MPa gate level

Figure A-7 : Rain flow histogram for clipped and gated spectra (10 MPa, 15 MPa, 20 MPa and 25 MPa gate levels)

A.4 Life predictions

In order to evaluate the effects on life of the manipulations described above, the fatigue life of a non-reinforced M(T) sample was calculated with different spectra which are clipped and/or gated.

The aim of these life predictions were to explore if the clipping manipulation was a convenient method to reduce the limits of the original spectrum. If the clipping manipulation that is carried out on the original spectrum is good, the number of repeats of spectrum (life prediction) should not change in a large amount between the original spectrum and the clipped one.

Regarding the gating manipulation, several gate levels have been investigated in order to reduce the time duration of the tests. Nevertheless it was necessary to study what was the optimum gate to use – optimum range in the spectrum – in order to get results that were still representative of the original spectrum.

The life predictions were calculated with AFGROW (v4.0009e.12). The details of the life prediction are given hereafter.

Model:

The model used was a through crack with a user defined beta solution. The analytical solution of beta for a MT specimen was used in that case:

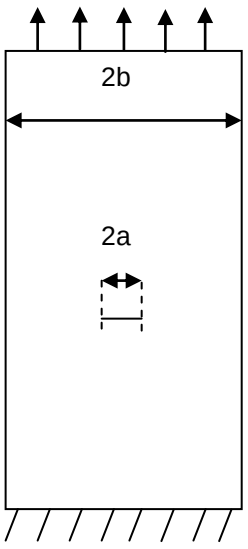

$$\beta = \sqrt{\frac{1}{cos\left(\frac{\pi a}{2b}\right)}} \quad \textbf{(A-1)}$$

Figure A-8 : M(T) coupon and beta analytical solution

The dimensions applied were:

Width (W) = 0.070 m
Thickness (T) = 0.005 m
Crack length = 0.010 m

Material:

The material properties used for the simulation were those for 2624 – T351 (2024 HDT) that was used for part of the panels and coupons tested. The tabular lookup material input was used. The fatigue crack growth rates data at R = 0.1 and R = 0.5 were used for the calculations.

Retardation model:

The closure model was used in order to take into account the effect of retardation caused by the spectrum. During a variable amplitude fatigue crack growth test [161] performed on a non-reinforced specimen under a clipped and gated (25 MPa) spectrum, with maximum stress of 101 MPa, the fatigue life reached 222,788 cycles. This experimental value was used in order to calculate the closure factor in the crack growth model by tuning the calculation. The closure factor was determined as 0.6159 for that spectrum.

A.5 Results

Table A-4 hereafter gives the results of the simulation together with an estimate of the duration of the test in case of a test that is run at a frequency of 1 Hz.

Table A-4 : Life prediction simulation results

Spectrum	Gating	Nb cycles	No retardation			Retardation		
			Cycles	repeats	Duration (hours)	Cycles	repeats	Duration (hours)
Original	No	138,230	429,415	4	119	717,271	6	199
	10 MPa	107,584	334,219	4	93	558,206	6	156
	15 MPa	88,671	275,485	4	77	460,049	6	128
	20 MPa	66,558	210,755	4	59	345,152	6	96
	25 MPa	58,203	184,227	4	52	301,775	6	84
Clipped	No	138,230	454,966	4	127	572,062	5	159
	10 MPa	106,234	349,759	4	98	439,606	5	123
	15 MPa	88,479	291,360	4	81	367,084	5	102
	20 MPa	66,366	219,058	4	61	275,736	5	77
	25 MPa	58,010	191,455	4	54	240,454	5	67

- The fatigue life predictions for the original spectrum with no gating shows that gating is necessary as the tests can run for up to 9 days (1 Hz) for an unreinforced M(T) specimen (calculation with retardation).
- The gating manipulation demonstrates that the duration of the tests can be greatly reduced by a factor of more than two, going from a 119 hours test (Original spectrum – No gate) to a 52 hours test (Original spectrum – 25 MPa gate). This is explained by the fact that the number of cycles in the spectrum has been majorly reduced with the deletion of the less damaging cycles.

- Moreover, the number of repeats for the no gate case and the gated cases stays to 4, which suggests that no highly damaging cycles were removed through this manipulation
- Clipping the spectrum did not change the number of repeats of the spectrum before failure for the case with no retardation. In fact, for all the cases of clipped spectrum the number of repeats stays approximately to 4. Nevertheless when the retardation is introduced in the calculations, the number of cycles increased slightly due to the retardation effect which appears to be higher for the original spectrum than for the clipped one. This is due to the larger amplitude cycles present in the original cycles which are reduced in the clipped spectrum.
- Nevertheless, one can observe an increase in the duration of the tests; 119 hours for the non-gated original spectrum compared to 127 hours for the non-gated clipped spectrum. This increase can be attributed to the fact that the clipping manipulation has removed the largest load excursions which were damaging. Once the retardation effects were included in the model the effect was reversed with lower duration of test. This is due to the retardation effect mentioned in the previous paragraph.
- The experimental value of 2.22×10^5 cycles can be compared with the predicted life of 2.4×10^5 cycles- an over prediction of less than 8% of the original life. This gives confidence in the AFGROW model and in the calculated values of the effects of spectrum manipulation in the table above.

A.6 Conclusions

The main conclusion of this computation is that the clipping method was a satisfactory method for the truncation of the spectrum.

For the clipped spectrum, the lives obtained are slightly reduced compared to the lives of the original spectrum, which confirms that the clipping manipulation did not remove the most damaging cycles. The changes in lives are mainly due to the changes in the retardation effect. With no retardation

effect, a slight increase in the duration of the tests can be explained by the fact that the largest load excursions have been removed and that these cycles were more damaging cycles. Nevertheless with the retardation effect, this outcome is reversed with longer lives for the original spectrum than for the clipped one. There is a certain balance here between whether or not the largest excursion are present which will reduce the fatigue life of a specimen but also increase it at the same time due to a larger retardation effect.

Moreover, the gating manipulation proves to be a mean to reduce the duration of the tests by a factor of approximately 2 as proved the example of the unreinforced M(T) sample with 6 days test for a non-gated clipped spectrum and a 3 days tests for a 25 MPa gated clipped spectrum.

That is why the clipped spectrum with respective maximum and minimum stresses of 101 MPa and -19 MPa together with a 25 MPa gate level was chosen in order to perform the tests.

A.7 Late modifications

During the course of the project, it appeared during the calibration stage of the panel tests that the cross sections of some of the panels (reinforced ones) were greater than expected. Hence, the maximum stress limit of 101 MPa was no longer achievable by the test machine. It was found that the maximum stress had to be reduced to 97.7 MPa.

Hence a second clipping manipulation was applied to the spectrum in order to reduce the maximum stress from 101 MPa to 97.7 MPa. The gate level was kept to 25 MPa.

A simulation was performed in order to evaluate the consequence of that change in maximum stress on the fatigue life of the specimen. As a reminder of the results for the clipped spectrum (101 MPa) with a gate of 25 MPa, and the retardation effect, the life was estimated to 240,454 cycles. For the newly clipped spectrum (97.7 MPa), with the 25 MPa gate and retardation effect, the life was calculated to be 216,757 cycles. Hence there was a difference of 10%.

Appendix B : Panels detailed drawings

B.1 Bolted panel skin

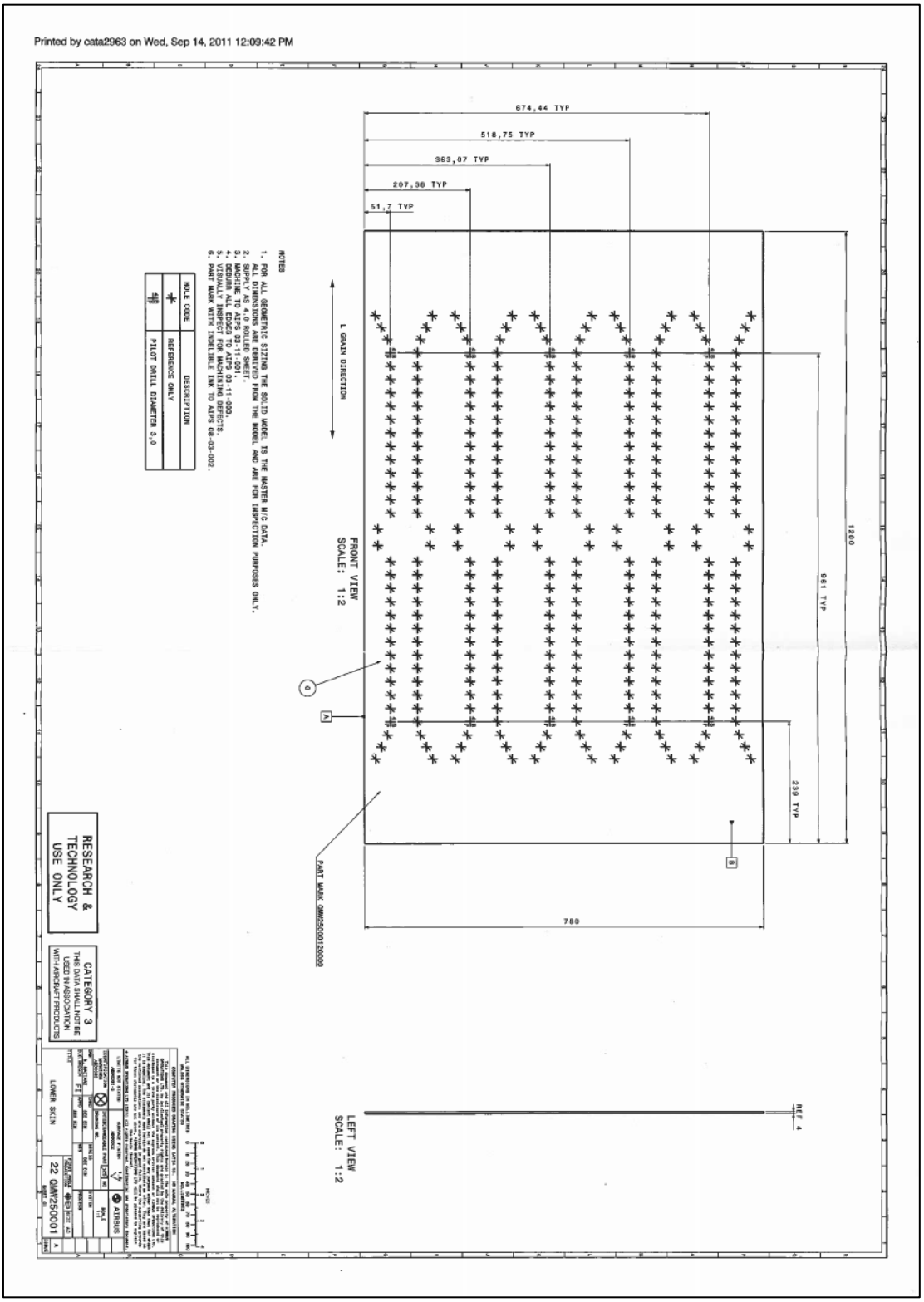

B.2 Bolted panel stringer

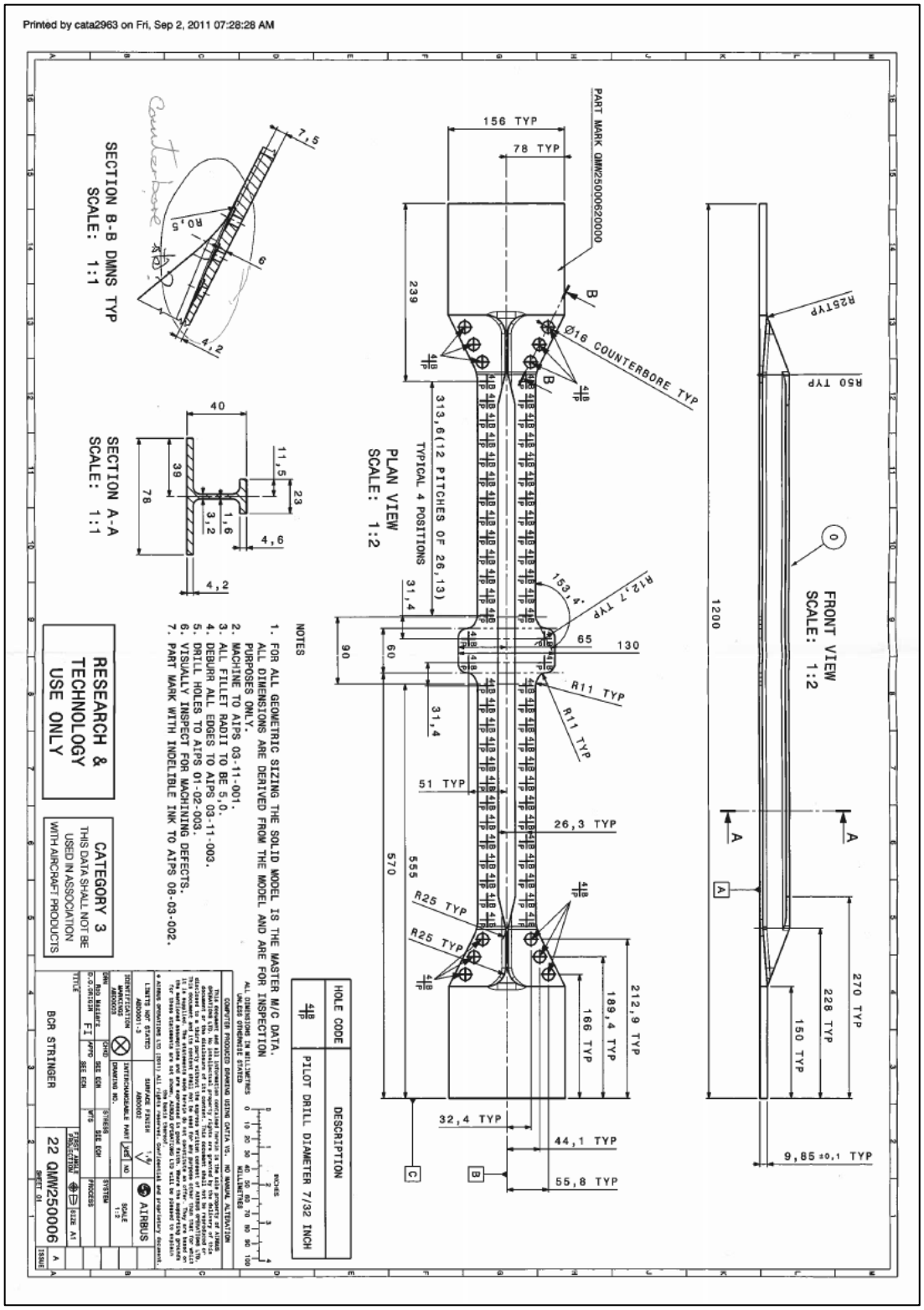

B.3 Bolted panel rib

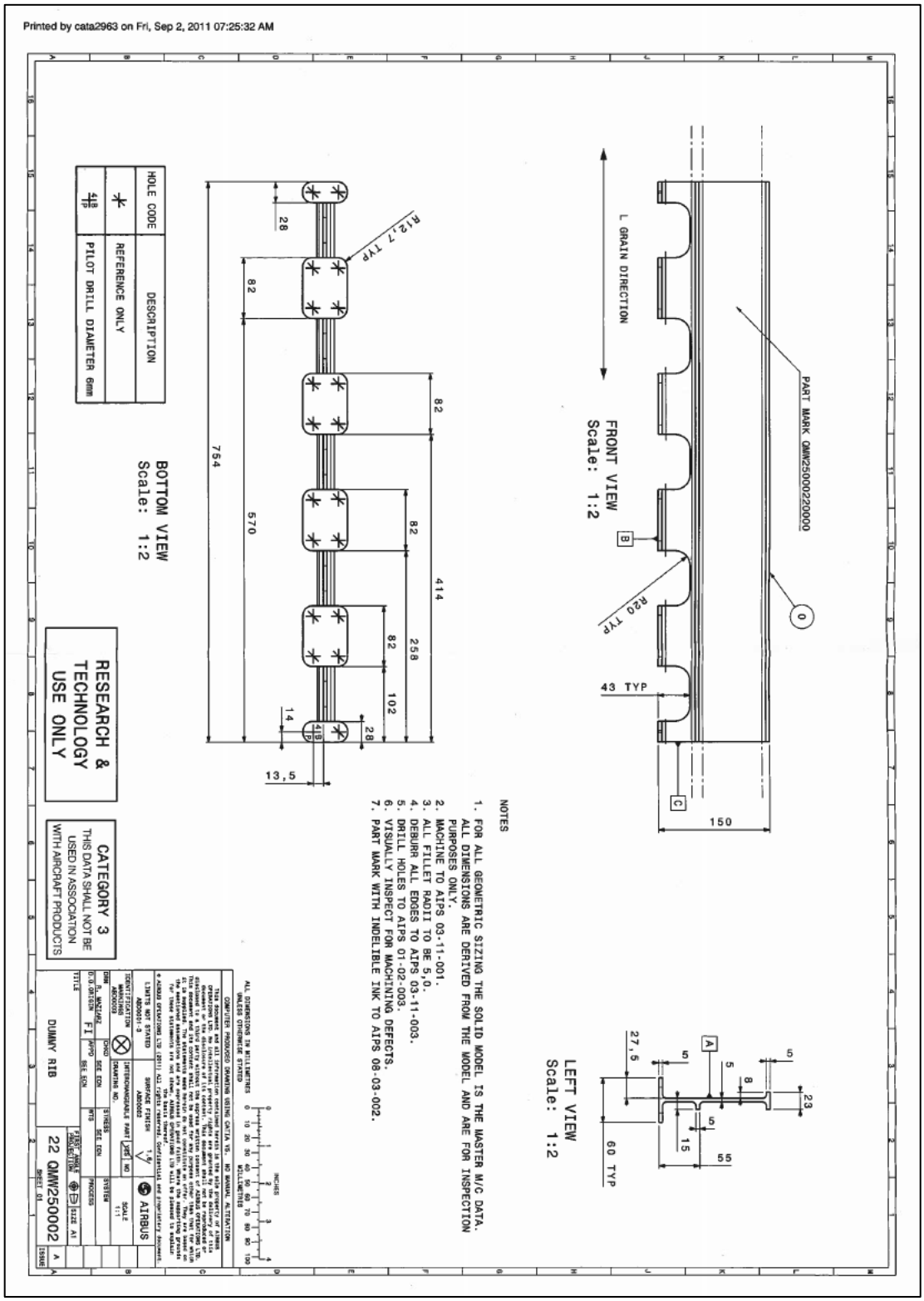

B.4 Bolted panel Glare bonded crack retarder strap

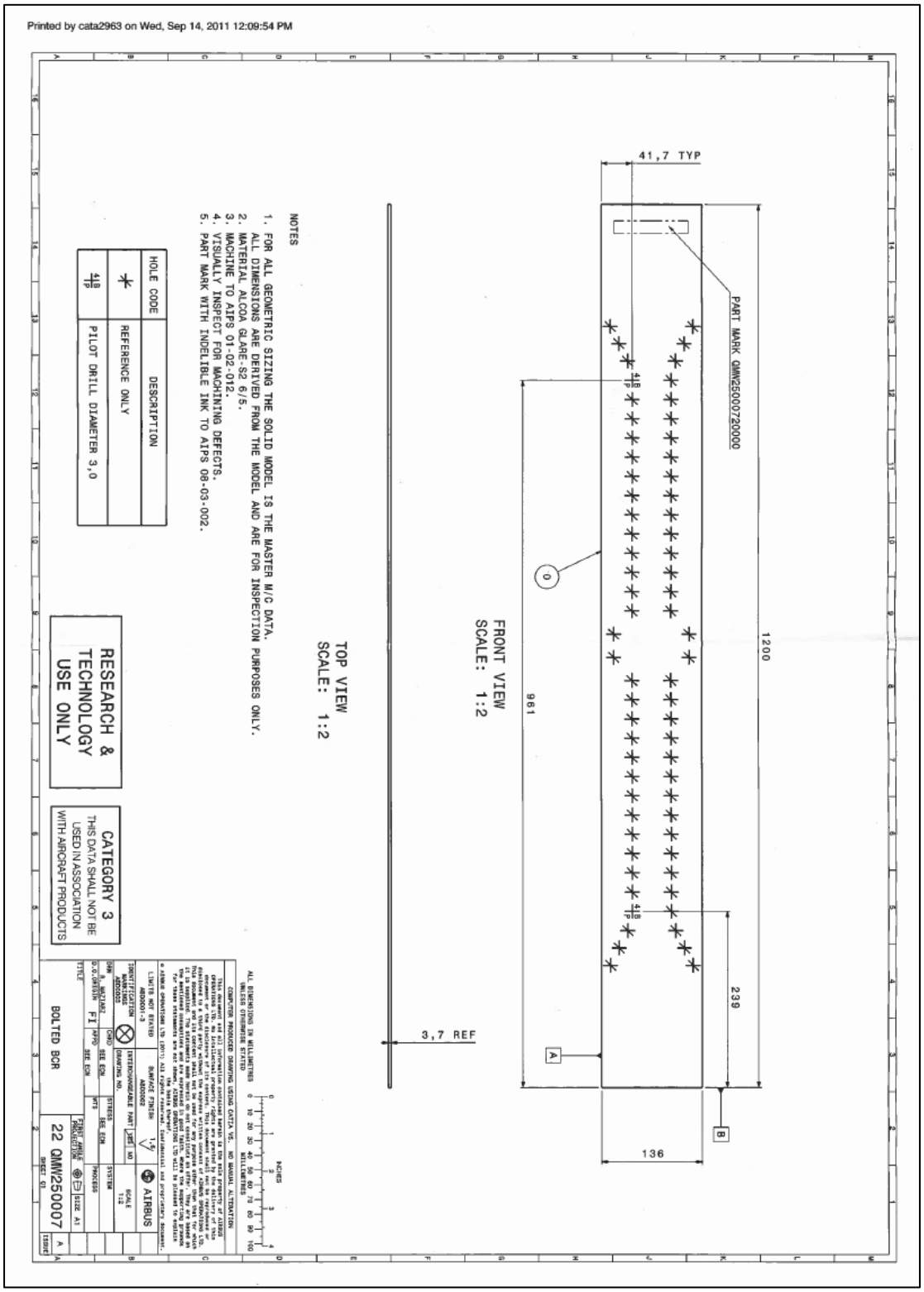

B.5 Bolted panel assembly

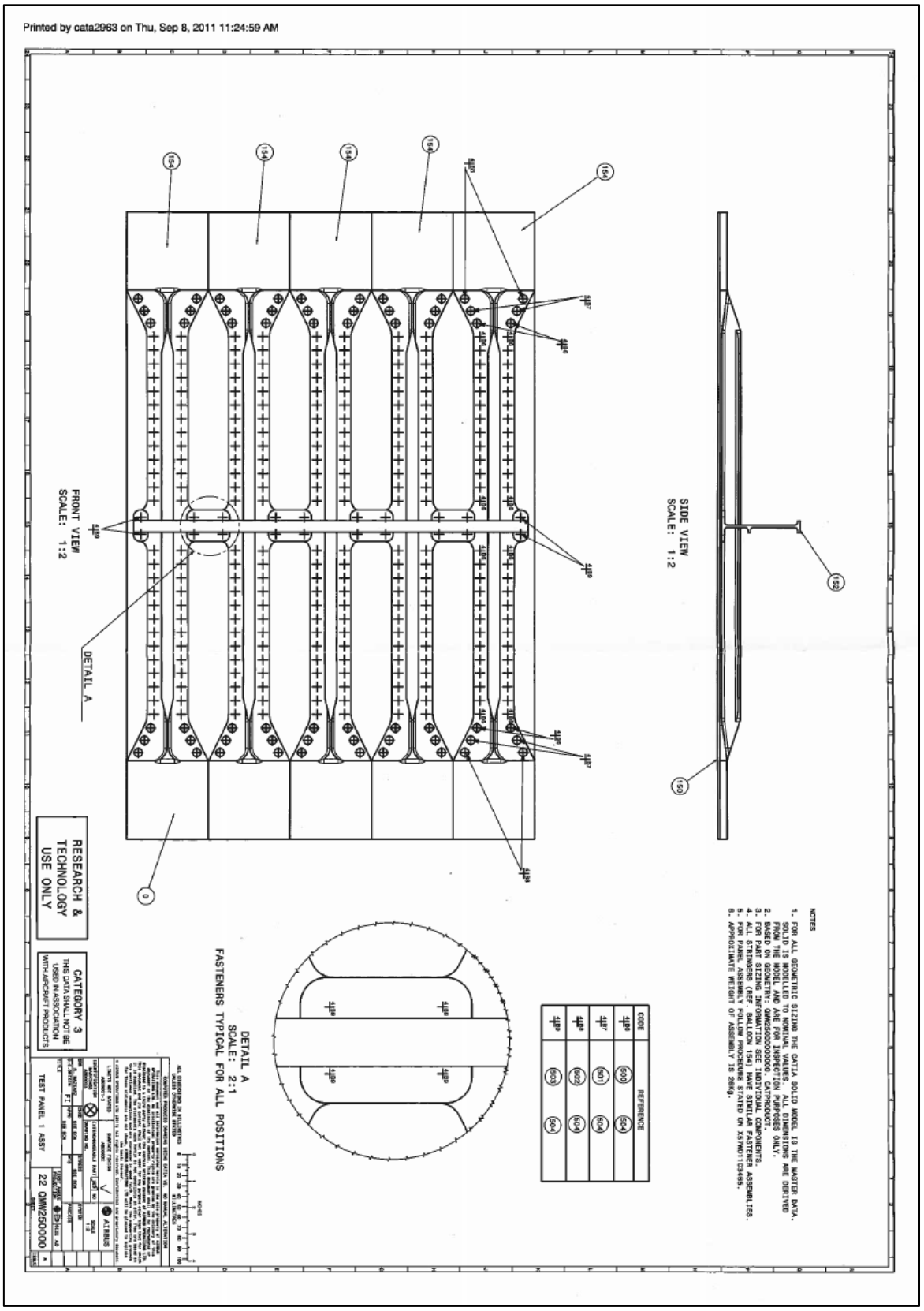

B.6 Integrally machined stiffened panel, reinforcement

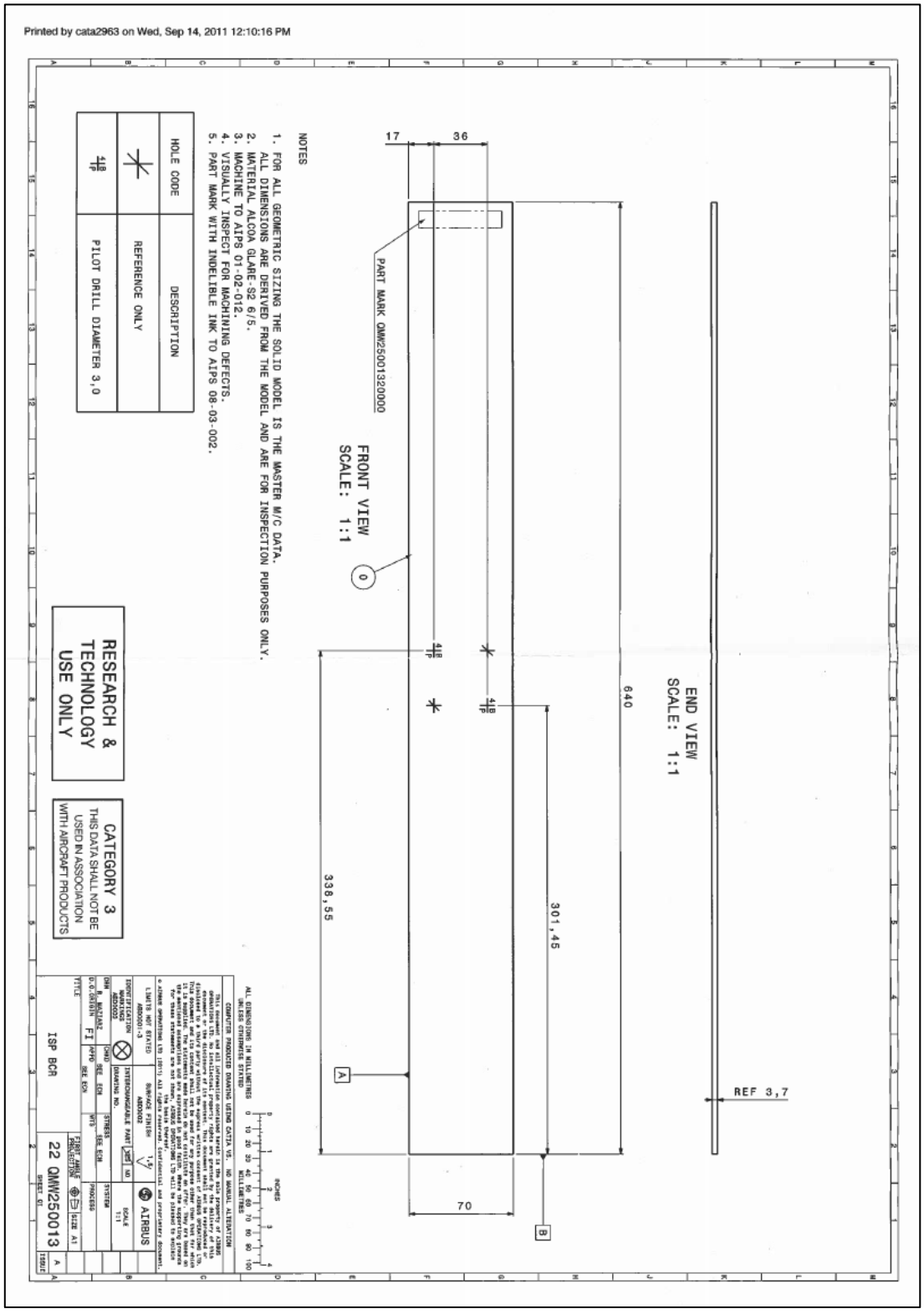

B.7 Integrally machined stiffened panel, rib

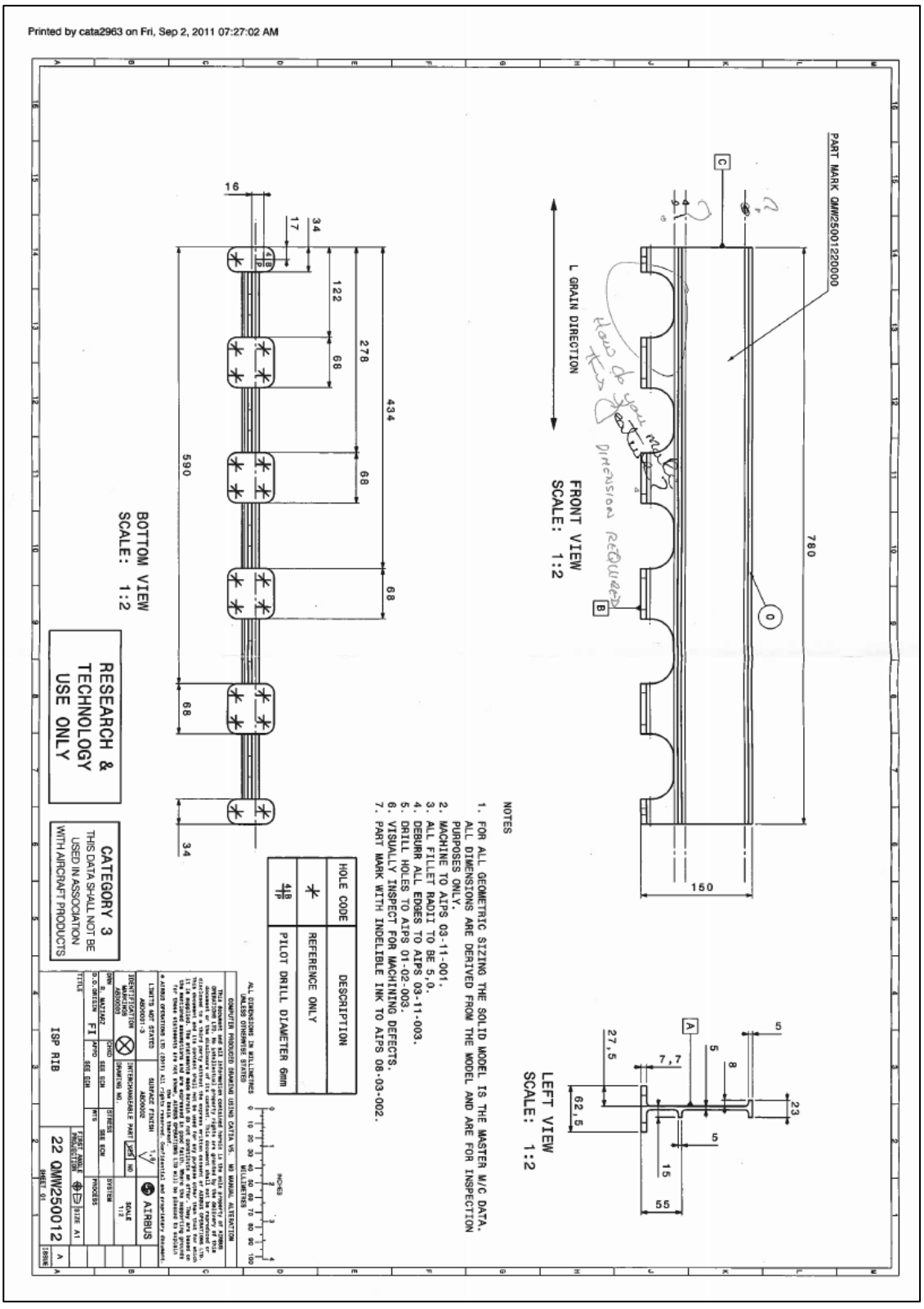

B.8 Integrally machined stiffened panel, assembly

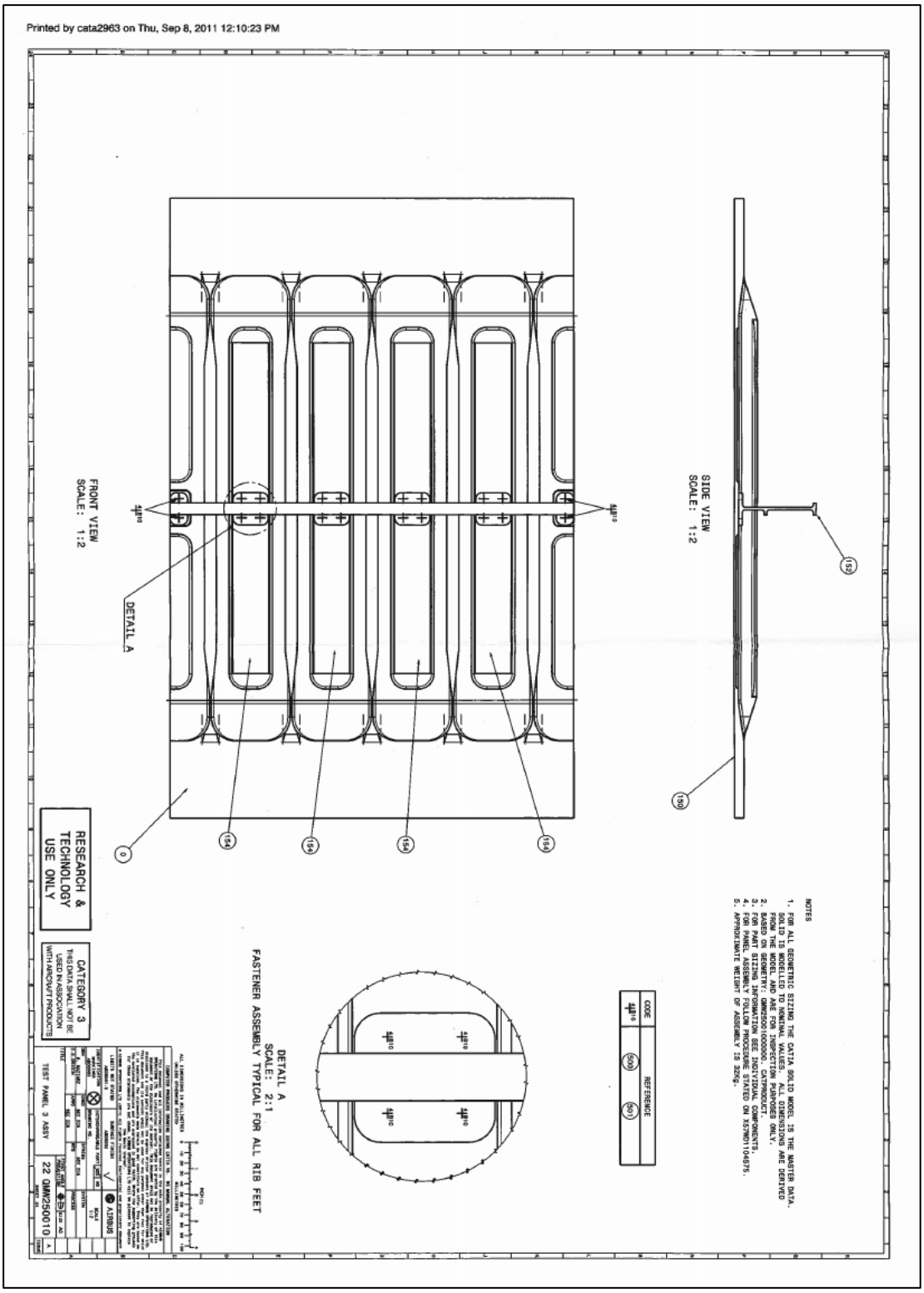

B.9 Integrally machined stiffened panel, initial damage

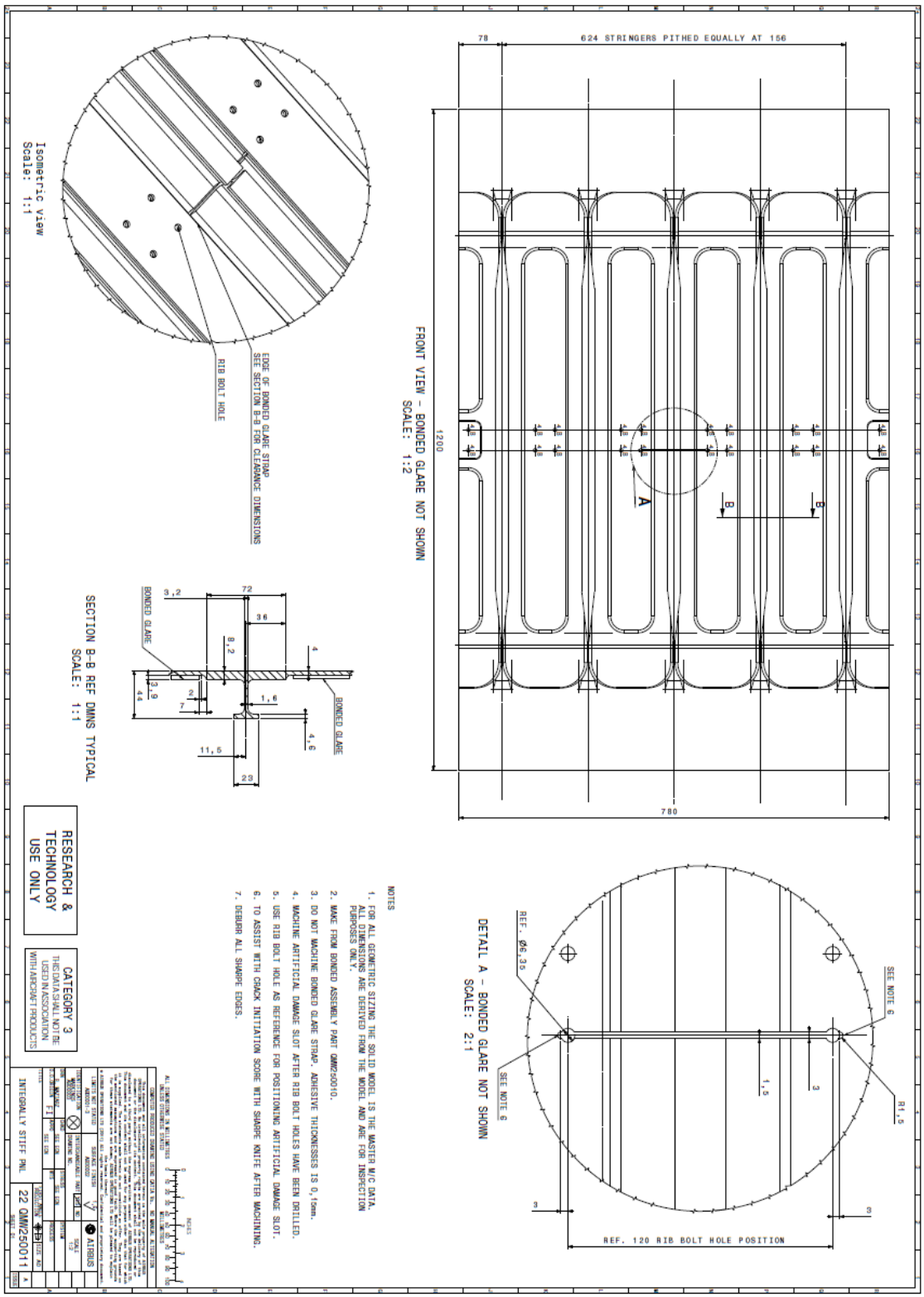

Appendix C : Strain gauge measures for 2199 Al-lith panels and 2099 ISP panel

C.1 Panel 3: 2199-T8E80 – bolted – no reinforcement (P_ALC_01) calibration

Figure C-1 and Figure C-2 show the strain gauge locations for this panel. Because the maximum stress achievable for panel 2 (2024HDT reinforced) was 97.7 MPa, it was decided to perform panel 3 at the same value of stress. A series of 5 calibration ramps was used in order to find the exact load that will provide 97.7 MPa in the reference strain gauge (strain gauge #3 here). It was found that a load of 582 kN should be used, translating the strains to stress using a skin stiffness for 2199 alloy of 75.2 GPa.

The calibration measures are given in Figure C-3 to Figure C-7. The results obtained during the calibration at maximum load are given in Table C-1. It shows the maximum strain and corresponding stress obtained for each strain gauge. The modulus used to convert measured strains to stresses is 75.2 GPa for the skin mounted gauges on 2199 alloy, and 78.7 GPa for the stringer strain gauges mounted on 2099 alloy.

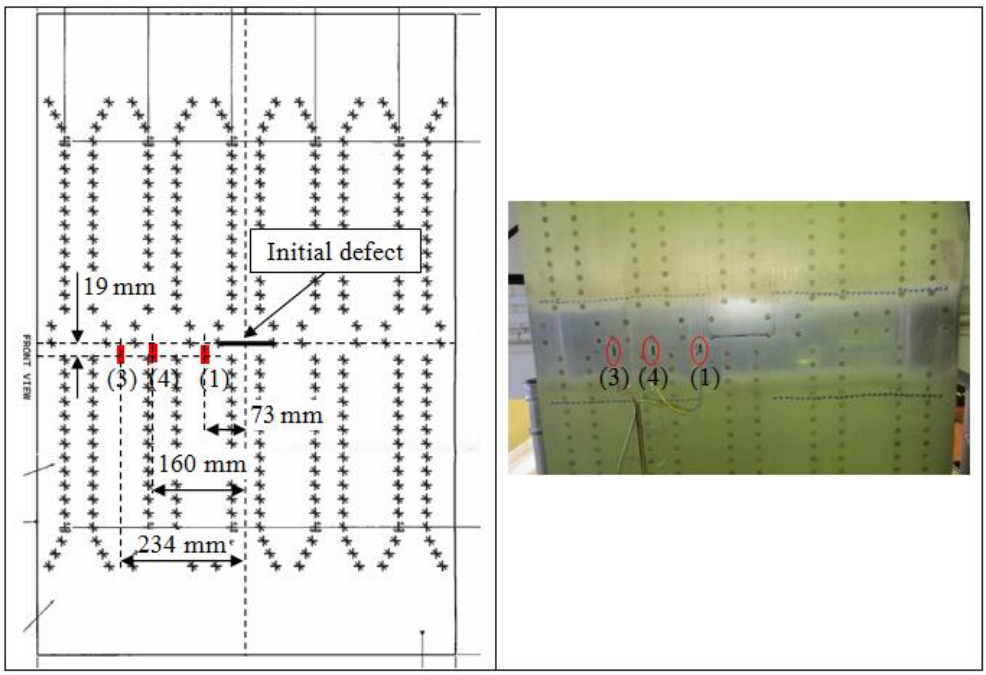

Figure C-1 : Panel 3 strain gauge location – front view (strain gauge 1, 4, 3)

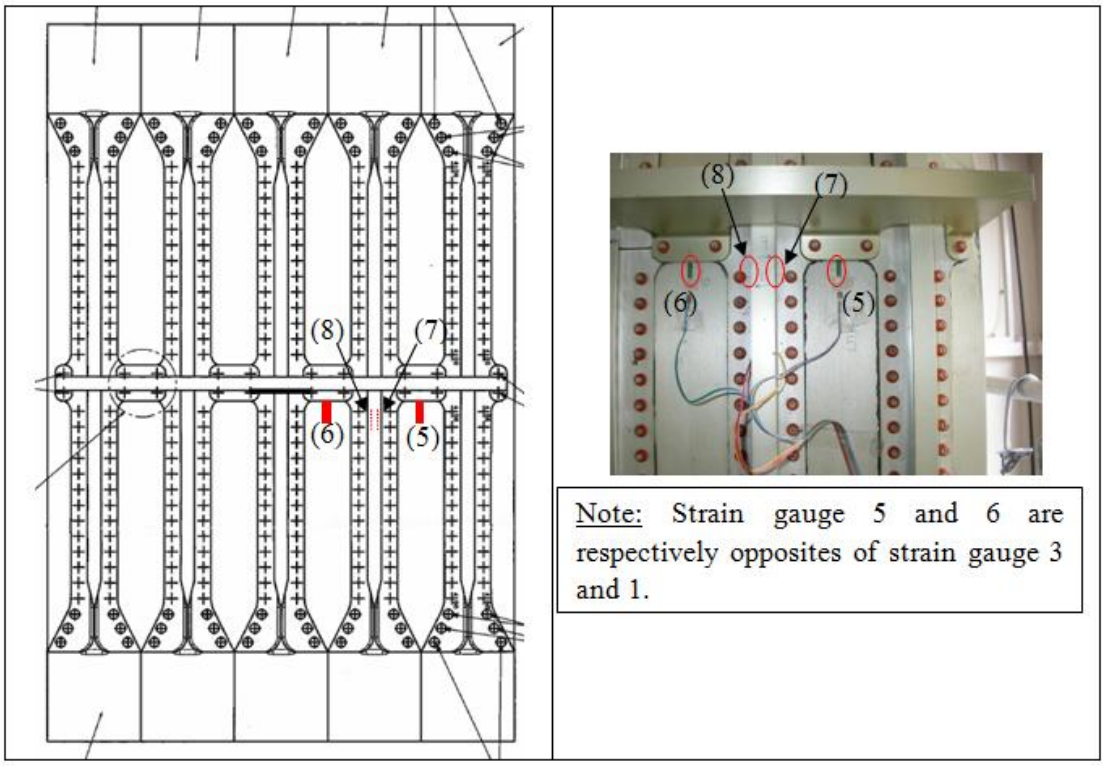

Figure C-2 : Panel 3 strain gauge location – Back view (strain gauge 5, 6; 7 and 8)

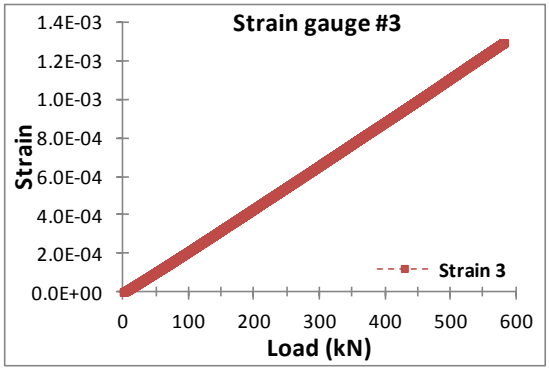

Figure C-3 : Strain gauge results from calibration at maximum load for strain gauge 3 – Panel 3

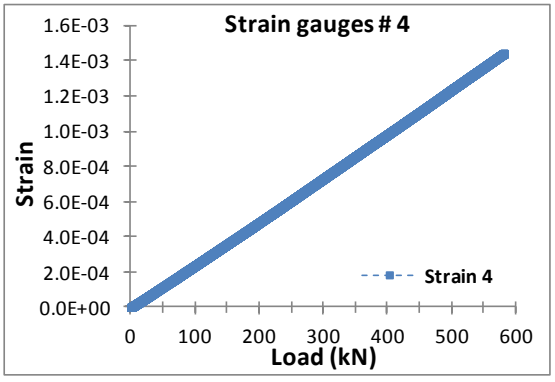

Figure C-4 : Strain gauge results from calibration at maximum load for strain gauge 4 – Panel 3

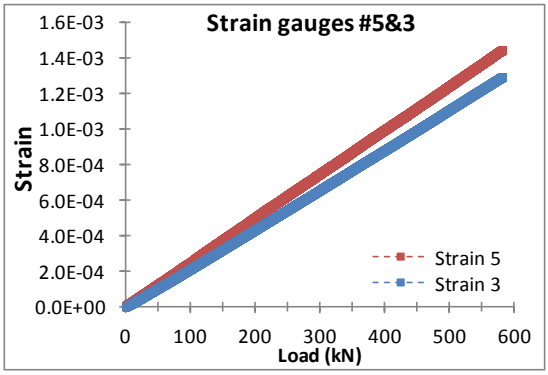

Figure C-5 : Strain gauge results from calibration at maximum load for strain gauges 5 and 3; opposite strain gauge on skin side and stringer side – panel 3

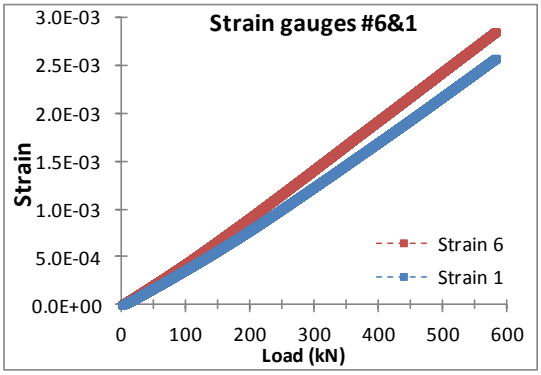

Figure C-6 : Strain gauge results from calibration at maximum load for strain gauges 6 and 1; opposite strain gauge on skin side and stringer side – panel 3

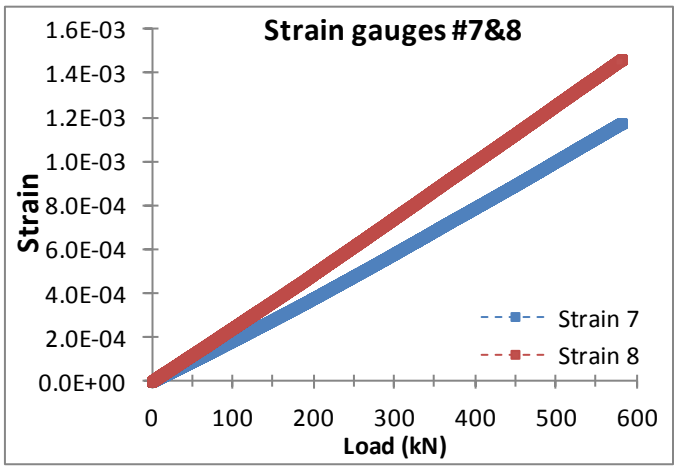

Figure C-7 : Strain gauge results from calibration at maximum load for strain gauge 7 and 8; opposite strain gauges located on the stringer – panel 3

Table C-1 : Strain gauge measurements for 2199 baseline panel

Strain gauge	Max load (N)	Max strain	Modulus (MPa)	Max stress (MPa)
#1	582,000	2.58×10^{-3}	75,200	194
#4		1.45×10^{-3}		109
#3		1.30×10^{-3}		**97.6**
#5		1.45×10^{-3}		109
#6		2.86×10^{-3}		215
#7		1.18×10^{-3}	78,700	92.7
#8		1.47×10^{-3}		116

Strain gauge #3 was used to check that the stress used for the test is close to the chosen 97.7 MPa. The strain gauges closer to the initial notch have much higher strains than the reference strain gauge #3 with 194 MPa for strain gauge #1 and 215 MPa for its coupled strain gauge #6. Strain gauges #4 and #5 have much reduced strains but higher than strain gauge #3 due to their location.

Figure C-3 shows linear behaviour obtained for strain gauge #3. As shown in Table C-1 the maximum strain is 1.30×10^{-3}. It is observed that the level of strain increases as the strain gauge is closer to the initial notch. It was observed that strain gauge #1 had a slight non-linear behaviour. Regarding coupled strain gauges 1&6 and 3&5, there is a higher strain for the stringer side than for the skin side.

C.2 Panel 4: 2199-T8E80 – bolted – Glare reinforced (P_ALC_02)

Two sets of strain gauges have been used in order to check the level of stress in the panel. The first set was the same as the previous panel (2199 al-lith) and the second one was used in order to check the stresses that compared to the other two panels (2024 HDT).

Figure C-8 and Figure C-9 show the location of the first set of strain gauges. The calibration measures are given in Figure C-10 to Figure C-14. The results obtained during the calibration at maximum load are given in Table C-2. It shows the maximum strain and corresponding stress obtained for each strain gauge.

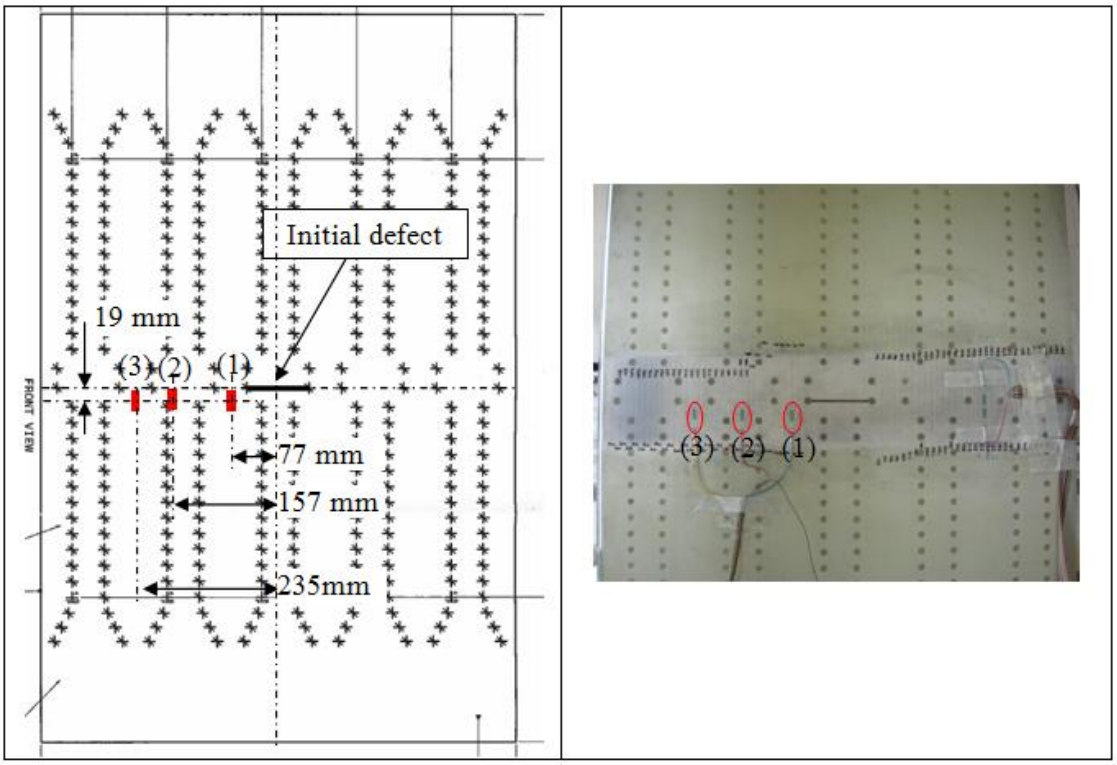

Figure C-8 : Panel 4 strain gauge location – front view (strain gauge 1, 2, 3)

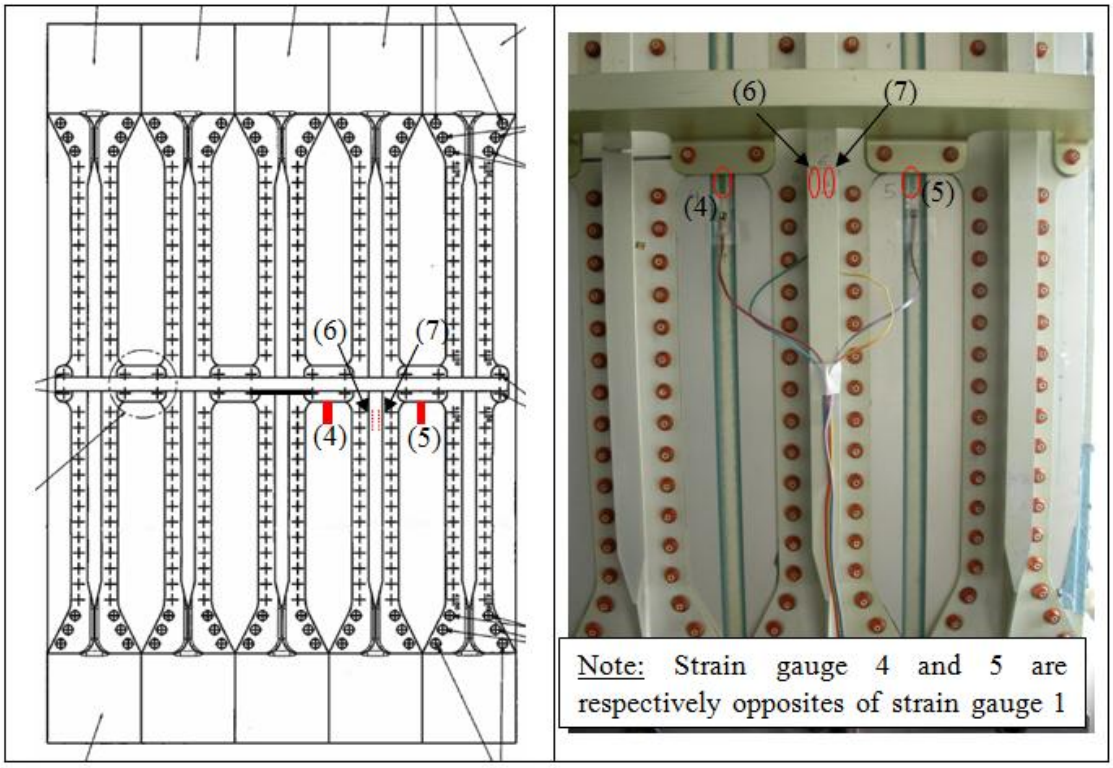

Figure C-9 : Panel 4 strain gauge location – Back view (strain gauge 4, 5; 6 and 7)

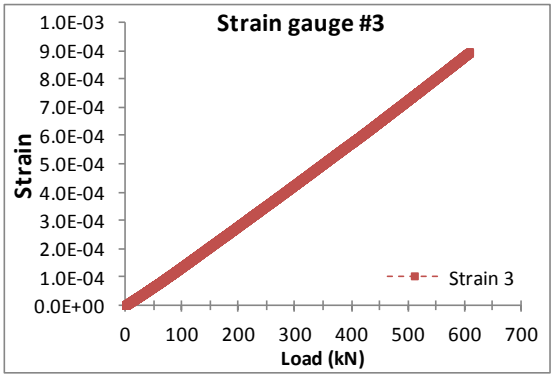

Figure C-10 : Strain gauge results from calibration at maximum load for strain gauge 3 – Panel 4

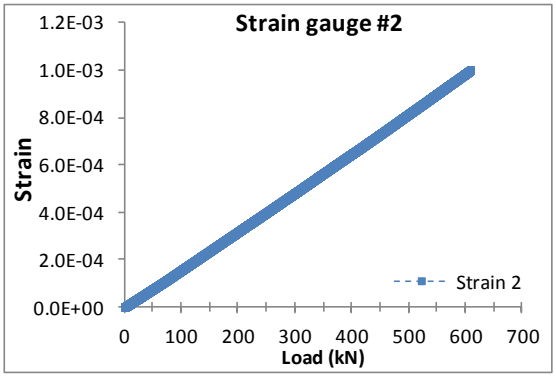

Figure C-11 : Strain gauge results from calibration at maximum load for strain gauge 2 – Panel 4

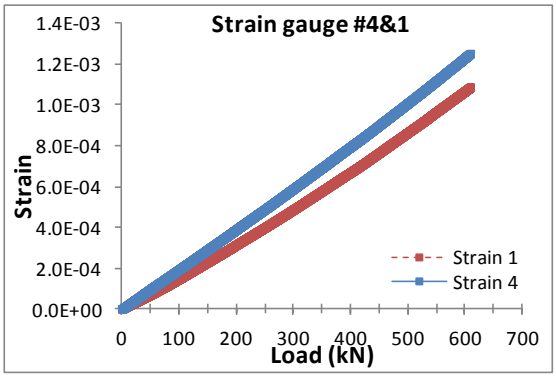

Figure C-12 : Strain gauge results from calibration at maximum load for strain gauges 4 and 1 ; opposite strain gauge on skin side and stringer side – panel 4

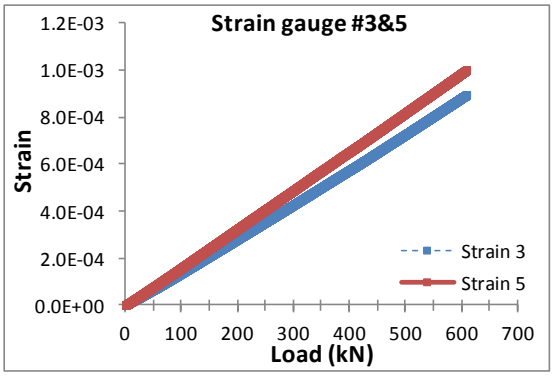

Figure C-13 : Strain gauge results from calibration at maximum load for strain gauges 5 and 3 ; opposite strain gauge on skin side and stringer side – panel 4

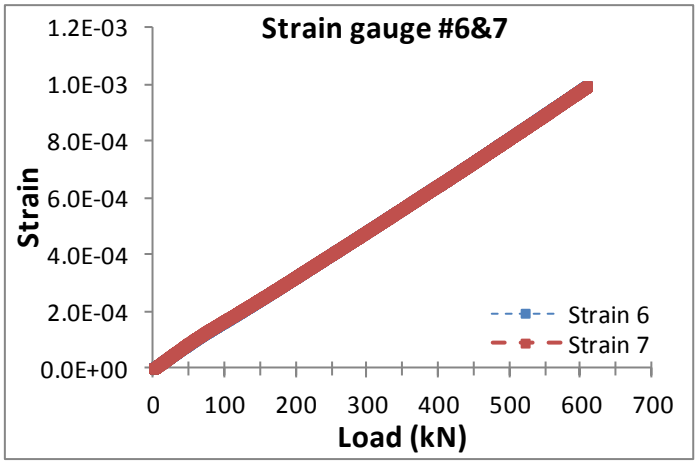

Figure C-14 : Strain gauge results from calibration at maximum load for strain gauge 6 and 7; opposite strain gauges located on the stringer – panel 4

Table C-2 : Strain gauge measurements for 2199 al-lith reinforced panel

Strain gauge	Max load (N)	Max strain	Modulus (MPa)	Max stress (MPa)
#1	790,000	$1.47x10^{-3}$	75,200	110
#2		$1.31x10^{-3}$		98.7
#3		$1.18x10^{-3}$		**89.0**
#4		$1.67x10^{-3}$		126
#5		$1.31x10^{-3}$		98.4
#6		$1.31x10^{-3}$	78,700	98.1
#7		$1.30x10^{-3}$		98.1

The reference strain gauge that is used for the comparisons to the baseline 2199 al-lith panel is strain gauge #3. It shows here a level of strain of 89.0 MPa instead of 97.7 MPa. That is why a second set of strain gauge was used, with a strain gauge symmetrically opposite to strain gauge #3 in order to verify the results obtained from strain gauge #3.

One can observe an increase in the strain level for the strain gauges closer to the initial notch (strain gauges 1, 2 and 3). Figure C-10 shows the linear behaviour obtained at strain gauge #3. As outlined in Table C-3, it shows a maximum strain of $1.18x10^{-3}$.

The second set of strain gauges used to establish the level of stresses uses similar position to the 2024 HDT panels as illustrated in Figure C-15. In that case the analysis focused on the stresses on the front of the panel.

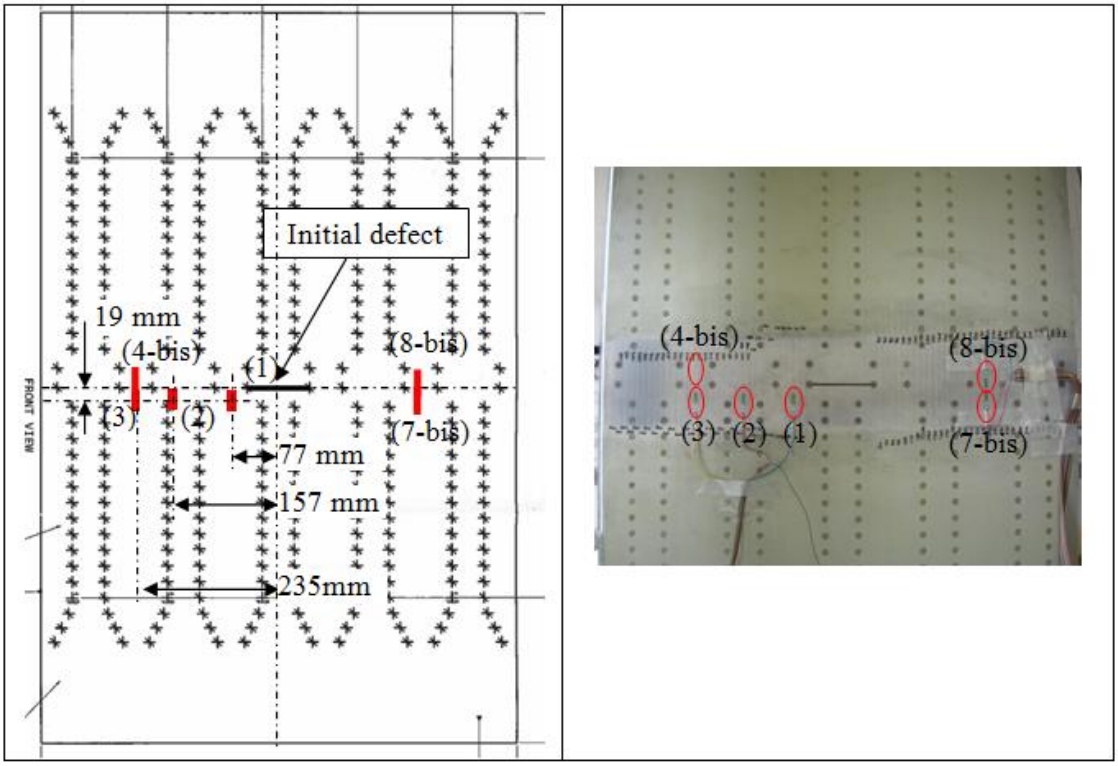

Figure C-15 : Panel 4 strain gauge location for second measurements – front view (strain gauge 1, 2, 3, 4-bis , 7-bis and 8-bis)

Note: Strain gauges 4-bis and 8-bis are aligned with the crack and symmetrically opposite while strain gauges 3 and 7-bis are symmetrically opposite from the centre line of the panel.

The results obtained from the strain gauges for this second set are given in Table C-3. It shows the maximum values obtained for each strain gauge. The analysis focuses on strain gauge 3, 4-bis, 7-bis and 8 bis.

Table C-3 : Strain gauge measurements for 2199 al-lith reinforced panel

Strain gauge	Max load (N)	Max strain	Modulus (MPa)	Max stress (MPa)
#3	790,000	1.17×10^{-3}	75,200	88.0
#4-bis		1.28×10^{-3}		96.3
#7-bis		1.22×10^{-3}		92.0
#8-bis		1.27×10^{-3}		95.8

Strain gauges #3 and #7-bis have two different level of strain with respectively $1.17x10^{-3}$and $1.22x10^{-3}$ while strain gauges #4-bis and #8-bis have similar strain levels with respectively $1.28x10^{-3}$ and $1.27x10^{-3}$. This suggests an error in the reading of strain gauge #3 as it should give a similar level of strain as strain gauges #7-bis. Hence results obtained from strain gauge #3 were discarded and the strain gauge was removed from the panel.

C.3 Panel 5: 2099 – T81 ISP – reinforced (P_COU_03)

Figure C-16 and Figure C-17 show the strain gauge locations for this panel. Calculations showed that the cross section of this panel was 7180 mm^2. Hence the calculated maximum load to reach 101 MPa is 725,180 N. The panel was loaded using a ramp loading up to that maximum load while recording the strain gauge measurements. Strain gauge #3 was used as a reference strain gauge to determine the load to produce a stress of 101 MPa as the maximum stress in the load spectrum. The results obtained for all the strain gauges are given in Table C-4. It shows the maximum values obtained for each strain gauge. The calibration measures are given in Figure C-18 to Figure C-21.

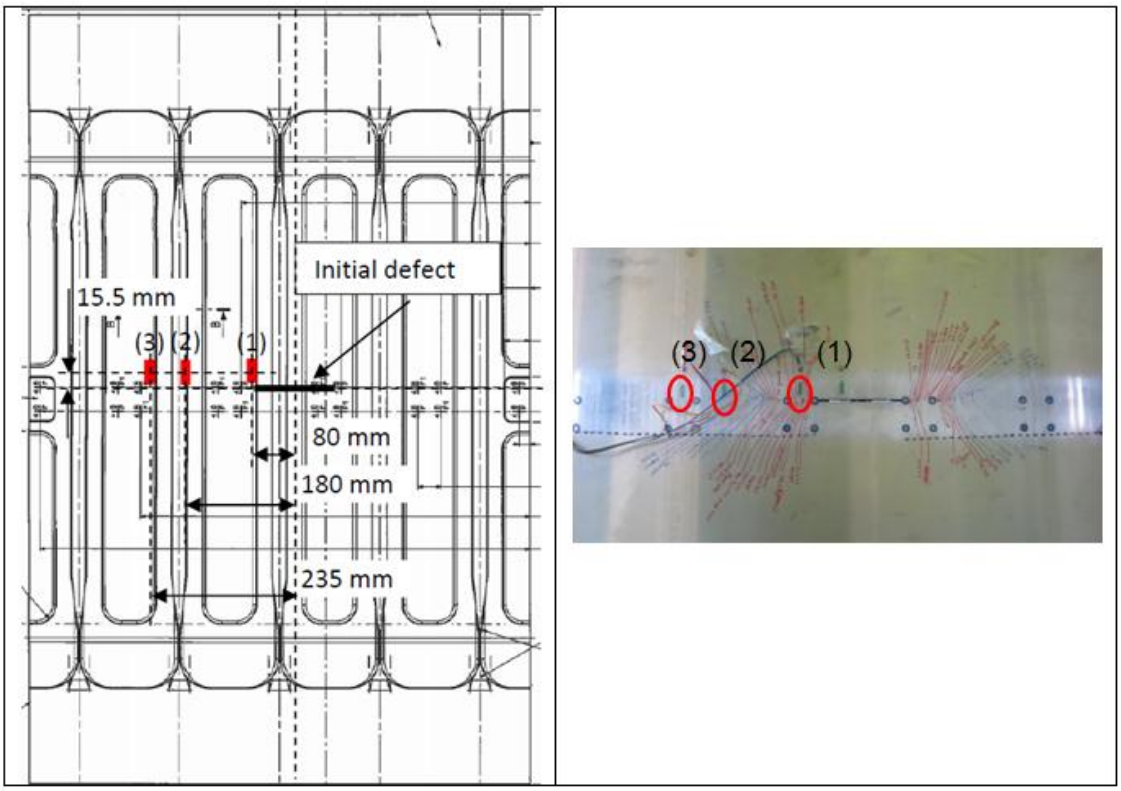

Figure C-16 : Panel 5 strain gauge location – front view (strain gauge 1, 2, 3)

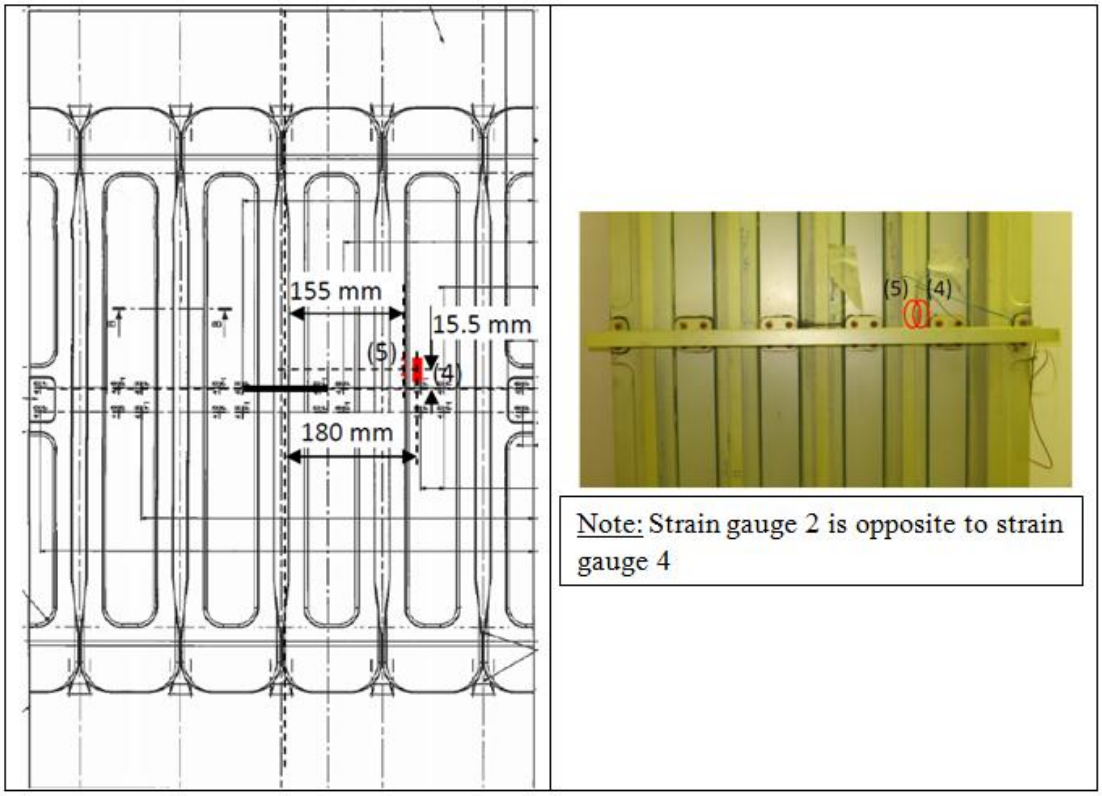

Figure C-17 : Panel 5 strain gauge location – Back view (strain gauge 4, 5)

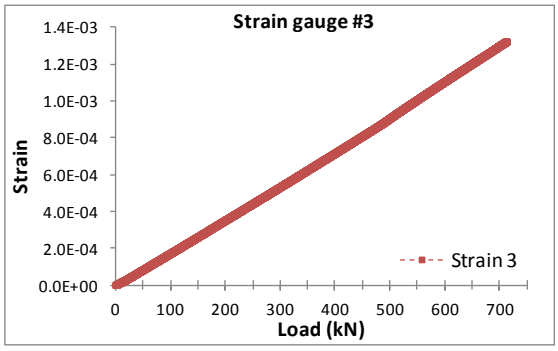

Figure C-18 : Strain gauge results from calibration at maximum load for strain gauge 3 – Panel 5

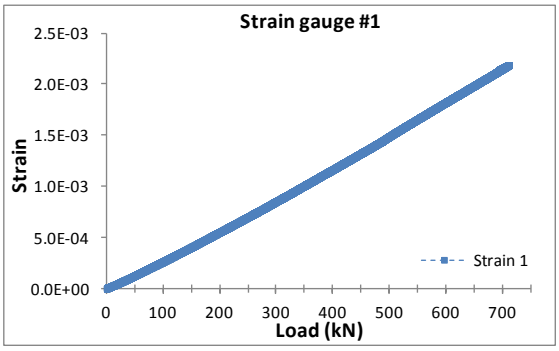

Figure C-19 : Strain gauge results from calibration at maximum load for strain gauge 1 – Panel 5

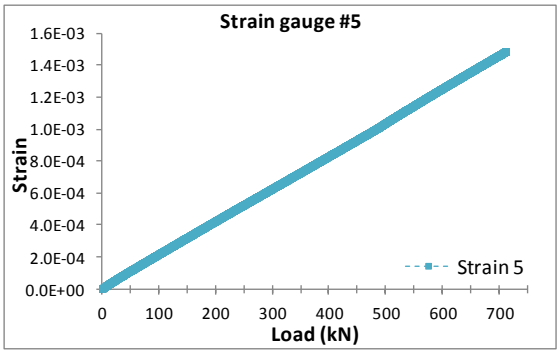

Figure C-20 : Strain gauge results from calibration at maximum load for strain gauge 5 – Panel 5

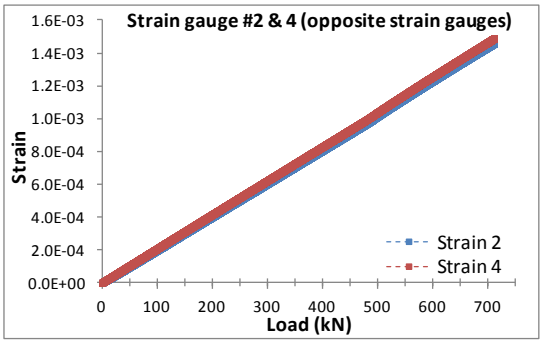

Figure C-21 : Strain gauge results from calibration at maximum load for strain gauges 2 and 4 ; opposite strain gauge on skin side and stringer side – panel 5

Table C-4 : Strain gauge measurements for 2099 – T81 ISP reinforced panel

Strain gauge	Max load (N)	Max strain	Modulus (MPa)	Max stress (MPa)
#1	712,555	2.19×10^{-3}	78,700	172
#2		1.46×10^{-3}		115
#3		1.33×10^{-3}		104
#4		1.49×10^{-3}		117
#5		1.49×10^{-3}		117

Table C-4 shows the results obtained for the three strain gauges positioned on the front of the panel. As for the other panel tested in the program, it shows a higher stress level at the strain gauge closer to the initial notch, with strain gauge #1 showing the highest level of strain. Strain gauges # 3 show a linear behaviour, while a slight nonlinear behaviour was observed for strain gauge #1 which can be interpreted as a consequence of the proximity of initial notch. Strain gauges #4 and #5 which are located close to each other on the stringer demonstrate similar level of strain. Strain gauges #2 and 4, opposite strain gauges, respectively on the front and on the back also show almost identical results.

Appendix D : Calculation of K_{eq}^{res}, equivalent residual stress intensity factor

The equivalent residual stress intensity factor K_{eq}^{res} is defined as the combination of the thermal residual stresses stress intensity factor and the effect of coupling between thermal residual stress and mechanical loads. It is assumed that the coupling is the same under maximum and minimum applied loads.

Hence $K_{eq}^{res} = K^T + K^C$ **(D-1)**.

By definition, the effective stress intensity factor is given as $R_{eff} = \frac{K_{min}}{K_{max}}$ **(D-2)** where K_{min} and K_{max} are both the combination of mechanical loads, thermal residual stress and coupling stress intensity factors at maximum and minimum applied loads.

Hence,

$$R_{eff} = \frac{K_{min}}{K_{max}} = \frac{K_{applied\ load\ (Fmin)} + K^T + K^C}{K_{applied\ load\ (Fmax)} + K^T + K^C} = \frac{K_{applied\ load\ (Fmin)} + K_{eq}^{res}}{K_{applied\ load\ (Fmax)} + K_{eq}^{res}}$$ **(D-3)**.

This equation, then leads to

$$K_{eq}^{res} = \frac{K_{applied\ load\ (Fmax)} R_{eff} - K_{applied\ load\ (Fmin)}}{1 - R_{eff}}$$ **(D-4)**.

Assuming that the non-linear effect is negligible, one can define

$$R = \frac{K_{applied\ load\ (Fmin)}}{K_{applied\ load\ (Fmax)}} = \frac{\sigma_{min}}{\sigma_{max}}$$ **(D-5)**

and it leads to $K_{eq}^{res} = \frac{K_{applied\ load\ (Fmax)}(R_{eff} - R)}{1 - R_{eff}}$ **(D-6)**.

By definition, $\Delta K = K_{applied\ load\ (Fmax)} - K_{applied\ load\ (Fmin)}$ **(D-7)**.

Hence one can deduce $\Delta K = K_{applied\ load\ (Fmax)}(1 - R)$ **(D-8)** which gives $K_{applied\ load\ (Fmax)} = \frac{\Delta K}{(1-R)}$ **(D-9)**.

All the expression developed above, once combined give:

$$K_{eq}^{res} = \frac{\frac{\Delta K}{(1-R)}(R_{eff}-R)}{1-R_{eff}}$$ **(D-10)**

Hence two major assumptions are considered here for the calculation of K_{eq}^{res} with:

1) the fact that the thermal residuals stress intensity factor and coupling are the same at maximum and minimum applied loads and
2) the fact that the non-linearity is negligible for the expression of the R-ratio.

This value of K_{eq}^{res} is calculated from the simulation at maximum and minimum loads and then used for the fatigue life calculation performed in AFGROW. Hence it incorporates the effects of thermal residual stresses and non-linearity of the BCR geometry.